Measurement of the Branching Fraction and Search for Direct CP-Violation in the Radiative Decay $B \to K^* \gamma$ with the BABAR Detector

Von der Fakultät
Mathematik und Naturwissenschaften
der Technischen Universität Dresden
zur Erlangung des akademischen Grades eines
DOKTORS DER NATURWISSENSCHAFTEN
genehmigte

DISSERTATION

vorgelegt von
Diplom-Physiker Tilmann Colberg
aus Mölln

Dresden
Februar 2002

1. Gutachter	:	Prof. Dr. Klaus R. Schubert
2. Gutachter	:	Prof. Dr. Bernhard Spaan
3. Gutachter	:	Prof. Dr. Gerald Eigen

Eingereicht am : 21. Februar 2002

Abstract

The presented study of the radiative electroweak "penguin"-decay $B \to K^*(892)\gamma$, proceeding by the $b \to s\gamma$ "loop"-transition, provides an important test of the Standard Model and a candidate of the search for New Physics. The used data sample of 22.7×10^6 $B\overline{B}$ decays, corresponding to an integrated luminosity of 20.7 fb^{-1}, has been recorded at the $\Upsilon(4S)$ resonance with the *BABAR* detector at the asymmetric e^+e^- collider PEP-II of the Stanford Linear Accelerator Center (SLAC) in California. The $B \to K^*\gamma$ branching fractions are measured in the four decay modes $K^{*\pm} \to K^\pm\pi^0$, $K^{*\pm} \to K_S\pi^\pm$, $K^{*0} \to K^+\pi^-$, and $K^{*0} \to K_S\pi^0$. The weighted average of the respective two charged and neutral modes yields $\mathcal{B}(B^0 \to K^{*0}\gamma) = (4.23 \pm 0.40(\text{stat.}) \pm 0.22(\text{sys.})) \times 10^{-5}$ and $\mathcal{B}(B^\pm \to K^{*\pm}\gamma) = (3.83 \pm 0.62(\text{stat.}) \pm 0.22(\text{sys.})) \times 10^{-5}$. A search for direct *CP*-violation in the first three self-tagging modes leads to a combined *CP*-asymmetry of $A_{CP}(B \to K^*\gamma) = -0.044 \pm 0.076(\text{stat.}) \pm 0.012(\text{sys.})$, constraining the *CP*-violating charge asymmetry to be $-0.17 < A_{CP}(B \to K^*\gamma) < 0.08$ at 90% confidence level.

Furthermore, the π^0-reconstruction efficiency and mass distribution in the real data set mentioned above and its corresponding Monte Carlo simulation is compared using τ 1-on-1 decays involving one or two resulting π^0 mesons. For π^0 energies E_{π^0} up to 3.5 GeV, a correction factor of $(-5.0 \pm 2.5)\%$ is determined for the Monte-Carlo π^0-efficiency.

Kurzfassung

Die hier vorgestellte Untersuchung des radiativen elektroschwachen "Pinguin"-Zerfalls $B \to K^*(892)\gamma$, der durch den "Schleifen"-Übergang $b \to s\gamma$ stattfindet, stellt einen wichtigen Test des Standardmodells und einen Kandidaten für die Suche nach Neuer Physik dar. Der benutzte Datensatz in Höhe von 22.7×10^6 $B\overline{B}$ Zerfällen, einer integrierten Luminosität von 20.7 fb^{-1} entsprechend, wurde auf der $\Upsilon(4S)$-Resonanz mit dem *BABAR*-Detektor am asymmetrischen e^+e^-- Speicherring PEP-II des Stanford Linear Accelerator Centers (SLAC) aufgezeichnet. Die $B \to K^*\gamma$ Verzweigungsverhältnisse wurden in den vier Zerfallskanälen $K^{*\pm} \to K^\pm\pi^0$, $K^{*\pm} \to K_S\pi^\pm$, $K^{*0} \to K^+\pi^-$ und $K^{*0} \to K_S\pi^0$ gemessen. Das gewichtete Mittel der jeweils zwei geladenen und neutralen Kanäle ergibt sich zu $\mathcal{B}(B^0 \to K^{*0}\gamma) = (4.23 \pm 0.40(\text{stat.}) \pm 0.22(\text{sys.})) \times 10^{-5}$ und $\mathcal{B}(B^\pm \to K^{*\pm}\gamma) = (3.83 \pm 0.62(\text{stat.}) \pm 0.22(\text{sys.})) \times 10^{-5}$. Eine Suche nach direkter *CP*-Verletzung in den ersten drei Kanälen führt zu einer zusammengefassten *CP*-Asymmetrie von $A_{CP}(B \to K^*\gamma) = -0.044 \pm 0.076(\text{stat.}) \pm 0.012(\text{sys.})$ und beschränkt somit die *CP*-verletzende Ladungs-Asymmetrie auf $-0.17 < A_{CP}(B \to K^*\gamma) < 0.08$ bei einem Konfidenz-Niveau von 90%.

Des Weiteren wurde die Rekonstruktions-Effizienz und die Massenverteilung für π^0-Mesonen im obig genannten realen Datensatz und der zugehörigen Monte-Carlo-Simulation verglichen, unter Verwendung von τ-"1-gegen-1"-Zerfällen mit einem oder zwei resultierenden π^0s. Für π^0-Energien E_{π^0} bis zu 3.5 GeV wurde ein Korrekturfaktor in Höhe von $(-5.0 \pm 2.5)\%$ für die π^0-Effizienz in der Monte-Carlo-Simulation bestimmt.

Contents

List of Figures

List of Tables

Abbreviations

ADC	**A**nalog to **D**igital **C**onverter
BABAR	**B** a**n**d **Bbar** Experiment
CKM	**C**abibbo-**K**obayashi-**M**askawa
CM	**C**enter of **M**ass
CP	**C**harge **P**arity
DCH	**D**rift**ch**amber
DIRC	**D**etection of **i**nternally **r**eflected **C**herenkov Light
EMC	**E**lectro**m**agnetic **C**alorimeter
FCNC	**F**lavour **C**hanging **N**eutral **C**urrents
FEE	**F**ront-**E**nd **E**lectronics
IFR	**I**nstrumented **F**lux **R**eturn
IOB	**I**nput **O**utput **B**oard
ISR	**I**nitial **S**tate **R**adiation
KANGA	**K**ind **An**d **G**entle **A**nalysis With ROOT
LAB	**Lab**oratory
MC	**M**onte **C**arlo
NLO	**N**ext **t**o **L**eading **O**rder
NP	**N**ew **P**hysics
ODF	**O**nline **D**ata **F**low
OEP	**O**nline **E**vent **P**rocessing
OPR	**O**nline **P**rompt **R**econstruction
ORC	**O**nline **R**un **C**ontrol
PDF	**P**robability **D**ensity **F**unction
PDG	**P**article **D**ata **G**roup
PEP	**P**ositron **E**lectron **P**roject
PID	**P**article **Id**entification
PMT	**P**hoto**m**ultiplier **T**ube
QCD	**Q**uantum **C**hromo **D**ynamics
ROM	**R**ead-**O**ut **M**odule
RPC	**R**esistive **P**late **C**hamber
SLAC	**S**tanford **L**inear **C**ollider **C**enter
SM	**S**tandard **M**odel
SVT	**S**ilicon **V**ertex **T**racker
XTC	**E**xtended **T**agged **C**ontainer

Chapter 1

Introduction

At the beginning of the twenty-first century, the picture embodied in the "*Standard Model* " of particle physics represents our understanding of the fundamental nature and gauge structure of the universe in terms of four forces acting on the elementary constituents of matter, being three families of quarks and leptons. Guided by the unification and simplification principle, there has been a continuous interplay between theory and precision measurements over the past 20 years, among them the discovery of the W and Z mediators of the electroweak force and the gluons as mediators of the strong force. This culminated in the LEP project at CERN, the HERA accelerator at DESY, and the detection of the top-quark at the TEVATRON at Fermilab. The absence of any deviation between experimental data and theoretical predictions at a per-mil precision has established the Standard Model ("*SM* ") to rest on solid grounds.

The major unsolved questions of contemporary particle physics consist of the reason for the matter-antimatter asymmetry in the universe, the elucidation of the origin of mass, the reason for the existence of three families of elementary particles, and the nature of the "*dark matter*" in the universe.

Bringing together particle physics and cosmology, A. Sakharov in 1967 [1] proposed that the violation of charge and parity symmetry in subatomic processes ("*CP violation*") gives a natural explanation of the matter-antimatter disequilibrium in the primordial universe and its relic, the fact that the bulk of the universe nowadays is entirely made up of matter while antimatter disappeared shortly after the Big Bang when both are believed to have been produced in equal quantities. Hence the reasons for and details of *CP* violation are vital not only for our understanding of particle physics but also for many aspects of the evolution of the Universe. The conditions which pertained infinitesimally close to the time of the Big Bang can be artificially re-created in more and more powerful and complex accelerators, thereby giving information that allow us to deduce the simple patterns and symmetries normally hidden by the complexities of the current, cool universe.

At least three families of quarks are required for a sufficient number of parameters to allow for the effect of *CP* violation, which in turn was one of the motivations for Kobayashi and Maskawa to construct their theory in 1973 [2] that describes the origin of the electroweak quark-mixing by the *CKM matrix* and had only been observed in difficult experiments on neutral K mesons [3]. Therefore, this insufficiently inves-

tigated subject has been addressed by the ambitious *BABAR* project at the world's largest linear particle accelerator and e^+e^- storage ring PEP-II at the Stanford Linear Accelerator Center (SLAC), California, and its competitor, the Belle experiment at KEK, Japan, which are both asymmetric electron-positron colliders and constitute the current pioneering, frontier discovery machines in particle physics. The main goal is a detailed study of B-meson decays, offering one of the major opportunities to search for flaws and extensions of the SM by precision measurements of various non-constrained CKM parameters, and especially to discover and understand the origin of *CP* violation in the b-quark system [4]. The *BABAR* and Belle collaborations started taking data in 1999 and have already observed a fundamental asymmetry in the disintegration of B mesons and their antimatter equivalent. The reported value of $\sin 2\beta$ from *BABAR* is 0.59 ± 0.14 [5], substantially different from zero. Although these new results agree with the current theoretical framework of the SM, the present theory is not sufficient to explain the great abundance of matter in the universe. Thus, physicists are eager to find additional *CP*-violating processes beyond the SM.
Whereas *CP* violation in the quark sector will be clarified by the B program, *CP* violation in the lepton sector will require powerful future neutrino factories. The evidence for non-zero neutrino-masses and hence mixing recently reached maturity for the first time after 50 years of neutrino studies [6]. Another cornerstone of the SM, the massive Higgs boson, is the particle believed to to give mass to quarks and other subatomic building blocks. For its discovery, or whatever more complex mechanism nature has chosen to break the symmetries involved in mass generation, and the study of its properties, the future accelerator LHC that is currently under construction at CERN will be the key experimental venue with help from the Tevatron and a planned linear electron-positron collider (TESLA). The ultimate future goal is the search for experimental signatures of a wider unification of all fundamental forces. Also theoretical particle physics has undergone a revolution over the last twenty years which can for example be seen in the areas of lattice gauge theory which did not exist 20 years ago. In particular, lattice calculations of hadronic matrix elements in the decay of the b-quark are essential for full interpretation of measurements made in the *BABAR* experiment.

1.1 Motivation

The thesis work presented here has been realized in the framework of the *BABAR* experiment that, due to the clean environment of e^+e^- collisions and the wealth of experimental data, allows access to rare B-decay channels. These measurements can be exploited to over-constrain the *unitarity triangle* of the SM through the analysis of many different B-decay modes in a precise, exhaustive and redundant way. One of these modes is the exclusive radiative decay $B \to K^*\gamma$, a representative of processes requiring flavour-changing neutral currents ("*FCNC*") and proceeding by $b \to s\gamma$ at the quark level. Within the SM there is no direct coupling between the bottom quark and the strange quark. Therefore such transitions are induced by one-loop diagrams, which are also called "*penguin* diagrams". They involve double $W^\pm$ vertices and are strongly suppressed. The coupling by the intermediate quark is dominated by the top

quark and provides access to the CKM-matrix element V_{ts}, consequently being a low-energy window to high-mass physics. The caveat in the theoretical predictions is the missing knowledge about the hadronic matrix elements needed for calculations of QCD corrections. However, there has been considerable interest and progress recently [7, 8, 9], putting precision measurements of the exclusive branching fractions $\mathcal{B}(B^0 \to K^{*0}\gamma)$ and $\mathcal{B}(B^+ \to K^{*+}\gamma)$ into the position of an important benchmark for improvements of the QCD calculations, which cause the largest theoretical uncertainty for most exclusive decays.

Furthermore, radiative penguin decays are also sensitive to "New Physics". Many extensions of the SM like super-symmetric models provide new virtual high-mass fermions and gauge bosons, like a charged Higgs boson, that might appear in the loop instead of the $W^{\pm}$. This leads to additional Feynman diagrams that can interfere with the SM decay and cause significant deviations in the decay rate, yet the effect on the *CP*-violating charge asymmetries might be even more dramatic. Whereas contributions from the SM alone are expected to be $< 1\%$ due to the dominance of one Feynman diagram, in non-SM processes there can be several diagrams of comparable weight interfering with each other and producing charge asymmetries at a level as high as 20% [10]. Accordingly, detecting a considerable *CP* asymmetry in $B \to K^*\gamma$ would be an immediate proof of a SM deficiency.

1.2 Outline

A signal for the $B \to K^*\gamma$ decay was first found by CLEO in 1999 [11], a measurement which provided the only published results before the accomplishment of the study by *BABAR* presented here, consisting of the measurement of the exclusive branching fractions $\mathcal{B}(B^0 \to K^{*0}\gamma)$ in the $K^{*0} \to K^+\pi^-$, $K_S\pi^0$ modes and $\mathcal{B}(B^+ \to K^{*+}\gamma)$ considering the $K^{*+} \to K^+\pi^0$, $K_S\pi^+$ modes, with $K_S \to \pi^+\pi^-$. Here, K^* refers to the $K^*(892)$ resonance and the charge conjugate decays are implied unless otherwise stated. The $K^{*0} \to K^+\pi^-$ and $K^{*+} \to K^+\pi^0$, $K_S\pi^+$ modes have been used to search for CP-violating charge-asymmetries.

Since the $B \to K^*\gamma$ analysis has been carried out within a *BABAR* working group, it is justified to point out my personal contributions, being the entire analysis of the two modes involving π^0s, including the necessary π^0-efficiency study, some parts of the mode $K^{*0} \to K^+\pi^-$, and the establishment of the K_S reconstruction procedure that is also used in $K^{*+} \to K_S\pi^+$. The study is based upon an integrated luminosity of 20.7 fb^{-1} of data, corresponding to 22.7×10^6 $B\overline{B}$ meson pairs and recorded at the $\Upsilon(4S)$ resonance ("on-resonance"), and 2.6 fb^{-1} at 40 Mev below this energy ("off-resonance"). The results have been accepted as a *BABAR* publication by Physical Review Letters [12]. Analysis details are covered extensively in *BABAR* analysis documents [13, 14, 15].

This thesis report is structured as follows:

- Chapter 2 provides a comprehensive overview of the underlying theory. The first part is a reminder about the main features of the SM, whereas the second section gives a retrospective of the mathematical formalism generally used for the treatment of FCNC processes, applied to our special case of the $B \to K^*\gamma$

decay mode. Considerable theoretical effort is caused by the relatively poor knowledge of the form factors involved in the hadronic quark transition, limiting the prediction power of the theory.

- Chapter 3 gives a description of the experimental device deployed for the measurement, being composed of the linear accelerator and e^+e^- storage ring PEP-II producing the B decays, and the *BABAR* detector to reconstruct them. The principal components of *BABAR* for the purpose of this $B \to K^*\gamma$ analysis are the electromagnetic calorimeter and the drift chamber. Furthermore, *BABAR* holds the advantage over the previous experiments running on the $\Upsilon(4S)$ resonance, ARGUS and CLEO, of possessing an excellent kaon identification by a new type of Cherenkov detector, the DIRC.
- Chapter 4 is devoted to the event selection process. The main issue in the measurement of the rare decay $B \to K^*\gamma$ is the suppression of the abundant background that arises dominantly from continuum $udsc$ events. The reconstruction of the high-energy photon, the tracks and π^0 mesons from the K^* decay, and finally the B candidate is followed by cuts on certain event shape variables and the kinematic quantity ΔE^*. In order to keep the reconstruction efficiency as high as possible, nearly all event selection criteria are optimized using Monte Carlo data only.
- Chapter 5 addresses the determination of the signal efficiency in the first section, using simulated data and applying various efficiency corrections for small differences between data and Monte Carlo. The second part illustrates the π^0-efficiency study that has been carried out using τ events to provide the data-MC π^0-efficiency correction to the *BABAR* collaboration.
- Chapter 6 covers the extraction of the measured branching fractions. It contains the explanation of the simultaneous maximum likelihood fit to all available real data samples, applied to estimate the signal yields from the B-mass distributions of the final event-selection. After the summary of the systematic uncertainties, the results for $\mathcal{B}(B^0 \to K^{*0}\gamma)$ and $\mathcal{B}(B^+ \to K^{*+}\gamma)$ are presented.
- Chapter 7 is aimed to describe the search for CP-violating charge asymmetries A_{CP} in $B \to K^*\gamma$ by a simultaneous extended maximum likelihood fit to the separated samples of B and $\overline{B}$ candidates. The chapter proceeds with the investigation of systematic errors and closes with the discussion of the results for A_{CP}.
- Chapter 8 summarizes the path that has been followed in this analysis and compiles the obtained results for the branching fractions $\mathcal{B}(B^0 \to K^{*0}\gamma)$ and $\mathcal{B}(B^+ \to K^{*+}\gamma)$, the CP asymmetry $A_{CP}(B \to K^*\gamma)$, and the global π^0-efficiency correction.

Chapter 2

Theoretical Motivation

In this chapter, the theoretical background and the still existing unknowns of the underlying model of the B-meson decay mode $B \to K^*\gamma$ are explained, which automatically illustrates the motivation for investigating this radiative decay. In the first section, a general introduction to the relevant aspects of the Standard Model is given, whereas in the second section the concrete treatment of the exclusive B-decay is provided.

2.1 The Standard Model of Particle Physics

The ultimate goal of research in particle physics is the discovery of the fundamental theory explaining the composition of matter in the universe and the way its constituents interact. The *Standard Model (SM)* of particle physics is the self-contained theory that represents our current knowledge and has not been contradicted conclusively yet. The ingredients of the SM are the symmetry groups of the Lagrangian, the representation of the elementary particles in the these symmetry groups, and a model for the breaking of certain symmetries. The SM consists of the *Quantum Chromodynamics* describing the *Strong Interaction* and the theory of the *Electroweak Interaction*. Both frameworks rest in a similar way on two fundamental formalisms:

- The theory of *Gauge Fields* assures the renormalizability of the formalisms. It is deduced from the *gauge principle*, saying that the Dirac equation is invariant under arbitrary local unitarity-transformations. This is impossible in a space free from any fields and therefore implies the existence of vector fields that have to be gauge-transformed at the same time.
- The *Quantum Field Theory* formalism assures that both, the laws of quantum mechanics as well as the rules of Einstein's special relativity are respected.

2.1.1 The Particles of the Standard Model

In the context of the SM, the elementary particles are grouped in three families of fermion pairs, six quarks (*u*p, *d*own, *s*trange, *c*harm, *b*ottom, *t*op) and six leptons (e, μ, τ, ν_e, ν_μ, ν_τ). The families only differ in the masses of their particles, the way they

interact is the same for each family. This is known as the principle of *Universality*. The interactions are described by the following gauge symmetry group:

$$SU(3)_C \otimes SU(2)_L \otimes U(1)_Y \tag{2.1}$$

$SU(3)_C$ is the symmetry group of *Quantum Chromodynamics (QCD)*, representing the Strong Interaction. $SU(2)_L \otimes SU(1)_Y$ refers to the Electroweak Interaction, where $Y = 2(Q - I_3)$ denotes the weak hypercharge.

The Elementary Particles of the Strong Interaction

The elementary particles of the *Quantum Chromodynamics (QCD)* are the quarks since leptons do not take part in the Strong Interaction. They are grouped in triplets $\mathbf{u} = (u, c, t)$ and $\mathbf{d} = (d, s, b)$, and form a $SU(N_f)$ with the number of quark flavours $N_f = 6$. The Pauli principle of fermions has to be guaranteed for quarks composing hadrons. Therefore, besides the spin each quark has another degree of freedom called the *colour* charge, with three available colour states (red, green and blue). This denotation was motivated by analogy to white light consisting of all visible colours in optics, since in nature only colour-neutral bound quark states exist.

The Elementary Particles of the Electroweak Interaction

In the Weak Interaction, the left-handed leptons and quarks are grouped in $SU(2)_L$ doublets of the *weak isospin* (I =1/2, $I_3 = \pm 1/2$), whereas the right-handed fermions are isospin singlets ($I = I_3$ =0):

$$\begin{aligned}
\mathbf{q'_L} &= \left(\begin{pmatrix} u' \\ d' \end{pmatrix}_L, \begin{pmatrix} c' \\ s' \end{pmatrix}_L, \begin{pmatrix} t' \\ b' \end{pmatrix}_L \right), \qquad \mathbf{u'_R} = (u'_R, c'_R, t'_R), \quad \mathbf{d'_R} = (d'_R, s'_R, b'_R) \\
\mathbf{l_L} &= \left(\begin{pmatrix} \nu_e \\ e^- \end{pmatrix}_L, \begin{pmatrix} \nu_\mu \\ \mu^- \end{pmatrix}_L, \begin{pmatrix} \nu_\tau \\ \tau^- \end{pmatrix}_L \right), \quad \mathbf{e_R} = \left(e^-_R, \mu^-_R, \tau^-_R\right)
\end{aligned} \tag{2.2}$$

Here, the neutrinos are assumed to be massless. The fermions (leptons and quarks) are described by the spin-dependent part of the Dirac-Spinor with positive energy, e.g. u'_R stands for the right-handed up-quark which carries spin 1/2 parallel to its momentum and is represented by $\psi_{uR} = u'_R \cdot exp(i\hbar p \cdot x)$. The exclusive negative helicity of the neutrinos, which is a synonym for parity violation, is one of the major aspects of the theory of Weak Interaction [16] (besides the existence of neutral weak currents [17]). Fermions and anti-fermions have opposite eigen-parity. In the formalism this is automatically accounted for by introducing the chiral projection operator, e.g. for the up quark:

$$u' = \frac{1}{2}(1 - \gamma^5)u' + \frac{1}{2}(1 + \gamma^5)u' = P_L u' + P_R u' = u'_L + u'_R \tag{2.3}$$

The eigenstates of the Electroweak Interaction q' in equation 2.2 are *a priori* not identical to the flavour eigenstates of the Strong Interaction, yet they are linked as derived in section 2.1.3 and 2.1.4.

2.1.2 The Lagrangian of the SM

The dynamics of the SM is represented by the fundamental Lagrangian:

$$\mathcal{L}_{SM} = \mathcal{L}_{QCD} + \mathcal{L}_{EW} + \mathcal{L}_{Higgs}, \qquad \mathcal{L}_{EW} = \mathcal{L}_{CC} + \mathcal{L}_{NC} \tag{2.4}$$

The Strong Interactions between the quarks are represented by the exchange of massless gauge bosons called gluons G_α. The $SU(3)$ transformations are described by the *Gell-Mann matrices* λ_i which, as a generalisation of the Pauli matrices, are eight linear independent hermitian 3×3 matrices with trace zero, constraining the number of gluons to eight. This means that there is no ninth singlet gluon. The strong forces are flavour blind, entailing flavour conservation in QCD processes. Since the symmetry group $SU(3)$ is non-abelian, the gluons interact with each other and, as opposed to the photon in the electromagnetic case, carry colour charge themselves. This is the origin of the *asymptotic freedom* of the quarks at low momentum transfers and the confinement at high momentum transfers, expressed by the quark-antiquark potential (in the strongest bound colour-singlet state) $V_{\overline{q}q} = -4/3 \cdot \alpha_S/r + \sigma r$. The QCD Lagrangian is given by:

$$\begin{aligned} \mathcal{L}_{QCD} \;=\; & -\tfrac{1}{4}(\partial_\mu A^a_\nu - \partial_\nu A^a_\mu)(\partial^\mu A^{a\nu} - \partial^\nu A^{a\mu}) - \tfrac{1}{2}(\partial_\mu A^a_\mu)^2 \\ & + \overline{q}_\alpha (i\, \not{\partial} - m_q) q_\alpha - g_s \overline{q}_\alpha T^a_{\alpha\beta} \gamma^\mu q_\beta A^a_\mu \\ & + \tfrac{g_s}{2} f^{abc} (\partial_\mu A^a_\nu - \partial_\nu A^a_\mu) A^{b\mu} A^{c\nu} - \tfrac{g_s}{4} f^{abe} f^{cde} A^a_\mu A^b_\nu A^{c\mu} A^{d\nu} \end{aligned} \tag{2.5}$$

Here, A^a_ν are the gluon fields with $(a, b, c = 1, ..., 8)$, and $q = (q_1, q_2, q_3)$ is the colour triplet of quark flavour with $q = u, d, s, c, b, t$. $g_s = \sqrt{4\pi\alpha_S}$ is the QCD coupling. T^a and f^{abc} are the generators and structure constants of $SU(3)_C$, respectively. Furthermore, the abbreviation $\not{\partial} = \gamma^\mu \partial_\mu$ is used.

The Electroweak Interactions are mediated by the massive gauge bosons $W^\pm$ and Z^0, the massless γ, and the neutral Higgs boson H^0. As the $SU(3)$ of the QCD, the $SU(2)$ is non-abelian, implying self-interaction of the field quanta. The W and Z bosons carry a weak charge themselves and therefore differ substantially from the electrically neutral photon. As a consequence, there are no plane W-, Z^0- or gluon-waves since these weak gauge bosons do not fulfil a homogeneous wave equation, which leads to the finite range of the interaction. The Electroweak Interactions can be divided into the *charged* and *neutral current* interactions $\mathcal{L}_{CC}$ and $\mathcal{L}_{NC}$ (see equation 2.4), where the charged current interaction is generated by two charged $W^\pm$ bosons:

$$\mathcal{L}_{CC} = \frac{g}{\sqrt{2}} \left(j^+_\alpha W^{+\alpha} + j^-_\alpha W^{-\alpha} \right) \tag{2.6}$$

Here, g is the weak coupling constant, playing an analogue role as the elementary charge in the electromagnetic interaction (see appendix A.3). j^-_α and j^+_α are hermitian conjugates (h.c.). According to equation 2.3, the current elements of $j^\pm_\alpha$ have the general *V-A* form, i.e. they contain a vector current and an axial-vector current part, leading to the observed non-invariance under parity inversion [18]:

$$j^+_\alpha = \overline{\nu}_\mathbf{L} \gamma_\alpha \mathbf{e_L} + \overline{\mathbf{u}}'_\mathbf{L} \gamma_\alpha \mathbf{d}'_\mathbf{L}, \qquad \overline{\mathbf{u}}'_\mathbf{L} \gamma_\alpha \mathbf{d}'_\mathbf{L} = \overline{\mathbf{u}}' \gamma_\alpha \frac{1 - \gamma^5}{2} \mathbf{d}' \tag{2.7}$$

The $W^{\pm\alpha}$ gauge bosons mediating the weak charged current need to have a high mass because of the short scope of this interaction. The third component I_3 varies by one in inter-doublet transitions like $d' \to u'$ and the spin of the W is one. The existence of a third, neutral W^0 has to be postulated to ensure invariance of the weak isospin doublets like (u'_L, d'_L) under any $SU(2)_L$ transformation, implying the existence of neutral weak currents. According to equation 2.1, also the electromagnetic $U(1)$ gauge invariance has to be accounted for. We therefore introduce a triplet $\mathbf{W}^\alpha = (W_1^\alpha, W_2^\alpha, W_3^\alpha)$, with $W^{\pm\alpha} = 1/\sqrt{2}(W_1^\alpha \pm W_2^\alpha)$, $W_3 = W^0$, and a single vector field B^α. The quantum $W^{1,2}$ of the Weak Interaction field has to be massless since only for massless vector-fields the gauge invariance is fulfilled. The Dirac equation of the Electroweak Interaction can be written as:

$$(i\gamma_\alpha D^\alpha - m)\psi = 0 \qquad \text{with} \qquad D^\alpha = \partial^\alpha + ig\mathbf{T}\cdot\mathbf{W}^\alpha + i\frac{g'}{2}YB^\alpha \tag{2.8}$$

$\mathbf{T}$ is zero for right-handed fermions whereas for left-handed ones it is given by the triplet of standard Pauli matrices (see appendix A.1) with $\mathbf{T} = \sigma/2$. The coupling constant g' is connected to g by the weak mixing angle, also called *Weinberg angle* Θ_W:

$$\cos\theta_W = \frac{g}{\sqrt{g^2 + g'^2}} \tag{2.9}$$

The Neutral Current Interaction is consequently represented by two parts:

$$A^\alpha = B^\alpha\cos\theta_W + W_3^\alpha\sin\theta_W, \qquad Z^\alpha = -B^\alpha\sin\theta_W + W_3^\alpha\cos\theta_W \tag{2.10}$$

The electromagnetic component is described by the electromagnetic potential A^α and the photon as exchange boson. The Weak Interaction part is denoted by Z^α. Together both parts constitute the neutral Electroweak Interaction,

$$\mathcal{L}_{NC} = ej_\alpha^{EM}A^\alpha + \frac{g}{2\cos\Theta_W}j_\alpha^0 Z^\alpha, \tag{2.11}$$

The neutral electromagnetic and weak currents, j_α^{EM} and j_α^0, can be expressed by:

$$j_\alpha^{EM} = \sum_f Q_f\overline{f}\gamma_\mu f \qquad \text{with} \qquad f = (\nu_e, e, \nu_\mu, \mu, \nu_\tau, \tau, u, d, s, c, b, t) \tag{2.12}$$

$$j_\alpha^0 = \sum_f \overline{f}\gamma_\alpha(v_f - a_f\gamma_5)f \qquad \text{with} \qquad v_f = I_3 - 2Q_f\sin^2\theta_W, \qquad a_f = I_3, \tag{2.13}$$

with Q_f being the fermion charge.

Proceeding this partial simplification, hints of further unification with the Strong Interactions at a high mass scale, the *Grand Unification Theory* (GUT) scale, are provided by e.g. super-symmetric extensions of the SM. Ultimately, theorists seek a model that also includes a correct quantum version of gravitational interactions which can still be neglected under high-energy physics situations.

2.1.3 The Higgs Mechanism in the Standard Model

The inconsistency due to the considerable mass of the $W^{\pm}$, composed from the massless $W^{1,2}$ bosons, seeks for a process of mass generation. In the SM this is provided by the interaction of the quark and lepton fields with the "*Higgs*" field [19], which is represented by an isospin doublet of a scalar Higgs-particle $\Phi = (\Phi_1, \Phi_2)$, obeying

$$\mathcal{L}_{Higgs} = (\partial^{\alpha}\Phi)^{\dagger}(\partial_{\alpha}\Phi) - V(\Phi^{\dagger}, \Phi), \qquad V(\Phi^{\dagger}, \Phi) = -\mu^2\Phi^{\dagger}\Phi + \lambda(\Phi^{\dagger}\Phi)^2. \tag{2.14}$$

A vivid interpretation of the Higgs hypothesis is the following; the gauge bosons of the Weak Interaction are *a priori* massless and therefore have infinite range like the photon. This is exponentially attenuated by interaction with the omni-existent Higgs-field. Since the Higgs field is not sensed experimentally, it is ignored by assigning effective masses to the W and Z bosons. The "Mexican-hat" shape of the Higgs potential entails a non-zero expectation value at the ground-state energy-minimum, implying self-interaction of the corresponding field. Setting $\Phi^{\dagger}\Phi = \rho^2$, the Higgs potential has a minimum at $\rho^2 = v^2 = \mu^2/\lambda$. The fermion-coupling to the Higgs field has the general *Yukawa* form [20]:

$$\mathcal{L}_{Yukawa} = \mathbf{G_l}\bar{\mathbf{l}}_{\mathbf{L}}\Phi\mathbf{e_R} + \mathbf{G_q^u}\overline{\mathbf{q}}'_{\mathbf{L}}\tilde{\Phi}\mathbf{u}'_{\mathbf{R}} + \mathbf{G_q^d}\overline{\mathbf{q}}'_{\mathbf{L}}\Phi\mathbf{d}'_{\mathbf{R}} + \text{h.c.} \tag{2.15}$$

The G matrices contain the Yukawa-coupling constants which are complex and represent the source of *CP* violation in the SM [21]. Within the process of *spontaneous symmetry breaking*, the Higgs doublet is developed around its vacuum expectation value v by the small field $h(x)$:

$$\Phi(x) = \begin{pmatrix} \Phi_1 \\ \Phi_2 \end{pmatrix} = \frac{1}{\sqrt{2}} \begin{pmatrix} 0 \\ v + h(x) \end{pmatrix} \tag{2.16}$$

This choice for Φ prevents the mechanism from assigning a mass to the photon [17] (and automatically leads to the masses $m_{Higgs} = \sqrt{2}\mu$ of the Higgs particle, $m_W = gv/2$ of the W boson, and $m_Z = m_W/\cos\theta_W$ of the Z boson). The real effective Higgs-field $h(x)$ is relevant for quark-Higgs interaction processes. These should be experimentally observable and can thus be deployed for Higgs searches. The discovery of the Higgs boson, which would convert this model into a valid theory but has not been achieved yet, is the main goal of the future LHC project at CERN.
With equation 2.16 the two components of the quark doublets become distinguishable [21] and the quark-mass terms arise from equation 2.15:

$$\mathcal{L}^q_{mass} = \mathbf{m^u}\overline{\mathbf{u}}'_{\mathbf{L}}\mathbf{u}'_{\mathbf{R}} + \mathbf{m^d}\overline{\mathbf{d}}'_{\mathbf{L}}\mathbf{d}'_{\mathbf{R}} + \text{h.c.} \qquad \mathbf{m^{u,d}} = \mathbf{G_q^{u,d}}\frac{v}{\sqrt{2}} \tag{2.17}$$

The two mass matrices $\mathbf{m^{u,d}}$ cannot be diagonalised simultaneously, i.e. by using the same set of unitarity matrices for the transformations that have to be performed to yield the quark masses (of the Strong-Interaction flavour-eigenstates) [20]:

$$(\mathbf{V_L^u})^{\dagger}\mathbf{m^u}\mathbf{V_R^u} = \begin{pmatrix} m_u & 0 & 0 \\ 0 & m_c & 0 \\ 0 & 0 & m_t \end{pmatrix}, \quad (\mathbf{V_L^d})^{\dagger}\mathbf{m^d}\mathbf{V_R^d} = \begin{pmatrix} m_d & 0 & 0 \\ 0 & m_s & 0 \\ 0 & 0 & m_b \end{pmatrix} \tag{2.18}$$

Hence, $2 \times 2 = 4$ unitarity matrices $\mathbf{V^{u,d}_{L,R}}$ are needed, defined as [20]:

$$\mathbf{u}'_{\mathbf{L}} = \mathbf{V^u_L}\mathbf{u_L}, \quad \mathbf{u}'_{\mathbf{R}} = \mathbf{V^u_R}\mathbf{u_R}, \quad \mathbf{d}'_{\mathbf{L}} = \mathbf{V^d_L}\mathbf{d_L}, \quad \mathbf{d}'_{\mathbf{R}} = \mathbf{V^d_R}\mathbf{d_R} \tag{2.19}$$

2.1.4 The Cabibbo-Kobayashi-Maskawa-Matrix

Using the two matrices $\mathbf{V_L^u}$ and $\mathbf{V_L^d}$ from equation 2.19, we can rewrite equation 2.7 as a function of the mass eigen-states:

$$j_\alpha^+ = \overline{\nu}_\mathbf{L}\gamma_\alpha \mathbf{e_L} + \overline{\mathbf{u}}_\mathbf{L}\gamma_\alpha \mathbf{V_{CKM}} \mathbf{d_L} \tag{2.20}$$

Here, the introduced unitary matrix $\mathbf{V_{CKM}} = \mathbf{V_L^u}(\mathbf{V_L^d})^\dagger$ is the *Cabibbo-Kobayashi-Maskawa-Matrix* [22, 23, 2]. The *CKM-Matrix* expresses the d', s' and b' quark Eigenstates of the Electroweak Interaction in equation 2.2 as linear combinations of the d, s and b quark Eigenstates of the Strong Interaction:

$$\begin{pmatrix} d' \\ s' \\ b' \end{pmatrix} = \begin{pmatrix} V_{ud} & V_{us} & V_{ub} \\ V_{cd} & V_{cs} & V_{cb} \\ V_{td} & V_{ts} & V_{tb} \end{pmatrix} \begin{pmatrix} d \\ s \\ b \end{pmatrix} = \mathbf{V_{CKM}} \begin{pmatrix} d \\ s \\ b \end{pmatrix} \tag{2.21}$$

The basis has hence been chosen in such a way that weak-interaction quark-states u', c' and t' are identical with the flavour eigenstates u, c and t, i.e. $\mathbf{u'_{L,R}} = \mathbf{u_{L,R}}$. There could *a priori* be $2 \cdot 3^2 = 18$ independent real parameters in $\mathbf{V_{CKM}}$ since it is a complex 3×3 matrix. It is, however, a unitarity matrix which imposes 9 constraints, reducing the number of parameters to 9 because of the orthogonality relations:

$$\mathbf{V_{CKM}^\dagger V_{CKM}} = \mathbf{V_{CKM} V_{CKM}^\dagger} = \mathbf{1} \qquad \Rightarrow \qquad \sum_k V_{ik} V_{jk}^* = \sum_k V_{ki} V_{kj}^* = \delta_{ij} \tag{2.22}$$

Furthermore, one can absorb five phases in the six wave functions of the quarks. Therefore, four independent parameters remain, three real angles θ_{ij} $(i \neq j)$ and one complex phase δ which is the only source of CP violation within the SM. The SM does not provide any predictions for these four values, they have to be considered as free parameters. With the three mixing angles abbreviated by $c_{ij} = \cos\theta_{ij}$ and $s_{ij} = \sin\theta_{ij}$, equation 2.21 can be rewritten as:

$$\mathbf{V_{CKM}} = \begin{pmatrix} c_{12}c_{13} & s_{12}c_{13} & s_{13}e^{-i\delta} \\ -s_{12}c_{23} - c_{12}s_{23}s_{13}e^{-i\delta} & c_{12}c_{23} - s_{12}s_{23}s_{13}e^{-i\delta} & s_{23}c_{13} \\ s_{12}c_{23} - c_{12}c_{23}s_{13}e^{-i\delta} & -c_{12}c_{23} - s_{12}c_{23}s_{13}e^{-i\delta} & c_{23}c_{13} \end{pmatrix} \tag{2.23}$$

The Unitarity Triangle

The *Wolfenstein approximation* [24] is the favourable representation of the CKM matrix to manifest its properties. This parametrisation takes advantage of the fact that the values of the diagonal elements are close to one, meaning that inter-family transitions are suppressed and intra-family transitions are enhanced. The order of magnitude of the matrix elements depends on $\lambda \approx 0.22$. With $\lambda = s_{12}$, $A\lambda^2 = s_{23}$ and $s_{13}e^{-i\delta} = A\lambda(\rho - i\eta)$ one obtains:

$$\mathbf{V_{CKM}} = \begin{pmatrix} 1 - \lambda^2 & \lambda & A\lambda^3(\rho - i\eta) \\ -\lambda & 1 - \frac{\lambda^2}{2} & A\lambda^2 \\ A\lambda^3(1 - \rho - i\eta) & -A\lambda^2 & 1 \end{pmatrix} + \mathcal{O}(\lambda^4) \tag{2.24}$$

This form of the CKM matrix leads to simple presentations of one of the unitarity relations (equation 2.22) in the complex (ρ, η) plane; with

$$\begin{array}{ll} V_{ud}V_{ub}^* + V_{cd}V_{cb}^* + V_{td}V_{tb}^* = V_{us}V_{ub}^* + V_{cs}V_{cb}^* + V_{ts}V_{tb}^* = 0 & \text{(Unitarity)} \\ V_{cd}V_{cb}^* \approx -A\lambda^3, \quad V_{ud} \approx 1 & \text{(Wolfenstein appr.)} \end{array} \tag{2.25}$$

we obtain the "*Unitary Triangle*" shown in figure 2.1 and described by:

$$(\overline{\rho} + i\overline{\eta}) - 1 + (1 - \overline{\rho} - i\overline{\eta}) = 0, \qquad \overline{\rho} = \rho(1 - \lambda^2/2), \quad \overline{\eta} = \eta(1 - \lambda^2/2) \tag{2.26}$$

In the case of CP violation, the angles α, β and γ are different from 0^o and 180^o, whereas for perfect CP symmetry the triangle would be completely flat. The precise determination of the CKM-matrix elements and the corresponding over-constraining of the unitarity triangle is the aim of the *BABAR* experiment.

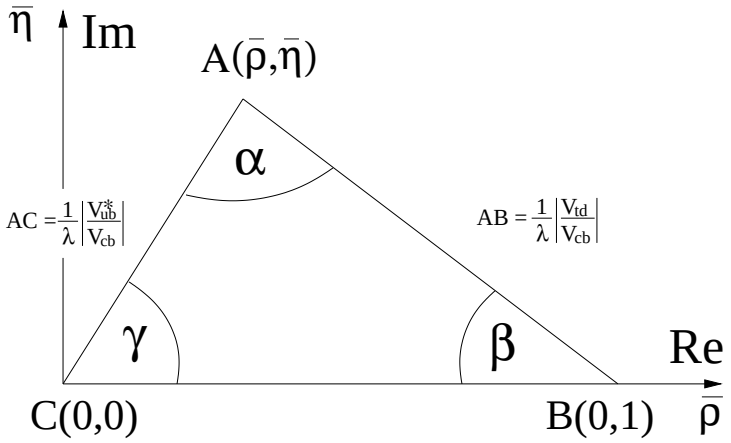

Figure 2.1: *The Unitary Triangle: Using the CKM matrix in the Wolfenstein parametrisation (equation 2.24) and the orthogonality relations for the unitarity (equation 2.22) one obtains the angle parameters of the triangle:* $\alpha = [-V_{td}V_{tb}^*/V_{ud}V_{ub}^*]$, $\beta = [-V_{cd}V_{cb}^*/V_{td}V_{tb}^*]$, $\gamma = [-V_{ud}V_{ub}^*/V_{cd}V_{cb}^*]$.

2.2 Flavour Changing Neutral Currents

In the SM, *flavour-changing neutral currents (FCNC)* at tree level are absent due to the *GIM* mechanism [25] which explains this observed suppression by mutual cancellation of Feynman diagrams associated to the opposite corresponding quarks of a doublet, for example the strange and the charm quark. The GIM hypothesis entails the direct consequence that charm hadrons decay preferably to particles with strangeness rather than to hadrons containing a down quark. Beyond tree level, the conditions for a complete GIM cancellation of FCNC processes are the unitarity of the CKM matrix and exact horizontal flavour symmetry, implying equality of all quark masses with a given charge. Since the latter is certainly broken at low energy scales, the disparity of the quark masses is the origin of the breakdown of GIM at the one-loop level and

the appearance of FCNC transitions. These loop diagrams, also called "*penguins*", are mediated via the flavour-changing $W^{\pm}$ vertex. The radiative penguin decay $B \to K^*\gamma$ shown in figure 2.2 is an example of such a loop transition. The bottom quark emits and re-absorbs a W boson and changes flavour twice. *A priori*, the intermediate virtual quark could be a top, charm or up quark, yet the amplitude is dominated by the top quark. The first reason is GIM suppression since the amplitudes are a function of $m^2_{u,c,t}/m^2_W$. In the case of the up quark there also is "*CKM suppression*", i.e. the CKM-matrix elements V_{ub} and V_{us} are proportional to λ^3 and λ, respectively, and consequently very small. In the Fermi theory of Weak Interactions, loop transitions can be described by effective triple and quartic vertices but, being higher order in the gauge couplings, they are suppressed relative to elementary transitions. On the other hand, FCNC reactions are characterised by their high sensitivity to *New Physics (NP)*. Replacing the $W^{\pm}$ in the loop by new massive gauge bosons from models beyond the SM like for example a charged Higgs or other super-symmetric particles would lead to additional diagrams. This could cause the branching fraction to vary, yet the effect on the CP asymmetry might be even larger (see section 2.3.3).

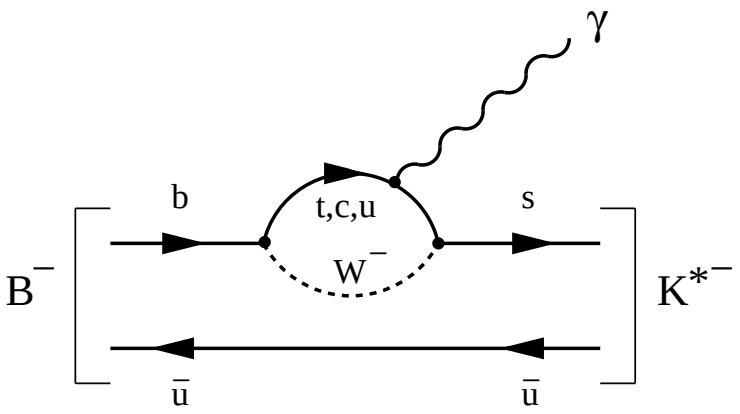

Figure 2.2: *Feynman diagram of the decay* $B \to K^*\gamma$

2.2.1 Operator Product Expansion

The Strong Interactions binding quarks into hadrons typically are at a scale $\mathcal{O}(1\text{ GeV})$, much lower than the weak-interaction scale $\mathcal{O}(M_{W,Z})$. The effective vertices are calculable functions of the elementary Feynman-diagrams. The *operator product expansion (OPE)* is a framework to derive an effective low-energy theory describing the Weak Interaction of quarks bound in hadrons [26]. The product of two current operators is expanded into a series of point-like local operators O_i whose contributions are weighted by effective, process-independent coupling constants, the *Wilson coefficients* C_i. Consequently, an effective Hamiltonian and the corresponding amplitude $A(B \to F)$ can be written as:

$$\mathcal{H}^{FCNC}_{eff} = \sum_i C_i(\mu) O_i, \qquad A(B \to F) = \langle F|\mathcal{H}_{eff}|B\rangle \tag{2.27}$$

In going from the full to this effective theory, the W boson is removed as an explicit, dynamical degree of freedom; it is "integrated out" and does not appear explicitly in the theory any more, but its effects are hidden in the effective Wilson coefficients [27]. The short-range force mediated by a heavy boson exchange is approximated by a point interaction, familiar from the Fermi Theory. Similarly one can "contract out" heavy quarks. This leads to *effective f-quark theories*, where f denotes the quarks that have not been integrated out.
Concerning the Strong-Interaction QCD-corrections to any transition due to all kinds of gluon exchanges (see figure 2.3 for examples), the *a priori* arbitrary mass scale μ in OPE allows to separate the calculation of the decay amplitude $A(B \to F)$ in two distinct parts: the *long-distance* (generally non-perturbative QCD) computation of the matrix elements $\langle O_i(\mu) \rangle$ at energy scales lower than μ and the *short-distance* (perturbative) calculation of the effective coupling constants $C_i(\mu)$ at energy scales higher than μ. This procedure is called *factorization*. It is customary to choose μ to the order of the mass of the decaying hadron which in the case of B decays is $\mathcal{O}(m_b)$, meaning $f = 5$. The $C_i(\mu_b)$ then include the contributions from the top quark and other heavy particles such as W, Z-bosons (and charged Higgs particles beyond the SM). Therefore, the $C_i(\mu_b)$ depend on m_t (and the masses of new particles if extensions of the SM are considered).

2.2.2 The Wilson Coefficients Functions

The Wilson coefficients C_i are universal, i.e. they are independent of the external states and calculable in perturbation theory. They include QCD corrections (see figure 2.3) that are described by the QCD Lagrangian (equation 2.5) from which the Feynman rules for QCD are derived.

Renormalization Theory

In the above QCD calculations, one encounters divergencies in Greens functions for whose parametrisation a regularisation is needed. The most common rules for this manipulation of Dirac matrices is the *naive dimensional regularisation (NDR)* given in appendix A.4.1, in which the Feynman diagrams are evaluated in $D = 4 - 2\epsilon$ space-time dimensions and singularities are extracted as poles for $\epsilon \to 0$. Two other sets of rules, the *dimensional reduction (DRED)* and the *t'Hooft-Veltman (HV)* scheme, are also used in the literature.
The fields and parameters A^a_ν, g_s, q and m have to be renormalised by *renormalisation constants* Z_i to eliminate singularities in the Greens functions. The Z_i are expansions in orders of $\alpha_S/4\pi$. The simplest implementation of the renormalisation rules is provided by the counter-term method; the original Lagrangian in equation 2.5, being a function of the unrenormalized quantities, is expressed as the sum of the renormalized Lagrangian and a counter-term Lagrangian. The latter provides new interactions canceling divergencies in the Greens function. The simplest renormalization scheme used in the counter-term method is the *Minimal Subtraction Scheme* or $\overline{MS}$ *scheme* in which only divergencies are subtracted. In this process of renormalization the arbitrary mass

scale μ is also introduced. The corresponding μ-dependence of several quantities is determined by the renormalization group equations given in appendix A.4.2. They follow from the fact that the unrenormalized Wilson coefficients do not depend on μ and are solved by the *renormalization group functions* $\hat{\beta}(g)$ and $\hat{\gamma}(g)$, where $\hat{\beta}(g)$ governs the μ dependence of the coupling $g(\mu)$ and the *anomalous dimension* $\hat{\gamma}(g)$ the μ dependence of the mass $m(\mu)$. Both, the QCD coupling α_S and the quark masses are obtained to be "running" with μ; both decrease with increasing μ. Expanding $\alpha_S(\mu_b)$ in orders of M_W one has to conclude that the solution of the renormalization group equations A.4.2 automatically sums large logarithms $\ln(M_Z/\mu_b)$ which appear for $\mu_b \ll M_{W,Z}, m_t$ at $\mathcal{O}(m_b)$.

Evaluation of the Wilson Coefficients

The large logarithms $\ln M_W/\mu_b$ compensate the smallness of α_S in the evaluation of $C_i(\mu_b)$, and resummation to all orders of α_S has to be performed to obtain a meaningful result. This problem is solved by means of the *Renormalization-Group (RG) Improved Pertubative Expansion*; the calculation of the the Wilson coefficients $C_i(\mu_W)$ at scale $\mu_W = \mathcal{O}(M_W)$ is performed to the desired order in α_S. Logarithms of the form $\ln(\mu_W/M_W)$ are small, consequently this can be done in perturbation theory. The amplitudes are calculated in the full and effective theories and the $C_i(\mu_W)$ are extracted by the *matching* $A_{full} = A_{eff}$. The *renormalization group evolution* of the coefficients from μ_W down to the low appropriate hadronic scale $\mathcal{O}(1\ GeV)$ is achieved by $C_i(\mu) = \sum_j U_{ij}(\mu, \mu_W) C_j(\mu_W)$, where the evolution function $U_{ij}(\mu, \mu_W)$ is a function of the anomalous dimension $\hat{\gamma}$. The resulting Wilson coefficients for the usual set of operators (section 2.2.3) are given in appendix A.3.2. The $\overline{MS}$-renormalized couplings $C_i(\mu_b)$ are known in the following terms in their perturbative expansion [28]:

$$C_i(\mu_b) = C_i^{(0)}(\mu_b) + \frac{\alpha_{em}}{\alpha_S(\mu_b)} C_i^{(0)em}(\mu_b) + \frac{\alpha_S(\mu_b)}{4\pi} C_i^{(1)}(\mu_b) + \ldots \tag{2.28}$$

Once the Wilson coefficients $C_i(\mu_b)$ are known, the b-quark decay amplitudes are given by matrix elements of the operators O_i between the appropriate partonic states. The last and hardest step thus is the calculation of the hadronic matrix elements $\langle O_i \rangle$ by means of non-perturbative methods.

The μ-dependence of the couplings C_i has to cancel the one of the operators O_i since the amplitude cannot depend on the scale. Due to mixing under re-normalisation this cancellation may involve simultaneously several operators. Besides the μ-dependence there is also a dependence on the applied renormalisation scheme. The theoretical challenge is the incorporation of the dependencies in the non-perturbative evaluation of the matrix elements $\langle O_i(\mu) \rangle$, otherwise the resulting decay amplitude contains large uncertainties due to the scale and renormalisation dependence.

The property that the physical amplitudes cannot depend on the scale μ is broken in perturbation theory through the truncation of the perturbative series. This causes scale ambiguities which can be reduced considerably by going from LO to NLO calculations, including additional gluon exchanges. Furthermore, the renormalisation-scheme dependence of the Wilson coefficients appears first at NLO.

2.2.3 The Electroweak Operators

Usually the full set of four-fermion operators that closes under renormalisation is given by two *current-current* operators (O_1, O_2), representing simple W exchange, and by four *gluonic penguin* operators $(O_3 - O_6)$. The current-current operators for $\Delta B = 1$ decays with $\Delta S = 1$ read as [29]:

$$O_1^q = (\overline{q}_\alpha b_\beta)_{V-A}(\overline{s}_\beta q_\alpha)_{V-A}, \qquad O_2 = (\overline{q}b)_{V-A}(\overline{s}q)_{V-A} \qquad \text{with} \qquad q = u, c \tag{2.29}$$

The QCD-penguin operators are given by:

$$\begin{aligned} O_3 &= (\overline{s}b)_{V-A} \sum_{q=u,d,s,c,b} (\overline{q}q)_{V-A}, & O_4 &= (\overline{s}_\alpha b_\beta)_{V-A} \sum_{q=u,d,s,c,b} (\overline{q}_\beta q_\alpha)_{V-A}, \\ O_5 &= (\overline{s}b)_{V-A} \sum_{q=u,d,s,c,b} (\overline{q}q)_{V+A}, & O_6 &= (\overline{s}_\alpha b_\beta)_{V-A} \sum_{q=u,d,s,c,b} (\overline{q}_\beta q_\alpha)_{V+A}, \end{aligned} \tag{2.30}$$

Here, we have rewritten equation 2.7 for the quarks inserting equation 2.21:

$$(\overline{m}_\alpha n_\beta)_{V-A} = \overline{n}'_\beta \gamma_\mu \frac{(1-\gamma^5)}{2} m'_\alpha, \qquad (\overline{m}n)_{V-A} = (\overline{m}_\alpha n_\alpha)_{V-A} \tag{2.31}$$

The effective Hamiltonian is given by:

$$\begin{aligned} \mathcal{H}_{eff} = \tfrac{G_F}{\sqrt{2}} \; & [V_{us}^* V_{ub} \left(C_1(\mu_b) O_1^u + C_2(\mu_b) O_2^u\right) + V_{cs}^* V_{cb} \left(C_1(\mu_b) O_1^c + C_2(\mu_b) O_2^c\right) \\ & - V_{ts}^* V_{tb} \textstyle\sum_{i=3}^{6} C_i(\mu) O_i \end{aligned} \tag{2.32}$$

2.3 The Radiative Penguin Decay $B \to K^*\gamma$

In B decays, the penguin modes are important since the b quark has no kinematically-allowed CKM-favoured decay like in the transitions $c \to s$ and $t \to b$. The radiative decays $b \to s\gamma$ are among the most valuable probes of flavour physics. Proceeding at rates of order of $G_F^2\alpha$, radiative penguin decays are enhanced compared to non-radiative ones which are proportional to $G_F^2\alpha^2$. In the special case of $B \to X_s\gamma$ with an on-shell photon, two characteristic operators appear in the renormalization group analysis additional to the set $O_1, ..., O_6$ given in equation 2.29 and 2.30. Due to the appearance of $\sigma^{\mu\nu}$ these new operators O_7 and O_8 are called *electromagnetic* and *chromo-magnetic penguins*, respectively [8]:

$$O_7 = \tfrac{e}{8\pi^2} m_b \overline{s}_\alpha \sigma^{\mu\nu}(1+\gamma_5) b_\alpha F_{\mu\nu}, \qquad O_8 = \tfrac{g}{8\pi^2} m_b \overline{s}_\alpha \sigma^{\mu\nu}(1+\gamma_5) T^a_{\alpha\beta} b_\beta G^a_{\mu\nu} \tag{2.33}$$

The $B \to X_s\gamma$ decay is governed by the magnetic γ-penguin operator O_7, corresponding to the effective vertex $\overline{s}\gamma' b = f(D_0'(x_i)$ (see appendix A.3.1). However, also the corresponding magnetic gluon penguin O_8 represented by $\overline{s}G\prime^a b = f(E_0'(x_i)$, and the dominant current-current operator O_1 play a role. The explicit effective vertices are given in appendix A.3. Usually operators mix under renormalisation, which means that gluonic corrections to the matrix element of the original operator O_i are not just proportional to O_i itself but involve additional structure in the other operators O_j $(i \neq j)$. As a peculiar feature of this decay, the mixing between the sets (O_7, O_8) and $(O_1, ..., O_6)$ vanishes under renormalisation at the one-loop level. Therefore, two-loop calculations

have to be performed to obtain the leading entry in the anomalous dimension matrix, representing this mixing. At NLO, the corresponding three-loop calculations become necessary.
The key to the precise calculation of the exclusive decay amplitude $A(B \to K^*\gamma)$ is the knowledge of the long-distance contributions, described by the matrix elements of the operators between the relevant hadronic states $< K^*\gamma|O_i|B >$ (equation 2.27). Whereas the inclusive mode $b \to s\gamma$ can be computed perturbatively, the treatment of the exclusive channel $B \to K^*\gamma$ is much more complex. The theoretical difficulty consists of the need to describe the bound-state effects by non-perturbative hadronic form factors of the transition. There have been many attempts to determine the form factors using non-perturbative methods like quark models, QCD sum rules, lattice-QCD calculations, and heavy quark symmetries (chiral perturbation theory) [30, 31]. In order to calculate the $B \to K^*\gamma$ amplitude with better than 10% accuracy, one needs to include NLO QCD-corrections, i.e. non-logarithmic parts of two-loop diagrams and logarithmic parts of three-loop diagrams.

2.3.1 Heavy-Quark Effective Theory

As already indicated in section 2.2.2, weak decays of heavy mesons involve three fundamental scales; the Weak Interaction scale M_W, the b-quark mass m_b, and the intrinsic scale of Strong Interaction Λ_{QCD}. These are strongly ordered: $M_W \gg m_b \gg \Lambda_{QCD}$. The QCD effects involving virtualities above m_b are well understood (section 2.2.1). Therefore the theoretical problem is to compute the hadronic matrix elements, or at least to reduce them to simpler non-perturbative objects. This can be systematically done from first principles in the *heavy-quark limit*, using $m_b \gg \Lambda_{QCD}$. The *heavy-quark effective theory (HQET)* formalises this simplification that the heavy quarks interact with the spectator quark exclusively via soft gluon exchanges, characterised by momentum transfers much smaller than the heavy-quark mass, and allows to neglect power corrections in Λ_{QCD}/m_b. Accordingly, one obtains a factorisation of the matrix element of an operator into a short-distance form factor and a decay constant [32]. Figure 2.3.a stands for this leading term in the heavy-quark mass limit.

2.3.2 The Factorization Formula for $B \to K^*\gamma$

The HQET allows rigorous calculations, yet the factorization is broken at higher order in α_S since the heavy-quark symmetry is violated by short-distance hard radiative corrections shown in figure 2.3.d, implying large momentum transfers. Including the spectator quark in the discussion, the assumption that any interaction is soft would mean the vanishing of the diagrams 2.3.e but for *heavy-light* form factors at large recoil, as in this case, these contributions from hard-spectator interactions exist. The dilemma thus is the co-existence of soft and hard gluon exchange effects:

- In the case of the soft contributions, certain symmetries can be applied in the large-recoil assumption, i.e. when the momentum of the final meson is large [33]. It follows that the three pseudo-scalar form factors are all related to a single function ξ_P, and the seven vector-meson form factors are all related to two unknown

functions $\xi_\perp$ and $\xi_\parallel$ corresponding to transverse or longitudinal polarisation of the vector meson K^*. The *large recoil* symmetry relations consequently reduce the number of independent form factors from ten to three.

- The hard contributions can be treated in the *hard-scattering* approach, assuming domination by hard gluon exchange [34]. The corresponding amplitude is expressed as a convolution of a hard scattering factor with *light-cone distribution* wave functions Φ_B and Φ_{K^*} that represent the quark-antiquark Fock state of the B and K^*. The hard-vertex renormalisation C_a is then given by the leading term in an expansion in $C_a = 1 + \mathcal{O}(\Lambda_{QCD}/Q)$, where Q denotes the hard scale.

The one-loop diagram in figure 2.3.d contains the problem that the Bremsstrahlung gluons have to be incorporated into physical hadrons, making it necessary to consider three particle states (quark, antiquark and gluon). In [35] the corresponding logarithmic infrared-endpoint divergencies are removed by a cut-off parameter Λ_{had}. The approach can be interpreted as embodying gluons with momenta below a cut value Λ_{had} in the hadronic wave function. Thus there remains a dependence of the predicted branching fraction $B \to K^*\gamma$ on this cut-off parameter of the hadronic model. The most recent and complete approaches [7, 8, 9] provide a hadronic-model independent framework for the analysis of $B \to K^*\gamma$ by proposing a novel factorization formula for the transition matrix element in the heavy-quark limit; the fact that the hard and soft contributions to figure 2.3.d are not separately well-defined is accounted for, regulating the IR divergencies by introduction of a small mass term for the gluon as a factorization scale, and then factoring them into the soft form factor ξ_a. One obtains the factorization formula for the heavy-light amplitude at large recoil [36]:

$$\langle K_a^*\gamma|\mathcal{H}_{eff}|B\rangle = C_a\xi_a + \Phi_B \otimes T_a \otimes \Phi_{K^*} \tag{2.34}$$

The vector meson K^* in $B \to K^*\gamma$ is transversely polarised. T_a is a hard-scattering kernel that, as C_a, is calculable in perturbative QCD. The light-cone distributions Φ_B and Φ_{K^*} are non-perturbative objects. They describe the long-distance dynamics of the matrix elements which is factorized from the perturbative, short-distance interactions expressed in the hard-scattering kernels. The QCD factorization formula 2.34 implies that the hard spectator interaction (figure 2.3.d) is suppressed by one power of α_S relative to the soft contribution (figure 2.3.a) and holds up to corrections of order Λ_{QCD}/m_b, allowing evaluation for each operator O_i:

- In the leading logarithmic approximation of $\ln(M_W^2/m_b^2)$ (LO) and the leading power of Λ_{QCD}/m_b in the heavy quark limit, O_7 gives the only contribution to the amplitude of $B \to K^*\gamma$ and equation 2.34 is trivial.
- The matrix elements of the four-quark operators O_{1-6} and O_8 start contributing at next-to-leading order $\mathcal{O}(\alpha_S)$ (NLO). In this case the factorization formula 2.34 becomes non-trivial. The spectator scattering diagrams in figure 2.3.f and 2.3.g, and the diagrams 2.3.i, 2.3.j and 2.3.k involving QCD form factors represent the complete set of contributions from O_{1-6} and O_8 at $\mathcal{O}(\alpha_S)$ and to leading order of Λ_{QCD}/m_b in the heavy-quark. The QCD-penguin operators O_{3-6} are further suppressed by very small Wilson coefficients and thus neglected at leading order in Λ_{QCD}/m_b. Furthermore, at $\mathcal{O}(\alpha_S)$ the matrix element of O_2 is zero because of its colour structure.

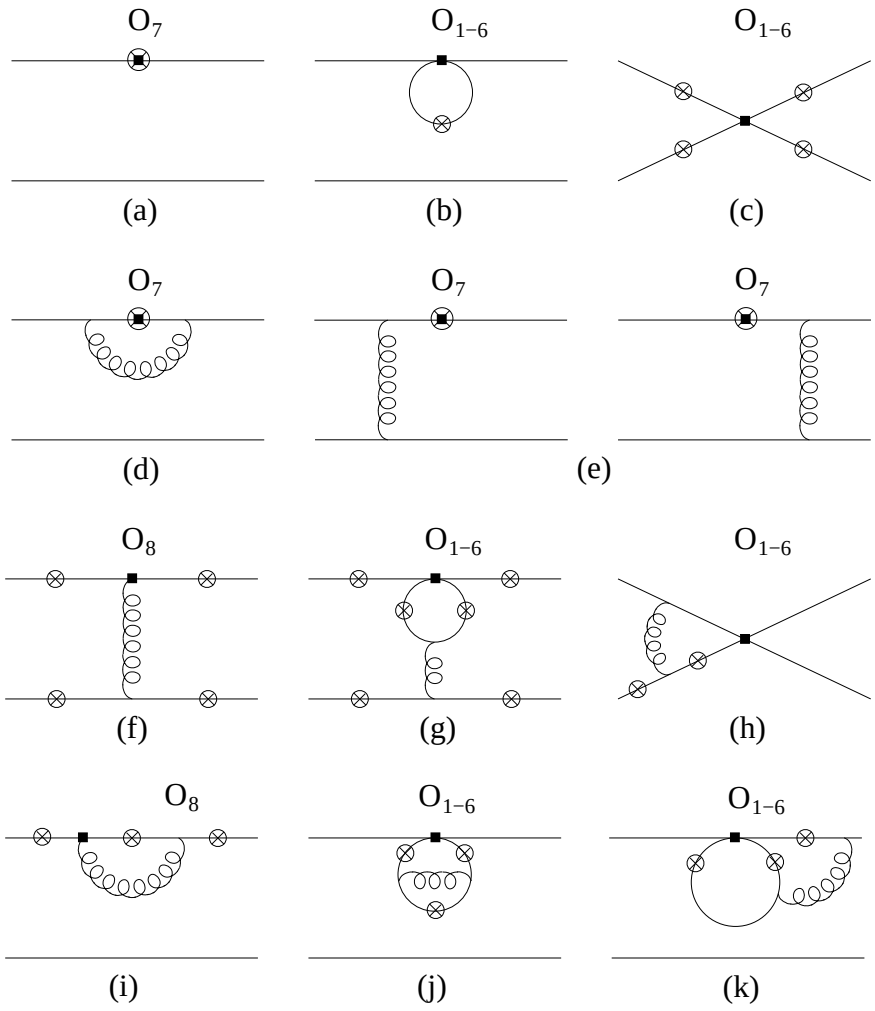

Figure 2.3: *Feynman diagrams contributing to the calculation of the $B \to K^*\gamma$ amplitude. The black square represents the operator insertion of the effective theory where the heavy degrees of freedom (W, Z, t) have been integrated out, i.e. the square corresponds to the W and t propagators being contracted to a point (see section 2.2.1). The crosses indicate the possible places of photon emission: a) Factorizable LO contributions associated with operator O_7. Only soft gluon interactions (not drawn) are present. b) Factorizable LO contributions associated with operators O_{1-6}. c) Non-factorizable LO contribution: Weak annihilation, i.e. contributions of the operators O_{1-6} with quark exchange. d) LO corrections for the b and s quark wave function renormalisation due to hard gluon exchange ("hard vertex renormalisation"). e) LO corrections to the matrix element due to hard gluon exchange with the spectator quark. f) Non-factorizable NLO corrections for the operator O_8 with hard gluon exchange with the spectator quark. g) Non-factorizable NLO corrections to the matrix element of O_{1-6} with hard gluon exchange between the quark lines. h) Non-factorizable NLO corrections to the weak annihilation for the operators O_{1-6}. i,j,k) Non-factorizable NLO corrections for the operators O_{1-6} and O_8 including only soft gluon exchange with the spectator quark.*

- Another mechanism, the *weak annihilation* shown in figure 2.3.c, is also suppressed by Λ_{QCD}/m_b. The dominant annihilation amplitude can be computed in QCD factorization in the heavy-quark limit. For the $B^\pm$ decay, there is an additional CKM-suppressed contribution involving current-current operators. The tiny radiative vertex corrections to the weak annihilation graph of the kind shown in figure 2.3.h are not included in the calculations.
- Finally, the penguin-annihilation diagram 2.3.g, and the spectator diagrams 2.3.f from O_8 display the remaining diagrams with power suppression in Λ_{QCD}/m_b.

Even including all these NLO contributions there remains a residual slight scale-dependence of the physics quantities on μ. However, the uncertainty of the branching fraction is currently dominated by the still remaining dependence on the form factor F_{K^*} of the K^* and the light-cone distribution of the B meson. The presented approach does not circumvent the need to know the heavy-to-light form factors, yet one may hope that in the future lattice QCD will provide them at smaller q^2 and more reliably than at present. Taking into account the above considerations and using the CKM-unitarity relation 2.25, the amplitude from the effective Hamiltonian in equation 2.32 can be rewritten for $B \to K^*\gamma$ [7]:

$$\begin{aligned} A(B \to K^*\gamma) &= \frac{G_F}{\sqrt{2}} \sum_q \lambda_q^s (C_7\langle O_7\rangle + C_1\langle O_1^q\rangle + C_8\langle O_8\rangle) = \frac{G_F}{\sqrt{2}} \left[\sum_q \lambda_q^s a_7^q(K^*\gamma)\right] \langle O_7\rangle \\ \mathcal{B}(B \to K^*\gamma) &= \tau_B \frac{G_F^2 \alpha m_b^2 m_B^3}{32\pi^4} \left(1 - \frac{m_{K^*}^2}{m_B^2}\right)^3 \left|\sum_q \lambda_q^s a_7^q(K^*\gamma)\right|^2 |F_{K^*}|^2 \end{aligned} \tag{2.35}$$

Here, $\lambda_q^s = V_{qs}V_{qb}^*$ and $q = u, c$. The matrix elements $\langle O_1\rangle$ and $\langle O_8\rangle$ can be written as a function $a_7^q(K^*\gamma)$ of $\langle O_7\rangle$. Contributions corresponding to an up-quark in the loop are doubly CKM-suppressed by $|V_{us}^*V_{ub}/V_{ts}^*V_{tb}| < 0.02$. The prediction for the branching fraction includes that $\langle O_7\rangle$ is a function of the form factor F_{K^*} [7].
In the work of Beneke *et al.* [8], the central value of the branching fraction is given as $\mathcal{B}(B^0 \to K^{*0}\gamma) = (7.90^{+3.5}_{-3.0}) \times 10^{-5}$ and no difference of the neutral and charged B meson decay rates are predicted at leading order in the heavy-quark expansion. At NLO in the heavy-quark expansion, the coincidence of the amplitude for the charged and neutral mode starts being lifted and spectator-dependent isospin-breaking contributions are introduced. They are due to the chromo-magnetic dipole operator (figure 2.3.f), charm penguins (figure 2.3.g) and annihilation contributions from 4-quark operators (figure 2.3.c). The prediction by Bosch & Buchalla [7] for the neutral decay is $\mathcal{B}(B^0 \to K^{*0}\gamma) = (7.09^{+2.5}_{-2.3}) \times 10^{-5}$, the value for the charged mode is very close with $\mathcal{B}(B^+ \to K^{*+}\gamma) = 7.45 \times 10^{-5}$. In contrast, Kagan & Neubert [9] predict the neutral decay rate $B^0 \to K^{*0}\gamma$ to be slightly larger than for $B^\pm \to K^{*\pm}\gamma$ with the largest contribution coming from the annihilation diagram with the insertion of the operator O_6. They express the decay-rate asymmetry by the quantity $\Delta_{0\pm}$:

$$\Delta_{0\pm} = \frac{\Gamma(B^0 \to K^{*0}\gamma) - \Gamma(B^\pm \to K^{*\pm}\gamma)}{\Gamma(B^0 \to K^{*0}\gamma) + \Gamma(B^\pm \to K^{*\pm}\gamma)} \tag{2.36}$$

Here, the *relative* branching fractions $\mathcal{B}$ are "corrected" for the difference in the B-meson lifetimes, τ_{B^0} and $\tau_{B^\pm}$ [37], to yield the decay rates Γ:

$$\begin{aligned}\Gamma(B^0 \to K^{*0}\gamma) &= \mathcal{B}(B^0 \to K^{*0}\gamma)/\tau_{B^0} \\ \Gamma(B^\pm \to K^{*\pm}\gamma) &= \mathcal{B}(B^\pm \to K^{*\pm}\gamma)/\tau_{B^\pm}.\end{aligned} \tag{2.37}$$

In the result $\Delta_{0\pm} = (8.0^{+2.1}_{-3.2})\% \times 0.3/T_1^{B\to K^*}$ of Kagan & Neubert, the tensor form factor $T_1^{B\to K^*}$ with possible values between 0.30 and 0.44 introduces the dominant uncertainty.
Comparison to earlier predictions shows that the amplitude increases as the calculations become more sophisticated. Including all NLO single-gluon corrections calculated so far, the branching fraction grows by a factor of two with respect to the typical LO value like $\mathcal{B}(B^0 \to K^{*0}\gamma) = 4.1 \times 10^{-5}$ obtained by Ligeti and Wise [31] in LO calculations using measured form factors from $D \to K^* \overline{l}\nu$, or a value of $\mathcal{B}(B \to K^*\gamma) = (5.2 \pm 0.5) \cdot 10^{-5}$ predicted by Asatryan *et al.* [35] and taking into account certain NLO contributions but with an infrared cut-off parameter due to the simple hadronic model that was applied. The quantitative effect from the NLO calculations is this large due to the big logarithm $\ln(M_W^2/m_b^2)$ [38].
The calculation of the matrix elements of bilinear quark currents between a B meson and a light pseudo-scalar or vector meson encodes Strong Interaction effects in radiative *and* exclusive semi-leptonic B decays, so besides $B \to K^*\gamma$ also $B \to \pi l\nu$ etc. The knowledge of the form factors therefore also helps to determine the CKM coupling $|V_{ub}|$ and to predict *CP* violating asymmetries and other quantities in rare B decays.

2.3.3 Direct CP Violation

Studies of rare B-decays have the potential to uncover the origin of *CP* violation. The theoretical predictions for direct *CP*-violation in the exclusive decay $B \to K^*\gamma$ are obscured by Strong Interaction effects, but a sizable *CP*-asymmetry in the inclusive case $b \to s\gamma$ would persist in the exclusive decay mode $B \to K^*\gamma$ [39]. In the SM, there is only a single complex phase in the Wolfenstein parametrisation of the CKM matrix attributed to V_{ub} and V_{td}, which is the only source of *CP* violation. The measurement of the *CP* asymmetry will thus make it possible to test whether the CKM-matrix paradigm is correct or if additional sources of *CP* violation are required. A positive observation of a sizable *CP*-asymmetry would be a clear signal of NP and provide hints about the nature of physics beyond the SM, whereas a negative result would impose constraints on many New Physics scenarios.

Direct CP Violation in $B \to K^*\gamma$ Decays

For the occurrence of direct *CP* violation, in general as in $B \to X_s\gamma$ decays, there has to be interference of non-trivial weak phases with strong phases of two individual diagrams (1 and 2) that leads to different rates Γ of the $B \to X_s\gamma$ decay and its *CP* conjugate:

$$\Gamma = \left|a_1 e^{i\delta_1} e^{i\phi_1} + a_2 e^{i\delta_2} e^{i\phi_2}\right|^2 \qquad \overline{\Gamma} = \left|a_1 e^{i\delta_1} e^{-i\phi_1} + a_2 e^{i\delta_2} e^{-i\phi_2}\right|^2 \tag{2.38}$$

The weak phases ϕ_j are contained in the CKM matrix. There are two mechanisms from which strong phases δ_j arise. In the heavy-quark limit, both effects account for the re-scattering phases in two-body decays like e.g. $B \to \pi\pi$ [40]; the hard gluon exchange between outgoing particles at hadron level is called *"final state interaction" (FSI)*, whereas the production of Strong Interaction phases through involved penguin transitions at parton level is commonly referred to as the *BSS* mechanism; Bander, Silvermann & Soni [41] stated in 1979 that a direct *CP* asymmetry in the decays of heavy mesons does not occur at tree-diagram level but corresponds to the generation of a non-vanishing absorptive, imaginary part whenever the quark line in the penguin loop can be put on its perturbative-QCD mass shell. In the formalism, the strong phases are provided by the imaginary parts of the matrix elements of the operators in the effective Hamiltonian 2.35.
In the case of $B \to K^*\gamma$, FSI are absent due to the photon but there are scenarios for BSS-like effects when the up or down spectator-quarks receive recoil momentum via one-gluon exchange with up or charm quarks in the loop. Considering the diagrams 2.3.g or 2.3.k, there can be interference between two diagrams with different quarks running around the loop, i.e. up or charm. For the up-quark loop, the $B \to K^*\gamma$ decay and its *CP*-conjugate possess the weak phases $\lambda_u^s = V_{us}V_{ub}^*$ and $\lambda_u^{s*} = V_{us}^*V_{ub}$, respectively, i.e. for the *CP*-conjugated decay the complex conjugated weak phase shows up. Moving to the charm-loop diagrams, we encounter a trivial weak phase of zero. Consequently, the relative weak phase of the two amplitudes is non-zero.
Concerning the strong phases, the amplitude depends on the mass of the quark in the loop. The charm loop acquires an imaginary part once the threshold is reached at which the momentum transferred by a hard gluon between the spectator quark and the loop-quark is large enough for the two intermediate charm quarks to become on-shell, consequently satisfying the BSS requirement. Yet, the strong phase is identical for B and $\overline{B}$ and thus *CP*-conserving. On the other hand, the up-quark always remains virtual since its mass is set to zero in the theory. In the interference of the up-loop and charm-loop diagram, a relative strong phase is hence created.
Finally, in the interference of the relative strong and weak phases the results deviate for $B \to K^*\gamma$ and $\overline{B} \to \overline{K}^*\gamma$ according to equation 2.38.
Experimentally, the *CP*-violating charge asymmetry is given by:

$$A_{CP} = \frac{\mathcal{B}(\overline{B} \to \overline{K}^*\gamma) - \mathcal{B}(B \to K^*\gamma)}{\mathcal{B}(\overline{B} \to \overline{K}^*\gamma) + \mathcal{B}(B \to K^*\gamma)} \tag{2.39}$$

The *CP*-violating effects from loop diagrams containing light quarks and gluons first arise at $\mathcal{O}(\alpha_S)$. The SM prediction for A_{CP} is thus suppressed by three small factors; α_S arising from the strong phases, $V_{us}^*V_{ub}/V_{ts}^*V_{tb} \sim \lambda^2$ reflecting the CKM suppression, and $(m_c/m_b)^2$ resulting from GIM suppression. The tiny predicted SM-asymmetry is around 0.5% [7].

New-Physics Impact on A_{CP}

The inclusive case $b \to s\gamma$ is referred to concerning the potential impact of New Physics on the *CP*-violating charge asymmetry A_{CP} since there are no such studies for the exclusive decay $B \to K^*\gamma$ explicitly yet. All predicted *CP* asymmetries remain almost

unaffected by a cut on the high-energy photon spectrum. Therefore, any large asymmetry in the inclusive mode will also show up in $B \to K^*\gamma$ [10]. Hence the predicted A_{CP} within the SM is of the same order of magnitude in the inclusive and exclusive decay [39].
In New Physics models, additional sources of *CP*-violation enter the game and larger *CP* asymmetries become possible with enhancement of the chromo-magnetic dipole operator. The suppression factors $(m_c/m_b)^2$ and λ^2, operative in the SM, can be avoided by additional contributions to the Wilson coefficients containing non-trivial weak phases. Exploring the structure of NP models, one has to take into account the constraint that they have to yield a consistent result for the overall, *CP* averaged branching fraction. This depends on the C_i through the combinations $\mathrm{Re}[C_i C_j^*]$, whereas A_{CP} is a function of the imaginary parts. In order to investigate such scenarios, the *CP* asymmetry in $b \to s\gamma$ can be written as [39]:

$$A_{CP} = \frac{1}{|C_7|^2}\left\{a_{27}\mathrm{Im}\left[C_2 C_7^*\right] + a_{87}\mathrm{Im}\left[C_8 C_7^*\right] + a_{28}\mathrm{Im}\left[C_2 C_8^*\right]\right\} \tag{2.40}$$

Here, the small CKM-factor $1 - V_{us}^* V_{ub}/V_{ts}^* V_{tb}$ has been neglected. The third term is generally very small whereas the first two can give rise to sizable effects; the ratio $a_{27} : a_{87} : a_{28}$ is roughly $1 : -10 : 0.1$. It is customary to parametrise the results in terms of the following ratio:

$$\xi = -3 \cdot C_7^{new}(m_W)/C_8^{new}(m_W) \tag{2.41}$$

The contribution of a NP scenario is given at its (large) scale M and can be evolved down to the electroweak scale m_W using the renormalisation group. In case of a single dominant NP contribution, such as the virtual exchange of a new heavy particle, the parameter ξ is real. Two classes of of models with moderate $|\xi|$ (class-1) and large $|\xi|$ (class-2) can be distinguished. Examples of class-1, which allow for large A_{CP} from $C_7 - C_8$ interference, are penguin diagrams containing new neutral scalars, and vector-like quarks with $\xi \approx 0.8$ [42], furthermore models with techniscalars ($\xi \approx -0.7$) and super-symmetric penguins containing light gluinos and squarks for which ξ is also negative [43]. In class-1 models there exists great potential for sizable *CP* asymmetries up to 20%. In class-2 scenarios the $C_7 - C_8$ interference becomes the more ineffective the larger $|\xi|$ becomes, and the $C_2 - C_7$ interference term gains importance. Models with gluino-squarks loops can have large negative values of $-2.9 < \xi < -1$, penguin graphs in left-right symmetric models with right-handed couplings of the W boson to the top and bottom quarks have $\xi \approx -6.7$. Charged-Higgs-top penguins in multi-Higgs models always have $\xi < -2$. Higgsino-stop penguins always lead to sizable negative values of $-24 < \xi < 2.6$. Finally, large positive values of $4.8 < \xi < 8.3$ arise from penguin graphs with a scalar diquark and-top quark in the loop. For large positive values, e.g. $\xi \approx 5$, *CP* asymmetries of 5-20% are seen to be consistent with the *CP*-averaged $B \to X_s\gamma$ bound whereas for negative values, e.g. $-5 < \xi < -2.5$, asymmetries of only a few percent are attainable [44].

Chapter 3

The *BABAR* Detector

The *BABAR* experiment has been conceived to study the physics of B mesons, especially *CP* violation in their decays, in order to test the consistency of the Standard Model. A high performance is required from both, the collider making available high luminosities and the detector providing excellent reconstruction, since typical B-meson branching fractions like $B \to K^*\gamma$ are in the order of 10^{-6} - 10^{-5} and thus very small.
The first section of this chapter gives a description of the e^+e^- collider PEP-II, whereas the second section explains the concept and various components of the *BABAR* detector.

3.1 The e^+e^- Storage Ring PEP-II

The *BABAR* detector is located at the *Stanford Linear Accelerator Center (SLAC)* in Stanford (California) and is part of a "B-Meson Factory" consisting of the *Linear* e^+e^--*Accelerator (LINAC)* and the e^+e^--collider PEP-II, which is an asymmetric storage ring (see figure 3.1). PEP-II has two rings to achieve the moving *centre-of-mass (CM)* system with respect to the laboratory frame; the *High Energy Ring (HER)* containing electrons with energy of 9.0 GeV and the *Low Energy Ring (LER)* with 3.1 GeV positrons. This leads to a Lorentz boost $\beta\gamma = 0.55$ of the CM and a centre-of-mass

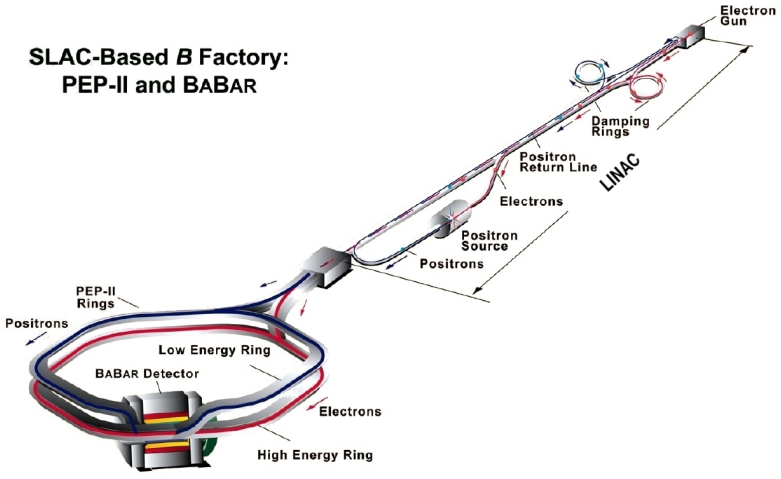

Figure 3.1: *The LINAC (right), the PEP-II ring (left) and the BABAR detector (bottom left).*

$e^+e^- \rightarrow$	$b\overline{b}$	$c\overline{c}$	$s\overline{s}$	$u\overline{u}$	$d\overline{d}$	$\tau^+\tau^-$	$\mu^+\mu^-$	e^+e^-
Cross-section [nb]	1.09	1.30	0.35	1.39	0.35	0.94	1.16	~50

Table 3.1: *Production cross-sections at* $\sqrt{s} = M_{\Upsilon(4S)}$.

energy of 10.58 GeV in the collision, which is the energy region where the $b\overline{b}$ bound state $\Upsilon(4S)$ is located. The $\Upsilon(4S)$ decays exclusively to $B^0\overline{B}^0$ and B^+B^- pairs. Whereas the boost of the centre-of-mass system is irrelevant for the $B \rightarrow K^*\gamma$ analysis, it is needed for the determination of the time difference of the B^0 and $\overline{B}^0$ decays in the measurement of the indirect CP-violation parameter $\sin 2\beta$ that is one of the primary goals of *BABAR*. As the energy of the $\Upsilon(4S)$ resonance is slightly larger than twice the B-meson mass, the latter are produced via the chain $e^+e^- \rightarrow \Upsilon(4S) \rightarrow B\overline{B}$ with the B mesons nearly at rest in the centre-of-mass frame. Besides the desired $B\overline{B}$ events, a considerable amount of continuum and lepton-antilepton events is produced in the e^+e^- collisions. In effect this is unwanted background but can also be used for additional physics analysis with *BABAR*. The cross sections for the most important background channels are listed in table 3.1.

In 1999 and 2000, 1658 particle bunches are stored in both rings of 2220 m circumference. In the HER, $1.9{\cdot}10^{10}$ electrons are comprised in one bunch, leading to an effective current of 0.7 A, whereas in the LER there are $3.7{\cdot}10^{10}$ positrons, corresponding to 1.3 A. In the interaction zone, the bunches are focused by quadrupol magnets to a vertical size of 6 μm and a horizontal size of 120 μm. The spread along the beam direction is much larger with $\sigma_z = 9$ mm [45].

PEP-II has been providing stable beams from the beginning of running in 1999. In the year 2000, data taking with up to 150 pb^{-1} per day and a peak luminosity of $3.1 \cdot 10^{33} cm^{-2} s^{-1}$ could be achieved. The injection from the LINAC into the rings usually takes place in the *top-off* mode where particles are added to the existing bunches. The small branching fractions of the investigated B-decay modes require a large number of $B\overline{B}$ events. The integrated recorded luminosity in the "*RUN 1*" of *BABAR* from October 1999 to October 2000 was 20.7 fb^{-1} on-resonance and 2.6 fb^{-1} off-resonance, i.e. 40 MeV below the $\Upsilon(4S)$ resonance. This corresponds to $22.7{\times}10^6$ produced $B\overline{B}$-pairs. Figure 3.2 shows the integrated luminosity in 1999 and 2000.

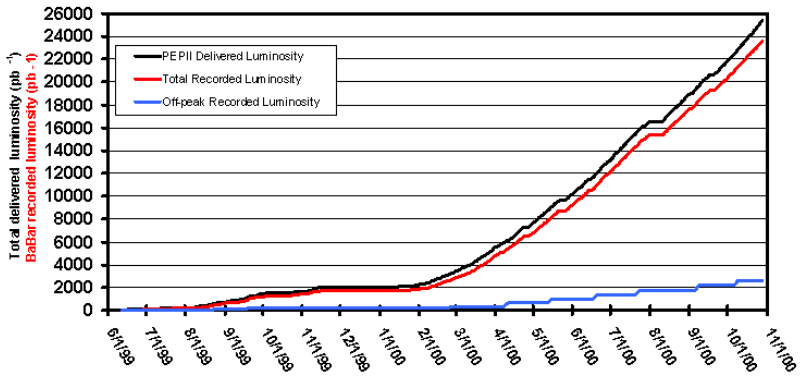

Figure 3.2: *The integrated luminosity in 1999 and 2000. Compared is the amount delivered by PEP-II and recorded by BABAR, furthermore the fraction of off-resonance data.*

There are several advantages of $e^+e^- \to \Upsilon(4S) \to B\overline{B}$ decays over other experimental conditions [46]:

- e^+e^- reactions have a better signal-to-background ratio ($\sigma_{b\bar{b}}/\sigma_{tot} \approx 0.28$) and, with a track multiplicity of ~ 11 per event, they are cleaner compared to a hadronic environment. This results in an increased ability to reconstruct photons and π^0s, which is important also for this analysis.
- Compared to e^+e^- experiments running at higher energies, on the $\Upsilon(4S)$ coherent $B\overline{B}$-pairs are produced, decreasing background from fragmentation and providing precise knowledge of kinematical constraints like the B energy in the CM frame.

3.2 The Components of the *BABAR* Detector

The international *BABAR* collaboration started its detector project at the interaction zone of electrons and positrons at PEP-II in 1993. *BABAR* is running and taking data since spring 1999 with a current rate of around 100 recorded events per second.
The physics goals of the *BABAR* project are the study of CP-violating asymmetries in the decays of B mesons and precision measurements of decays of bottom mesons. In order to achieve these goals one has to meet the following requirements [47]:

- A wide acceptance and preferably uniform efficiency of the reconstruction of charged particles by the tracking devices with high momentum resolution. For the $B \to K^*\gamma$ mode this affects the kaons and pions coming from the K^*. The precise reconstruction of decay vertices also plays a role in this analysis, yet it is not as crucial as in the measurement of CP-violating asymmetries in B^0 decays [5].
- An efficient measurement of photons with large angular acceptance in the centre-of-mass frame and in the whole energy range from 30 MeV to 4.5 GeV, associated with excellent energy and angular resolution, but also with exact shower shape information for background suppression. In this analysis this concerns the hard radiative photon and the somewhat softer photons from π^0s.
- An excellent *particle identification (PID)*, in our case to separate pions from kaons over a wide kinematic range.
- A computing and network system that is able to cope with the high volume of data and permits fast and reliable data analysis.

Figure 3.3 shows the six main subsystems of the detector. Each will be covered in more detail in the following sections. The e^- beam arrives from the left. Its direction, which is also the direction of the boost, defines the *forward direction* of the detector. The right-handed detector coordinate-system is defined in such a way that the z axis is parallel to the electron beam and the x axis points horizontally outside the ring with the origin lying at the nominal interaction point. The corresponding spherical coordinates are referred to as the radius r, the polar angle θ, and the azimuthal angle ϕ. The *BABAR* detector is designed asymmetric in θ to adjust the geometrical acceptance to the boosted centre of mass, in ϕ it features cylindrical symmetry around the beam axis. The overall acceptance of *BABAR* covers a polar angle range from 10^o to 135^o, corresponding to a region of -0.95$< \cos\theta_{CM} <$0.87 in the $\Upsilon(4S)$ centre-of-mass system.

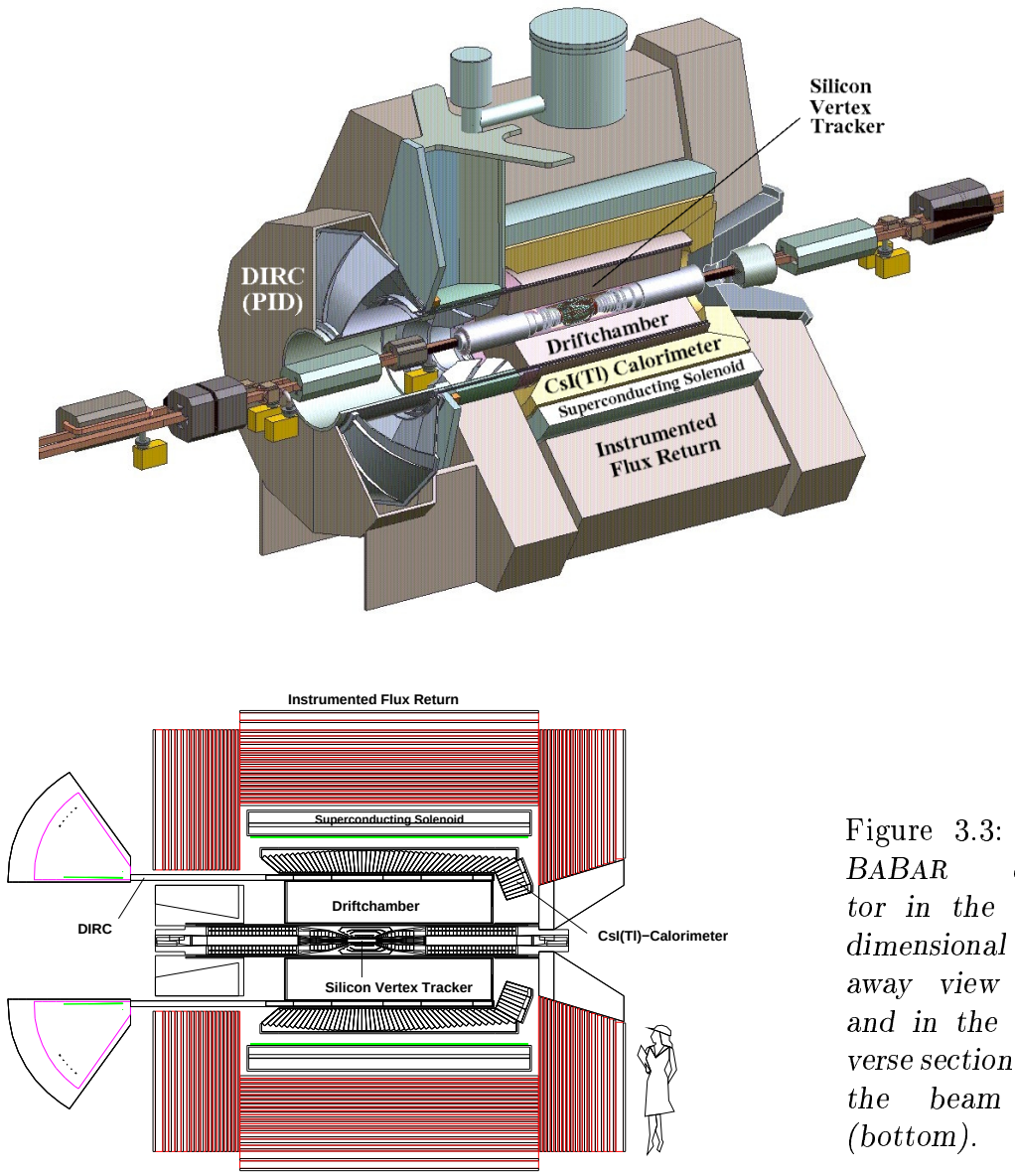

Figure 3.3: *The BABAR detector in the three-dimensional cut-away view (top) and in the transverse section along the beam axis (bottom).*

The main subdetectors of *BABAR* are:

1. The *Silicon Vertex Tracker (SVT)* provides momentum measurement and precise reconstruction of the origin of tracks.
2. The *Drift Chamber (DCH)* provides the tracking of charged particles including the momentum measurement, and dE/dx information for particle identification.
3. The *Detector of Internally Reflected Cherenkov light (DIRC)* is the main device for particle identification of charged particles.
4. The *Electromagnetic Calorimeter (EMC)* is responsible for the detection of neutral particles and the measurement of energies. Furthermore, it provides information for particle identification, especially electrons.
5. The *superconducting solenoid* produces a magnetic field of 1.5 T.
6. The *Instrumented Flux Return (IFR)* is the device for muon and neutral hadron identification.

3.2.1 The Silicon-Vertex-Tracker

The SVT is a reconstruction device for tracks inside the support tube of PEP-II, i.e. it is the innermost component of the detector. This allows the position measurement of tracks very close to the interaction point, especially the primary decay-vertices of the B mesons.
A particle entering the silicon creates electron-hole pairs along its path. These electrons are collected and form a signal because of the applied voltage. To measure these tracks, the SVT is built of five concentric cylindrical layers of double-sided silicon microstrip detectors (see figure 3.4). Each outer side has strips parallel to the z direction measuring the polar angle ϕ, whereas the inner sides have strips perpendicular to the beam axis measuring the position in z. The readout was moved to the two ends to reduce the material inside the acceptance volume. Concerning the *front-end electronics (FEE)*, the SVT disposes of about 150,000 single readout channels.
The SVT measurement provides the most accurate angular information of tracks since multiple scattering degrades the resolution of tracking as one moves away from the interaction point. Furthermore, the SVT is the only detector for tracks with a transverse momentum smaller than 100 MeV/c which do not reach the drift chamber. The radial distance of the SVT layers to the interaction point varies from 3 cm to 15 cm and the covered polar angle range is $20^o < \theta_{lab} < 150^o$ [48].

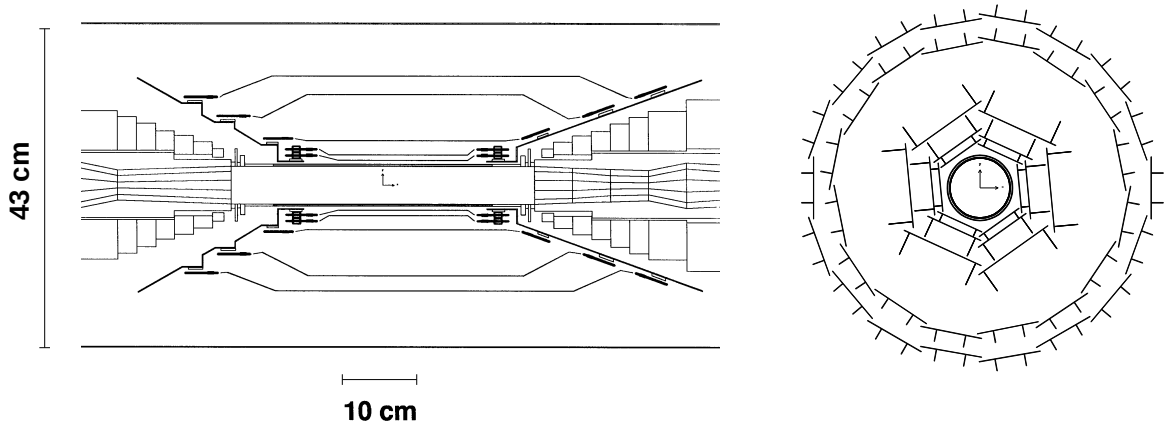

Figure 3.4: *Geometry of the silicon vertex tracker. The transverse section (left) and front view (right) show the inner three layers with six modules each and the outer two layers with 16 and 18 modules, respectively.*

3.2.2 The Drift Chamber

The drift chamber is the core tracking instrument of *BABAR*. Its design is optimized for tracks with transverse momentum larger than 100 MeV/c, additionally it is the main tracker for the pions coming from a K_S^0 that are not seen by the SVT. The drift chamber thus is the relevant tracking device for this analysis. Furthermore, below momenta of 700 MeV/c the drift chamber provides a complementary π/K separation to the DIRC, using the information from the specific ionization energy dE/dx.

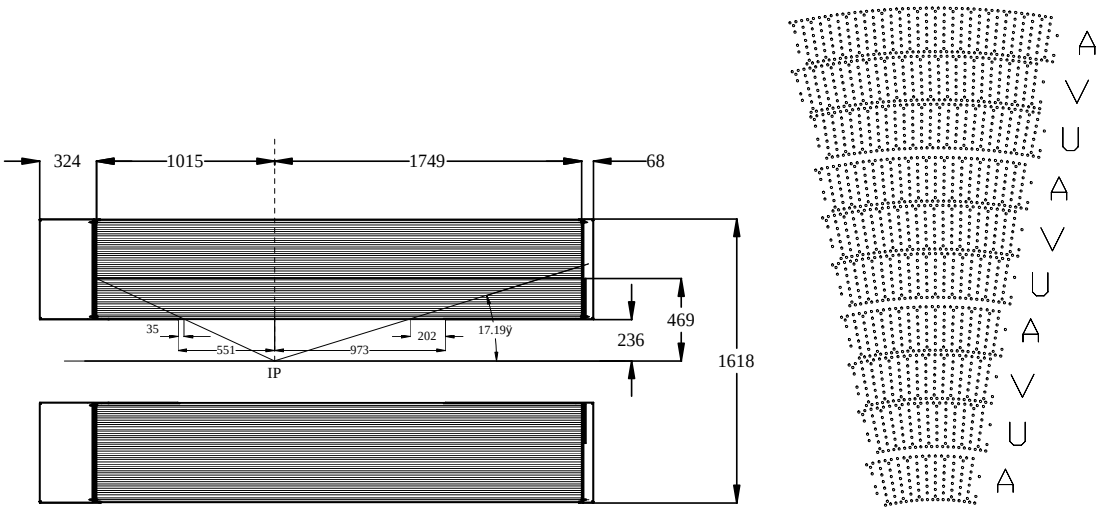

Figure 3.5: *Geometry of the drift chamber. The transverse section is illustrated on the left. The front section on the right shows the alternation of the axial (A) and stereo (U,V) superlayers. There are ten superlayers, each containing four layers.*

A charged particle flying through the drift chamber ionizes molecules of the gas along its track. The resulting electrons drift with constant speed towards the signal wires, where they are registered. Knowing the drift velocity and using different arrangements of the wires, the momentum vector of the particle can be accurately reconstructed.
A scheme of the drift chamber is shown in figure 3.5. Each drift cell contains one signal wire made of gold-plated tungsten and field wires made of gold-plated aluminium in a hexagonal structure. The cells are arranged in ten superlayers, each of them containing four layers of cells, resulting in a total of 7104 drift cells with a length of 2.80 m each. The superlayers are alternating between an axial and two stereo layouts two achieve optimal spatial resolution. The angular coverage of the drift chamber is $17^o < \theta_{lab} < 153^o$. The readout of the drift chamber is located at the backward end to minimize the material in front of the calorimeter endcap [49].
The DCH detector contains a gas mixture with 80 % helium and 20 % isobutane to minimize multiple scattering, drift time, and material (gas and wires correspond to 0.2% of the radiation length X_0 at 90^o [50]).

3.2.3 The Detector of Internally Reflected Cherenkov Light

The DIRC was conceived as the major particle identification instrument of *BABAR* since the separation of kaons and pions with the drift chamber is not efficient above momenta of $\approx$ 700 MeV/c. The DIRC provides excellent kaon-pion separation for particle momenta between 0.5 GeV/c and 4.5 GeV/c. The highest performance is reached in the momentum range below 2 GeV/c. This quality is needed in this analysis and for flavour-tagging in the measurements of the *CP* angles $\sin 2\beta$ and $\sin 2\alpha$.

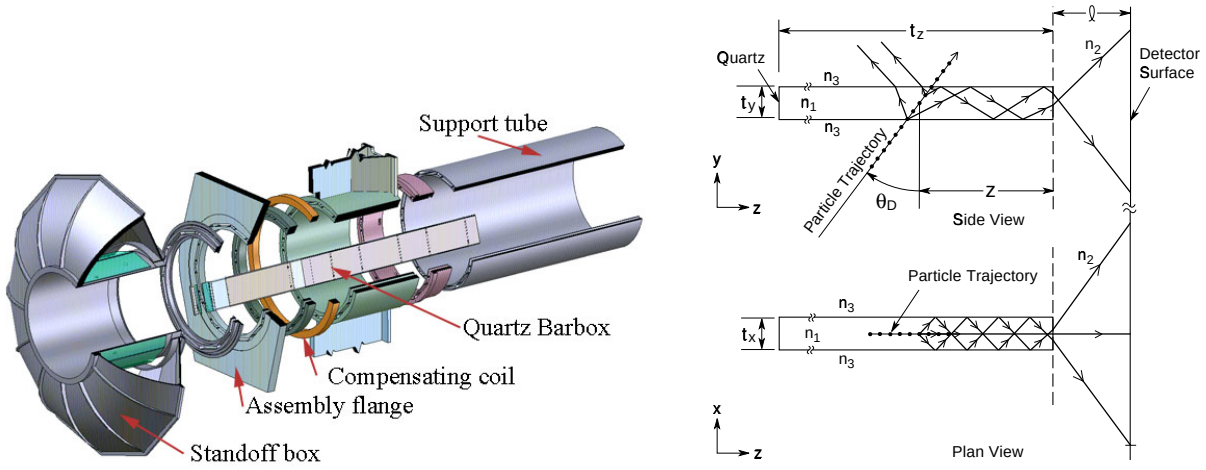

Figure 3.6: *Layout of the detector of internally reflected Cherenkov light (left) and scheme of a single DIRC radiator bar, illustrating the working principle (right). The photons arrive at the read out at the backward end by internal total reflection.*

The DIRC uses the Cherenkov effect to identify charged particles which emit cones of Cherenkov light when transversing the quartz medium of refractive index $n = 1.47$ with a velocity $\beta = v/c$ of $\beta > 1/n$. The expected Cherenkov angle θ_C of the photons with respect to the track direction is [51]:

$$\cos\theta_C = \frac{1}{\beta n} = \frac{1}{n}\sqrt{1+\left(\frac{m}{p}\right)^2} \qquad \text{since} \qquad p = m\frac{\beta}{\sqrt{1-\beta^2}} \tag{3.1}$$

To verify a particle mass hypothesis, the corresponding expected value of θ_C is compared to the actual measured Cherenkov angle.
An important design issue of the DIRC was to minimise the impact of the additional material on the performance of the calorimeter behind it [52]. Therefore the entire readout was moved to the backward end of the instrument, deploying a new principle of reflected Cherenkov-light for particle identification as illustrated in figure 3.6. In contrast to a conventional *ring-imaging Cherenkov detector (RICH)* where the *photomultiplier tubes (PMTs)* are located behind the radiators, in the DIRC the photons are propagated along the quartz bars by internal total reflection, preserving the angle of emission. Thereafter, they are detected at the rear end of the detector. The radiator bars are thus used for both, to generate the Cherenkov photons but also to trap and guide them to the water-filled toroidal readout reservoir outside of the *BABAR* detector. Besides the reduction of material inside the detector, the advantages of the DIRC design are that, outside the magnetic field, one can use faster and simpler photomultipliers. On the other hand, the reconstruction of the multiple reflected photons is more complex.
The actual implementation of the DIRC consists of 144 synthetic quartz bars with rectangular cross section (1.7 cm $\times$ 3.5 cm) and a length of 4.9 m, which are arranged

in a twelve-sided polygon structure. The radial thickness of the bars corresponds to 17% X_0 at normal incidence. The spatial coverage in the centre-of-mass system is 83% in θ and 94% in ϕ. The signal readout at the back wall of the rear 6,000-liter water-tank is performed by about 11,000 PMTs [53].

3.2.4 The Electromagnetic CsI(Tl)-Calorimeter

The main task of the EMC in *BABAR* is the reconstruction of photons down to an energy of 20 MeV, and the identification of electrons. The detection of the hard radiative photon and the (softer) photons from the π^0s is the key feature of the $B \to K^*\gamma$ analysis presented in this work, and requires very good electromagnetic calorimetry. The missing vertex information for the π^0s has to be compensated by an excellent energy and angular resolution to obtain a comparable quality of B-meson reconstruction to the decays with tracks only. An optimal compromise between high detection efficiency and shower separation has to be established for a good signal-to-background ratio since on one hand we deal with rare decays, while on the other hand there is a high shower multiplicity per event. Generic B-decays produce ~ 5.5 photons in average, about half of them at low energies below 200 MeV/c^2. These are accompanied by the electromagnetic showers caused by the charged particles and hadronic split-offs. Photons and electrons deposit their whole energy in the calorimeter whereas muons and hadrons are likely to pass it, only losing a certain amount of their energy.

Photons entering the crystals convert to e^+e^- pairs. The electrons and positrons emit *Bremsstrahlung*. By repetition of these processes an electromagnetic shower is created whose charged particles cause the atoms of the material to scintillate.

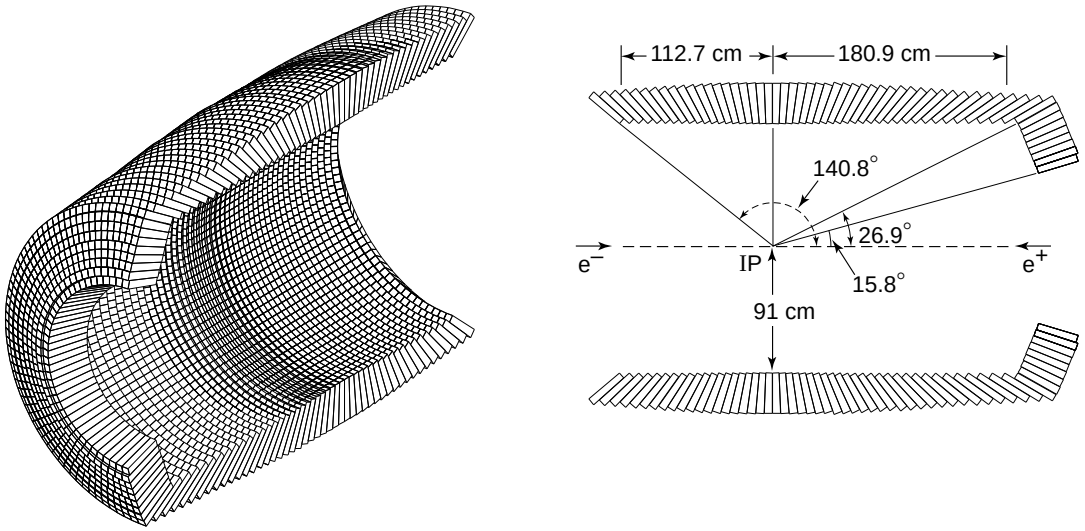

Figure 3.7: *Geometry of the electromagnetic calorimeter, illustrated by a 3-dimensional scheme (top) and a transverse section with respect to the interaction point (bottom). There are two main components, the barrel and the forward endcap.*

A scheme of the electromagnetic calorimeter is shown in figure 3.7. There is a forward endcap additional to the cylindric barrel to account for the fact that the decay products of the B mesons are boosted in the laboratory frame. The EMC has full coverage in azimuth and extends from 15.8^o to 141.8^o in polar angle, corresponding to a solid-angle coverage of 90%. Figure 3.7 illustrates the symmetric layout in the azimuthal angle ϕ and the quasi-projective arrangement of the crystals with respect to the nominal interaction-point in the polar angle θ. This non-projective alignment in θ was chosen to reduce the photon loss in the interstices between the crystals. The non-projectivity varies between ± 15 mrad for the bulk of crystals in the centre of the barrel and ± 45 mrad near the forward edge. The choice of thallium-doped caesium iodide as crystal material assures a high photon yield and high radiation resistance.

The barrel consists of 5760 trapezoidal crystals which are grouped in 48 θ-rows, each containing 120 identical crystals in ϕ at a radial distance of 91 cm from the beam axis. The 7×3 segmentation in θ and ϕ results in 280 modules which are supported from an external support structure. The geometric coverage of the barrel in the centre-of-mass frame is -0.916 $\leq \cos\theta_{CM} \leq$ 0.715. In the endcap there are 820 crystals arranged in eight θ-rings and possessing a 20-fold-symmetry in ϕ. The first three rings contain 120 crystals as in the barrel, the following three rings 100, and the two innermost rings 80 crystals. The endcap covers $0.718 \leq \cos\theta_{CM} \leq 0.895$. The dimensions of the crystals were motivated by the radiation length X_0 =1.85 cm and the Molière radius of 3.6 cm of the caesium iodide. Their length increases from 29.6 cm ($16.1X_0$) at the backward end to 32.4 cm ($17.6X_0$) at the front end of the barrel and in the endcap. The surfaces of the crystals measure 4.8 cm × 4.7 cm at the front and 6.1 cm × 6.0 cm in the rear [54].

The readout layout is a compromise between high performance and affordable costs. The scintillation light produced by an electromagnetic shower is received by two redundant photodiodes, propagated to the preamplifier on each crystal, and then processed by signal shapers. After another amplification by a *CARE* chip, the signals arrive at an *Analog to Digital Converter (ADC)* where the digital signals are extracted. The information from six crystals is collected in the *Input Output Boards (IOBs)* and sent to the *Read-Out Modules (ROMs)* [55].

Since a typical electromagnetic shower expands over many adjacent crystals, pattern recognition algorithms have to be applied to efficiently identify these *clusters*, and to separate single clusters with one energy maximum from *merged clusters* with several local maxima which are called *bumps* (see section 4.5.1). A second task of these algorithms is to provide the bump shapes used for the separation of electromagnetic and hadronic bumps.

The light yield of the crystals degrades with time due to radiation damage. The data from the electromagnetic calorimeter is therefore calibrated regularly in three main steps before being assigned to the energy of a particle. The electronics calibration takes care of the pedestals and removes non-linearities of the front-end-electronics using charge injection into the preamplifiers. The second stage is the calibration of the individual crystals. For the low energy range, this is performed with a radioactive source providing photons with a known energy of 6.13 MeV from the reaction chain $^{19}F(n,\alpha)^{16}N(\beta)^{16}O$ [56]. For the high energy range, non-radiative Bhabha events

$e^+e^- \to e^+e^-$ are exploited for an absolute crystal calibration [57]. The last step is the correction of the measured cluster energies for energy losses. Up to about 1 GeV, the π^0 mass peak position is used to adjust the photon energies [58, 59]. Above 500 MeV, a Monte Carlo simulation based calibration is deployed at the moment, soon radiative Bhabha events $e^+e^- \to e^+e^-\gamma$ will be used for the cluster calibration at high energies [60].

3.2.5 The Superconducting Solenoid and Instrumented Flux-Return

In a magnetic field, a moving particle experiences a deflection perpendicular to its flight direction due to the Lorentz force. Together with the tracking devices this is used to determine its momentum. The magnetic field of 1.5 T is created by the superconducting solenoid.
The IFR is the largest and outermost subdetector for muon and neutral hadron identification. It consists of a barrel, and forward and backward endcaps made of iron, all having a hexagonal profile. The thickness of the iron plates increases from 2 cm to 10 cm moving outwards, giving a total of 65 cm for the barrel and 60 cm for the endcaps. Single gap *resistive plate chambers (RPCs)* are inserted into the 3 cm wide interstices between the plates. The RPCs use ionization of a gas mixture of argon, freon and isobutane for particle identification. There are 21 layers of RPCs in the barrel and 18 in the endcap. The IFR is not needed for the $B \to K^*\gamma$ analysis.

3.2.6 The Trigger, Data-Taking and Data-Storage

The object-oriented programming language C++ was chosen for the *BABAR* software since the complexity and size of the software, and the high number of developing parties requires the structure and clarity of the code provided by object-oriented programming languages. There are several categories of *BABAR* software performing different tasks; to select B events of physics interest there are two triggers, the Level 1 hardware-trigger and the Level 3 software-trigger. With the current luminosity, there is no need for a Level 2 trigger yet. The Level 1 trigger uses basic data objects from the drift chamber for charged particles, from the electromagnetic calorimeter for neutral particles and from the IFR for cosmic rays and dimuons. Its fourth ingredient, the global trigger [61], combines the above three pieces of information by trying to match neutral objects with tracks, and creating a veto for cosmics. The Level 1 trigger filters an event rate of about 2000 events per second out of the PEP-II beam crossing rate of $\sim 250 \cdot 10^6$ events per second. The $B\overline{B}$ efficiency of the Level 1 trigger is 99.9 %. The following Level 3 trigger operates with more complex algorithms using the full information of the event from all subdetectors. About 100 events per second pass through the Level 3 trigger to the data processing, its $B\overline{B}$ efficiency is 99%.
During data taking, the *Online Run Control (ORC)* software permits the managing of *BABAR*, providing a graphical control interface to the shifters for directing the detector systems, starting and stopping runs, and performing calibrations. In the *Online Dataflow (ODF)* the events are composed from the digitized information coming

from the front-end electronics of all subdetectors via optical fibers. The next step is the data processing by the *Online Event Processing (OEP)* which takes care of calibration and monitoring of the events by partial reconstruction. The data are stored in *Extended Tagged Container (XTC)* files which are used by the *Online Prompt Reconstruction (OPR)* that transforms the raw data into physics objects like tracks and clusters, and combines these to particle candidates, thereby completely reconstructing all physics events. These final data are stored in the object-oriented database *Objectivity* and the sequential, *ROOT*-based database *KANGA* [62], from where they can be used for off-line physics analysis. There are two parts of data, the event database and the conditions database. The latter contains the state of PEP-II and the detector, i.e. calibration constants etc.

Chapter 4

Event Selection

This chapter provides an overview of the path that has been followed for the selection of events in this analysis. The main issue in the measurement of rare decays, as in this case of $B \to K^*\gamma$, is the separation of the signal from the abundant background on one hand while keeping a high signal reconstruction efficiency on the other hand. Less than one in ten thousand B decays is an event that is sought for. Besides the B production there are about five times more additional events coming from lepton-antilepton and quark-antiquark production (where the quark can be u, d, s or c, see table 3.1). The $B \to K^*\gamma$ analysis proceeds by detecting the high-energy photon from the B decay, reconstructing the tracks and π^0 mesons in the K^* decay, combining the K^* and γ to form the B candidate and finally applying cuts on certain event shape variables and the kinematic quantities.

4.1 The $B \to K^*\gamma$ Signal Mode

The $B \to K^*\gamma$ events have been reconstructed in the neutral mode $B^0 \to K^{*0}\gamma$ and the charged mode $B^\pm \to K^{*\pm}\gamma$. In the case of a B^+ the final state is an $\overline{s}u$ with J=1 which is a K^{*+}, whereas in the case of B^0 it is $\overline{s}d$ with J=1, a K^{*0}. The four considered final states are $K^{*0} \to \pi^- K^+$, $K^{*0} \to \pi^0 K_S$, $K^{*\pm} \to \pi^0 K^\pm$ and $K^{*\pm} \to \pi^\pm K_S$. The K_S have been reconstructed from charged pions, i.e. in the decay $K_S \to \pi^+\pi^-$. To establish the signal reconstruction procedure and the corresponding software code, simulated Monte Carlo data was used for the signal as well as for the various backgrounds (see section 4.3) before the real on-resonance data was analysed. Until the release of these results of *BABAR*, the only measurement of the decay rate and thus the PDG value [37] was the one from the CLEO experiment using 9.2 fb^{-1} of on-resonance and 4.6 fb^{-1} off-resonance data [11]. Their results are $\mathcal{B}(B^0 \to K^{*0}\gamma) = (4.55^{+0.72}_{-0.68} \pm 0.34) \cdot 10^{-5}$ and $\mathcal{B}(B^\pm \to K^{*\pm}\gamma) = (3.76^{+0.89}_{-0.83} \pm 0.28) \cdot 10^{-5}$.

4.2 Backgrounds

The background in this analysis is given by three contributions:

- The first possibility are continuum events, $e^+e^- \to u\overline{u}, d\overline{d}, s\overline{s}, c\overline{c}$, with *initial state radiation (ISR)* where a K^* is reconstructed in the continuum and, combined with the ISR photon, accidentally leads to a B candidate. This scenario is depicted on the top left of figure 4.1. In the detector, the topology of these events looks like two jets and a high-energy photon.
- The second considerable background, also from continuum events, arises from a high-energy photon originating from a π^0 or a *merged* π^0 whose photon-daughters cannot be separated (see section 4.7.2) and are thus identified as one photon. Such a candidate in one jet, combined with a K^* in the other jet, can fake a $B \to K^*\gamma$ event (see top right of figure 4.1).
- The third, yet quantitatively less important possibility, are events leaking into the signal from $B \to K^*\gamma$ decays with different K^* decay modes ("*cross-feed*") and from higher-resonance $b \to s\gamma$ decays ("*down-feed*").

One can take advantage of the different event topologies illustrated in figure 4.1 to separate the signal from background. Selection criteria will be applied on certain event-shape variables which reflect the fact that signal events are more or less spherical, whereas background from continuum sources will be much more jet-like.

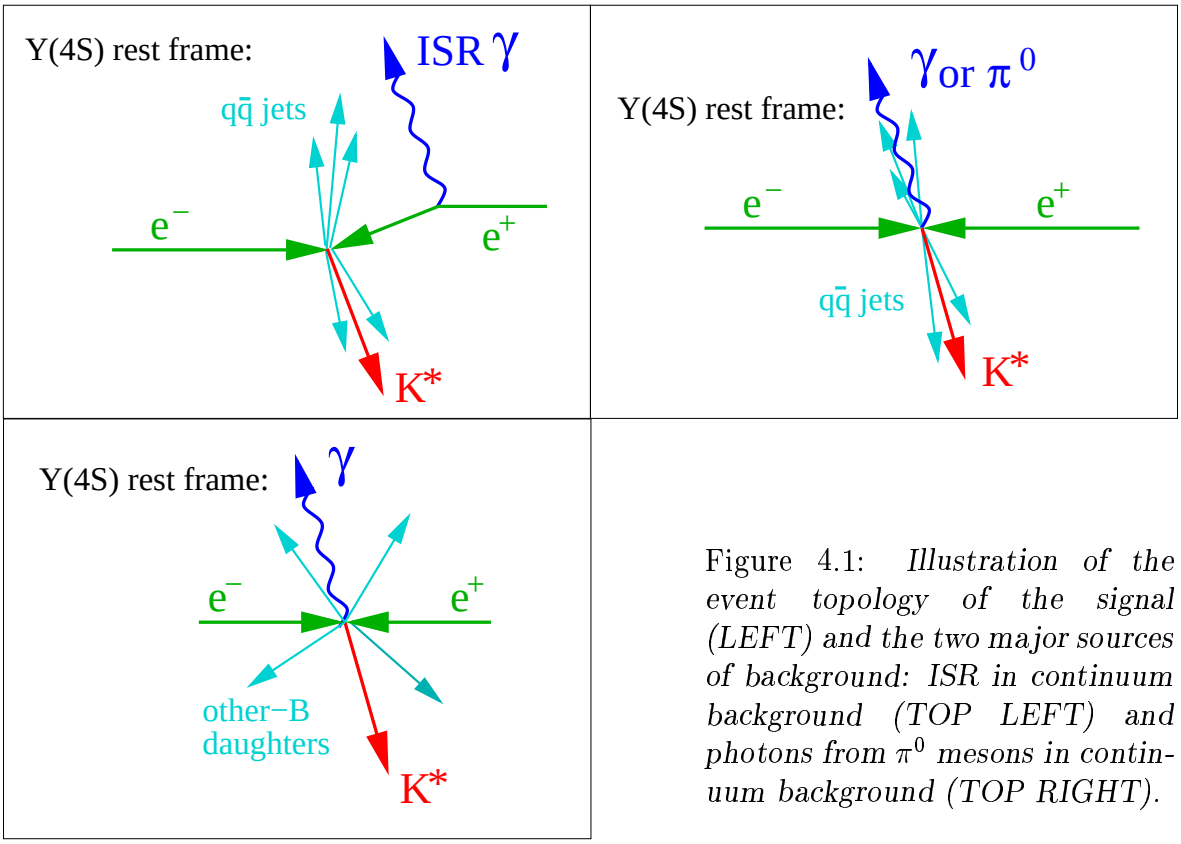

Figure 4.1: *Illustration of the event topology of the signal (LEFT) and the two major sources of background: ISR in continuum background (TOP LEFT) and photons from π^0 mesons in continuum background (TOP RIGHT).*

4.3 Used Data

The data set used in this analysis is the real on-resonance data of (20.7±0.2) fb^{-1}and off-resonance data (2.62±0.03) fb^{-1}[63] accumulated by *BABAR* in its RUN 1 from October 1999 until October 2000, corresponding to (22.74±0.36)×10^6$B\overline{B}$ pairs [64]. Furthermore, simulated Monte Carlo data was deployed to optimise the event selection criteria and to determine the signal efficiencies. Detailed lists of the used data are shown in appendix B. Using the PDG values of B($B \to K^*\gamma$) (see section 4.1), the numbers of produced decays can be estimated for each mode. They are listed in table 4.1.

Decay Mode	Branching Fraction	Produced Events
$B^0 \to K^{*0}\gamma$, $K^{*0} \to \pi^+K^-$	(2.77±0.41)·10^{-5}	630±94
$B^0 \to K^{*0}\gamma$, $K^{*0} \to \pi^0K_S$, $K_S \to \pi^+\pi^-$	(0.46±0.10)·10^{-5}	105±16
$B^+ \to K^{*+}\gamma$, $K^{*+} \to \pi^0K^+$	(1.39±0.31)·10^{-5}	315±47
$B^+ \to K^{*+}\gamma$, $K^{*+} \to \pi^+K_S$, $K_S \to \pi^+\pi^-$	(0.94±0.20)·10^{-5}	210±31

Table 4.1: *Estimated number of signal events in the BABAR-RUN 1 dataset using the current PDG value of $\mathcal{B}(B \to K^*\gamma)$ before this analysis.*

4.4 Optimisation of Selection Criteria

A number of selection criteria ("*cuts*") will be optimised for the analysis. The procedure is an iterative one, i.e. all other cuts of the analysis are applied if not stated otherwise and the variable in question is optimised. Having determined all cuts, the procedure is redone. Only one iteration has been necessary since there was no significant change of the cut values. As explained in detail in section 4.13, the finally reconstructed B candidates will be characterised by two quantities; their energy-substituted B-mass M_{ES} and their energy deficit ΔE^*.
The optimisation of cuts is done by varying the relevant cut and maximising the ratio $S^2/(S+B_g)$. Here, S and B_g are the expected number of signal and background events in the signal-box region. This box is defined by -225 MeV $< \Delta E^* <$ 125 MeV for modes containing π^0s and -200 MeV $< \Delta E^* <$ 100 MeV for the other two modes, and 5.27 GeV/c^2 $< M_{ES} <$ 5.29 GeV/c^2 for all four modes (see section 4.13). The signal yield S is obtained using signal Monte Carlo data scaled by luminosity assuming the PDG branching fraction of $3.8 \cdot 10^{-5}$ for the charged mode and $4.5 \cdot 10^{-5}$ for the neutral mode. B_g is gained from two sets of events; the continuum Monte Carlo (11.9 fb^{-1} of $e^+e^- \to c\overline{c}$ and 11.9 fb^{-1} of $e^+e^- \to u\overline{u}, d\overline{d}, s\overline{s}$) and the off-resonance data as a cross-check. To enhance background statistics, the event yields in the grand sideband region (-300 MeV $< \Delta E^* <$ 300 MeV , 5.2 GeV/c^2 $< M_{ES} <$ 5.29 GeV/c^2) are scaled by luminosity and by the ratio of the sizes of the signal box and this grand sideband to determine the background yield. Examples of such a cut optimisation are shown in figure 4.23 and 4.28. For all optimisations done throughout the analysis there is good agreement between the results obtained by continuum Monte Carlo and by off-resonance data.

4.5 Particle Reconstruction

In order to reconstruct signal events, the necessary condition is to find all detectable daughter particles. A commensurate condition is the distinction between signal and background events. Hence, a high detection efficiency and good spatial and energy resolution are needed for all the detector components presented in chapter 3.2. In our case, the final neutral and charged particles seen in the detector are photons, charged pions and charged kaons.

4.5.1 Detection of Neutral Particles

In the *BABAR* experiment, photons are solely measured by the EMC component of the detector (section 3.2.4). If an initial crystal contains an energy of at least 10 MeV, a *cluster* is formed together with all contiguous crystals exceeding 1 MeV. Inside one cluster there can be several local maxima called *bumps*. The latter are identified by the requirement that the candidate's crystal measure an energy E_{max}^{local} of at least 20 MeV, that it exceed all neighbour crystals, and that $0.5(N-2.5) > E_{max}^{neigh}/E_{max}^{local}$ be satisfied, where E_{max}^{neigh} is the highest-energy neighbour and N is the number of neighbours with at least 2 MeV. During the division of the cluster into as many bumps as there are local maxima, each crystal is given a weight w_i for every bump by an iterative procedure:

$$w_i = E_i \frac{\exp(-2.5 r_i/M_R)}{\Sigma_i E_i \exp(-2.5 r_i/M_R)}, \quad E_{bump} = \sum_i w_i E_i, \quad \sum_{bumps} E_{bump} = \sum_i E_i \qquad (4.1)$$

Here, r_i is the 3-dimensional distance of the ith crystal from the centroid of the bump and M_R is the Molière radius of the crystals (3.8 cm). The sum Σ_i extends over all crystals i belonging to the cluster. The position $(\theta_{bump}, \phi_{bump})$ is determined by a centre-of-gravity method with logarithmic, rather than linear weights, and the two-dimensional centroid is projected onto the front face of the containing crystal.
The energy resolution σ_E/E for photons at 90^o and the angular resolution $\sigma_{\theta,\phi}$ can empirically be written as:

$$\frac{\sigma_E}{E} = \frac{a}{\sqrt[4]{E[GeV]}} \oplus b, \qquad \sigma_{\theta,\phi} = \frac{c}{\sqrt[2]{E[GeV]}} \oplus d \qquad (4.2)$$

The term a arises mainly from photon statistics and electronic and photon background noise, whereas b, which dominates at higher energies >1 GeV/c^2, includes radiation leakage (1%), calibration uncertainties (0.3%), and light collection non-uniformities (0.5%). The angular resolution is determined by the transverse crystal size and the distance from the interaction point. The design values of a, b, c and d are 1%, 1.2%, 3 and 2 mrad, respectively [65]. The achieved resolutions to date are $a = (2.32 \pm 0.30)\%$, $b = (1.85 \pm 0.12)\%$, $c = (3.87 \pm 0.07)$ mrad, and $d = (1.00 \pm 0.04)$ mrad [66].
Two statements are made about the neutrality of energy deposits; tracks measured by the SVT and DCH are extrapolated to the front surface of the calorimeter, taking into account energy losses using a pion hypothesis. A cluster is determined as neutral if any extrapolated track does not intersect any of its crystals. A bump is labelled as neutral if the significance level of matching is less than 10^{-6}. This quantity is determined with

Monte Carlo by comparison of the 3-dimensional separation of the track's intersection with the crystal's surface and the bump's centroid.

4.5.2 Tracking of Charged Particles

The two tracking devices of the *BABAR* detector are the SVT (section 3.2.1) and the DCH (section 3.2.2). A charged particle in a uniform magnetic field moves along a helix which can be decoupled into a circle in the xy-plane, needing three points to define it, and a straight line, asking for at least two points. Hence, a track has first to be found using pattern recognition. For the SVT this means finding three space points on different layers that might form a track. In the case of DCH, three *segments* in the axial layers form a circle and the addition of the z-measurement from the stereo layers completes the helix. The subsequent track fitting applies a Kalman Filter [68] which takes into account physics effects like multiple scattering, energy loss, non-uniform magnetic field etc. There are five standard "perigee" parameters of the helix for the track fits, which are [67]:

- The distance d_0 of closest approach ("DOCA") of the track to the nominal beam spot in the azimuthal xy-plane. In the *BABAR* coordinate-system the nominal beam spot is at (0,0,0.33 cm).
- The azimuthal angle ϕ_0, corresponding to the track direction in the xy-plane
- The geometrical curvature $\omega = 1/r$ with r being the radial distance to the origin
- The position z_0 of the orbit at the point of closest approach in the xy-plane
- The tangent of the dip angle $\tan\lambda = \cot\theta$, the slope of the track

The curvature radius r and the transverse track momentum p_T are related by $r \propto p_T/qB_z$ with the longitudinal magnetic field B_z and the charge q.

Track Quality

The SVT gives much better resolution on the position and angle measurements d_0, z_0, $\tan\lambda$, and ϕ_0, whereas the resolution on the momentum is dominated by the DCH information. The spatial resolution of the SVT reaches 10 μm for an incidence angle of 90^o in the three first layers and degrades to 40 μm for higher angles as well as for layers further outside [69]. As a comparison, the averaged value for the DCH is about 140 μm and the mean separation of conjugated B mesons is $\sim$250 μm. The overall track resolutions in z_0 and d_0 are about 40 μm and 25 μm, respectively, at $p_T = 3$ GeV/c. Concerning the transverse momentum p_T, the precision is given by the linear function of the width σ_{p_T} [70]:

$$\sigma_{p_T}/p_T = (0.13 \pm 0.01)\% \cdot p_T[\text{GeV/c}] + (0.45 \pm 0.03)\% \tag{4.3}$$

The quality of the track fitting depends on the number of drift chamber hits N_{DCH}, the distances of closest approach to the nominal interaction point d_0 and z_0, and the transverse momentum p_T. Thus, in order to classify the quality of a reconstructed track, the following criteria are used to label a "good" track:

- $N_{DCH} > 12$, $|d_0| < 1.5$ cm, $|z_0| < 10$ cm, 100 MeV/c $< p_T <$ 10 GeV/c .

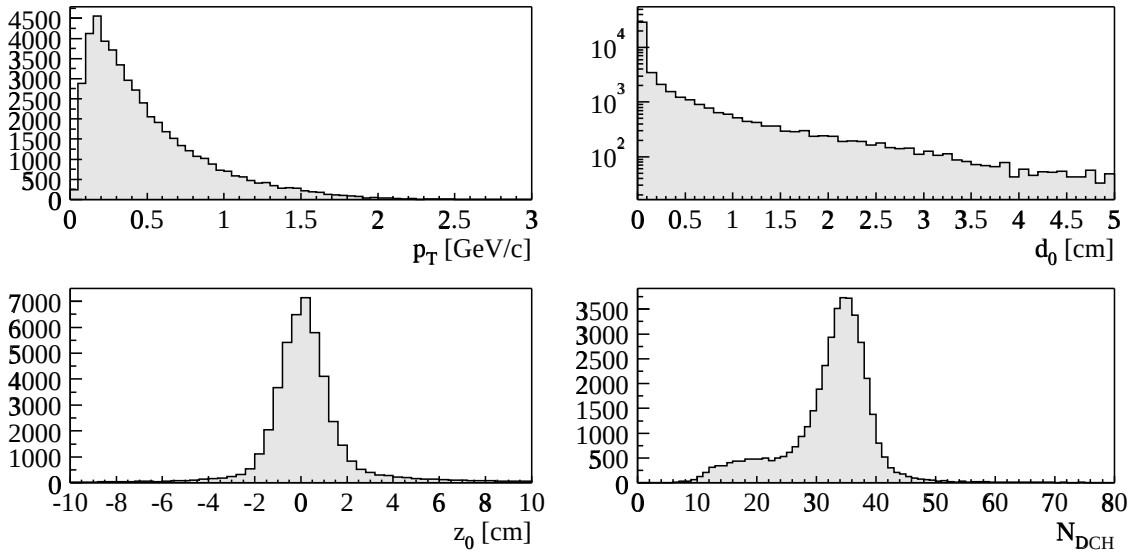

Figure 4.2: *The transverse momentum p_T, distances of closest approach to the nominal interaction point d_0 and z_0, and the number of drift chamber hits N_{DCH} for all tracks in $B^{\pm} \to K^{*\pm}\gamma$, $K^{*\pm} \to K^{\pm}\pi^0$, $B^{\mp} \to X$.*

The distributions of these quantities for all reconstructed tracks in $B^{\pm} \to K^{*\pm}\gamma$ Monte Carlo events are shown in figure 4.2. For the pions emerging from a K_S decay, these "good" track criteria cannot be applied due to the finite flight length of the K_S. Consequently, the K_S-daughter tracks will be selected in a different manner (see section 4.9).

4.5.3 Charged Particle Identification

As introduced in section 3.2.2 and 3.2.3, two means of kaon-pion separation are used in the *BABAR* experiment. The resolution gained from dE/dx measurements is better than 2σ up to a particle momentum of about 0.6 GeV/c in the SVT and 0.7 GeV/c in the DCH. For higher momenta the DIRC takes over, providing a 2.5 σ separation even at 4.0 GeV/c. The PID in this analysis almost entirely relies on the DIRC since the bulk of the pions and kaons from the K^* in $B \to K^*\gamma$ have momenta above 0.7 GeV/c as shown in figure 4.3. In the deployed likelihood-ratio strategy [71], kaons are separated from pions by a ratio criterion $g_K/g_\pi > 1$ where the g_i are the *likelihoods* for each particle hypothesis. For the example of the DIRC, a pull distribution for θ_C is defined the following way:

$$\Delta_C^i = (\theta_C - \theta_C^i)/\sigma_{\theta_C}, \qquad i = \pi, K \tag{4.4}$$

The mean Cherenkov angle θ_C^i is parametrised according to equation 3.1 for the particle types e, μ, π, K, p. The inclusive distribution of θ_C in simulated generic B decays is shown in figure 4.4. The PDF of Δ_C^i is a Gaussian g_i. The likelihood $\mathcal{L}$ for the DIRC is a combination of this Gaussian for θ_C and a Poissonian based on the counting of the number of photons. For the SVT and the DCH, the PDF is a truncated Gaussian distribution with the central dE/dx values parametrised by a phenomenological, Bethe-Bloch-like function. Any asymmetry effect due to detector material turns

out to be negligible and algorithm-induced charge asymmetries are carefully monitored (see section 7.3). The kaon-identification efficiency ϵ_K and pion-misidentification rate κ_π are determined from pure control samples which are selected without using particle-ID information but solely known physics processes and kinematic constraints. These samples are pions from $K^0_s \to \pi^+\pi^-$ and pions and kaons from the decay chain $D^* \to D^0\pi_{soft}, D^0 \to K\pi$.

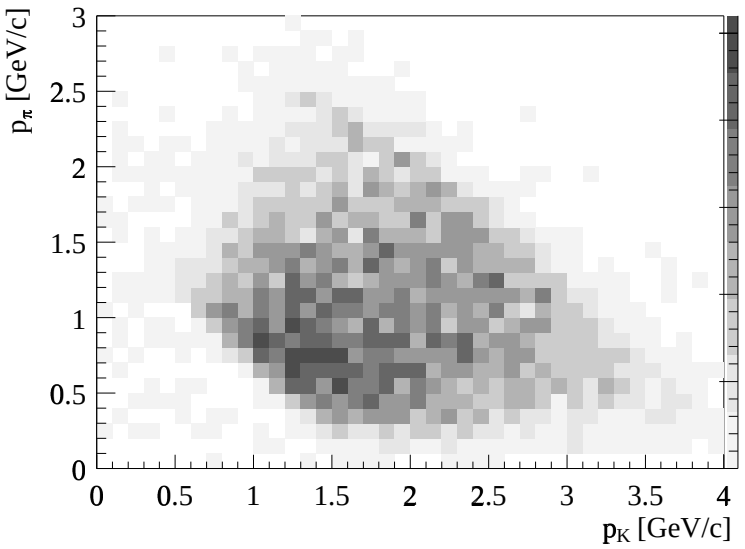

Figure 4.3: *The phase space in the laboratory frame of the momenta p_π versus p_K in $B^0 \to K^{*0}\gamma$, $K^{*0} \to K^+\pi^-$, $\overline{B}^0 \to X$ decays. The reconstructed tracks are matched to the Monte-Carlo generated candidates (*"truth-matched"*).*

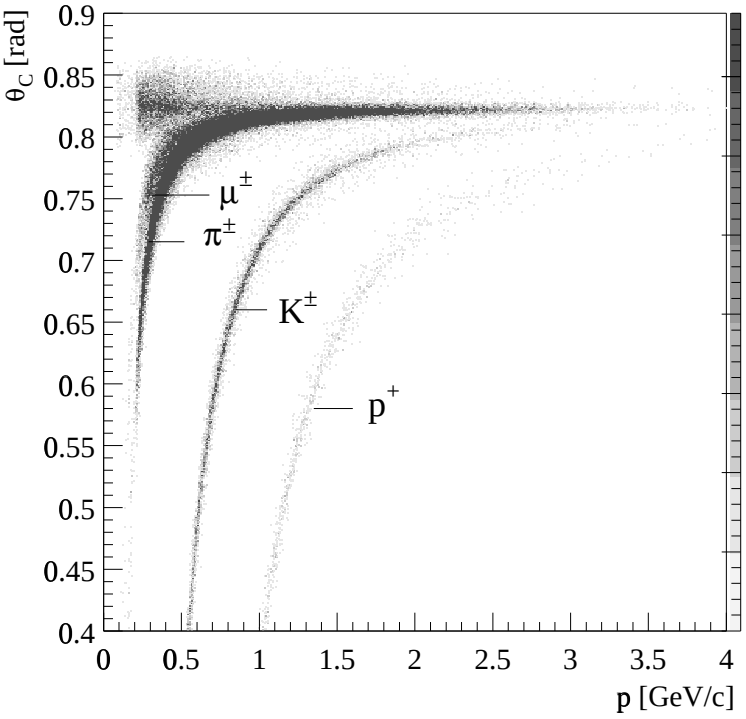

Figure 4.4: *Distribution of the Cherenkov angle θ_C versus momentum for the different particle types reconstructed from a generic B-meson Monte Carlo sample.*

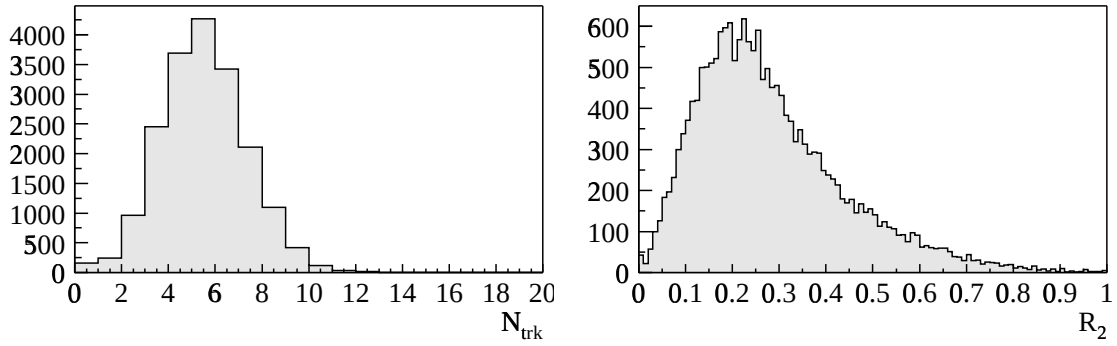

Figure 4.5: *The number of "good" tracks per event (LEFT) and the second Fox-Wolfram Moment R_2 (RIGHT) for $B^{\pm} \to K^{*\pm}\gamma$, $K^{*\pm} \to K^{\pm}\pi^0$, $B^{\mp} \to X$ Monte Carlo.*

The likelihood-based kaon selection is optimised for a certain efficiency and misidentification performance, which was done in a way to keep the mis-ID below 5% up to momenta of 4 GeV/c and using the DIRC at higher momenta only. Concerning the performance as a function of the momentum, the efficiency rises from about 80% at 0.6 GeV/c to over 90% between 1.5 and 2.5 GeV/c and then steadily degrades again to about 75% at 4 GeV/c [71]. The mis-ID rate starts off with 1% at 0.6 GeV/c and almost linearly increases towards higher momenta with about 5% at 4 GeV/c.

4.6 Pre-Selection Criteria

A pre-selection of multi-hadron events containing high-energy photon candidates with high efficiency has been performed to reduce the time needed to analyse the whole RUN 1 dataset. For each fb^{-1}of data this produces 4.9 $\times 10^5$ events which can then be used for further, more detailed analysis. The event pre-selection criteria are:

- At least one neutral cluster in the calorimeter with a centre-of-mass energy of 1.5 GeV $< E^*_\gamma <$ 3.5 GeV [1].
- The track multiplicity is used to remove low multiplicity events such as Bhabha and dimuon events. There must be at least three tracks that each satisfy the criteria of a "good" track explained in section 4.5.2. The multiplicity of tracks satisfying this requirement in signal $B \to K^*\gamma$ Monte Carlo events is shown in the left plot of figure 4.5.
- The second Fox-Wolfram moment R_2 quantifies the sphericality of an event. It is calculated using the momenta of all charged and neutral candidates:

$$R_l = H_l/H_0, \qquad H_l = \sum\nolimits_{ij} |p_i||p_j| P_l(\cos\theta_{ij}) \tag{4.5}$$

  Here, $P_l(\cos\theta_{ij})$ is the l^{th} Legendre polynomial. A loose requirement of $R_2 < 0.9$ is applied to remove Bhabha, radiative Bhabha, and $\tau\tau$ events that remain after the track multiplicity criterion. The efficiency of this cut for the signal $B \to K^*\gamma$ is nearly 100% as can be seen from right plot in figure 4.5.

[1] Kinematic quantities in the centre-of-mass frame are notated with an asterisk $*$, e.g. E^*_γ.

4.7 The High-Energy Photon

The high-energy photon is the most important experimental signature of $B \to K^*\gamma$ decays. The EMC procedure of clustering and splitting into bumps is described in section 4.5.1. When the bump has no track with a consistent match, it is called a "neutral bump" and used for this analysis with the additional requirement of $E_\gamma > 30$ MeV to remove beam background. Instead of using the vector from the *BABAR* origin (0,0,0) to the cluster's centroid as the momentum direction, the photon is "shifted" using the beam-spot information [72] which is the averaged primary vertex for all events of a run of data taking (typically 500,000 events). The momentum direction of the photon is set to point from this beam spot to the cluster centroid while the photon energy is conserved. This improves the angular reconstruction considerably, the mean difference of the generated and reconstructed polar angle in signal Monte Carlo is reduced from 5.4 to 0.5 mrad in the LAB frame and from 6.1 to 0.6 mrad in the CM system. Figure 4.6 shows the energy E_γ and polar angle $\cos\theta$ for signal Monte Carlo photon candidates from the decay $B \to K^*\gamma$ in the LAB frame. The loss of acceptance in the forward and backward regions is due to the fiducial coverage of the EMC. In the B frame, the radiative photon carries away an energy of approximately half the B mass. In the $\Upsilon(4S)$ CM-frame the B mesons decay nearly at rest, hence also here the photon energies cover a narrow range (see figure 4.6). The tail towards smaller E_γ-values is due to energy leakage at the borders of the crystals. The distributions of photon candidates in the azimuthal angle ϕ has been verified to be isotropic in the LAB and CM frame.

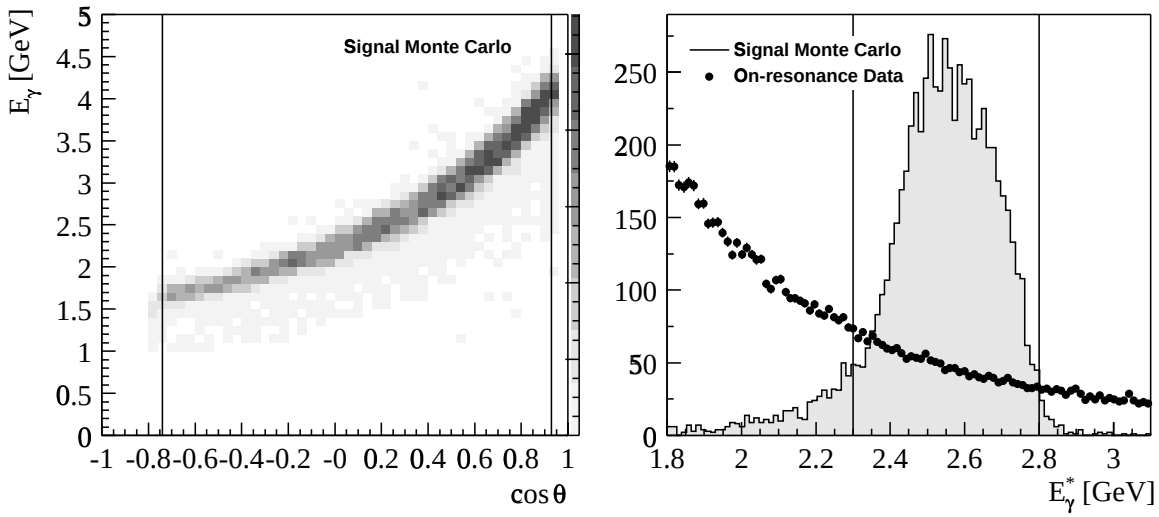

Figure 4.6: *LEFT: The reconstructed energy E_γ versus the polar angle $\cos\theta$ in the laboratory frame for truth-matched reconstructed photon candidates from $B^\pm \to K^{*\pm}\gamma$, $K^{*\pm} \to K^\pm\pi^0$, $B^\mp \to X$ signal Monte Carlo. The vertical lines indicate the fiducial cuts applied to the reconstructed centroid. RIGHT: The CM-energy E^*_γ for truth-matched reconstructed photon candidates in signal Monte Carlo (solid line) and all inclusive photon candidates in on-resonance data before any cuts of the $B \to K^*\gamma$ analysis (points), normalised to the number of Monte Carlo entries. The vertical lines depict the cut on E^*_γ.*

The energy cut for the photon is chosen by optimising $S^2/(S+B_g)$ as presented in section 4.4, varying the lower and upper E^*_γ-cut values simultaneously with all other cuts of the analysis applied. The optimal cut values are 2.3 GeV $< E^*_\gamma <$ 2.8 GeV (see figure 4.6).
Various control samples have been used to study the photon efficiency, the energy scale, and the energy resolution. The investigation of the photon efficiency is described in the sections 5.1.4 and 5.2 of chapter 5 which is entirely devoted to efficiency studies. The study of the energy scale and resolution are also covered posterior in section 6.2.1 because of the correlation to the ΔE^* cut that is introduced at a later stage.
In the next steps, a series of quality selections is made to ensure that the neutral bump is a good photon candidate. Fake photons may arise from noisy regions ("hot towers") in the calorimeter, non-electromagnetic showers, beam background, cosmic rays, and π^0s where the two photons are merged to form a single cluster.

4.7.1 Photon Quality

Several criteria are applied to exclude fake photons due to detector effects:

- The fiducial cut on the polar angle in the LAB frame of $-0.74 < \cos\theta_\gamma < 0.93$. This is defined by the region covering good tracking efficiency since we need a negative track match for a neutral cluster to be valid. The first three rows in the forward end-cap of the EMC are outside this acceptance. Figure 4.6 illustrates the acceptance cuts applied in the phase space of the signal photons in the LAB frame. We also require that the centroid of the cluster not be in the extreme two rings of the backward barrel to have full containment of the cluster.
- The cluster does not contain a noisy or dead crystal.
- The cut on the number of crystals $N_{Xtal} > 4$ removes a pathological class of clusters which are not tagged as containing a noisy or dead crystal, yet have all the energy in a small number of crystals. This is inconsistent with a high-energy electromagnetic shower.

4.7.2 Suppression of (Merged) π^0s and Hadronic Split-Offs

π^0 mesons can be responsible for photon candidates that are misinterpreted as a radiative photon from $B \to K^*\gamma$ in three ways:

- If the π^0 decay into two photons is very asymmetric, there are two photon clusters with one bump each ($2c2b$ class). One of them can be misinterpreted as the photon from $B \to K^*\gamma$ in case the energy is high enough.
- For higher momenta, the geometrical separation of the photons decreases and thus one merged-π^0 cluster containing two bumps ($1c2b$ class) becomes more likely.
- Further increasing the momenta, the two photons are close enough to cause a merged π^0 with only one bump ($1c1b$ class).

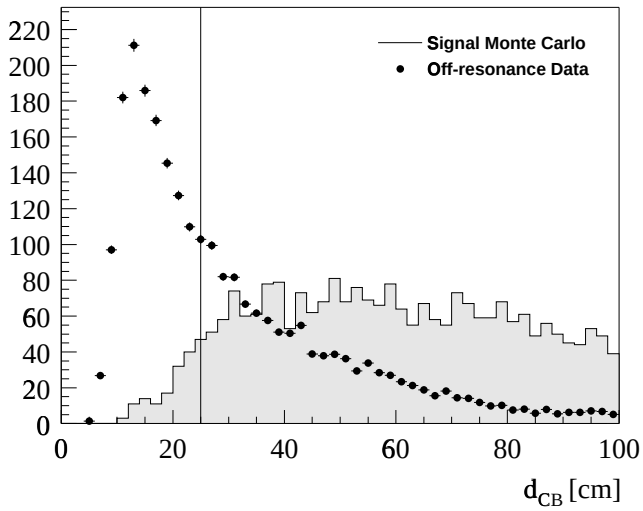

Figure 4.7: *Distributions of the photon-centroid distance to the closest neighboured bump for truth-matched reconstructed photons in* $B^{\pm} \to K^{*\pm}\gamma$, $K^{*\pm} \to K^{\pm}\pi^0$, $B^{\mp} \to X$ *signal Monte Carlo (solid line) and for photons with* $2.3\ GeV < E^*_\gamma < 2.8\ GeV$ *in off-resonance data (points), normalised to the number of MC events. The vertical line indicates the applied cut.*

A study on simulated π^0s [73] indicates that at momenta of less than 1 GeV/c there are no merged π^0s. Going to higher momenta the number of $2c2b$ π^0s drops rapidly and accordingly the number of $1c2b$ π^0s raises and dominates at p_{π^0} >2 GeV/c. The class of $1c1b$ π^0s starts being seen above 2 GeV/c and dominates from 4 GeV/c on, the number of $1c2b$ π^0s becomes insignificant at such high momenta.

Nearest Bump Distance Cut

This criterion aims to reduce the background from π^0s of the classes $1c2b$ and $2c2b$, but also from hadronic split-offs which are secondary signals that can occur close to an electromagnetic shower caused by a hadron. The signal photon bump is required to be isolated from all other bumps, i.e. the distance d_{CB} of its centroid to the closest charged or neutral bump has to be larger than 25 cm, a value that has been optimised as presented in section 4.4. The distributions of the distance to the closest bump in signal Monte Carlo and continuum background Monte Carlo are shown in figure 4.7. The efficiency for the bump distance cut has been studied using radiative Bhabha events, $e^+e^- \to e^+e^-\gamma$, where the photon is kinematically constrained, resulting in a pure sample of high-energy photons [14]. These clusters have been embedded into reconstructed B-events from the on-resonance data and generic $B\overline{B}$ Monte Carlo events. The study results in a discrepancy of 2% between the Monte-Carlo embedded photons and the B sample. This is assigned as a possible systematic error on the efficiency of this cut.

Second Moment of the Cluster

The next step is to look at the cluster of the photon itself. The quantity describing the shape of a cluster, called the "*Second Moment*", is defined as:

$$2^{nd}\ \text{Moment} = \sum_{crystal\ i} \frac{E_i \cdot ((\theta_i - \theta_{cluster})^2 + (\phi_i - \phi_{cluster})^2)}{\sum_i E_i} \tag{4.6}$$

The significance of the Second Moment is depicted in figure 4.8. The Monte Carlo

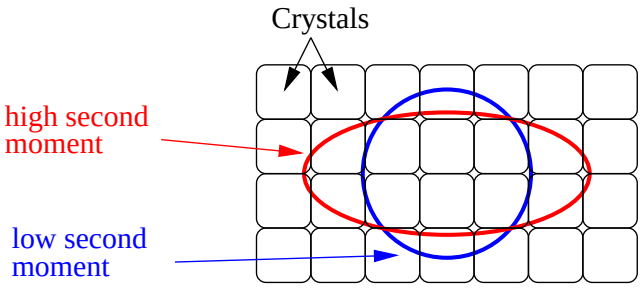

Figure 4.8: *Illustration of the Second Moment of a cluster in the calorimeter.*

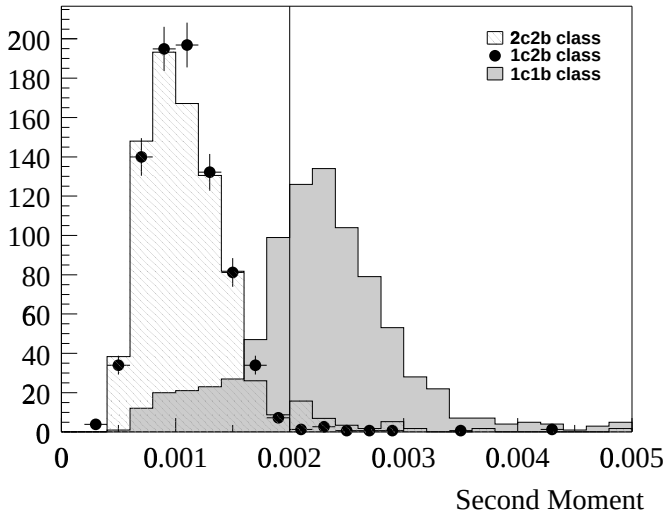

Figure 4.9: *Distributions of the Second Moment for truth-matched reconstructed photons from single-π^0 Monte Carlo in 2c2b (hashed) and 1c2b clusters (points), furthermore the Second Moment of the cluster for merged π^0s of class 1c1b (solid fill). All candidates have an energy of 1.5 GeV $< E_\gamma <$ 4.5 GeV as the radiative photon in $B \to K^*\gamma$ The vertical line depicts the applied cut.*

distributions in figure 4.9 show that spherical clusters from real photons lead to very small values of the Second Moment whereas for merged π^0s it tends to larger ones. An optimisation according to section 4.4 yields a cut value of 0.002. A study using merged π^0s in $\tau\tau$ 1-on-1 decays shows that the cut efficiency for the Second Moment is consistent in data and Monte Carlo [74].

π^0 and η Veto for Unmerged Bumps

Decays of energetic π^0 and η mesons that can release high-energy photons into an event constitute one of the major backgrounds in this analysis. A photon originating from such a decay would have a sister photon that, if it lies in the acceptance of the calorimeter and when paired with the radiative photon candidate γ_{rad}, will lead to the π^0 or η mass. The measure to suppress these photon candidates consequently is the following veto; the high-energy photon γ_{rad} is combined with any other photon γ_{sec} in the event. The radiative photon candidate is ignored if the resulting invariant mass is consistent with the nominal π^0 or η mass, which translates into the conditions:

- 115 MeV $/c^2 < m(\gamma_{rad}, \gamma_{sec}) <$ 155 MeV/c^2 ($E_{\gamma_{sec}} >$ 50 MeV/c^2)
- 508 MeV $/c^2 < m(\gamma_{rad}, \gamma_{sec}) <$ 588 MeV/c^2 ($E_{\gamma_{sec}} >$ 250 MeV/c^2)

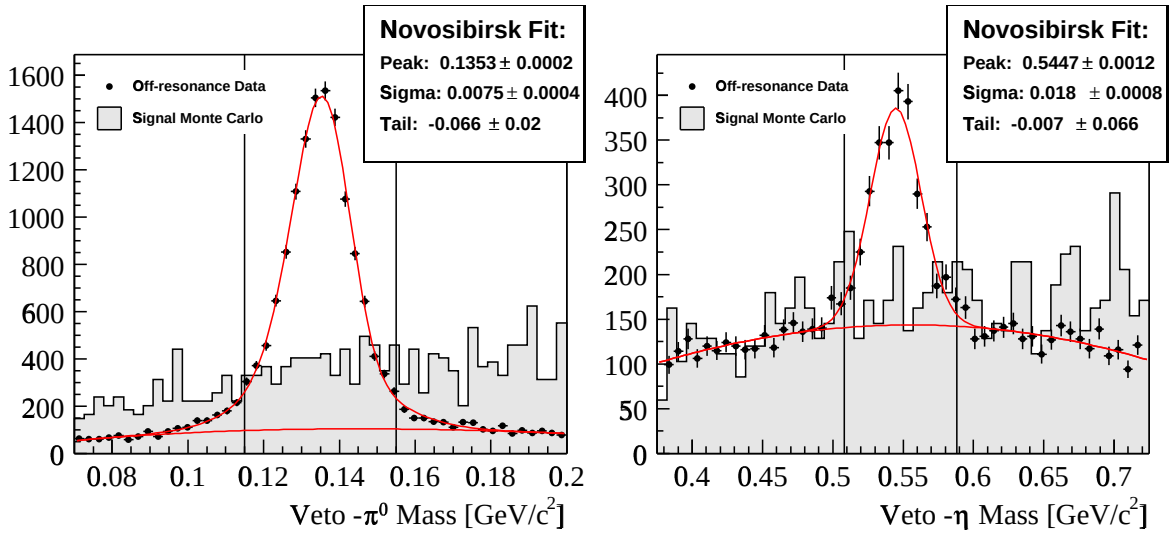

Figure 4.10: *Invariant-mass distribution of the π^0 (LEFT) and η (RIGHT) veto after the fiducial and E^*_γ cut but before all other cuts of the analysis. Shown are high-energy photon candidates in off-resonance data (points) and matched photons in $B^\pm \to K^{*\pm}\gamma$, $K^{*\pm} \to K^\pm\pi^0$, $B^\mp \to X$ signal Monte Carlo (solid fill), normalised to the number of off-resonance events. A Novosibirsk-signal function (equation 4.7) plus third-order polynomial background is used for the off-resonance data fit.*

This cut suppresses π^0 decays which are outside the coverage of the bump distance cut described above. The π^0 and η vetoes have been optimised as presented in section 4.4 by maximising $S^2/(S+B_g)$. The distributions of the invariant π^0 and η masses are shown in figure 4.10 for $B \to K^*\gamma$ signal Monte Carlo and off-resonance data. The fitted line-shape is a *Novosibirsk* function f_{Novo} [75] which takes into account the tail $\tau_{M_{ES}}$ due to photon leakage in the calorimeter:

$$f_{Novo}(m) \propto exp\left[-\frac{1}{2}\left(\frac{ln^2\left(1+\frac{m-\overline{m}}{\sigma}\cdot\tau\cdot\frac{sinh(\tau\sqrt{ln4})}{\tau\sqrt{ln4}}\right)}{\tau} + \tau^2 \right)\right] \tag{4.7}$$

The photon multiplicity and spectrum in $B\overline{B}$ events must be well represented in signal Monte Carlo if the (in)efficiency of the π^0 and η veto shall be reliably estimated. Besides the other B, beam related backgrounds are the second main source of photons. To verify the consistency of on-resonance data and simulation, 2.5 GeV photons with isotropic angular distribution are generated and boosted in the CM frame. One of these candidates representing our signal photon is inserted in each event and combined with any other photon, then the veto procedures are applied as described above. The event samples used were simulated generic B decays, simulated continuum events, and real on- and off-resonance data. In the continuum samples the efficiencies are slightly higher than in the generic B decays, and the data tend to have slightly higher efficiency than the Monte Carlo simulation. However, the corresponding efficiencies between data and Monte Carlo agree within 1%. The systematic uncertainty for the veto efficiencies is taken as this discrepancy.

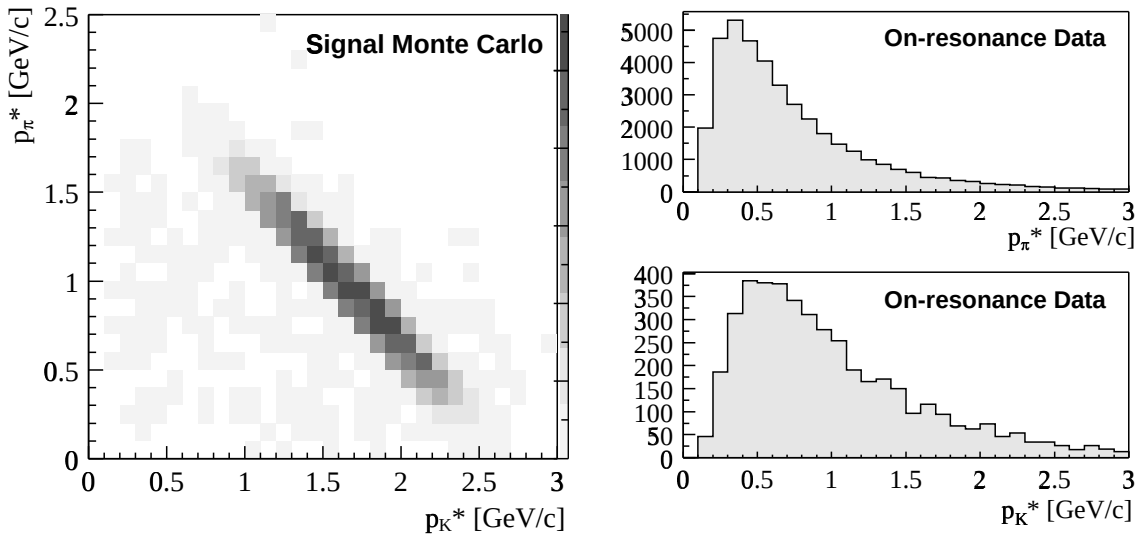

Figure 4.11: *The CM momentum of the kaons versus pions, selected by requiring "good" tracks and using PID. LEFT: Truth-matched kaons and pions from the K^* decay in $B^0 \to K^{*0}\gamma$, $K^{*0} \to K^+\pi^-$, $\overline{B}^0 \to X$ signal Monte Carlo RIGHT: All kaons and pions in on-resonance data without any other cut of the analysis.*

4.8 Reconstruction of Kaons and Pions

The charged K^* daughter candidates, namely $\pi^\pm$ and $K^\pm$, are selected by requiring that the criteria for a "good" track are met, which have been introduced in section 4.5.2. The separation between the two particle types is achieved by applying the PID presented in section 4.5.3. The identification is primarily provided by the DIRC since most of our kaons and pions have LAB momenta between 1 and 3 GeV/c^2.

The PID reduces the combinatorial background from continuum by about a factor of seven in $B^\pm \to K^{*\pm}\gamma, K^{*\pm} \to K^\pm\pi^0$, and by four in $B^0 \to K^{*0}\gamma, K^{*0} \to K^+\pi^-$. The correlation in the CM phase-space between truth-matched reconstructed kaon and pion tracks originating in the decay of the K^{*0} is shown in figure 4.11 for signal Monte Carlo. At a later stage of the analysis (section 4.12.3), a cut on the K^*-helicity angle will be applied, and there is a nearly perfect correlation between this variable and the pion and kaon momenta. Therefore, no cut on the CM momenta of the K^* daughters is carried out here.

4.9 K^0_S Reconstruction

The K^0_S candidates are reconstructed in the $K_S \to \pi^+\pi^-$ decay mode only. The K_S decays in flight because of its finite lifetime and the secondary vertex is displaced from the primary one. Therefore, the "good" track criteria of section 4.5.2 including the distance of closest approach d_0 cannot be applied for these pions. Hence two oppositely charged tracks, reconstructed with the pion mass hypothesis, are combined to form a K_S and no PID is used. If the invariant mass is within the range

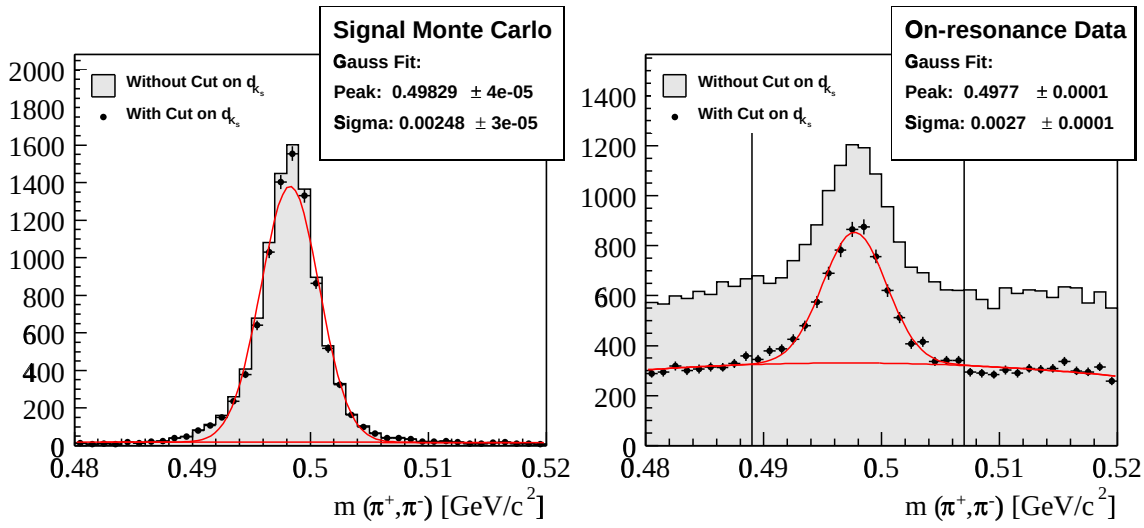

Figure 4.12: *Distribution of the invariant mass of the $K_S \to \pi^+\pi^-$ candidates with converged vertex fit in signal Monte Carlo (LEFT) and on-resonance data (RIGHT). The CM-momentum range is $0.75\ GeV/c < p^*_{K_S} < 2.75\ GeV/c$. The K^0_S in $B^0 \to K^{*0}\gamma$, $K^{*0} \to K_S\pi^0$, $\overline{B}^0 \to X$ signal Monte Carlo have matched pion daughters. The samples without and with the cut on the K^0_S flight length are compared. The function of the fit to the latter distribution is a Gaussian for the signal, plus a third-order polynomial background in the real-data case.*

300 MeV/c^2 $< m_{\pi^+\pi^-} <$ 700 MeV/c^2, a vertex fit is performed, providing the information if the two tracks are consistent with coming from the same vertex by the χ^2 of the fit. The inclusive invariant mass distribution of the K^0_S candidates after the vertex fit without any further cuts can be found in figure 4.12 for signal Monte Carlo and on-resonance data. In figure 4.13, the probability from the χ^2 of the fit is shown. Even for the signal K_S in Monte Carlo the probability is close to zero for a large number of events. Therefore there is no cut on this quantity, the fit having converged is the only requirement. The *flight distance* d_{K_S} of the K^0_S decay vertex from the primary vertex of the event is also shown in figure 4.13. Only the distance cut is applied since there is a correlation between this flight length and the CM-momentum of the K^0_S. The $S^2/(S+B_g)$ optimisation as introduced in section 4.4 motivates the cut value $d_{Ks} > 0.2$ cm. Another variable that has been investigated is the angle between the flight direction of the K^0_S and the momentum direction of (π^+, π^-) which also can be seen in figure 4.13, but it turned out that a cut on this quantity is not effective enough to justify the considerable systematic problems associated with it [76]. Applying the cuts on the flight length, the background for the invariant mass is reduced as shown in figure 4.12 where the fit function is a Gaussian with peak $\overline{m}$ and width σ_m. The central value of the K_S-mass width in real data and Monte Carlo agree within 1 σ, yet the K_S-mass peak is shifted by $\sim 0.2\ \sigma$. The invariant mass is required to be 489 MeV $/c^2 < m_{K_S} <$ 507 MeV/c^2 to be considered in the further analysis. The associated systematic uncertainties due to the K_S reconstruction are covered in section 5.1.3.

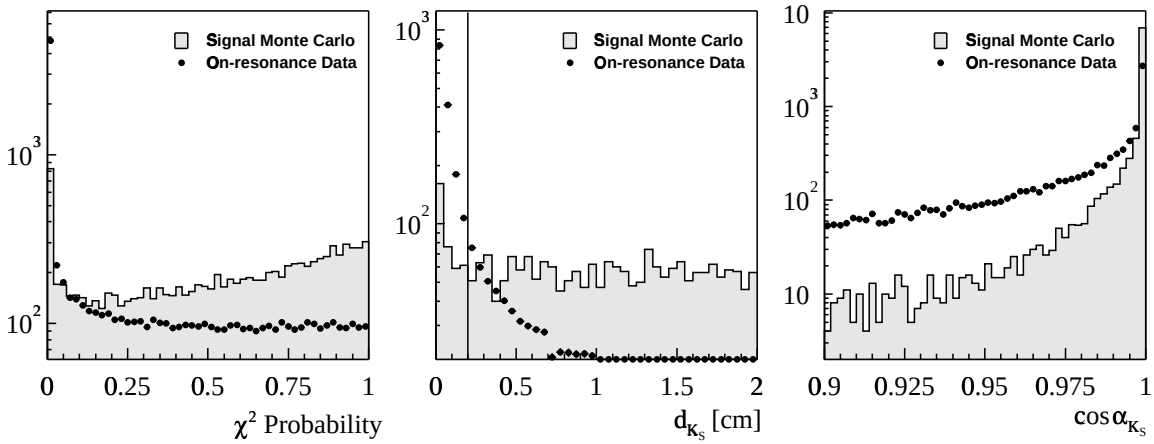

Figure 4.13: *Distributions of several K^0_S properties. For the $B^0 \to K^{*0}\gamma$, $K^{*0} \to K_S\pi^0$, $\overline{B}^0 \to X$ signal Monte Carlo, the reconstructed pions are truth-matched. LEFT: Distribution of the probability of the $K^0_S \to \pi^+\pi^-$ fit in signal Monte Carlo (points) and on-resonance data (solid line). MIDDLE: Distribution of the distance d_{K_S} of the K^0_S to the primary vertex. The vertical line indicates the cut. RIGHT: Distribution of the angle $\cos\alpha_{K_S}$ between the flight direction of the K^0_S and the momentum of (π^+, π^-).*

4.10 π^0 Reconstruction

The π^0 candidates are reconstructed in the decay mode $\pi^0 \to \gamma\gamma$. In the selection of these photons, the different signature of electromagnetic showers in the EMC and the showers of hadronic interactions is accounted for by a cut of $LAT < 0.8$ on the lateral energy distribution, also called the *lateral moment* [77]:

$$LAT = \frac{\sum_{i=3}^{n} E_i r_i^2}{\sum_{i=3}^{n} E_i r_i^2 + E_1 r_0^2 + E_2 r_0^2} \qquad E_1 \geq E_2 \geq ... \geq E_n \tag{4.8}$$

Here, the sum extends over all crystals covered by the shower. $r_0 = 5$ cm is the average distance between two crystal front-faces and r_i is the distance from the shower centre to the i^{th} crystal. The LAT parameter of electromagnetic showers is smaller than for hadronic showers since they have most of their energy deposited in one or two crystals. Furthermore, only bumps in the EMC without a track match in the DCH are accepted to reject electromagnetic showers from electrons.

To suppress photon beam-background at low energies, the γ and π^0 candidates must have an energy of $E_\gamma > 30$ MeV and $E_{\pi^0} > 200$ MeV, respectively.

In the first step, the photons are combined by simple Lorentz-vector addition. The resulting invariant mass distribution of the π^0 candidates is shown in figure 4.14 for signal Monte Carlo and on-resonance data. A fit of a Novosibirsk function (see equation 4.7) shows that the mass peak position in real data is slightly lower and the width turns out to be somewhat broader than in Monte Carlo, a fact that is confirmed by the separate π^0-efficiency study in section 5.2 where the corresponding systematics are also studied. For π^0 candidates with an invariant mass within the range

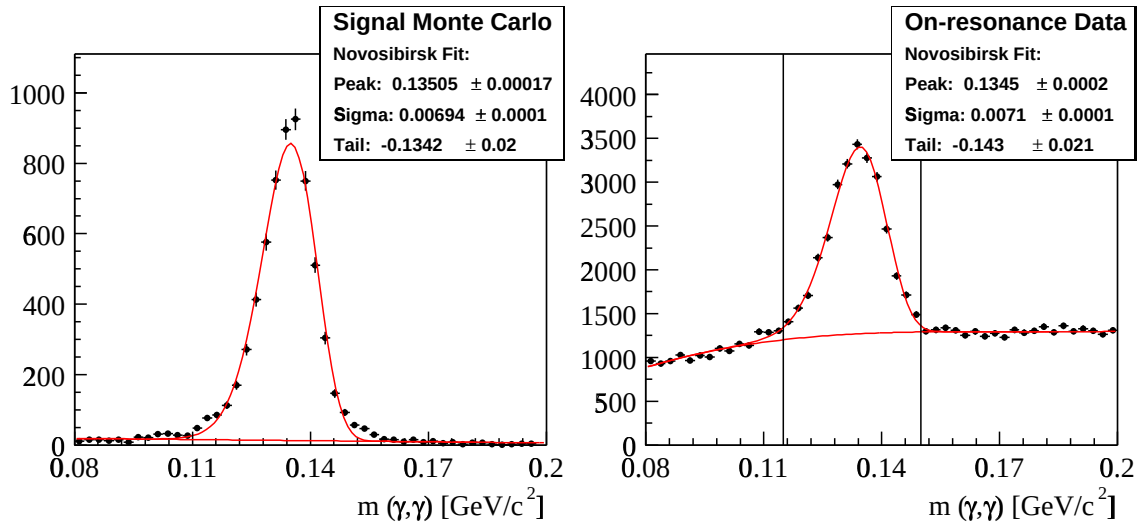

Figure 4.14: *Distribution of the invariant mass of the $\pi^0 \to \gamma\gamma$ candidates in $B^\pm \to K^{*\pm}\gamma$, $K^{*\pm} \to K^\pm\pi^0$, $B^\mp \to X$ signal Monte Carlo (LEFT) where the π^0s have truth-matched photon daughters, and inclusively in on-resonance data (RIGHT). The π^0 CM-momentum range is 0.5 GeV/c $< p^*_{\pi^0} <$ 1.5 GeV/c. The fit function for the signal is a Novosibirsk shape, plus a third-order polynomial background in the real-data case. The vertical lines indicate the applied cut.*

0.115 GeV/c^2 $< m(\gamma\gamma) <$ 0.150 GeV/c^2, the combination of the photons is redone using a *mass-constrained fit* where the π^0 mass is fixed to the PDG value [37] and the photon momenta are altered to yield the least χ^2. If the fit converges, the π^0s are stored for further use in the analysis.

4.11 K^* Reconstruction

The K^* candidates are reconstructed in the two charged modes $K^{*\pm} \to \pi^0 K^\pm, \pi^\pm K_S$, and the two neutral modes $K^{*0} \to \pi^- K^+, \pi^0 K_S$. From the point of view of the reconstruction, there are two different groups to be treated separately: two channels involving π^0s and two without them. For the modes in which the K^* has a π^0 daughter, there is no vertex information for the π^0 since only two photon clusters in the EMC are present. Consequently, the K^* candidate is formed by simple Lorentz-vector addition of the two daughters. In the two remaining modes only charged daughters and granddaughters are detected, providing vertex information by their reconstructed tracks. Hence, a vertex fit of the K^* is used in these cases and a K^* candidate is only retained if there is an acceptable χ^2 probability of the hypothesis that the charged daughter-kaon and -pion emerged from a common vertex. Figure 4.15 shows the χ^2 distribution of the vertex fit in signal Monte Carlo and on-resonance data, only K^* candidates with $\chi^2 < 10$ are accepted to remove poorly reconstructed particles. In order to verify the consistency of the vertex fit in real data and simulation, K^* candidates are explored in continuum Monte Carlo and off-resonance events that look very similar to $B \to K^*\gamma$ events [14], i.e. the K^* CM-momentum and mass are in the appropriate range and there is a high-energy photon present. In these data taken below

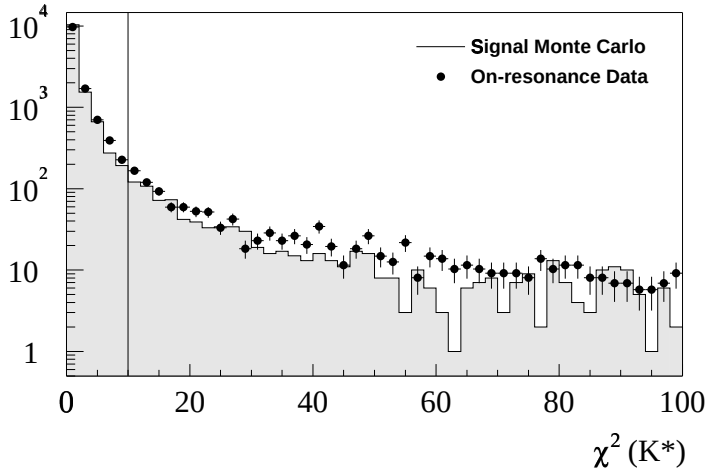

Figure 4.15: *The χ^2 distribution of the K^* vertex fit in $B^0 \to K^{*0}\gamma$, $K^{*0} \to K^+\pi^-$, $\overline{B}^0 \to X$ signal Monte Carlo (solid line) and in on-resonance data (points). The vertical line indicates the cut of $\chi^2 > 10$.*

the $\Upsilon(4S)$ resonance, most tracks and also the two K^* daughters emerge from the common interaction point which is thus well known. The fraction of K^* candidates with $\chi^2 > 10$ yields very good agreement within about 0.3 σ (statistical error of the study), confirming that the efficiency of the vertex-χ^2 cut is understood to approximately one percent.

The inclusive distribution of the K^* CM-momentum, $p^*_{K^*}$, for signal Monte Carlo and on-resonance data in figure 4.16 displays the very distinct CM-momentum range of the signal K^*. In the B rest-frame it would be a delta function that is only slightly broadened due to the m_{K^*} width. The selection criterion for the K^* CM-momentum is 2.35 GeV/c $< p^*_{K^*} <$ 2.8 GeV/c.

Figure 4.17 shows the inclusive invariant $m(K^\pm, \pi^0)$ distribution for the momentum range of 2.35 GeV/c $< p^*_{K^*} <$ 2.8 GeV/c in Monte Carlo and real data. The on-resonance data distribution is represented by a relativistic P-wave Breit-Wigner with Blatt-Weisskopf barrier functions, which is explained in more detail in appendix C.1:

$$f_{relBW}(M) \propto \frac{M \cdot \Gamma_{rel}}{(M^2 - \overline{M}^2)^2 + (\overline{M} \cdot \Gamma_{rel})^2} \tag{4.9}$$

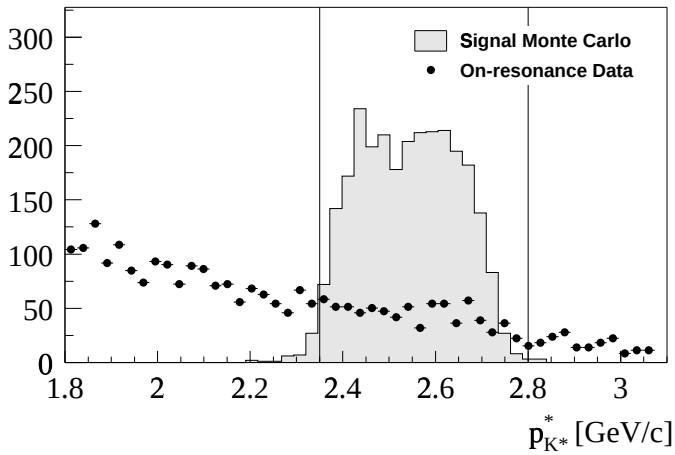

Figure 4.16: *The CM-momentum distribution of all $K^{*\pm}$ candidates with 792 MeV/c^2 $< m_{K^*} <$ 992 MeV/c^2 in $B^\pm \to K^{*\pm}\gamma$, $K^{*\pm} \to K^\pm\pi^0$, $B^\mp \to X$ signal Monte Carlo (solid line) and on-resonance data (points). The vertical lines illustrate the applied cut.*

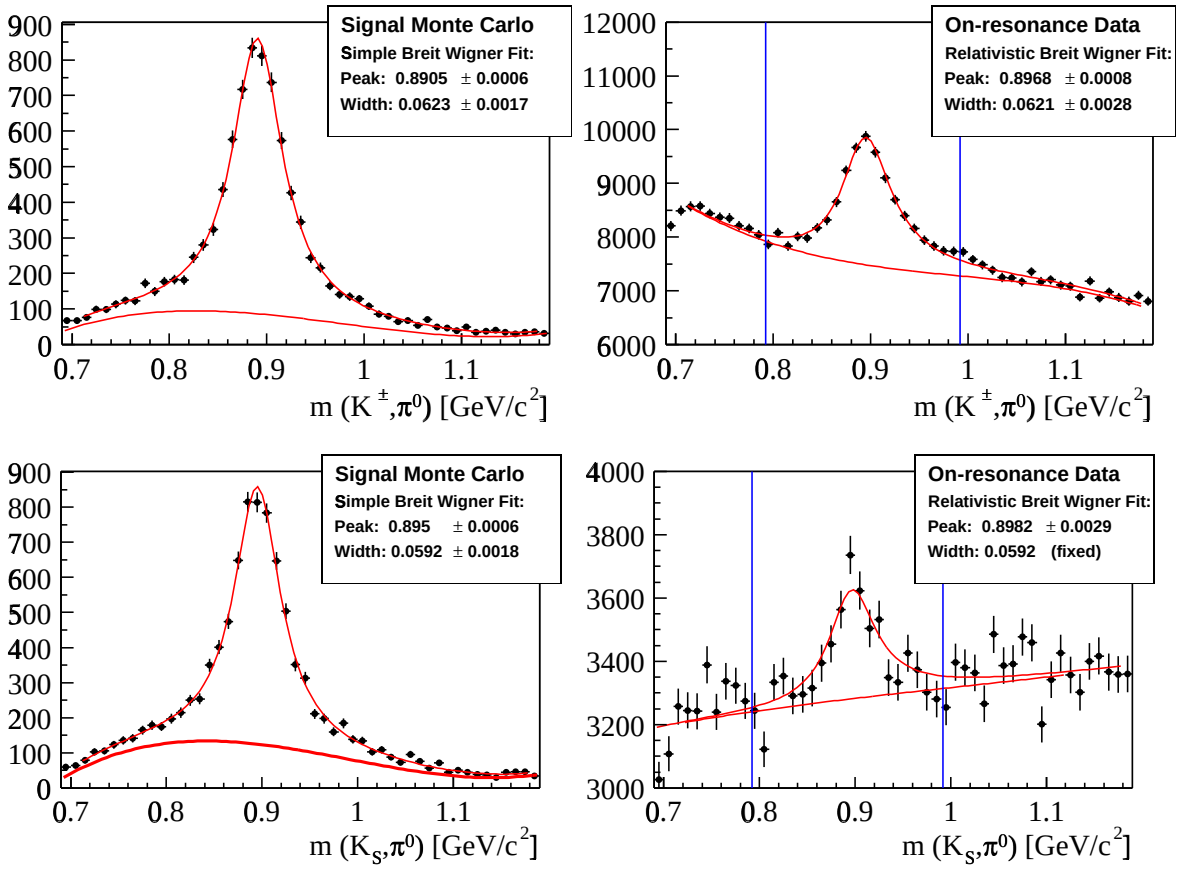

Figure 4.17: *The inclusive invariant mass spectra of K^* candidates for the momentum range of 2.35 GeV/c $< p^*_{K^*} <$ 2.8 GeV/c in signal Monte Carlo (LEFT) and on-resonance data (RIGHT). Shown are the two modes $K^{*\pm} \to K^{\pm}\pi^0$ (TOP) and $K^{*0} \to K_S\pi^0$ (BOTTOM). The fit functions are a simple Breit-Wigner (equation 4.10) for the Monte Carlo (generated with this shape) and a relativistic p-wave Breit-Wigner (equation 4.9) for the on-resonance data. The background is a third order polynomial in all fits.*

For technical reasons, the K^* was generated with a simple Breit-Wigner shape in the simulation. Therefore, this function is also used for the Monte Carlo fit in figure 4.17:

$$f_{BW}(M) \propto \frac{\Gamma}{(M - \overline{M})^2 + (\Gamma/2)^2} \tag{4.10}$$

The fit of the inclusive $K^{*\pm} \to K^{\pm}\pi^0$ distribution in figure 4.17 illustrates that the width Γ is in very good agreement for data and Monte Carlo. (For $K^{*0} \to K_S\pi^0$ statistics are very low, therefore the width is fixed to the Monte Carlo value in the fit.)

The $S^2/(S + B_g)$ optimisation of the K^* mass window is done as described in 4.4. We obtain a cut on the invariant mass of 792 MeV/c^2 $< m_{K^*} <$ 992 MeV/c^2 for the $K^{*\pm}$, and 796 MeV/c^2 $< m_{K^*} <$ 996 MeV/c^2 for the K^{*0} candidates.

4.12 Event Shape Variables

The K^* and γ candidates are boosted into the $\Upsilon(4S)$ CM-frame and then combined to the B candidate by simple Lorentz-vector addition. Thereafter, the different event shapes for signal and background as introduced in section 4.2 are explored. The event shape variables explained below provide powerful cuts to suppress these backgrounds.

4.12.1 Angle between High-Energy Photon and Thrust Axis

When a B candidate is reconstructed from a high-energy photon and a K^* candidate, all other particle candidates in the event are considered to belong to the other B. The thrust vector T^*, representing the overall direction of a group of particles, is defined as:

$$\mathbf{T}^* = \max_{\forall \mathbf{v}, |\mathbf{v}|=1} \frac{\sum_i |\mathbf{v} \cdot \mathbf{p_i^*}|}{\sum_i |\mathbf{p_i^*}|} \tag{4.11}$$

For the signal, the distribution of the angle α_T^* between the high-energy photon and the thrust of the other B in the $\Upsilon(4S)$ frame is more or less isotropic since the thrust axes of the two B decays are uncorrelated and $B\overline{B}$ events are more or less spherical. However, the distribution for the jet-like background from a high-energy photon coming from the residual of a non-$B\overline{B}$ event exhibits a huge concentration for α_T^* at 0^o and 180^o. The cut on this variable reduces the background considerably. The distributions of $|\cos\alpha_T^*|$ for signal and background are shown in figure 4.18. Off-resonance data and continuum Monte Carlo are in good agreement within statistics. Because of the correlation between the second Fox-Wolfram R_2 moment and α_T^*, there is only a very loose cut on R_2 <0.9 at pre-selection level to reject Bhabha events (see section 4.6). The major cut is applied on $|\cos(\alpha_T^*)|$ now and there will be no tighter cut on R_2.

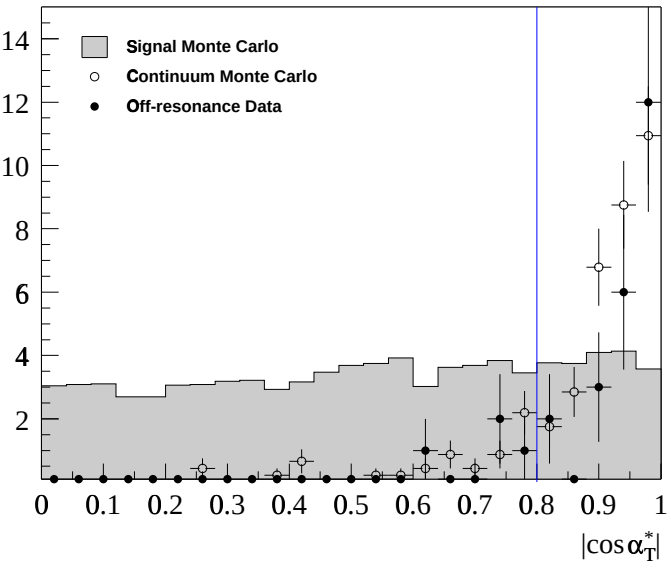

Figure 4.18: $|\cos\alpha_T^*|$ *of the angle between the radiative photon and the thrust of the other B in the CM frame for off-resonance data (black points),* $B^\pm \to K^{*\pm}\gamma$, $K^{*\pm} \to K^\pm\pi^0$, $B^\mp \to X$ *signal Monte Carlo (solid fill) and continuum Monte Carlo (white points), scaled to the off-resonance luminosity. Except for the cut on the B angle and the* K^* *helicity, all analysis cuts are applied. The* M_{ES}-ΔE^* *window is [5.27 GeV/*c^2*,5.29 GeV/*c^2*] and [-0.225 GeV,0.125 GeV]. The vertical line depicts the cut.*

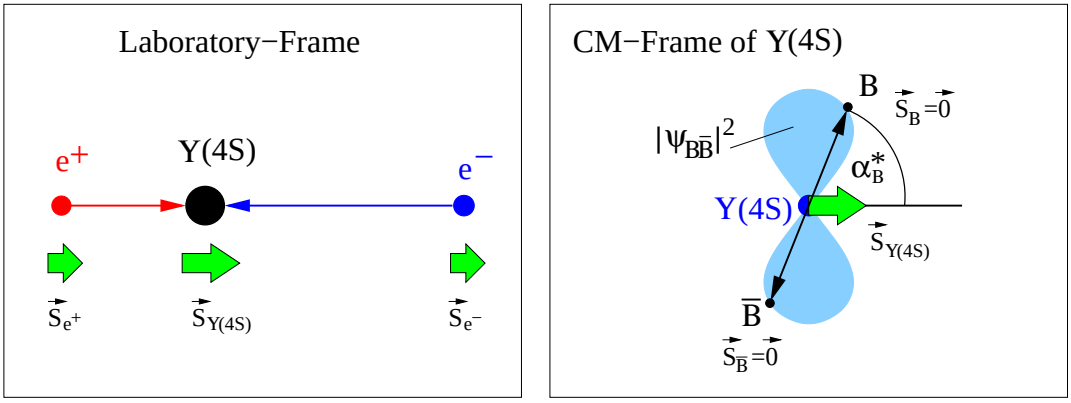

Figure 4.19: *Illustration of the B angle α^*_B. LEFT: The production of the $\Upsilon(4S)$ in the LAB frame by the collision of e^+ and e^-, both with helicity h_e=±1. The spin of the $\Upsilon(4S)$ is oriented parallel to the beam, i.e. the z axis. RIGHT: The decay of the $\Upsilon(4S)$ in the CM-frame. Since the B mesons carry no spin, their angular momentum is $|\mathbf{L}_{B\overline{B}}| = 1$ and their spatial probability density proportional to $\sin^2 \alpha^*_B$.*

4.12.2 Angle between Reconstructed B Meson and Beam

The colliding electron and positron are highly relativistic. Therefore, they have an almost pure helicity $h_e = \frac{\mathbf{S}\cdot\mathbf{p}}{|\mathbf{S}|\cdot|\mathbf{p}|} = \pm 1$ as illustrated on the left of figure 4.19. Hence in the production of an $\Upsilon(4S)$, the spins of the e^+ and e^-, both of magnitude $|\mathbf{S}_{e^+}| = |\mathbf{S}_{e^-}| = 1/2$, are pointing in the same direction, resulting in a total spin $\mathbf{S}_{\Upsilon(4S)}$ of the $\Upsilon(4S)$ resonance that has a magnitude of $|\mathbf{S}_{\Upsilon(4S)}| = 1$ and is oriented parallel to the beam axis. The $\Upsilon(4S)$ instantaneously decays into two B mesons, each carrying no spin $\mathbf{S}_B = \mathbf{0}$. Thus for conservation of angular momentum, the $B\overline{B}$ system possesses an angular momentum of $|\mathbf{L}_{B\overline{B}}| = 1$ parallel to the former spin $\mathbf{S}_{\Upsilon(4S)}$.
The spatial probability density $|\Psi_{B\overline{B}}(\phi,\theta)|^2$ of the B mesons in the $\Upsilon(4S)$ CM-frame is

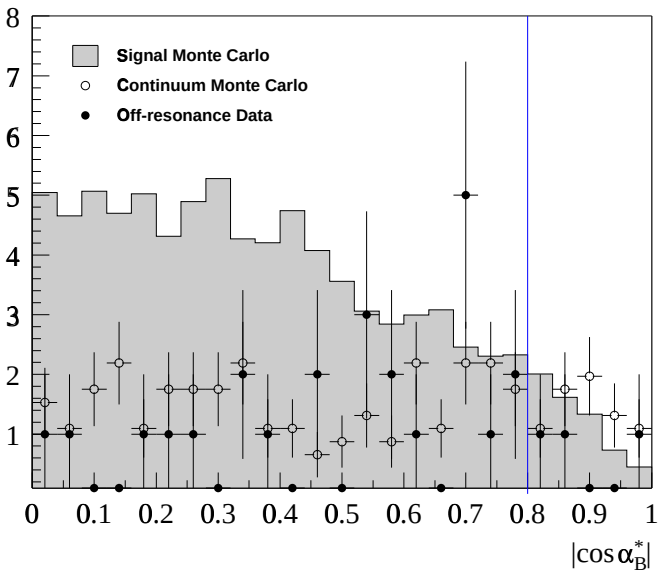

Figure 4.20: *$|\cos\alpha^*_B|$ of the angle between the B and the z-axis in the CM frame for off-resonance data (black points), $B^\pm \to K^{*\pm}\gamma$, $K^{*\pm} \to K^\pm\pi^0$, $B^\mp \to X$ signal Monte Carlo (solid fill) and continuum Monte Carlo (white points), scaled to the off-resonance luminosity. Except for the cut on α^*_T and the K^* helicity, all analysis cuts are applied. The M_{ES}-ΔE^* window is [5.27 GeV/c^2,5.29 GeV/c^2] and [-0.225 GeV,0.125 GeV]. The vertical line depicts the cut.*

consequently determined by the Spherical Harmonics Y_m^l and is depicted on the right of figure 4.19 for $l = 1$ and $m \pm 1$, resulting in a $\sin^2 \alpha_B^*$ distribution of the angle between the reconstructed B in the $\Upsilon(4S)$ CM-frame and the beam line which is defined as the z-axis. The distributions of $|\cos \alpha_B^*|$ in signal and background are shown in figure 4.20. Because of the $\sin^2 \alpha_B^*$ distribution and $\cos^2 \alpha_B^* = 1 - \sin^2 \alpha_B^*$, the signal peaks at zero in $|\cos \alpha_B^*|$ whereas the background is flat. The agreement of the off-resonance data and the continuum Monte Carlo is good within statistics. This variable offers another possibility to apply an anti-background cut.

4.12.3 K^*-Helicity Angle

The B meson with spin $\mathbf{S}_B = \mathbf{0}$ decays into the two spin-1 particles γ and K^*. The photon by nature possesses helicity $h_\gamma = \pm 1$, i.e. its spin is parallel to its momentum. To conserve total angular momentum, the spin $\mathbf{S}_{K^*}$ of the K^* needs to be opposite to $\mathbf{S}_\gamma$ and (anti-)parallel to the momentum direction of the K^* in the B CM-frame where the K^* and γ momenta are head-on (180^o) as illustrated on the left of figure 4.21.
To consult the $K^* \to \pi K$ decay, we move into the K^* CM-frame (see right of figure 4.21). Since the pion and kaon are spin-0 particles, their angular momentum is $|\mathbf{L}_{\pi K}| = 1$ for the same argumentation of angular momentum conservation as in section 4.12.2. The spatial probability density $|\Psi_{\pi K}(\phi, \theta)|^2$ shows a $\sin^2 \alpha_H$ behaviour with respect to the direction of $\mathbf{S}_{K^*}$ which is equivalent to the direction of the K^* momentum in the B CM-frame as explained above. To use this piece of information, the K^*-helicity angle is defined between the momentum vector of the kaon in the K^* CM-frame and the K^* direction in the B CM-frame.
The distributions of $|\cos \alpha_H|$ are shown in figure 4.22 for signal and background. The $\sin^2 \alpha_H$ probability for the signal leads to a peak of $|\cos \alpha_H|$ at zero, whereas for background events the distribution is almost isotropic. In figure 4.22, one can also see the agreement of the off-resonance data and the continuum Monte Carlo within

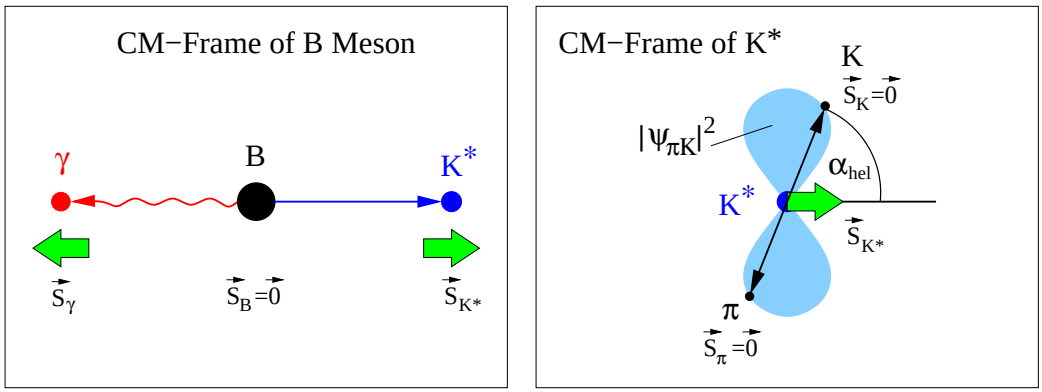

Figure 4.21: *Illustration of the K^*-helicity angle α_H. LEFT: The decay $B \to K^*\gamma$ in the B-meson CM-frame. The spin of the K^* is oriented (anti-)parallel to its momentum because of h_γ=±1 and angular momentum conservation. RIGHT: The decay of the K^* in the K^* CM-frame. Since the π and K mesons carry no spin, their angular momentum is $|\mathbf{L}_{\pi K}| = 1$ and their spatial probability density proportional to $\sin^2 \alpha_H$.*

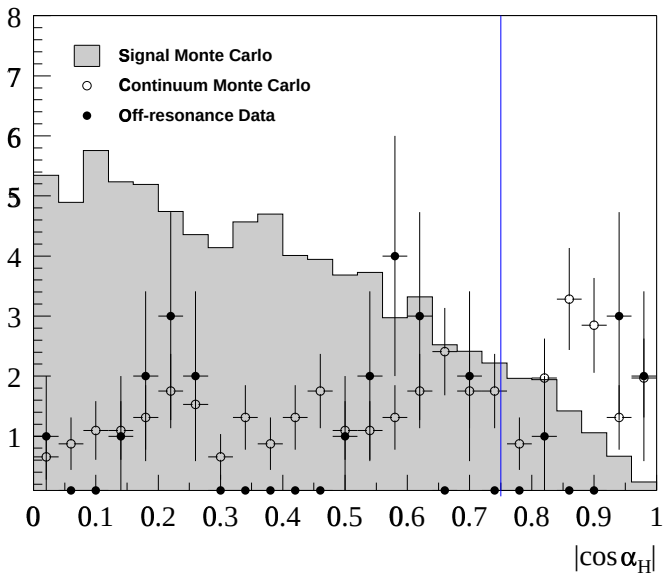

Figure 4.22: $|\cos\alpha_H|$ *of the* K^**-helicity angle of the kaon momentum in the* K^* *frame to the* K^* *momentum in the* B *frame for off-resonance data (black points),* $B^\pm \to K^{*\pm}\gamma$, $K^{*\pm} \to K^\pm\pi^0$, $B^\mp \to X$ *signal Monte Carlo (solid fill) and continuum Monte Carlo (white points), scaled to the off-resonance luminosity. Except for the cut on* α_T^* *and* α_B^**, all analysis cuts are applied. The* M_{ES}*-*ΔE^* *window is [5.27 GeV/*c^2*,5.29 GeV/*c^2*] and [-0.225 GeV,0.125 GeV]. The vertical line depicts the cut.*

statistics. There is only a cut on α_H and no cuts are made on the CM-momenta of the K^* daughters since there is a trivial, well-defined correlation between the CM-momenta of the kaon and the pion and the helicity angle.

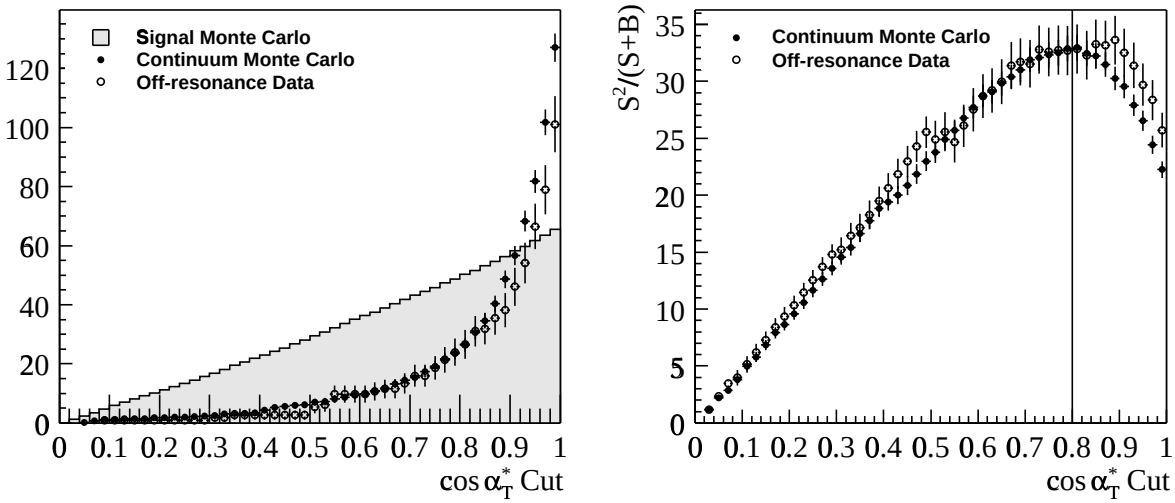

Figure 4.23: *The* $S^2/(S+B_g)$ *optimisation of the* α_T^* *cut as presented in section 4.4 (No cuts on* α_B^* *and* α_H *are applied to gain statistics). LEFT: Signal yield* S *in* $B^\pm \to K^{*\pm}\gamma$, $K^{*\pm} \to K^\pm\pi^0$, $B^\mp \to X$ *signal Monte Carlo (solid line) and background yields* B *from off-resonance data (white points) and continuum Monte Carlo (black points) as a function of the* $|\cos\alpha_T^*|$ *cut. RIGHT:* $S^2/(S+B_g)$ *as a function of the* $|\cos\alpha_T^*|$ *cut obtained with continuum Monte Carlo as background sample and off-resonance data. The vertical line indicates the chosen cut value.*

4.12.4 Optimisation of Event Shape Criteria

To find the best cut values for the three event shape angles $|\cos\alpha_T^*|$, $|\cos\alpha_B^*|$ and $|\cos\alpha_H|$, the ratio $S^2/(S+B_g)$ is evaluated as explained in 4.4 with one difference; since the three angles are not correlated, one is optimised without cutting on the other two to increase statistics.
The dependence of the α_T^* cut of the signal yield S in signal Monte Carlo, and the background yields B_g in continuum Monte Carlo and off-resonance data are shown on the left of figure 4.23 for the example of $|\cos\alpha_T^*|$ and the $B^\pm \to K^{*\pm}\gamma, K^{*\pm} \to K^\pm\pi^0$ mode. The distribution for $S^2/(S+B_g)$ as a function of α_T^* can be seen on the right. There is a clear maximum at $|\cos\alpha_T^*| = 0.8$ for all four $B \to K^*\gamma$ modes. Because of the consistency, this value is used as the cut on α_T^* across all modes. In the same manner we obtain the cut values of $|\cos\alpha_B^*| = 0.8$ and $|\cos\alpha_H| = 0.75$. Again these are common cuts for all four modes, justified by their same behaviour of $S^2/(S+B_g)$.

4.13 B Mass and Energy

Since the beam energy E_{beam}^*, which is the available energy for each of the the two B mesons, is known to higher precision than the measured energies of the B daughters, we can use this constraint for the calculation of kinematic variables that characterise the quality of the reconstructed B mesons and can hence be used to separate signal from background. These two quantities that are largely uncorrelated [78] are the *energy deficit* ΔE^* and the *beam-energy substituted mass* M_{ES} of the B meson, which are both Lorentz-invariants. ΔE^* and M_{ES} will be treated in detail in the next two subsections, their distributions for the reconstructed B candidates having survived all selection

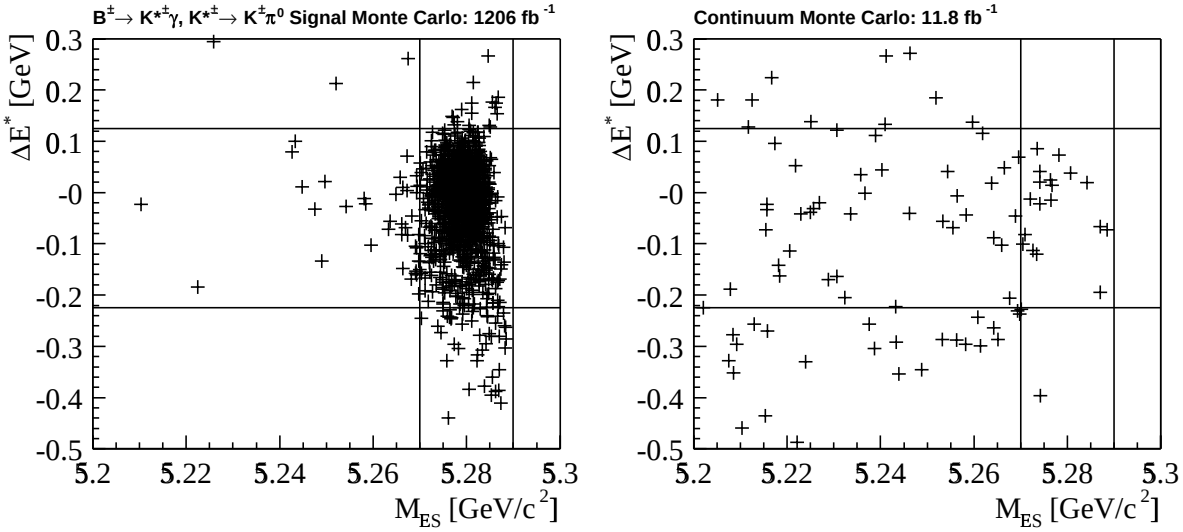

Figure 4.24: *The scatter plot of M_{ES} versus ΔE^* for the B candidates passing all selection criteria in $B^\pm \to K^{*\pm}\gamma$, $K^{*\pm} \to K^\pm\pi^0$, $B^\mp \to X$ signal (LEFT) and continuum Monte Carlo (RIGHT). The lines indicate the projection planes for the ΔE^* and M_{ES} distributions in figure 4.26 and 4.30.*

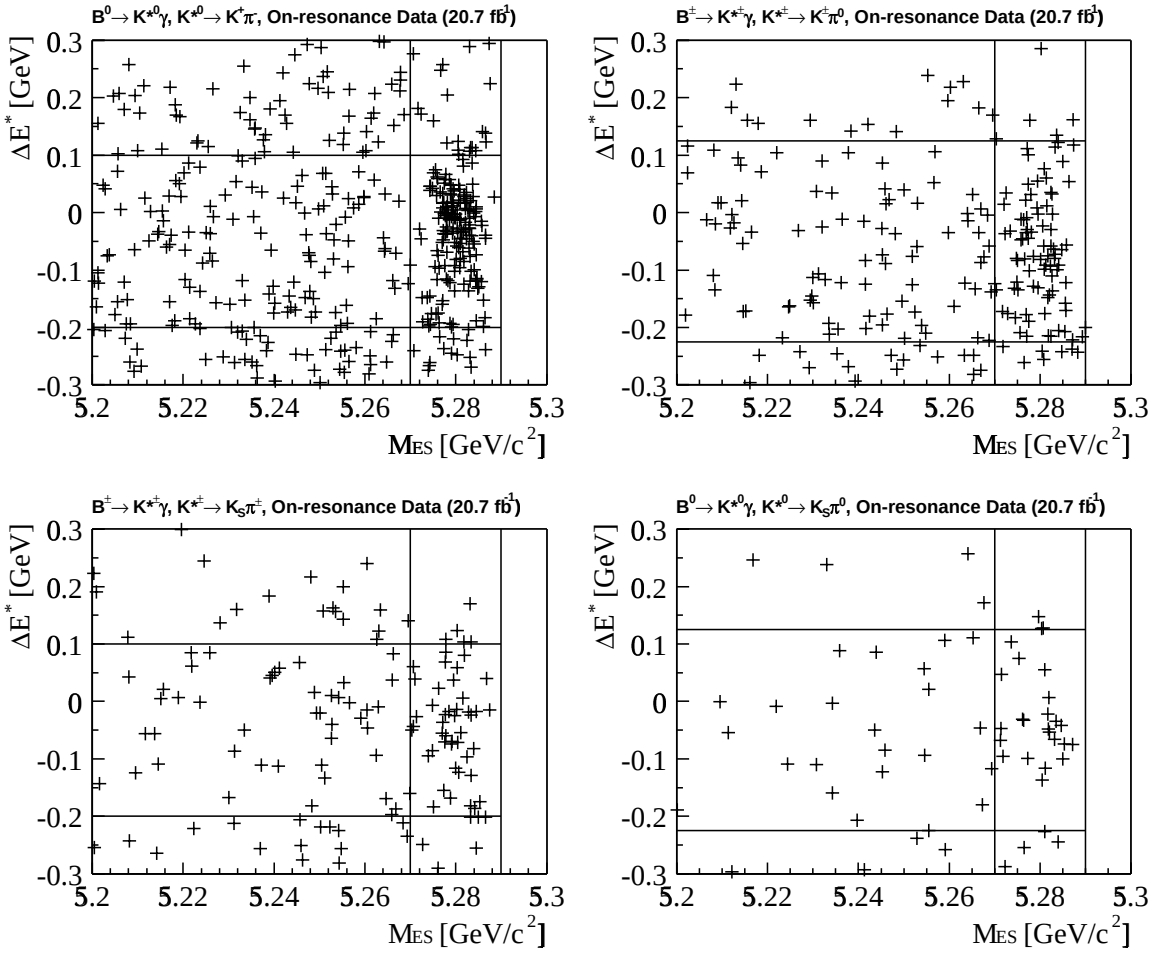

Figure 4.25: *The scatter plot of M_{ES} versus ΔE^* for the B candidates passing all selection criteria for 22.7×10^6 B decays in on-resonance data. The two $B \to K^*\gamma$ modes involving π^0s are on the right and the two other modes on the left. The lines indicate the projection planes for the ΔE^* and M_{ES} distributions in figure 6.6 and 6.7, which also corresponds to region used for the final fit to the M_{ES} distributions.*

criteria are shown in the scatter plots in figure 4.24 for signal and background Monte Carlo, and in figure 4.25 for all four $B \to K^*\gamma$ modes in on-resonance data.

4.13.1 The Energy Deficit ΔE^*

The energy of the B meson is equal to the CM energy E^*_{beam} of the beam which is precisely known. To quantify the discrepancy between the reconstructed and the expected B energy, we define:

$$\Delta E^* = E^*_B - E^*_{beam} \qquad \text{where} \qquad E^*_B = E^*_{K^*} + E^*_\gamma \tag{4.12}$$

In figure 4.26 you can see the ΔE^* projection of the example of $B^\pm \to K^{*\pm}\gamma$, $K^{*\pm} \to K^\pm\pi^0$ signal Monte Carlo for 5.27 GeV/c^2 $< M_{ES} <$ 5.29 GeV/c^2, corresponding to a 3 σ window in M_{ES}.

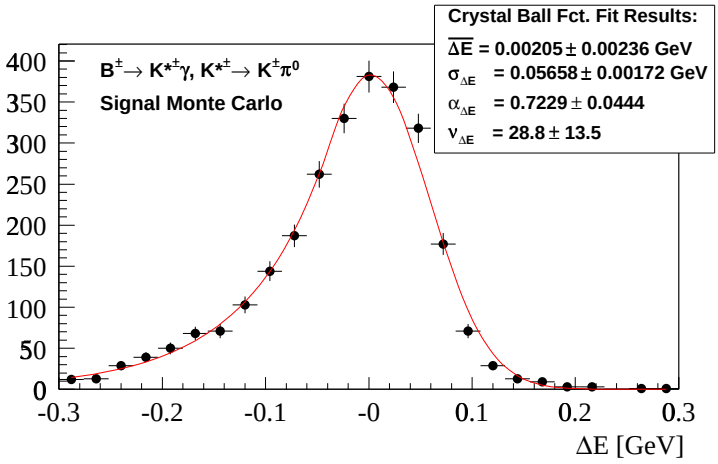

Figure 4.26: *ΔE^* distribution of the reconstructed B candidates in $B^\pm \to K^{*\pm}\gamma$, $K^{*\pm} \to K^\pm\pi^0$, $B^\mp \to X$ Monte Carlo. The function of the unbinned maximum likelihood fit is the Crystal Ball line shape.*

Energy Resolution in Monte Carlo

The ΔE^* distribution receives a small contribution from the beam-energy spread but is dominated by the calorimeter resolution of the photon energy. ΔE^* should have a distribution peaking at zero, the tail at lower energies is due to leakage in the EMC. To account for this, a *Crystal-Ball* function f_{CB} [79] is fitted to the ΔE^* distribution in order to determine the energy resolution:

$$f_{CB}(\Delta E^*) \propto \begin{cases} exp(-(\Delta E^* - \overline{\Delta E^*})^2/(2\sigma^2)) & , \Delta E^* > \overline{\Delta E^*} - \alpha\sigma \\ \frac{(\nu/\alpha)^\nu \cdot exp(-\alpha^2/2)}{((\overline{\Delta E^*} - \Delta E^*)/\sigma + \nu/\alpha - \alpha)^\nu} & , \Delta E^* \leq \overline{\Delta E^*} - \alpha\sigma \end{cases} \tag{4.13}$$

Here, $\overline{\Delta E^*}$ is the peak, σ the width, α the *cut*, and ν the *power* parameter of the Crystal-Ball line-shape. The fit results are compared to data in table 6.3. The resolution in Monte Carlo is of the order 57 MeV in the modes involving π^0s and 39 MeV for the modes containing only tracks except for the radiative photon.

The meaning of the ΔE^* peak and width needs to be understood to interpret the Monte Carlo ΔE^*-distribution. For this purpose, the reconstructed and generated energies of the K^* and the radiative photon in the CM-frame are compared. The distributions of $dE^* = E^*_{rec} - E^*_{true}$ (see figure 4.27) reflect that for the K^* candidates, the dE^* peak is situated at zero. Only for modes containing π^0s there is a tail from leakage in the EMC. For the high-energy γ, the peak resides at ≈ 19 MeV because, due to the EMC calibration for the simulation, the photon energies are reconstructed $\sim 1\%$ too high in the whole γ-energy range (see also fig.5.7), resulting in this average energy excess of 19 MeV. For the modes without π^0s, this corresponds to $\overline{\Delta E^*}$ of the reconstructed B mesons whereas for the modes with π^0s, the combination of two particles with asymmetric energy distributions leads to a resulting ΔE^* Crystal-Ball shape of the Bs peaking at ~ 0 MeV(see table 6.3). Consequently for modes with π^0s, the expected $\overline{\Delta E^*}$ in on-resonance data is ~ -20 MeV if the EMC calibration for real data is correct. This is verified by a study on symmetric η decays in real data [14]. In the energy range [1 GeV, 4 GeV] the η mass hits the PDG value [37] within 0.5%.

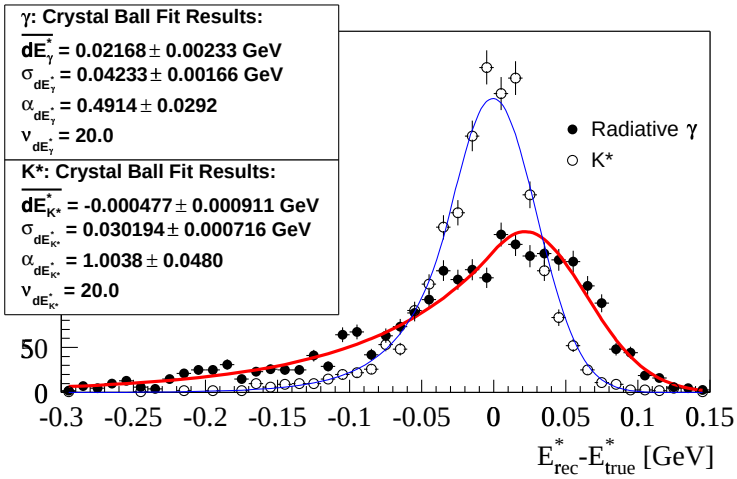

Figure 4.27: *The energy deviation* $dE^* = E^*_{rec} - E^*_{true}$ *for the radiative photons (top) and the* K^* *mesons (bottom) in* $B^\pm \to K^{*\pm}\gamma$, $K^{*\pm} \to K^\pm\pi^0$, $B^\mp \to X$ *signal Monte Carlo.*

Optimisation of ΔE^* Criterion

To determine the ΔE^* range to be considered as signal region, an $S^2/(S+B_g)$ optimisation as explained in section 4.4 (with 5.27 GeV/c^2 $< M_{ES} <$ 5.29 GeV/c^2) motivates the cut values of -225 MeV $< \Delta E^* <$ 125 MeV for modes with π^0s, and -200 MeV $< \Delta E^* <$ 100 MeV otherwise. The variation of $S^2/(S+B_g)$ with changing lower and upper ΔE^* cut is shown for $B^\pm \to K^{*\pm}\gamma$, $K^{*\pm} \to K^\pm\pi^0$ in fig.4.28.

The asymmetric ΔE^* cut, which is the last cut of the analysis, accepts $\approx 96\%$ of the signal, including most of the tail due to energy leakage. If more than one B candidate is found in an event, only the one with lowest absolute value of ΔE^* is considered.

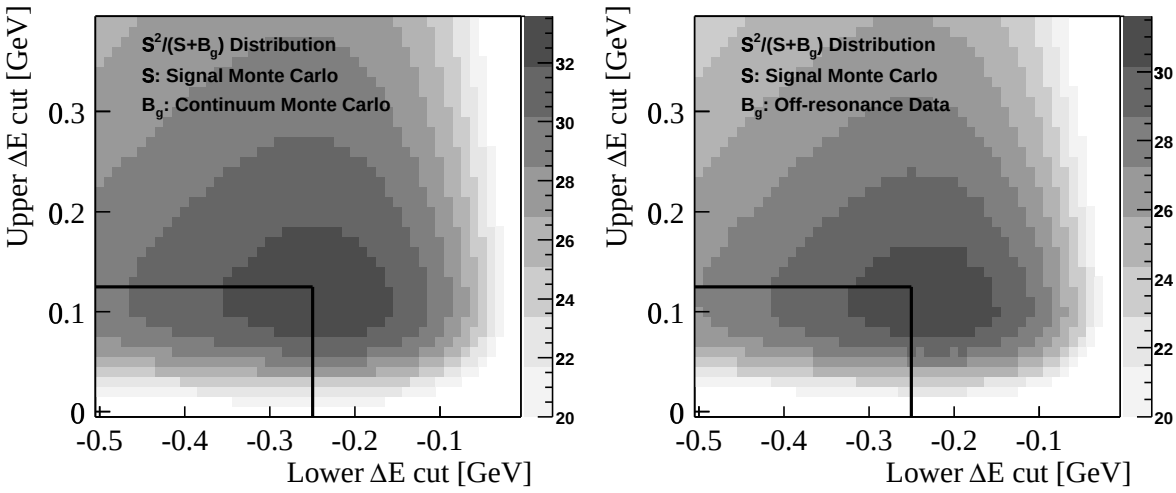

Figure 4.28: *The distribution of* $S^2/(S+B_g)$ *for varying lower and upper* ΔE^* *cut. The signal Monte Carlo is* $B^\pm \to K^{*\pm}\gamma$, $K^{*\pm} \to K^\pm\pi^0$, $B^\mp \to X$. *The result using continuum Monte Carlo (LEFT) confirms the off-resonance data (RIGHT). The optimisation procedure is according to section 4.4 with* 5.27 GeV/c^2 $< M_{ES} <$ 5.29 GeV/c^2.

4.13.2 The Energy Substituted B-Mass M_{ES}

The beam-energy substituted B-mass, M_{ES}, is evaluated by replacing the reconstructed B-energy with its expectation from the well known beam energy, while the reconstructed B-momentum remains untouched. The B mass is then re-calculated by

$$M_{ES} = \sqrt{{E^*_{beam}}^2 - {\vec{p^*_B}}^2}, \qquad \vec{p^*_B} = \vec{p^*_{K^*}} + \vec{p^*_\gamma}, \tag{4.14}$$

Here, $\vec{p^*_{K^*}}$ and $\vec{p^*_\gamma}$ represent the CM momenta of the B daughters.
M_{ES} can be determined either in the LAB frame where E^2_{beam} is equivalent to $s^2/2$, or in the CM frame. The latter is the choice of this analysis and requires that the momenta of the charged K^* daughters contributing to $\vec{p}_{K^*}$ are boosted using the correct mass assignments. Deploying this constraint from the beam information improves the B-mass resolution by roughly an order of magnitude.
Additionally, for the modes without π^0s we take advantage of the fact that in these decays the major uncertainty in ΔE^* and M_{ES} arises from the energy measurement of the high-energy photon. The photon energy can be rescaled, applying the kinematic constraint $\Delta E^* = 0$, which leads to a correction for the leakage effects in the EMC. The rescaled photon energy is then used for $\vec{p}_\gamma$ to re-calculate M_{ES}:

$$M_{ES} = M^{old}_{ES} + \frac{\Delta E^* \cdot p_\gamma}{M^{old}_{ES}} + \frac{\Delta E^* \cdot \vec{p}_{K^*} \cdot \vec{p}_\gamma}{M^{old}_{ES} \cdot p_\gamma} - \frac{{\Delta E^*}^2}{2M^{old}_{ES}} \tag{4.15}$$

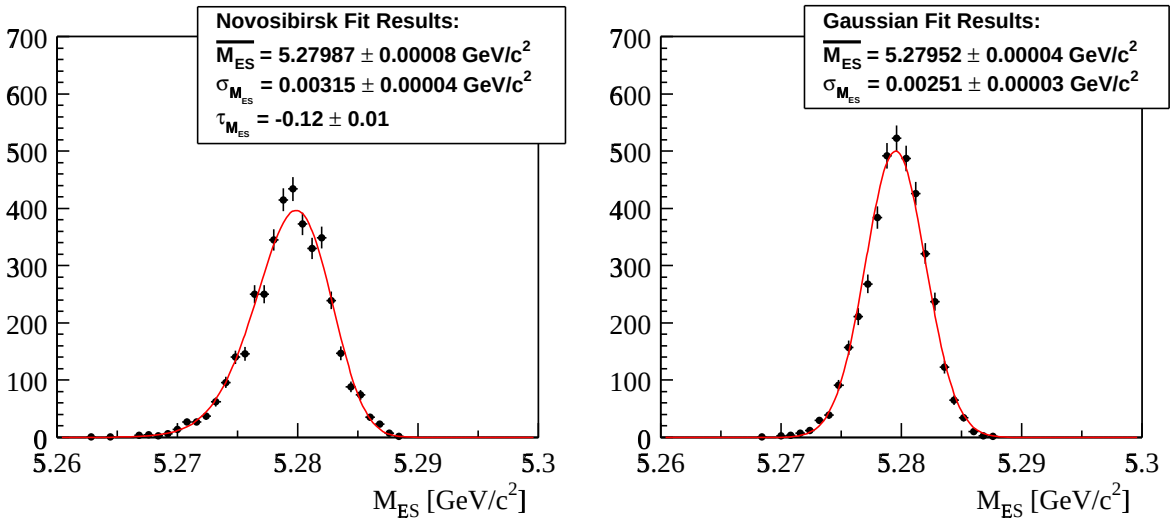

Figure 4.29: *The M_{ES} distribution for reconstructed $B^0 \to K^{*0}\gamma$, $K^{*0} \to K^+\pi^-$ signal Monte Carlo before (LEFT) and after (RIGHT) the procedure of rescaling the energy of the high-energy photon. The ΔE^* region is [-0.2 GeV, 0.1 GeV]. The solid line shows the unbinned maximum-likelihood fit of a Gauss function in both cases.*

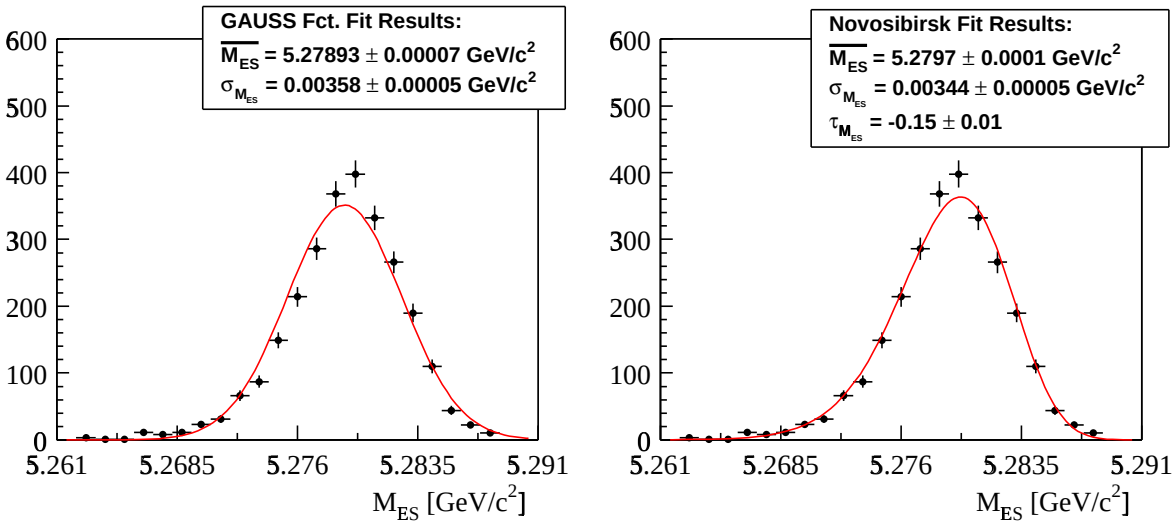

Figure 4.30: *The M_{ES} distribution for reconstructed $B^{\pm} \to K^{*\pm}\gamma$, $K^{*\pm} \to K^{\pm}\pi^0$ signal Monte Carlo. The ΔE^* region is [-0.225 GeV, 0.125 GeV]. The solid line indicates the unbinned maximum-likelihood fit of a Gaussian (LEFT) and a Novosibirsk function (RIGHT).*

The photon rescaling has been studied using Monte Carlo samples and off-resonance data. Figure 4.29 indicates that the non-Gaussian tail in the M_{ES} signal shape is removed by this procedure. The fit function used is a Gaussian with peak $\overline{M}_{ES}$ and width $\sigma_{M_{ES}}$. The mass resolution in signal Monte Carlo is improved from 3.1 MeV/c^2 to 2.5 MeV/c^2 for the $B^0 \to K^{*0}\gamma$, $K^{*0} \to K^+\pi^-$ mode, and from 3.2 MeV/c^2 to 2.6 MeV/c^2 for $B^{\pm} \to K^{*\pm}\gamma$, $K^{*\pm} \to K_S\pi^{\pm}$. It has been checked separately in off-resonance data and continuum Monte Carlo that the photon rescaling does not create pathological changes in the background shape.
For the $B \to K^*\gamma$ decay modes involving π^0s, the photon rescaling cannot be applied since the missing energy from leakage in the EMC can *a priori* be due to the two π^0-daughter photons as well as the high-energy photon. The M_{ES} distribution for $B^{\pm} \to K^{*\pm}\gamma$, $K^{*\pm} \to K_S\pi^{\pm}$ signal Monte Carlo is shown in figure 4.30. Two approaches are tested to describe the M_{ES} shape in the two modes containing π^0s, a fit of a Gauss function and a Novosibirsk function f_{Novo} (equation 4.7) which takes into account the tail $\tau_{M_{ES}}$ due to photon leakage. The Novosibirsk function leads to the more satisfying result. The signal fit of the on-resonance data will therefore use the Novosibirsk shape for modes with π^0s. Concerning the mass resolution, the width in signal Monte Carlo is determined to be 3.4 MeV/c^2 for $B^{\pm} \to K^{*\pm}\gamma$, $K^{*\pm} \to K^{\pm}\pi^0$ and 3.5 MeV/c^2 for $B^0 \to K^{*0}\gamma$, $K^{*0} \to K_S\pi^0$. These values are compared to real data in table 6.4. The M_{ES} region defined for the cut optimisation in section 4.4 corresponds to $\sim 3\ \sigma_{M_{ES}}$.

Chapter 5

Efficiency Studies

Once we have found a certain number of $B \to K^*\gamma$ events in our data sample, we will need the reconstruction efficiency to convert the determined event yield into a result for the branching fraction. This chapter explains how the signal reconstruction efficiency is first determined using simulated data, and then corrected for the various slight differences between data and Monte Carlo. The π^0 study presented in the second part of this chapter has been carried out independently of the $B \to K^*\gamma$ analysis to provide the π^0 and photon efficiency correction between data and Monte Carlo to the *BABAR* collaboration.

5.1 Determination of Signal Efficiencies

The signal efficiency of the $B \to K^*\gamma$ analysis is determined by applying the same procedures and cuts, that are used for real data, to signal Monte Carlo events. The numbers for the individual efficiencies of the various selection criteria listed in table 5.1 are extracted requiring that the detected photons and tracks in the $B \to K^*\gamma$ decay are *truth-matched*. Likewise for the composite K^* and B candidates, the efficiencies are for the combinations in which all the individual elements comprising the candidate are truth-matched. The meaning of "truth-matched" is that the reconstructed candidate is verified to originate from the generated particle by a back-trace through the whole chain of particle generation, detector response, and candidate reconstruction.

The listed efficiencies are relative, i.e. the number of events surviving a certain cut is the denominator for the subsequent one. The efficiencies obtained in Monte Carlo need to be corrected for the slightly different tracking, PID, photon and K_S efficiency in real data. Efficiencies marked by an asterisk (*) represent these empirically determined corrections based on comparison of control samples in data and Monte Carlo (see section 5.1.1 - 5.1.4).

Ignoring any Monte-Carlo-generator information, i.e. not requiring truth-matched candidates, we find the overall efficiencies listed in table 5.2. Those efficiencies are larger than the truth-matched ones, reflecting the number of "mis-matched" B candidates where wrong daughters lead to a successful B reconstruction that passes all cuts.

Section	Cut description	efficiency[%]			
		$\pi^0 K^\pm$	$\pi^\pm K_S$	$\pi^\pm K^\mp$	$\pi^0 K_S$
	Global event criteria				
4.6	$R_2 < 0.9$	99.8	99.6	99.9	99.9
4.6	$N_{trk} > 2$	96.8	97.0	97.1	98.1
4.6	1.5 GeV$< E_{max} <$ 3.5 GeV	80.1	80.3	80.5	80.4
	Cumulative global event efficiency	77.4	77.5	78.1	78.9
	Photon selection				
4.7	Fiducial cut: $-0.74 < \cos\theta < 0.93$	93.9	92.7	94.3	94.0
4.7	No problematic crystals	98.2	98.0	98.0	98.3
4.7	CM energy cut: 2.3 GeV $< E^*_\gamma <$ 2.8 GeV	89.8	90.7	92.5	89.7
4.7	$N_{Xtal} > 4$	99.3	100.0	100.0	99.2
4.7	Bump isolation $d_{CB} > 25$ cm	90.5	91.1	90.5	90.8
4.7	Second moment < 0.002	99.1	99.3	99.4	99.1
4.7	π^0 veto	94.0	95.9	96.0	94.0
4.7	η veto	96.2	96.0	96.2	95.9
5.1.4	Data/MC correction*	97.5	97.5	97.5	97.5
	Cumulative photon efficiency	69.3	66.9	68.6	69.2
	Kaon selection				
4.8	"Good" track criteria	90.2	-	91.0	-
4.8	Positive kaon PID	77.6	-	85.7	-
	Cumulative kaon efficiency	72.7	-	78.0	-
	Pion selection				
4.8	"Good" track criteria	-	87.1	90.4	-
4.8	Negative kaon PID selection	-	98.0	98.0	-
	Cumulative pion efficiency	-	85.4	88.6	-
5.1.1	Correction for tracking efficiency*	99.4	98.9	97.7	-
	π^0 selection				
4.10	γ from π^0 reconstructed	78.5	-	-	77.0
4.10	π^0 mass cut: 115 MeV/c^2 $< m_{\pi^0} <$ 150 MeV/c^2	87.4	-	-	87.7
4.10	π^0 fit converged	99.5	-	-	99.7
5.1.4	π^0 efficiency correction*	95.0	-	-	95.0
	Cumulative π^0 reconstruction	50.9	-	-	49.2
	K_S selection				
4.9	π from K_S reconstructed	-	87.2	-	87.8
4.9	K_S loose mass cut: 300 MeV/c^2 $< m_{K_S} <$ 700 MeV/c^2	-	90.0	-	90.8
4.9	K_S vertex fit converged	-	100.0	-	98.1
4.9	K_S mass cut: 489 MeV/c^2 $< m_{K_S} <$ 507 MeV/c^2	-	91.2	-	95.0
4.9	K_S flight distance $d_{K_S} > 0.2$ cm	-	97.0	-	96.4
5.1.3	K_S efficiency correction*	-	103.0	-	104.2
	Cumulative K^0_S reconstruction	-	62.3	-	65.5
	K^* selection				
4.11	Loose mass selection	-	99.6	99.7	-
4.11	vertex $\chi^2 > 0$	-	95.3	97.9	-
4.11	K^* mass cut: $\Delta m_{K^*} <$ 100 MeV/c^2	91.4	91.2	90.7	91.4
4.12.3	$\lvert\cos\alpha_H\rvert < 0.75$	92.4	92.6	91.9	92.9
4.11	2.35 GeV/c $< P_{K^*} <$ 2.80 GeV/c	98.7	99.7	99.6	99.1
	Cumulative K^* efficiency	83.5	79.8	81.0	84.1
	Event shape				
4.12.1	$\lvert\cos\alpha^*_T\rvert < 0.80$	77.3	81.3	79.7	78.1
4.12.2	$\lvert\cos\alpha^*_B\rvert < 0.80$	92.6	93.0	93.7	91.9
	Cumulative event shape efficiency	71.6	75.5	74.7	71.8
	B reconstruction				
4.13.1	ΔE^* cut	96.6	95.4	96.2	96.1
	Cumulative efficiency	11.3	15.9	21.0	11.3

Table 5.1: Reconstruction efficiencies from truth-matched signal Monte Carlo.

Quantity	Mode			
	$K^{*\pm} \to K^{\pm}\pi^0$	$K^{*\pm} \to K_S\pi^{\pm}$	$K^{*0} \to K^{+}\pi^{-}$	$K^{*0} \to K_S\pi^0$
Total signal ϵ [%]	12.9	17.2	21.0	12.6
Rel. mis-matched rate [%]	12.4	7.6	0.1	10.3
# MC events	19,000	29,000	18,000	19,000
Rel. stat. error [%]	2.1	1.5	1.9	2.4

Table 5.2: *The total signal efficiency ϵ from signal Monte Carlo without truth-matching, the relative mis-matched rate of reconstructed signal events with wrong daughter particle, the used number of signal MC events, and the relative statistical error of ϵ.*

Whereas for the $K^{*0} \to K^{+}\pi^{-}$ mode this contribution from non-truth-matched combinations in the final sample, called the "*mis-matched rate*" in the succeeding, is very small with 0.1%, for $K^{*\pm} \to K_S\pi^{\pm}$ it is about 8%, and in the channels involving π^0s it turns out to be of the order of 10-12%. This is due to the high abundance of low energy photons and pions that can lead to positive K_S and π^0 reconstruction even if one of the real π^0 or K_S daughters was not detected. The *final* efficiency for the complete selection includes this contribution.

Because of the limited statistics of the signal Monte Carlo samples, there is a small associated systematic error contribution to the branching fraction measurement (see table 5.2).

5.1.1 Efficiency Corrections from Tracking

To correct for slightly different tracking efficiencies in real data and Monte Carlo, we use their ratio for the "good" track selection as a function of the track momentum. The latter is provided by a method that takes advantage of the fact that *BABAR* possesses two tracking devices and measures the efficiency of the DCH by using the detection of a track in the SVT as trigger, i.e. to signal that a charged particle is present [80]. Physics events are used for additional cross-checks; the number of reconstructed $D^* \to \pi_{slow} D^0, D^0 \to K\pi\pi\pi$ for which all four tracks satisfy the "good" track criteria is compared to the cases where one track is not classified as "good" [80]. Furthermore, 3+1 τ-events are selected based on an isolated lepton recoiling against two tracks and the occurrence of a fourth "good" track [81]. From the technical point of view, the correction factors are looked up for the ultimately accepted candidates in signal Monte Carlo on a track-by-track basis to determine their average $\delta\epsilon_{trk}$. Since there were two periods of data taking during RUN 1 with different drift-chamber high-voltage settings, Block 1 with 1960 V and Block 2 with 1900 V, the two blocks are investigated separately and their overall corrections are combined by a weighted mean. The values of $\delta\epsilon_{trk}$ in table 5.3 indicate that the tracking efficiency in real data is somewhat smaller than in simulation. The statistical errors on $\delta\epsilon_{trk}$ are considered as systematic uncertainties on the overall signal reconstruction efficiency.

Quantity	Mode			
	$K^{*\pm} \to K^{\pm}\pi^0$	$K^{*\pm} \to K_S\pi^{\pm}$	$K^{*0} \to K^{+}\pi^{-}$	$K^{*0} \to K_S\pi^0$
$\delta\epsilon_{trk}$ [%]	-0.6±1.3	-1.1±1.2	-2.3±2.4	-

Table 5.3: *The correction $\delta\epsilon_{trk}$ for different tracking efficiency in real data and MC.*

5.1.2 Efficiency Corrections from Kaon PID

The deviations of the kaon PID-efficiency and pion mis-ID rates in real data from the ones in simulation have been investigated using pions from $K^0_s \to \pi^+\pi^-$ and pions and kaons from the slow-pion tagged decay chain $D^* \to D^0\pi_{soft}, D^0 \to K\pi$ [71]. The corrections and their errors are tabulated as a function of track momentum. Both, efficiency and mis-ID corrections are taken into account in the treatment of the Monte Carlo on the reconstruction level already by randomly removing tracks with the probability given by the data-MC discrepancy. Hence, no overall correction factor due to particle identification needs to be multiplied in table 5.1, yet the associated systematic error needs to be quantified. For this purpose, the statistical error $\delta\epsilon_{pid}(p_{kaon})$ in each momentum bin of the PID correction tables is weighted by the phase space density of the kaon momentum:

$$\overline{\epsilon_{pid}} = \sum_{kaons} \epsilon_{pid}(p_{kaon}) / \sum_{kaons} \qquad \overline{\delta\epsilon_{pid}} = \sum_{kaons} \delta\epsilon_{pid}(p_{kaon}) / \sum_{kaons} \tag{5.1}$$

As for the tracking, the weighted mean of Block 1 and Block 2 of RUN 1 is formed, and the resulting statistical error is used as the sought-after systematic uncertainty. To study the systematic effect due to the chosen binning of the tables, the number of bins is reduced progressively using the weighted mean of the contents, and the change of the overall efficiency is plotted in figure 5.1. The decrease of the statistical error when reducing the number of bins is compensated by a shift of the average value that introduces an uncertainty of the same size as the initial statistical error. This reflects the difference in phase space between our kaon sample and the PID control-sample used to determine these efficiencies. We deduce a systematic error of 1% for the $K^{*\pm} \to K^{\pm}\pi^0$ mode and 0.7% for $K^{*0} \to K^{+}\pi^{-}$.

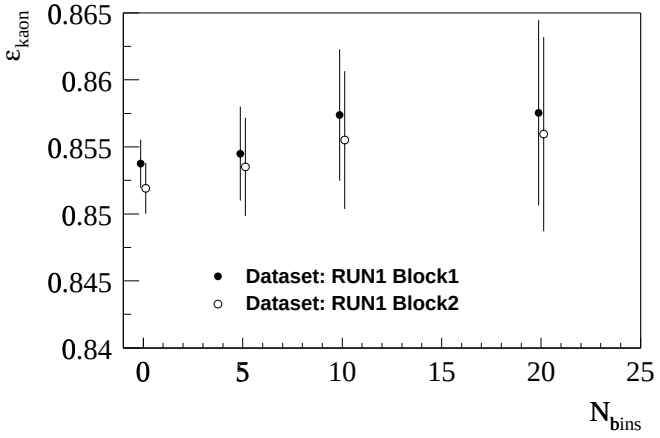

Figure 5.1: *The overall kaon-PID efficiency ϵ^{pid}_{kaon} for the $B^{\pm} \to K^{*\pm}\gamma$, $K^{*\pm} \to K^{\pm}\pi^0$ kaon sample, using different numbers of bins N_{bins} in the PID efficiency tables that cover the kaon momentum range of [0 GeV/c,5 GeV/c].*

5.1.3 Efficiency Corrections from K_S^0 Reconstruction

The K_S reconstruction efficiency has been studied by looking at inclusive spectra of reconstructed K_S in real data and Monte Carlo [76]. The efficiency corrections are tabulated as a function of the K_S flight length and are applied to the Monte Carlo spectrum of our finally accepted K_S. There are two sets of correction tables, set A was obtained using all K_S whereas for set B an additional momentum-cut $p(K_S) > 1$ GeV/c was applied. Set B is used for the central value of the efficiency correction since with the momentum cut the extraction of the correction is cleaner. The two sets are also broken up into Block 1 (B1) and Block 2 (B2), corresponding to the different drift-chamber conditions. The overall efficiency correction is given as the weighted mean of the averaged values for B1 and B2. The statistical error $\sigma_{\delta\epsilon}^{stat}$ is found by propagating the correction errors in the tables. The systematic error $\sigma_{\delta\epsilon}^{sys}$ is evaluated as the relative difference of the corrections obtained using set A and set B. Furthermore, the systematic error $\sigma_{\delta\epsilon}^{trk}$ from the tracking efficiency of 1% per track, as it pertains to K_S, has to be considered and added in quadrature. We find a K_S efficiency correction $\delta\epsilon_{K_S} = (4.2 \pm 4.5)\%$ for $K^{*0} \to K_S\pi^0$ and $(3.0 \pm 4.5)\%$ for $K^{*\pm} \to K_S\pi^\pm$. The K_S reconstruction efficiency is hence larger in real data than in simulated data.

5.1.4 Efficiency Corrections from Neutral Reconstruction

A comparative study of the π^0 efficiency, mass and width in data and Monte Carlo simulation has been performed independently of the $B \to K^*\gamma$ analysis to provide the Monte Carlo efficiency correction for π^0s and photons to the *BABAR* collaboration [15]. It is presented in the next section 5.2 and has been done using π^0 mesons from $\tau\tau$ 1-on-1 decays. The energy range covered by this study is [0 GeV,3.5 GeV]. The π^0-energy distribution of $B \to K^*\gamma, K^{*\pm} \to \pi^0 K^\pm$ in figure 5.2 proves that our π^0s lie well within the covered energy range. The elaborated recipe of the study is to randomly remove 2.5% of the photons in Monte Carlo and smear the photon energies by 1.5%. The estimated systematic error on the reconstruction efficiency is 2.5% per π^0 and 1.3% per radiative photon (see section 5.2). However, the photon-energy smearing should not be applied for our radiative photon since for high energies, real data and simulation agree with respect to the energy resolution as demonstrated in section 5.2.4. For technical reasons, the photon smearing can only be switched on for the whole event

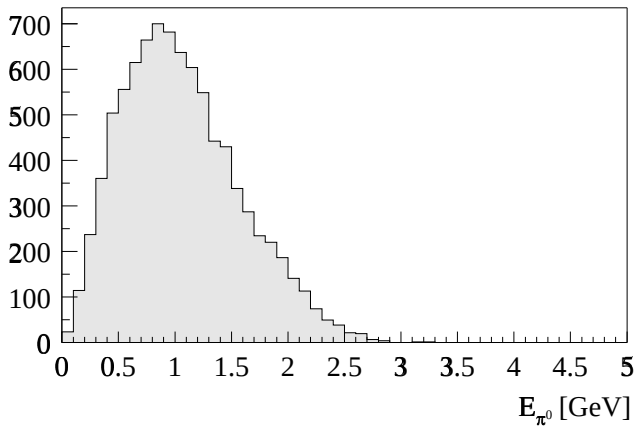

Figure 5.2: *Distribution of the reconstructed truth-matched π^0 energy in $B^\pm \to K^{*\pm}\gamma$, $K^{*\pm} \to K^\pm\pi^0$, $B^\mp \to X$ signal Monte Carlo.*

and not for single candidates. Therefore, in our case only the efficiency correction of 2.5% per photon is used for both, the photon and the π^0. To inspect if an extra systematic error is introduced by the slightly different π^0 mass resolution in data and Monte Carlo below a π^0 energy of 2 GeV (see section 5.2.4), the cut on the π^0 mass is varied in the $B \to K^*\gamma$ analysis. Table 5.4 reflects the impact on the measured branching fraction. The fluctuations are statistical, a systematic effect would expose variations of the opposite sign than the measured ones. Hence, since a relatively wide π^0 mass range is chosen, no additional systematic error needs to be assigned apart from the 2.5% mentioned above.

π^0 mass window [MeV]	[115,150]	[117,148]	[119,146]	[121,144]	[123,142]	[125,140]
$\mathcal{B}(B^\pm \to K^{*\pm}\gamma)$ change [%]	-	+7.7	+3.3	-3.6	-9.8	-2.0

Table 5.4: *The variation of the branching fraction $\mathcal{B}(B^\pm \to K^{*\pm}\gamma)$ for different cuts on the π^0 mass.*

5.2 The π^0 and γ Efficiency Study

The aim of this study is to validate the simulation of the EMC hardware, reconstruction software and calibration in terms of π^0 efficiency, mass scale and resolution. It covers the whole on-resonance *BABAR*-RUN 1 data of 20.7 fb^{-1}. For the simulation, 5.2×10^6 generic $e^+e^- \to \tau^+\tau^-$ Monte Carlo events processed with the same reconstruction software have been used.
The study is a data-MC comparison which determines the relative difference in π^0 efficiency between the two samples. It concludes with a *recipe* for the estimation of the reconstruction efficiencies of final states containing any number of photons or π^0s, and the corresponding systematic error. Using π^0 mesons from τ decays allows to extend this study up to π^0 energies of $\sim$ 4.5 GeV. Measurements of the branching fractions $\tau^- \to h^- N\pi^0$ with $(N = 2, 3, 4)$ relative to $N = 1$ have been published by CLEO [82], and this work follows the basic methods of that analysis.

5.2.1 Strategy

The strategy consists of exploiting $\tau\tau$ "1-on-1 decays", $e^+e^- \to \tau^+\tau^-$, with the "*tag*" τ decaying into $e^\pm$ plus neutrinos and the other 1-prong τ to a neutrino, a hadron (mostly $\pi^\pm$), and one or two π^0 mesons. One therefore has to identify the electron and search for one or two π^0 mesons associated with a hadron on the opposite side. The yields for the one-π^0 and two-π^0 decays are compared to remove any dependency on the tracking efficiencies and luminosities in data and Monte Carlo. This ratio is mainly sensitive to the decay kinematics (which will be shown to be well modelled by the Monte Carlo) and the π^0 efficiency, since the branching fractions are known to the level of 1%. In addition, a very clean high-statistics sample of π^0s is provided by the 1-on-1 topology with an electron tag, allowing a comparison of the π^0 characteristics like the mass peak and width in real data and Monte Carlo. Muon decays on the tag side have been considered and were found to suffer from the high pion contamination, which limits

the precision of this analysis because of $q\overline{q}$-background. Therefore, only electron events are presented here in order to well separate $\tau\tau$ events from low-multiplicity $q\overline{q}$ events.

5.2.2 Event Selection

As a starting point, exactly two "good" tracks fulfilling the criteria of section 4.5.2 are required with net charge zero. The electron candidate has to pass the following selection of a cut-based electron identification [83] that has a π mis-identification probability of $\sim 0.12\%$:

- 500 a.u. $< dE/dx <$ 1000 a.u.[1] for the energy loss in the DCH
- $N_{Xtal} \geq 3$ for the number of EMC crystals
- $0.75 < E/p < 1.3$ for the ratio of deposited energy in the EMC and momentum measured in the DCH
- $0 < LAT < 0.6$ for the shower shape in the EMC
- $-10 < A_{42} < 10$ for the Zernike moment of the showers (see appendix D.1)

The hadron candidate has to fail these electron criteria. There also is a fiducial cut on the CM angle for each of the two tracks, requiring $2.45 > \theta_{CM} > 0.41$, and a topology cut between the CM angle of the two tracks, demanding $-0.99 < \cos\alpha_{2tracks} < 0$. Knowledge of the absolute efficiency of these selections is not needed since it cancels in the double ratio of equation 5.4. The neutrinos in the event are taken into account by using the information contained in the missing momentum vector:

$$\vec{p}_{mis} = \vec{p}_{e^-} + \vec{p}_{e^+} - \vec{p}_{charged} - \vec{p}_{neutral}, \tag{5.2}$$

where $\vec{p}_{e^\pm}$ are the beam momenta and $\vec{p}_{charged}$, $\vec{p}_{neutral}$ is the momentum sum of all charged and neutral candidates, respectively. All vectors are evaluated in the LAB frame. We require the missing momentum to point into a fiducial volume, defined by $-0.76 < \cos\alpha(\vec{p}_{mis}) < 0.96$, to make sure that the missing momentum is really due to neutrinos and not simply carried away by e.g. a photon which is outside the calorimeter acceptance.
For the π^0 reconstruction we accept the best two π^0 candidates in the event compared to the PDG mass value [37] with:

- 0.095 GeV/c^2 $< m(\gamma\gamma) <$ 0.175 GeV/c^2
- $E_\gamma > 30$ MeV
- $E(\pi^0) > 200$ MeV, $E(\pi^0_{slow}) > 200$ MeV, $E(\pi^0_{fast}) > 1$ GeV

The π^0 momentum must point into the hadron hemisphere, i.e. $\cos\alpha(\pi^0, had) > 0$ whereas there is no such cut on the photons. The photon three-vectors are constructed assuming they come from the detector origin and no kinematic constraints are applied. The π^0 and the hadron are combined using simple Lorentz-vector addition.
To minimise remaining backgrounds we require that there be no unused photon in the event with considerable energy, i.e. $E_\gamma > 80$ MeV.

[1] a.u. is a *BABAR*-specific unit for dE/dx, proportional to eV/cm

The only considerable background after the above selection comes from other τ events. A study of the information from the event generation shows that this background mainly consists of down-feed from τ decays with more π^0s where one or even two π^0s are not detected, or up-feed events with less π^0s in which an additional, random π^0 candidate is accepted. For the one-π^0 case the main background is the two-π^0 channel (3.6%) and for the two-π^0 case the $3\pi^0$ (3.1%) as well as the one-π^0 mode (2.6%). These contributions are considered to be the same for data and Monte Carlo since generic τ Monte Carlo is used.

5.2.3 Data/MC Consistency for Event Shapes and Kinematics

To disentangle the π^0 efficiency from the dependence of the ratio in equation 5.3 on the modelling of the kinematics, one has to prove that the event shape and kinematics are well represented by the simulation.
The distributions of a variety of variables have been investigated for discrepancies between data and Monte Carlo and very good agreement was found in all studied cases, i.e for the total energies in the event, E^{tot}_{LAB} and E^{tot}_{CM}, the total energy in the EMC, E_{calo}, the polar angle Θ_e and CM-momentum p^*_e of the $e^{\pm}$, the angle $\alpha(e,h)$ between the $e^{\pm}$ and the hadron, the transverse momentum $p_T(e,h)$ of the $e^{\pm}$ and the hadron, the invariant masses $M(e,h,\pi^0)$, $M(e,h,\pi^0,\pi^0)$, $M(h,\pi^0,\pi^0)$ and $M(h,\pi^0)$, the angle of the missing momentum $\alpha(\vec{p}_{mis})$, the angles of the π^0s, the angles $\alpha(h,\pi^0)$

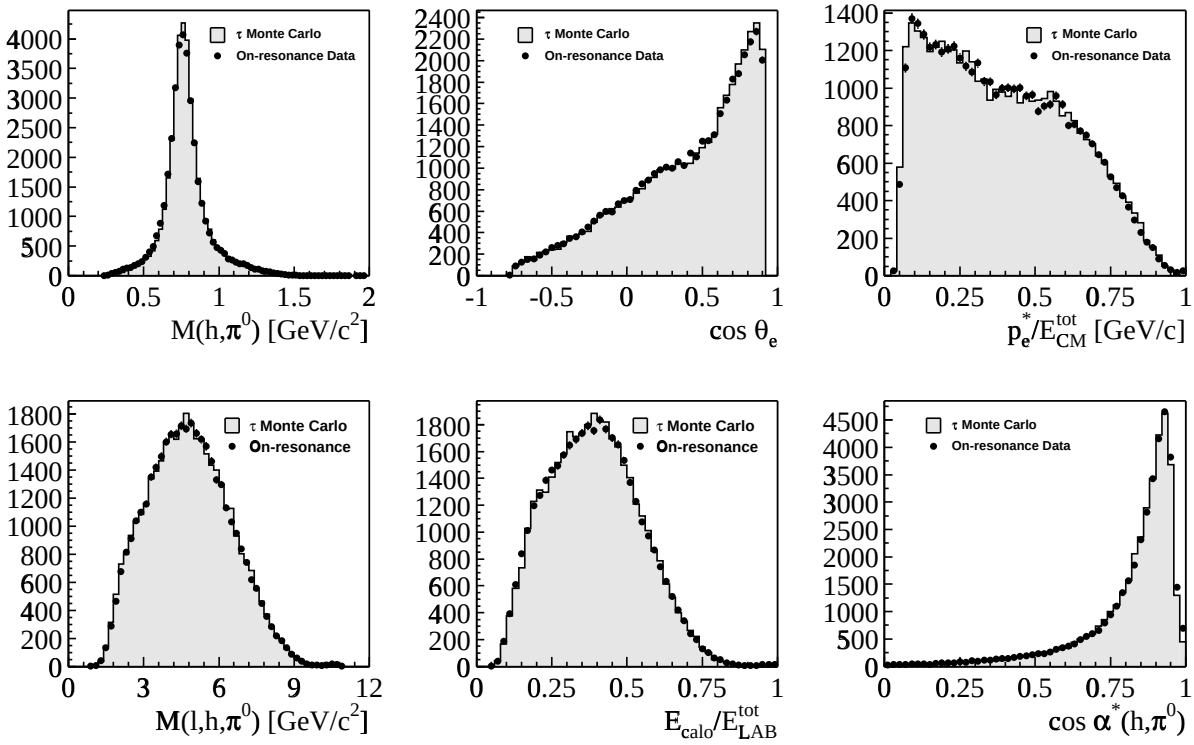

Figure 5.3: *The comparison between real data (points) and $e^+e^- \to \tau^+\tau^-$ Monte Carlo (solid line with grey fill) for some examples of event shape and kinematic variables in $\tau\tau$ 1-on-1 decays. The distributions are normalised to the total number of events.*

between the hadron and π^0, the energies and angles of the photons, their helicity angles, and the mutual distances of their centroids.
Some examples of distributions for the one-π^0 case are shown in figure 5.3. The conclusion is that the kinematics of the τ decays are well modelled by the Monte Carlo.

5.2.4 Comparison of π^0-Mass Peak and Width

The π^0 mesons found after the event selection explained in chapter 5.2.2 form a very pure sample. It is used to investigate the π^0-mass peak and width in data and Monte Carlo by applying a fit of a Novosibirsk function (equation 4.7) plus a first order polynomial to the π^0-mass spectra for various π^0-energy ranges. Examples of those fits are shown in figure D.1. The π^0-mass peak $\overline{m}_{\pi^0}$ and width $\sigma_{m_{\pi^0}}$ for different π^0 energies obtained from those fits are shown in figure 5.4 for real data and simulation. This comparison can be summarised in the following way:

1. The π^0-mass peak in real data increases from 134.3 MeV/c^2 to 136.2 MeV/c^2 between 1 GeV $< E_{\pi^0} <$ 4 GeV, corresponding to a relative change of 1.4%. This mass-peak variation reflects the quality of the photon-energy and -position calibration in the EMC reconstruction of RUN 1.
2. The π^0-mass width in real data grows from 6.5 MeV/c^2 to 8.0 MeV/c^2 in the same energy range, corresponding to a relative broadening by 23%.
3. The important issue in this data-MC comparison study is the agreement of real and simulated data. Whereas above 2 GeV, data and Monte Carlo agree for the π^0-mass peak and width, below 2 GeV the discrepancy is up to 0.5 MeV/c^2 in $\overline{m}_{\pi^0}$ and 0.5 MeV/c^2 in $\sigma_{m_{\pi^0}}$ for the lowest π^0 energies. This corresponds to a relative discrepancy of 0.4% for the mass peak and 7% for the width in this low π^0 energy range $E_{\pi^0} <$ 1.5 GeV.

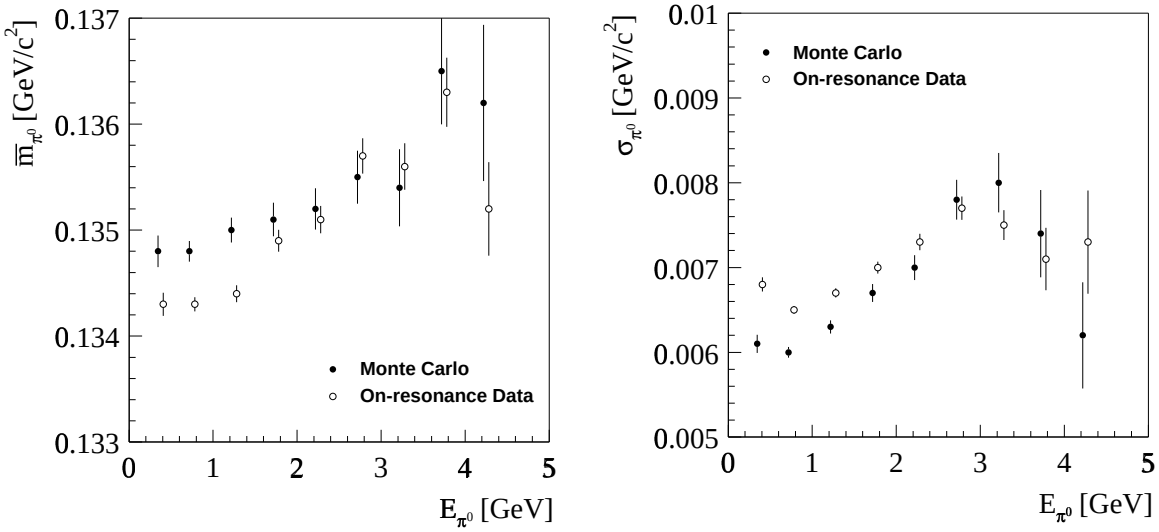

Figure 5.4: *The peak $\overline{m}_{\pi^0}$ of the π^0 mass (LEFT) and width $\sigma_{m_{\pi^0}}$ (RIGHT) as a function of the π^0 energy for real data and Monte Carlo in $\tau\tau$ 1-on-1 decays. The underlying fits are shown in figure D.1.*

We conclude that, when extracting the Monte Carlo π^0 efficiency correction, an energy smearing should be applied to account for the data-simulation discrepancy in the π^0 width (see chapter 5.2.6). The π^0-mass peak discrepancy between data and MC will be included in the systematic error by applying an energy shift to all reconstructed neutral objects in the simulation (see chapter 5.2.6).

5.2.5 Analysis of π^0 Efficiency

In order to study the stability of the π^0 efficiency as a function of energy, we first look at the energy distributions of the π^0s in the one-π^0 and two-π^0 case. The good agreement between real data and Monte Carlo is shown in figure 5.5.
The goal of the present study is not to measure the absolute π^0 efficiency of the *BABAR* calorimeter, but rather to validate the detector simulation by measuring in Monte Carlo and real data a quantity that depends dominantly on the π^0 efficiency. This quantity is the ratio $\mathcal{R}$ of $\tau\tau$ 1-on-1 events with two and one π^0 mesons in them:

$$\mathcal{R} = N(\tau^{\pm} \to h^{\pm}2\pi^0)/N(\tau^{\pm} \to h^{\pm}1\pi^0) \tag{5.3}$$

The ratio $\mathcal{R}$ is evaluated for different π^0-energy ranges in two ways:

1. Varying the π^0 energy in the one-π^0 case and the *faster* π^0 *energy* in the two-π^0 case. All slow π^0s are taken into account.
2. Varying the π^0 energy in the one-π^0 case and the *slower* π^0 *energy* in the two-π^0 case. All fast π^0s are considered.

This procedure is carried out in the same manner for Monte Carlo and real data. To compare these energy-dependent ratios in data and simulation, we calculate the discrepancy $\mathcal{Q}_{DATA/MC}$. For data and simulation to agree well, $\mathcal{Q}_{DATA/MC}$ is desired to be zero:

$$\mathcal{Q}_{DATA/MC} = (\mathcal{R}_{DATA} - \mathcal{R}_{MC})/\mathcal{R}_{MC} \tag{5.4}$$

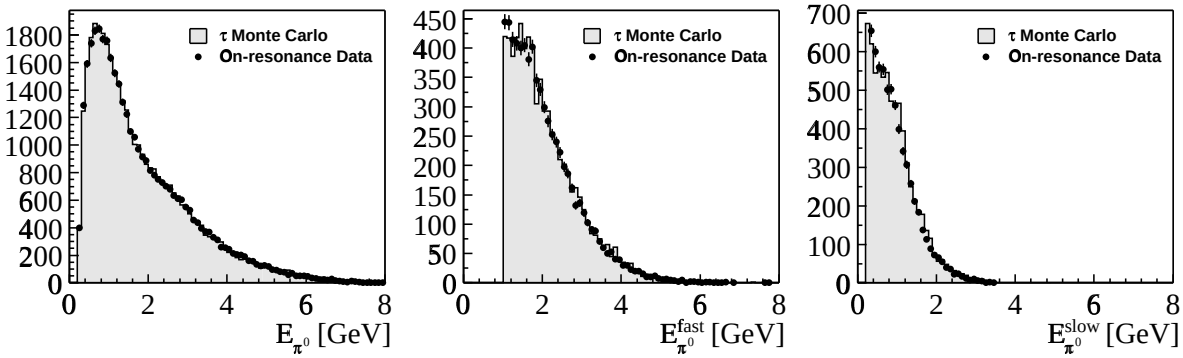

Figure 5.5: *The π^0-energy distributions in $\tau\tau$ 1-on-1 decays for the one-π^0 decays (LEFT), and the fast π^0 (MIDDLE) and the slow π^0 (RIGHT) in the two-π^0 case, as a comparison between real data (points) and $e^+e^- \to \tau^+\tau^-$ Monte Carlo (solid line with grey fill). The distributions are normalised to the total number of events.*

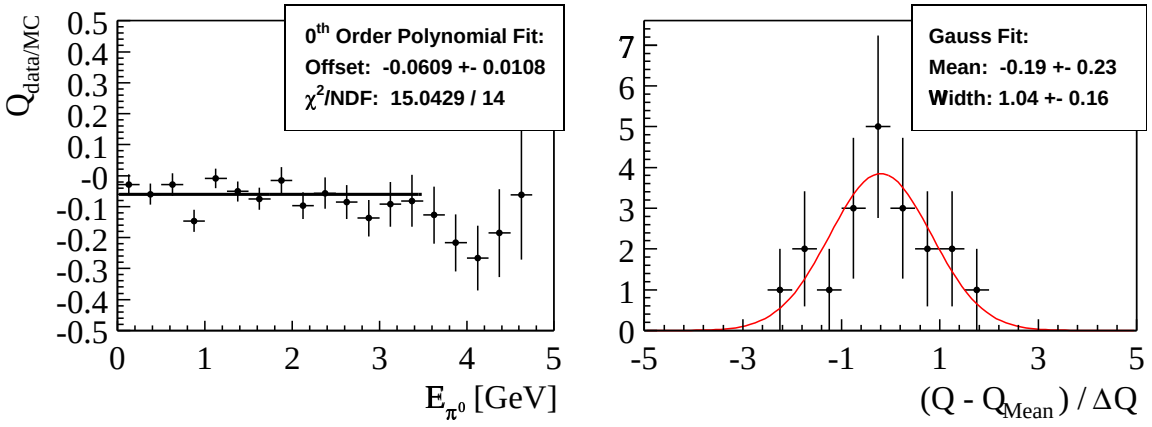

Figure 5.6: *LEFT: The discrepancy $\mathcal{Q}_{DATA/MC}$ (equation 5.4) between the two-π^0-to-one-π^0 ratio $\mathcal{R}$ (equation 5.3) in real data and Monte Carlo. RIGHT: The pull distribution of the ratio discrepancy $(\mathcal{Q}_{DATA/MC} - \mathcal{Q}_{MEAN})/\sigma_{\mathcal{Q}}$ for different π^0 energies. A Gaussian distribution is expected and used as fit function.*

We take the weighted mean of the contributions from the slow and fast π^0 energy variation to quantify the data-simulation π^0-efficiency difference. A constant is fitted to the resulting energy distribution shown in figure 5.6 between 0 and 3.5 GeV in order to obtain the average π^0 efficiency difference.

The quality of the simple straight line fit is illustrated on the right of figure 5.6. The distribution of the pulls $(\mathcal{Q}_{DATA/MC} - \mathcal{Q}_{MEAN})/\sigma_{\mathcal{Q}}$ has a random, and consequently Gaussian distribution around the mean value $\mathcal{Q}_{MEAN}$. The width of the Gaussian is consistent with one. We obtain that in the energy range $E(\pi^0)$ <3.5 GeV, the data-MC π^0-efficiency difference is (-6.1±1.1)%.

One plausible reason for the higher MC π^0-efficiency is that there is more material in the real detector than in the MC simulation, which would lead to a higher γ-conversion probability in data compared to Monte Carlo and thus to a smaller probability of photons reaching the EMC. This is in agreement with the observation of higher Bremsstrahlung rates for electrons from J/ψ [84] and Bhabha events [63]. The software GEANT3 [85] used for the simulation was missing material in the beam pipe and support tube. In the future the improved GEANT4 will be deployed, where the best known description of materials in the centre of the detector has been implemented.

To take care of the data-MC π^0-efficiency discrepancy from the technical point of view, the "*photon killing and smearing*" can be applied in the analysis software. This procedure means that 2.5% of all reconstructed neutral objects are removed randomly and the remaining candidates undergo a smearing of their energies by 1.5%. As a result, the efficiency discrepancy between data and MC becomes (0.5±1.2)% and thus consistent with zero. This recipe is therefore recommended to the *BABAR* collaboration for the treatment of the RUN 1 data set.

For very high π^0 energies larger than 3.5 GeV, one can see a dip for $\mathcal{Q}_{DATA/MC}$ in figure 5.6. As the total photon cross section decreases slightly with energy, conversions in extra material discussed above cannot be the explanation for this effect. An occupancy effect can also be ruled out due to the purity and low multiplicity (two tracks, no extra

energetic photon) of all events, independent of π^0 energies. The most likely explanation is the proximity of the two photons in the EMC. The position and energy determination of two photons, split from one single cluster, is known to deteriorate as the distance of the two photons decreases [86]. However, a detailed validation of the description of this effect between data and MC has not been performed, since the only analysis affected is the charm-less B-decay $B^+ \to h'^+ h^0$ with a non-negligible fraction of π^0 energies larger than 3.5 GeV, to which a special treatment has been provided [87].

5.2.6 Systematic Errors

Dependency on Lepton Tag

It has been investigated if there are any dependencies of the results on the lepton tag side, yet the ratio $\mathcal{R}$ does not vary as a function of the lepton energy E_{lep} or angle Θ_{lep}. Also, switching off the corrections for the electron PID and mis-ID in the Monte Carlo simulation, the result effectively does not change (from -6.09% to -6.12%). Hence, there is no systematic dependence on the lepton tag.

Energy Resolution

If the quality of the EMC calibration is different for data and Monte Carlo, this will have a systematic influence on the result of this study. Comparing the reconstructed and generated photon energies in the simulation, one finds that the average difference $(E_\gamma^{rec} - E_\gamma^{true})$ is $\sim +1\%$ for all photon energies (see figure 5.7). To get an idea of the effect of this calibration uncertainty, all MC π^0-energies were shifted by -1%, which leads to a reduction of the data-MC efficiency discrepancy to -5.4%. A problem arises from the missing knowledge of the calibration uncertainty in real data. As already pointed out in chapter 5.2.4, an energy shift has to be applied to find the systematic

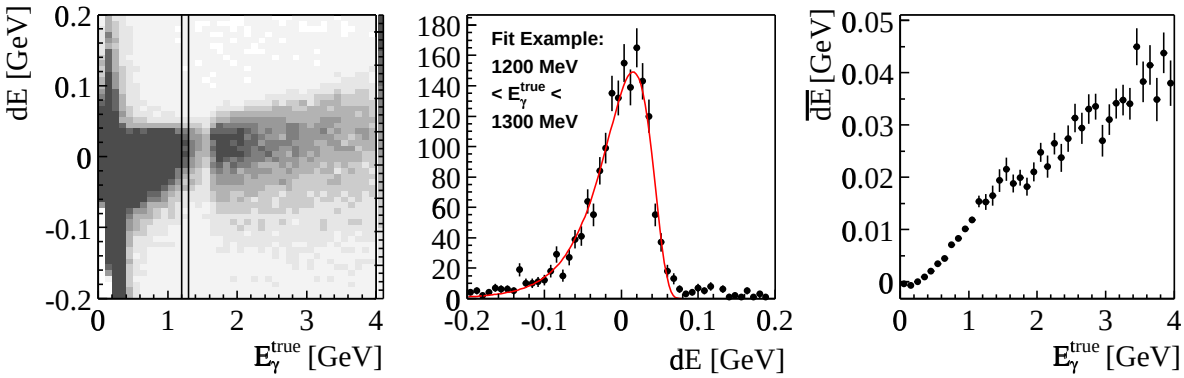

Figure 5.7: *LEFT: The difference between the reconstructed and generated energy* $dE = (E_\gamma^{rec} - E_\gamma^{true})$ *versus* E_{true} *for photons in* $B \to K^*\gamma$ *Monte Carlo. The vertical lines depict the slice used in the MIDDLE: Example of the fit of a Novosibirsk function (equation 4.7) to determine the peak* $\overline{dE}$ *for a given* E_{true}*, in this case for the slice* 1.2 *GeV* $< E_{true} <$ 1.3 *GeV. RIGHT: The peak of the energy shift* $\overline{dE}$ *of the photons as a function of* E_{true} *and with* $\overline{dE}$ *gained by the preceding Novosibirsk-fits.*

error associated with the energy uncertainty. Allowing a π^0-energy shift by $\pm 1\%$, the π^0-efficiency difference varies between -5.4% and -6.9%.

Relative Error on Branching Fractions

Taking into account the relative error of the branching fractions of the one-π^0 and two-π^0 mode [82], one obtains a systematic error of 1.6% on the data-MC efficiency determination in this analysis.

Occupancy effect

Because of the difference of multiplicities in τ and multi-hadron events, the data-MC ratio could be further decreased for $B\overline{B}$ events. The conservative, rough estimate of the systematic error due to this effect is 1.5%.

Difference of EMC Barrel and End-cap

In order to find out the dependency of our results on the polar angle of photons, the same analysis was carried out using only the barrel ($\theta_\gamma > 30^o$) and only the end-cap ($\theta_\gamma < 30^o$). Relying only on the barrel, the data-MC π^0 efficiency difference reduces to $(-5.2 \pm 1.3)\%$. Using solely the end-cap, one obtains $(-17.8 \pm 9.5)\%$. This is another indication that the problem is related to missing material in the simulation since the description of material in the forward region is known to be worse than in the central region of the detector.

Summary of Systematic Errors

The systematic errors discussed in the previous subsections are summarised in table 5.5. Combined with the statistical uncertainty we get a total error of 2.5% per π^0. To find the systematic error in special analyses with single photons, the systematic error should be obtained by varying the killing factor ($2.5\% \pm 1.3\%$) per photon and applying an energy smearing of 1.5%.

Error source	data-MC discrepancy	discrepancy change
PID (lepton tag side)	6.1%	+ 0.0%
Uncertainty of Branching Ratios		± 1.6%
Uncertainty of Energy Calibration	5.4% - 6.9%	- 0.7% + 0.8%
Occupancy effect		± 1.5%
Total		± 2.3%

Table 5.5: *The summary of the systematic errors on the π^0-efficiency correction between real data and Monte Carlo.*

Chapter 6

Determination of the Branching Fractions

In this chapter, the branching fractions are extracted from the sample of events reconstructed in chapter 4. First, the yields are extracted by a simultaneous maximum likelihood fit using information about the background from all available real data samples. Thereafter, the systematic errors are summarised, and finally the results are combined to give the measured values of $\mathcal{B}(B^{\pm} \to K^{*\pm}\gamma)$ and $\mathcal{B}(B^0 \to K^{*0}\gamma)$ making use of the signal efficiencies obtained in chapter 5.

6.1 Background Estimation

The sample of reconstructed $B \to K^*\gamma$ events in the RUN 1 on-resonance data consists of two components; in the M_{ES} distribution there is a signal peak and a background band beneath it (see figure 6.9). As explained in section 4.13.2, the signal is represented by a Novosibirsk function (equation 4.7) for modes containing π^0s and by a Gaussian for the two remaining channels.

6.1.1 Continuum Background Shape

The background is mainly given by continuum $e^+e^- \to q\overline{q}$ events with ISR or a high-energy photon originating from a π^0 as presented extensively in section 4.2. The on-resonance data sideband, off-resonance data, and continuum Monte Carlo data are used to investigate the M_{ES} shape of the background which is supposed to be parametrised by the "*ARGUS*" threshold function [88]:

$$f_{Argus}(M_{ES}) \propto \frac{M_{ES}}{E^*_{beam}} \cdot \sqrt{1 - \frac{{M_{ES}}^2}{{E^*_{beam}}^2}} \cdot exp\left[-\zeta\left(1 - \frac{{M_{ES}}^2}{{E^*_{beam}}^2}\right)\right] \tag{6.1}$$

The first term describes the threshold behaviour while the exponential factor is an empirical model of the drop in background towards smaller masses. From the two possibilities of either fitting the ARGUS shape parameter ζ or constraining it to a value obtained from fits to off-resonance data and continuum Monte-Carlo samples,

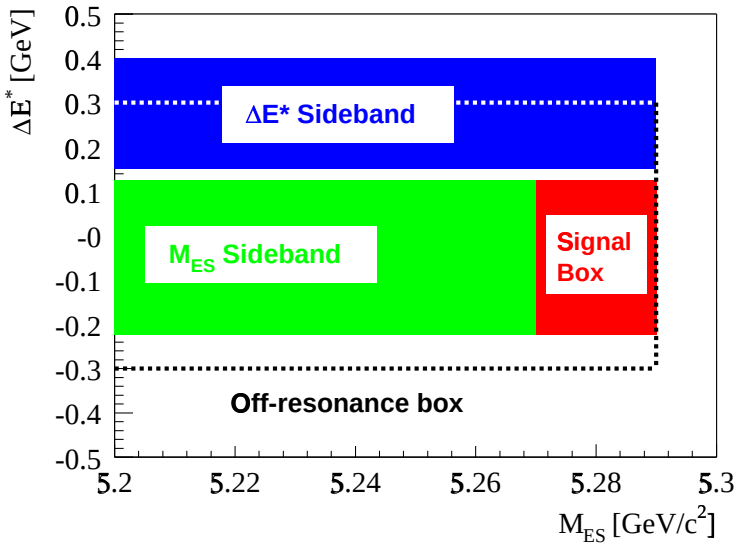

Figure 6.1: *Definition of the signal box, the M_{ES} and ΔE^* sideband, and the region used in off-resonance data for the ARGUS fit to the background shape. The range used for the on-resonance data fit in section 6.3 is the signal box plus the M_{ES} sideband.*

we will adopt the first approach in section 6.3. The threshold $E^*_{beam} = 5.290$ GeV is given by the mean value of the available energy from the beams in the CM frame. For off-resonance data this is an approximation. By comparison to the ARGUS-fit results for ζ using the correct value of $E^*_{beam} = 5.270$ GeV it has been verified that there is no bias on the shape parameter in off-resonance data, solely a shift of the M_{ES} spectrum by 20 MeV/c^2.

The ARGUS shape has been studied independently for various samples in on- and off-resonance data, and continuum Monte Carlo. Figure 6.1 illustrates the definition of the regions and sidebands used for the background fits that have been done to test the stability of the ARGUS shape ζ. Only the upper ΔE^*-sideband is used to avoid bias from leaking signal in the lower ΔE^*-sideband. An example of the unbinned maximum-likelihood fit is shown in figure 6.2 for the $K^{*\pm} \to K^{\pm}\pi^0$ mode in off-resonance data. The fit results for several cuts on the thrust angle α^*_T in on- and off-resonance data, and continuum Monte Carlo are displayed in figure 6.4.

In order to gain statistics, at least in the off-resonance background fit, one can think of removing the requirements on the kaon particle identification. Effectively, this means accepting more mis-identified pions (with the kaon mass assigned to them). The condition for this approach to be valid is the kinematics remaining the same when releasing the PID requirement, i.e. the phase-space distributions of the real and fake kaons should be the same. The two samples are expected to produce the same ARGUS distribution if their momentum spectra match each other. Figure 6.3 proves that within statistics this demand is satisfied. The background fit results with and without kaon PID are shown in figure 6.4 from which several lessons can be learned:

- The ARGUS parameters ζ in on-resonance, off-resonance, and continuum MC agree within errors for each α^*_T cut. The Monte Carlo ζ-values tend to be slightly higher than the shapes in on- and off-resonance data. Therefore, continuum MC data is only deployed to verify the ζ-independence of the PID, yet they will not be used in the determination of the actual *value* of the shape parameter ζ.

- Although the shape parameters ζ are consistent within statistical errors, they seem to depend slightly on the α_T^* cut. Therefore, this cut is not loosened to gain statistics in the background samples of the overall fit (section 6.3).
- The ζ values with and without kaon PID agree in on- and off-resonance data, and in continuum Monte Carlo (here with the most significant statistics) for each α_T^* cut.

We conclude that the kaon PID can be released for off-resonance data to enhance statistics in the fit of the background shape, resulting in a fourfold increase of the event yield for $K^{*0} \to K^+\pi^-$ and even a factor of seven for $K^{*\pm} \to K^\pm\pi^0$. The corresponding systematics are investigated in section 6.3.3.
As a consistency check, in table 6.1 the background-event yields in the M_{ES} sideband of on-resonance data is compared with the expected yields for a sample of 20.7 fb^{-1}from

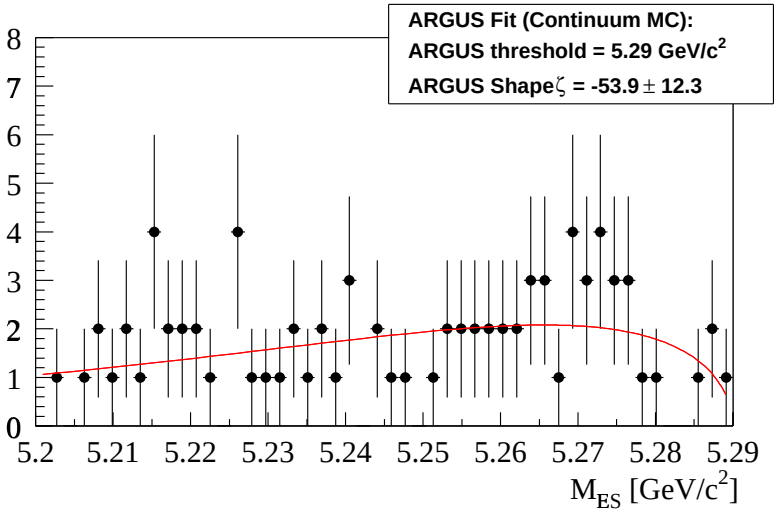

Figure 6.2: *The fit of the ARGUS function to the off-resonance data distribution without PID applied for the kaon.*

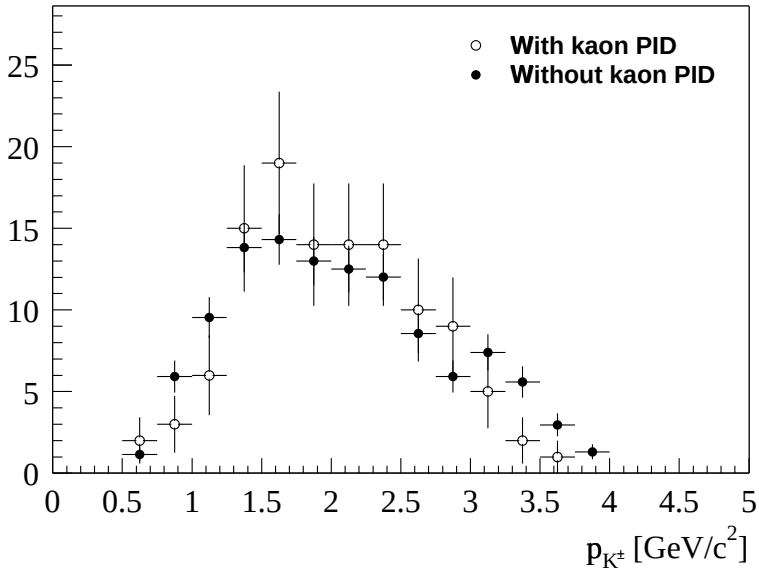

Figure 6.3: *The kaon momenta with PID (filled points) and without PID (hollow, normalised to the total number of events with PID) for the final B selection in the $K^{*\pm} \to K^\pm\pi^0$ mode and continuum Monte Carlo. The M_{ES} range of 5.20 GeV/c^2< M_{ES} <5.29 GeV/c^2 is the one used in the overall fit (section 6.3).*

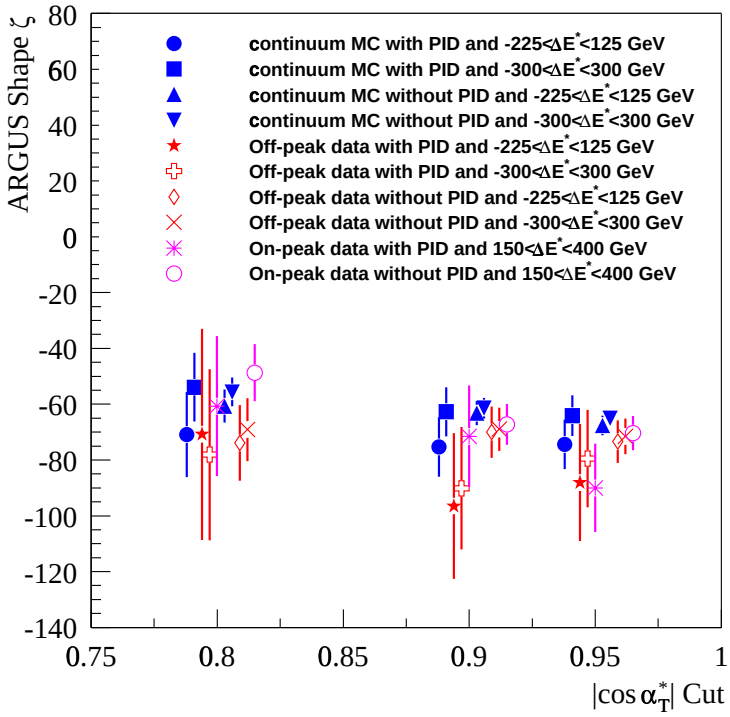

Figure 6.4: *Overview of the fitted ARGUS parameters ζ with and without kaon PID for the background samples in continuum Monte Carlo, off-resonance data, and the ΔE^* sideband in on-resonance data.*

continuum Monte Carlo and off-resonance data. In the $K^{*\pm} \to K^{\pm}\pi^0$ mode, the number of events in on-resonance is slightly higher, nevertheless the agreement is within 1σ for all cases.

6.1.2 Cross- and Down-feed from other $b \to s\gamma$ Modes

There are two further sources of background besides the continuum events presented in 6.1.1; the mis-identification of one decay mode of the $K^*(892)$ resonance as another one is referred to as "*cross-feed*". By "*down-feed*" we label the mis-reconstruction of $B \to K^*\gamma$ decays with higher K^*-resonance states and other processes associated with the $b \to s\gamma$ transition, i.e. $B^{\pm} \to X_{su}\gamma$ and $B^0 \to X_{sd}\gamma$ with final states like $K^+\pi^-\pi^+\gamma$, $K^+\pi^-\pi^0\gamma$, etc.

Quantity	Mode			
	$K^{*\pm} \to K^{\pm}\pi^0$	$K^{*\pm} \to K_S\pi^{\pm}$	$K^{*0} \to K^+\pi^-$	$K^{*0} \to K_S\pi^0$
MC M_{ES}-sideband yield	54.2 ± 9.6	39.0 ± 10.0	239.2 ± 20.0	12.8 ± 5.8
Off-resonance M_{ES}-sideband yield	59.6 ± 21.9	63.7 ± 22.5	207.0 ± 40.6	33.6 ± 16.6
On-resonance M_{ES}-sideband yield	70 ± 8.4	36 ± 6	231 ± 15.2	18 ± 4.2

Table 6.1: *Expected and measured yields of the $B \to K^*\gamma$ modes in the M_{ES}-sideband [5.20 GeV/c^2,5.26 GeV/c^2] in 20.7 fb^{-1}. The predictions are obtained using continuum Monte Carlo and off-resonance data.*

The number of expected cross-feed events in the M_{ES} signal-region for 20.7 fb^{-1} is determined by running the analysis for one $B \to K^*\gamma$ mode on the Monte Carlo samples of the three other decay modes. The signal yields are normalised by the branching fractions multiplied by the appropriate isospin factors. The down-feed is estimated by running on the inclusive $B^+ \to X_{su}\gamma$ and $B^0 \to X_{sd}\gamma$ Monte Carlo samples as well as the exclusively generated higher K^*-resonance modes (see table B.2), assuming that the spectrum of the inclusive hadronic mass $m_{\sum had}$ consists only of resonant $K^*(892)$ below 1.1 GeV/c^2. At this value a cut on $m_{\sum had}$ was thus made at generator level for the Monte Carlo $X_{su}\gamma$ and $X_{sd}\gamma$ samples. The modelling of the $B \to s\gamma$ composition is assumed to be correct in the Ali-Greub model that was used for the generator [89]. The branching fractions are assigned based on the theoretically predicted inclusive branching fraction of $\mathcal{B}(B \to s\gamma) = (3.29 \pm 0.33) \cdot 10^{-4}$ [38] from next-to-leading order calculations that has been confirmed by the CLEO measurement of $\mathcal{B}(B \to s\gamma) = (3.15 \pm 0.35 \pm 0.32 \pm 0.26) \cdot 10^{-4}$ [90]. The individual contributions are assumed to be 16% for the $K^*\gamma(892)$ modes, 19% for higher resonance $K^*\gamma$, and 65% for all other, non-resonant modes modelled in the $X_{su}\gamma$ and $X_{sd}\gamma$ samples.

The expected numbers of cross- and down-feed events in the signal region that will be subtracted from the signal yields in on-resonance data are listed in table 6.2. The composition of these numbers is shown in table E.1 for the example of $B^\pm \to K^{*\pm}\gamma$, $K^{*\pm} \to K^\pm\pi^0$. The systematic uncertainties from the cross- and down-feed subtraction on the $\mathcal{B}(B \to K^*\gamma)$ measurement are estimated taking into account the error on the inclusive $B \to s\gamma$ branching fraction. They are listed in table 6.8.

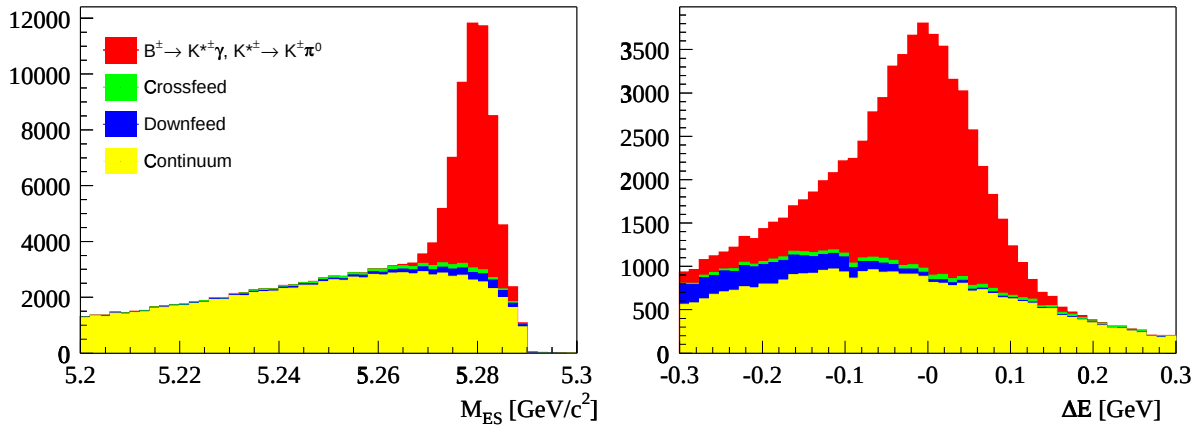

Figure 6.5: *The signal+background composition of the reconstructed $B \to K^*\gamma$ events in the $K^{*\pm} \to K^\pm\pi^0$ mode determined with Monte Carlo data for signal, continuum, and cross-and down-feed (see appendix E). The assumed branching fractions are $3.8 \cdot 10^{-5}$ for $B \to K^*\gamma$ [11], $3.3 \cdot 10^{-4}$ for $b \to s\gamma$ [38] and the $q\overline{q}$ cross-sections in table 3.1. The ΔE^* cut in the M_{ES} distribution on the left is [-0.225 GeV,0.125 GeV] and the M_{ES} cut in the ΔE^* spectrum on the right is [5.27 GeV/c^2,5.29 GeV/c^2]. Each contribution is added on top of the preceding one.*

Quantity	Mode			
	$K^{*\pm} \to K^{\pm}\pi^0$	$K^{*\pm} \to K_S\pi^{\pm}$	$K^{*0} \to K^{+}\pi^{-}$	$K^{*0} \to K_S\pi^0$
Expected cross-feed	1.20±0.22	0.74±0.12	0.44±0.96	0.42±0.09
Expected down-feed	2.63±0.43	1.16±0.19	0.60±0.10	0.96±0.24

Table 6.2: *Expected number of cross- and down-feed events contributing to the $B \to K^*\gamma$ signal yields for the four modes in 20.7 fb^{-1}, estimated by using Monte Carlo data.*

Figure 6.5 shows the expected composition of the signal for M_{ES} and ΔE^* in on-resonance data for the example of $B^{\pm} \to K^{*\pm}\gamma$, $K^{*\pm} \to K^{\pm}\pi^0$, obtained by fitting the shapes of all contributing background modes individually and adding them up according to their relative branching fractions (see table E.1). Possible distortions in the background shape due to cross- and down-feed contributions to the M_{ES} sideband are negligible and thus ignored in the on-resonance fit for the signal yields.

6.2 Energy Resolution in On-Resonance Data

To perform a cross-check and separately fit to the ΔE^* projections of the biplots in figure 4.25, a cut of 5.27 GeV/c^2 $< M_{ES} <$ 5.29 GeV/c^2 is made, corresponding to 3σ in M_{ES}. We obtain the ΔE^* distributions shown in figure 6.6 for the four $B \to K^*\gamma$ modes.
In the fits, the data is described by a Crystal-Ball function (equation 4.13) for the signal plus a background function. Only for the modes containing a π^0, a detailed study on MC data has been carried out to understand the ΔE^* background shape (see below) and thus a more sophisticated double Gaussian for the background is used, whereas for the modes without π^0s, the background is less abundant and its shape is assumed to be represented by a first-order polynomial.
For the modes without π^0s, the fitted ΔE^* peak and width in data are consistent with Monte Carlo, indicating that the calorimeter resolution should be correctly modelled. In the modes involving π^0s, there also is consistency within 1.5 σ, yet the peak-value $\overline{\Delta E^*}$ exhibits a shift of (-35±23) MeV for $K^{*\pm} \to K^{\pm}\pi^0$ and (-26±26) MeV for

Quantity	Mode			
	$K^{*\pm} \to K^{\pm}\pi^0$	$K^{*\pm} \to K_S\pi^{\pm}$	$K^{*0} \to K^{+}\pi^{-}$	$K^{*0} \to K_S\pi^0$
MC $\overline{\Delta E^*}$ [MeV]	2.1±2.4	19.3±4.3	18.1±1.9	1.7±2.6
data $\overline{\Delta E^*}$ [MeV]	-55.3±23.2	-26.6±25.0	0.0±9.7	-46.4±26.1
MC $\sigma_{\Delta E^*}$ [MeV]	56.6±1.7	38.4±2.7	38.5±1.3	57.7±17.3
data $\sigma_{\Delta E^*}$ [MeV]	80.1±20.4	49.0±23.6	47.0±12.2	57.7 fixed

Table 6.3: *The peak $\overline{\Delta E^*}$ and width $\sigma_{\Delta E^*}$ of the energy deficit in signal Monte Carlo and on-resonance data. It has to be beared in mind that the reconstructed energies E_γ in the simulation are known to be $\sim$ 19 MeV too high (see section 4.13.1).*

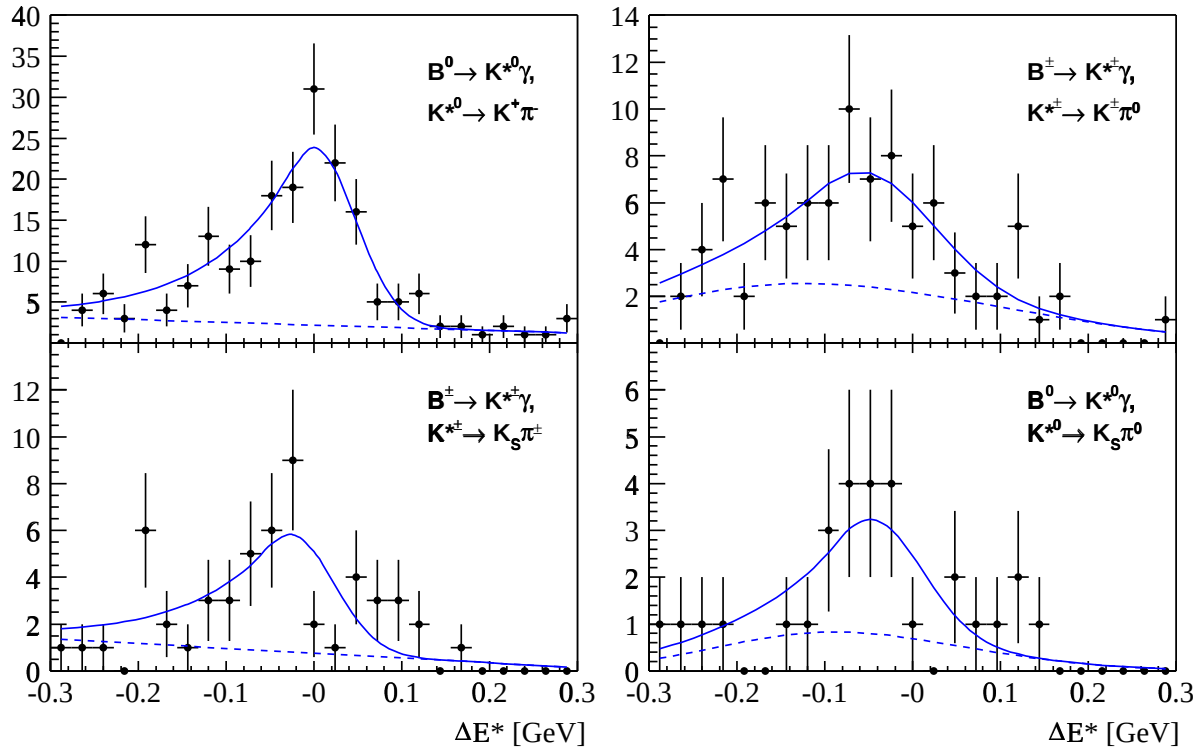

Figure 6.6: *The ΔE^* distributions of the four $B \to K^*\gamma$ modes for 22.7×10^6 B decays in on-resonance data. The accepted M_{ES} window is 5.27 GeV/c^2 < M_{ES} < 5.29 GeV/c^2. The two $B \to K^*\gamma$ modes involving π^0s are on the right and the two other modes on the left. The solid lines indicate the unbinned maximum-likelihood fit of a Crystal-Ball shape for the signal plus a linear function for the background in modes without π^0s, and plus a double Gaussian for the background otherwise.*

$K^{*0} \to K_S\pi^0$ compared to its position expected from Monte Carlo (see section 4.13.1). The reason for a slightly different ΔE^* scale in real data and Monte Carlo could be small uncertainties in the photon energy scale and resolution treated in the following subsection 6.2.1. A *toy Monte Carlo* study has been carried out in order to understand the slight ΔE^* shift. This is a set of random events generated according to a known PDF. In our case the composition of the background is parametrised by continuum, and cross-and down-feed Monte Carlo as presented in appendix E.2. With these parametrisations shown in figure 6.5, 1000 samples are generated with the number of events actually found in on-resonance data for 5.27 GeV/c^2 < M_{ES} <5.29 GeV/c^2. Hereafter, the toy-MC samples are fitted using the same fit function that has been applied to the on-resonance samples in figure 6.6. The probability of finding the observed ΔE^*-shift in a data sample of our size is ≈10%. Cross-checks have been made by cutting tighter on the K^* mass, thereby reducing the number of fake K^* candidates, and using a narrower M_{ES} window, resulting in a cleaner $B \to K^*\gamma$ sample. The effect in both cases is a vanishing of the ΔE^* shift, supporting the presumption that we are either dealing with a statistical fluctuation or with a deficient modelling of the ΔE^* background spectrum in Monte Carlo, e.g. of the cross- and down-feed. Since changing any cut at this stage of the analysis would be equivalent to being biased by the sample

that is used for the actual $\mathcal{B}(B \to K^*\gamma)$ measurement, in no case this can be an option. A slight ΔE^* shift in real data would lead to a small deviation in the signal efficiency determined by signal Monte Carlo (see section 5.1). To study the corresponding impact on the measurement of the branching fraction (section 6.4.4), the signal ΔE^* window in data is shifted progressively from [-225 MeV,125 MeV] to [-275 MeV,75 MeV]. The variations of the measured branching fractions are entirely consistent with statistical fluctuation and no hint for a systematic effect is found. Hence, any systematic due to a possible ΔE^* shift must be tiny and is covered by the systematic error on the cross- and down-feed modelling and the photon-energy scale (see section 6.2.1).

6.2.1 Photon Energy Scale and Resolution

As noticed above, any uncertainty in the photon-energy scale and resolution will affect the ΔE^* cut in the $B \to K^*\gamma$ analysis.

Symmetric η decays are used [14] to measure the uncertainty in the energy scale. These are η decays in which both photons from the decay are within a given energy range. Deviations of the η mass measured in these events from the nominal PDG-value provide a way to estimate the uncertainty on the photon-energy scale in the respective energy range. No deviation of the photon energy scale larger than 0.5% is observed for any interval of E_γ. The effects of this systematic uncertainty in the energy scale on the signal efficiency is obtained by shifting the photon energy in the signal Monte Carlo simulation by $\pm 0.5\%$ and re-processing the events through the $B \to K^*\gamma$ analysis. No deviation greater than 1.0% is observed in the simulation after application of all selection criteria. We therefore assign 1% as systematic uncertainty on the photon energy scale.

The study in section 5.2 has shown that the π^0 mass spectra are up to 10% broader in real data with respect to Monte Carlo. This effect has also been shown for π^0 and η spectra in hadronic events [86] and thus has to be incorporated as a systematic uncertainty on the energy resolution of the photon reconstruction. The impact of resolution degradation is studied by smearing the reconstructed energy, i.e. artificially widening the resolution of the photon energy with a Gaussian distribution in the signal Monte Carlo events. The impact on the signal efficiency is a smooth drop of efficiency with increased smearing, the overall efficiency deviates by no more than 2.5% with 10% degradation in resolution. As a conservative estimate, this is taken as the systematic uncertainty due to photon energy resolution.

6.3 Estimation of Signal Yield

Projecting the on-resonance ΔE^*-M_{ES}-biplots in figure 4.25 onto the M_{ES} axis, with the ΔE^* cuts of -225 MeV $< \Delta E^* < 125$ MeV in the two modes containing π^0s and -200 MeV $< \Delta E^* < 100$ MeV otherwise, we end up with the M_{ES} distributions shown in figure 6.7.

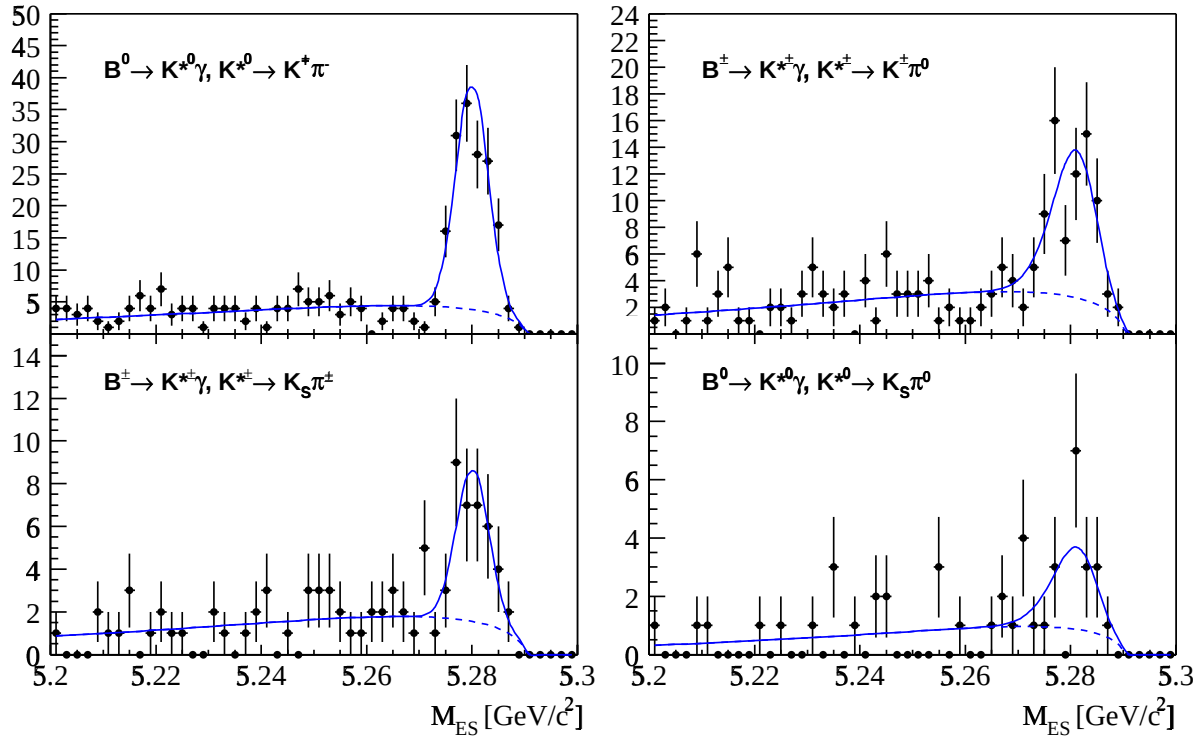

Figure 6.7: *The M_{ES} distributions of the four $B \to K^*\gamma$ modes for 22.7×10^6 B decays in on-resonance data. The two $B \to K^*\gamma$ modes involving π^0s are on the right and the two other modes on the left. The solid lines indicate the unbinned maximum-likelihood fit of an ARGUS function for the background plus a Novosibirsk shape for the signal in modes with π^0s, and plus a Gaussian for the signal otherwise. The simultaneous fit includes not only the on-resonance data, but also the on-resonance ΔE^*-sideband and the off-resonance data. It is illustrated in more detail in figure 6.9.*

6.3.1 The Simultaneous Maximum-Likelihood Fit

To use the maximum available information about the background shape in the determination of the signal yields, we do not solely use the on-resonance signal band but also the on-resonance ΔE^* sideband and the off-resonance data as defined in figure 6.1. No continuum Monte Carlo is used in the simultaneous fit, all information is gained from real data in order to avoid any dependence on the quality of the continuum simulation. An unbinned maximum-likelihood fit based on MINUIT [91] is applied simultaneously to all three samples for each $B \to K^*\gamma$ mode.

Generally, a fit model consists of a normalised *probability density function (PDF)*, $F(\vec{x};\vec{p})$, where the vector $\vec{x}$ represents the data points being fitted and $\vec{p}$ is the set of dependent variables in the PDF parametrising the probability distribution. The variables have a value and an error, and can be floating or fixed in the fit. The corresponding likelihood to be maximised for a sample of events, $\{\vec{x}_i\}_{i=1}^N$, is

$$\mathcal{L}(\vec{p}) = \prod_{i=1}^{N} F(\vec{x};\vec{p}) \tag{6.2}$$

The PDF must be normalised and positive over the range of $\vec{x}$ values covered. The overall PDF can be constructed from basic PDFs like in the example of our on-resonance signal band as the sum $F_{sig} = f_{ARGUS} + f_{Novo}$ of an ARGUS background PDF (equation 6.1) and a Novosibirsk (or Gaussian) signal shape (equation 4.7). For the ΔE^* sideband and off-resonance data, we simply have an ARGUS background shape $F_{side,off} = f_{ARGUS}$.
To fit several independent samples at the same time in order to determine a common set of parameters, the likelihood is factorized into three samples corresponding to the signal band ($\mathcal{L}_{sig}$), the ΔE^* sideband ($\mathcal{L}_{side}$) and the off-resonance data ($\mathcal{L}_{off}$), each of them of the form in equation 7.3. The product of the three individual likelihoods has to be maximised:

$$\mathcal{L}(\vec{p}) = \mathcal{L}_{sig}(\vec{p}) \cdot \mathcal{L}_{side}(\vec{p}) \cdot \mathcal{L}_{off}(\vec{p}) \tag{6.3}$$

with

$$\mathcal{L}_{sig} = \prod_{i=1}^{n} F_{sig}(\vec{x}_i;\vec{p}), \qquad \mathcal{L}_{side} = \prod_{i=1}^{l} F_{side}(\vec{y}_i;\vec{p}), \qquad \mathcal{L}_{off} = \prod_{i=1}^{k} F_{off}(\vec{z}_i;\vec{p}). \tag{6.4}$$

The combined likelihood is expressed in terms of a combined PDF ,$F_{all}(\vec{q};\vec{p})$, as

$$\mathcal{L}_{all}(\vec{p}) = N_{all} \prod_{j=1}^{n+l+k} F_{all}(\vec{q}_j;\vec{p}) \tag{6.5}$$

Here, $\vec{q} = (\vec{x},\vec{y},\vec{z},c)$ is the union of dependent variables used in the three data sets, together with the discrete category index c that represents the type of events being used in the fit, e.g. events from the on-resonance signal ($c = 1$), the sideband ($c = 2$) or the off-resonance background ($c = 3$).
Possible variations in ζ are reflected by the error of the signal fraction returned from the fit. The free parameters determined by the fit are:

- A common ARGUS parameter ζ for all three background shapes
- The signal PDF parameters, i.e. the peak $\overline{M}_{ES}$, width $\sigma_{M_{ES}}$ and tail $\tau_{M_{ES}}$ of the Novosibirsk or Gauss function, which are fixed or floating, depending on the $B \to K^*\gamma$ mode.
- The signal fraction r in the on-resonance PDF given by $r \cdot f_{Novo} + (1-r) f_{ARGUS}$

The signal yield N_{sig} is then extracted using the fitted signal fraction r and the total number of events N_{tot} in on-resonance data:

$$N_{sig} = r \cdot N_{tot}, \qquad \sigma^2(N_{sig}) = N_{tot}^2 \sigma^2(r) + r^2 \sigma^2(N_{tot}) \tag{6.6}$$

The performance of the fit procedure is tested by a toy Monte Carlo study. Generating and fitting many statistically independent samples using the same PDF verifies the technical correctness of the fit engine and provides a robust estimate of the distribution of the fit-parameter errors and their correlations. In our case, 1000 signal-, sideband-, and off-resonance-data samples are generated, respectively, with the PDFs describing

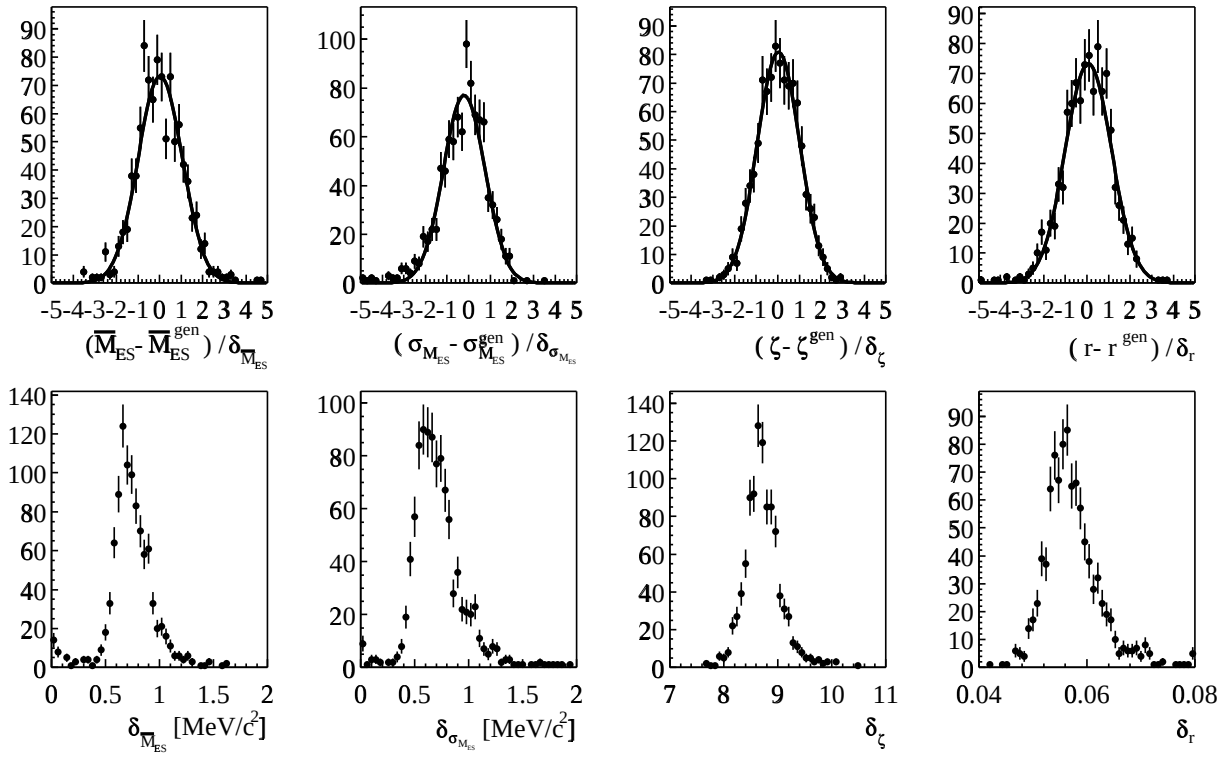

Figure 6.8: *Pull and error distributions of the signal peak $\overline{M}_{ES}$ and width $\sigma_{M_{ES}}$, the ARGUS shape parameter ζ, and the signal fraction r in the toy Monte Carlo study of the $B^{\pm} \to K^{*\pm}\gamma$, $K^{*\pm} \to K^{\pm}\pi^0$ mode, involving 1000 simultaneous $\mathcal{B}(B \to K^*\gamma)$ fits.*

their expected shape and number of events. In the subsequent simultaneous fits of the samples, the same routine as for the real-data fit is used. The distributions of the pulls and fit errors in figure 6.8 demonstrate that the fit reproduces the generated events in the desired way; the pull of a measured variable x_{fit} with respect to the generated x_{gen} is given by $(x_{fit} - x_{gen})/\delta_x$ and should have a normal distribution with a width of one if a fit is reasonable and errors are estimated correctly. This pull consistency has been verified for all fitted variables. The errors in the real data fit for the branching fractions are in the typical range predicted by the Monte Carlo study for all parameters, including the signal fraction.

The small cross- and down-feed contributions (see section 6.1.2) are not fitted but the expected number of those events is subtracted from the fitted data signal yield in table 6.4 to extract the final signal yields stated in table 6.7. The systematics due to this are estimated in section 6.3.2.

The simultaneous fit of an ARGUS-plus-Novosibirsk function for the extraction of the signal yield is shown in figure 6.9 for the example of the mode $B^{\pm} \to K^{*\pm}\gamma$, $K^{*\pm} \to K^{\pm}\pi^0$. The smaller statistics are in a certain mode, the more parameters have to be fixed to the value expected from Monte Carlo to allow the fit to converge and to obtain physically meaningful results. The covariance matrices corresponding to the fits of all four $B \to K^*\gamma$ modes shown in figure 6.7 are given in appendix E.3.

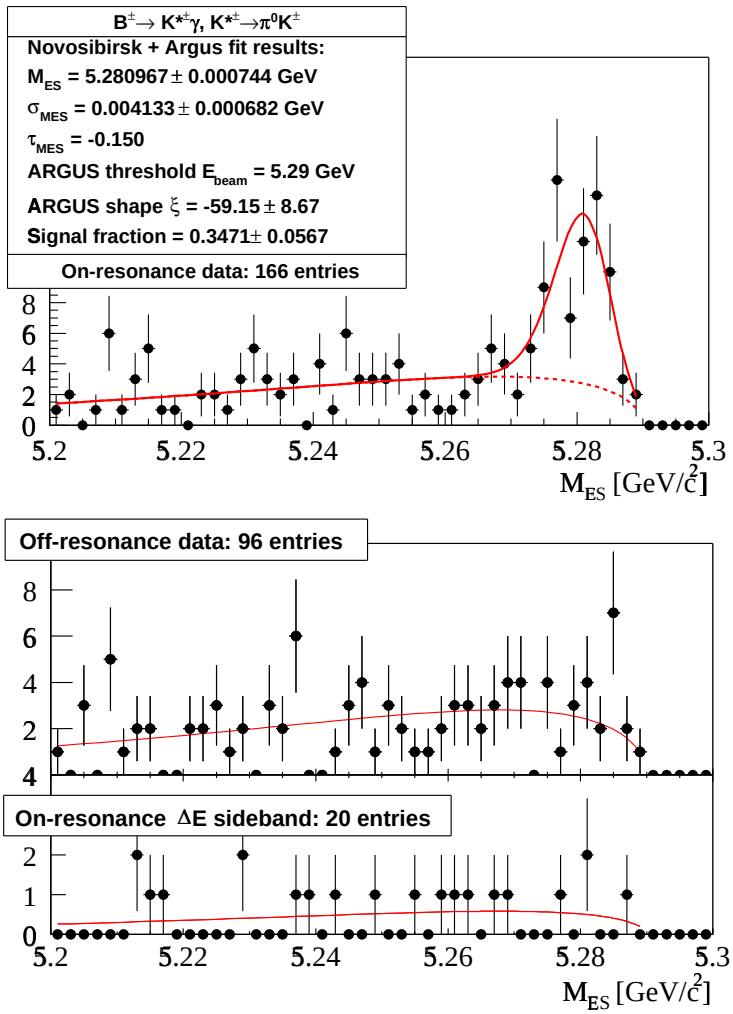

Figure 6.9: *The simultaneous unbinned maximum-likelihood fit of the ARGUS+Novosibirsk function to the M_{ES} distributions of the example of the $K^{*\pm} \to K^{\pm}\pi^0$ mode. Besides the on-resonance signal band (TOP), also the off-resonance data (MIDDLE) and on-resonance ΔE^* sideband (BOTTOM) are used to constrain the background shape in the simultaneous fit. The box displays the parameters determined by the simultaneous fit.*

Quantity	Mode			
	$K^{*\pm} \to K^{\pm}\pi^0$	$K^{*\pm} \to K_S\pi^{\pm}$	$K^{*0} \to K^{+}\pi^{-}$	$K^{*0} \to K_S\pi^0$
MC $\overline{M}_{ES}$ [MeV]	5279.72±0.10	5279.31 ± 0.05	5279.52 ± 0.04	5280.19±0.11
data $\overline{M}_{ES}$ [MeV]	5280.9±0.7	5280.2 ± 0.8	5280.0 ± 0.3	5281.1±1.5
MC $\sigma_{M_{ES}}$ [MeV]	3.44 ± 0.05	2.54 ± 0.03	2.51 ± 0.03	3.52 ± 0.05
data $\sigma_{M_{ES}}$ [MeV]	4.13±0.68	3.08 (fixed)	3.05 ± 0.23	4.19 (fixed)
MC $\tau_{M_{ES}}$ [MeV]	-0.15±0.02	-	-	-0.17±0.02
data $\tau_{M_{ES}}$ [MeV]	-0.15 (fixed)	-	-	-0.17 (fixed)
data ζ [MeV]	-59.2±8.7	-56.1 ± 12.5	-53.6 ± 6.2	-70.8±21.8
data yield [MeV]	57.61±10.42	28.06 ± 6.57	135.71 ± 13.27	14.77±5.58

Table 6.4: *The peak $\overline{M}_{ES}$, width $\sigma_{M_{ES}}$ and tail $\tau_{M_{ES}}$, furthermore ARGUS background shape parameter ζ in signal MC and on-resonance data. The fitted signal yield is the one before subtraction of the cross- and down-feed estimated in table 6.2. The fixed width $\sigma_{M_{ES}}$ in the low-statistics modes is determined by scaling the MC value with the beam energy spread of ∼20%, extracted from the high-statistics modes.*

In table 6.4, the parameters of the fit in on-resonance data are compared with the expectations from signal Monte Carlo. The fitted $\overline{M}_{ES}$-values agree well with the simulation but the widths $\sigma_{M_{ES}}$ are roughly 20% higher than in Monte Carlo for the two modes with floating $\sigma_{M_{ES}}$. This degradation of M_{ES} resolution has also been encountered in other exclusive B decays in *BABAR* [92, 93]. It is caused by the energy spreads of the LER and HER beams of 2.3 MeV and 5.5 MeV [78], respectively, which are not modelled perfectly. An incorrect tracking-resolution in the simulation can be excluded as the source of the effect; to account for the apparent $\sigma_{M_{ES}}$ broadening, the MC track-resolution would require a scaling by a factor of three, whereas independent tracking studies indicate that the data-MC discrepancy is at most 15% [80]. The magnitude of the M_{ES}-peak broadening $\Delta\sigma_{M_{ES}}$ with respect to the simulation can be extracted from the two high-statistics modes $K^{*0} \to K^+\pi^-$ and $K^{*\pm} \to K^\pm\pi^0$ as the difference

$$\Delta\sigma^i_{M_{ES}} = \sqrt{\sigma^i_{M_{ES}}(data)^2 - \sigma^i_{M_{ES}}(MC)^2}, \quad i = \text{with/without } \pi^0 \qquad (6.7)$$

For the lower-statistics modes $K^{*\pm} \to K_S\pi^\pm$ and $K^{*0} \to K_S\pi^0$, the $\sigma_{M_{ES}}(MC)$ is adjusted by adding in quadrature the appropriate $\Delta\sigma_{M_{ES}}$ to provide the fixed width ${\sigma_{fix}}^2 = \sigma_{M_{ES}}(MC)^2 + {\Delta\sigma_{M_{ES}}}^2$ for the fit. The systematic errors associated with pinning down the width is assessed by shifting σ_{fix} between its lower and upper bounds, redoing the fits, and re-extracting the yields. These bounds of σ_{fix} are given by the error on the scaling factor, leading to $\sigma_{fix} = (3.08 \pm 0.21)$ GeV/c^2 for $K^{*\pm} \to K_S\pi^\pm$, and $\sigma_{fix} = (4.19 \pm 0.67)$ GeV/c^2 for $K^{*0} \to K_S\pi^0$.

The tail $\tau_{M_{ES}}$ is fixed to the MC expectation in both modes involving π^0s. To study the systematic uncertainty, the fits are repeated letting $\tau_{M_{ES}}$ float in the physically meaningful region below zero. In both modes, $\tau_{M_{ES}}$ results very close to zero but consistent with the MC values within statistics.

The systematic errors assigned to the M_{ES} shape are 1.1% for the $K^{*\pm} \to K^\pm\pi^0$, 1.9% for the $K^{*\pm} \to K_S\pi^\pm$ mode, and 7.4% for $K^{*0} \to K_S\pi^0$. In the $K^{*0} \to K^+\pi^-$ channel all parameters are floating in the fit.

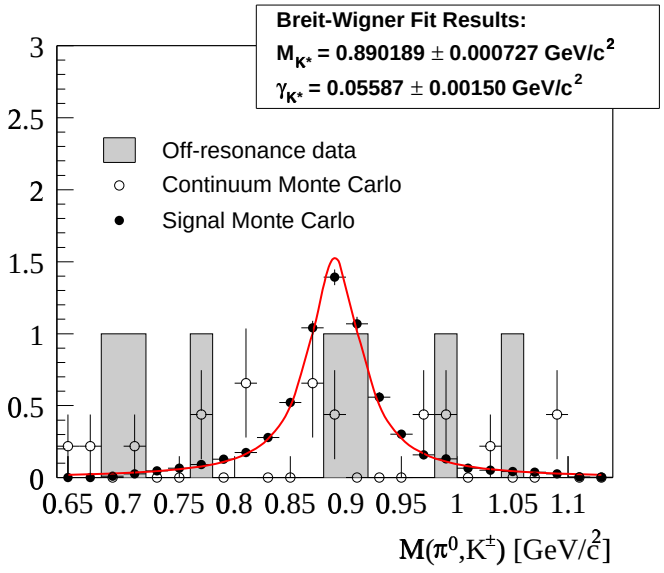

Figure 6.10: *Distributions of the (K, π^0) mass for off-resonance data (solid), continuum MC (hollow points), and $B^\pm \to K^{*\pm}\gamma$, $K^{*\pm} \to K^\pm\pi^0$ signal MC (black points), scaled to off-resonance luminosity (after the fit). The samples correspond to the final B selection in 5.27 GeV/c^2 < M_{ES} < 5.29 GeV/c^2 except for the K^*-mass cut. The fit function to the signal is a simple Breit-Wigner (equation 4.10) since it has been generated with this shape.*

Quantity	Mode			
	$K^{*\pm} \to K^{\pm}\pi^0$	$K^{*\pm} \to K_S\pi^{\pm}$	$K^{*0} \to K^{+}\pi^{-}$	$K^{*0} \to K_S\pi^0$
MC $\overline{m}_{\pi K}$ [MeV]	890.1 ± 0.7	890.9±0.6	895.7 ± 0.4	894.9 ± 0.8
data $\overline{m}_{\pi K}$ [MeV]	876.6 ± 8.5	879.4±7.0	896.1 ± 3.8	883.6±18.7
MC $\Gamma_{m_{\pi K}}$ [MeV]	55.9 ± 1.5	53.2±1.3	52.0 ± 1.0	58.4 ± 1.6
data $\Gamma_{m_{\pi K}}$ [MeV]	83.0 ± 18.7	53.2 (fixed)	65.7 ± 11.8	58.4 (fixed)

Table 6.5: *The fitted K^*-peak $\overline{m}_{\pi K}$ and width $\Gamma_{m_{\pi K}}$ in signal MC and on-resonance data.*

6.3.2 Cross-check of K^* Mass

The $K\pi$-mass spectra are inspected in order to verify that the $B \to K^*\gamma$ signals in on-resonance data can be attributed to the K^* resonance and not originate from non-resonant $K\pi$ combinations. For this purpose, the K^*-mass cut is removed from the analysis, and a 3 σ cut of 5.27 GeV/c^2 $< M_{ES} <$ 5.29 GeV/c^2 is performed instead, spawning the $K\pi$ distributions in figure 6.10 for signal and background Monte Carlo, and in figure 6.11 for on-resonance data. The fit of a relativistic P-wave Breit-Wigner

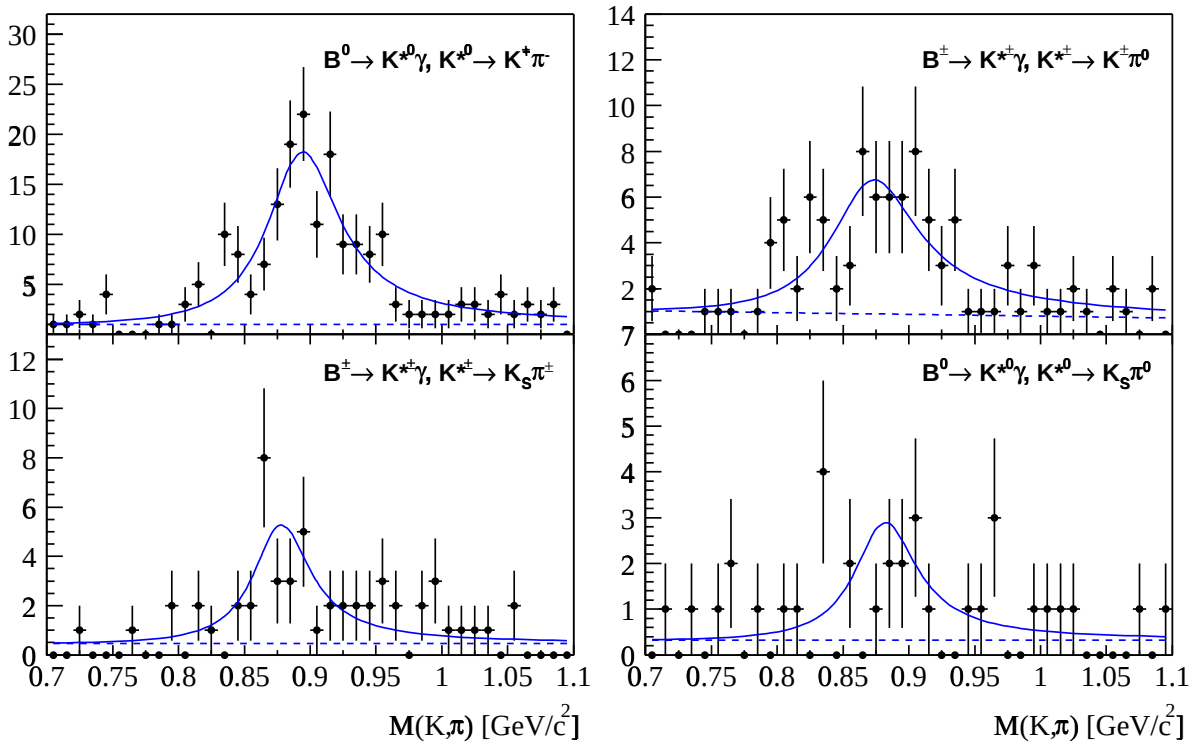

Figure 6.11: *The K^*-mass distributions of the four $B \to K^*\gamma$ modes for 22.7×10^6 B decays in on-resonance data. The two $B \to K^*\gamma$ modes involving π^0s are on the right and the two other modes on the left. The solid lines indicate the unbinned maximum-likelihood fit of a relativistic P-wave Breit-Wigner with Blatt-Weisskopf barrier functions (equ.4.9) plus linear background. The width of the distribution is fixed for the low statistics modes $K^{*\pm} \to K_S\pi^{\pm}$ and $K^{*0} \to K_S\pi^0$.*

with Blatt-Weisskopf barrier functions (equation 4.9) plus linear background to the $K\pi$ distribution confirms the provenience of the signal from the resonance $K^*(892)$. The fitted K^*-mass peak and width specified in table 6.5 are consistent with the signal Monte Carlo within 1.5 σ. Cross- and downfeed background contributions have been neglected in this crosscheck.

6.3.3 Systematics of Background Subtraction

The extraction of the signal yield involves a simultaneous fit to the background in on-and off-resonance data, and yet no systematic has been assigned to this treatment since variations of the shape are taken into account in the statistical error on the yield gained by the simultaneuos fit.
The small amount of off-resonance data (approximately 15% relative to the on-resonance data), together with systematic concerns associated with the initial idea of fixing the ζ parameter in the final background subtraction, motivated the study of the variations for ζ in on- and off-resonance data described in section 6.1.1. The particle identification of the $K^{\pm}$ candidate was removed in the off-resonance data in order to improve the statistical precision of the ARGUS parameter, and the effect was studied to ensure that no bias is introduced. The results for ζ from the simultaneous fit are consistent with the ARGUS shape parameters of the control samples shown in figure 6.4.
To estimate the systematic error on dropping the kaon PID in off-resonance data, the global fit is redone with an offset $\zeta \pm \Delta\zeta$ in the ARGUS PDF of the off-resonance data. Whereas for the central values of the yield and their statistical errors we only use real data samples and do not rely on simulated background, for the evaluation of this systematic uncertainty we take advantage of the higher statistics in continuum Monte Carlo compared to off-resonance data; we calculate $\Delta\zeta$ from the statistical uncertainty of the PID/no-PID values of ζ:

$$\Delta\zeta_i = \sqrt{\sigma_{\zeta_i}^{PID^2} + \sigma_{\zeta_i}^{noPID^2}} \qquad \text{with} \qquad i = K^{*\pm} \to K^{\pm}\pi^0, K^{*0} \to K^+\pi^- \tag{6.8}$$

The re-extracted yields with positive and negative offset $\Delta\zeta$ in the fit are given in table 6.6. Based on the observed deviation of the yields, a systematic error of 3.8% is assigned to the $K^{*\pm} \to K^{\pm}\pi^0$ mode, and 1.0% for $K^{*0} \to K^+\pi^-$.

Off-resonance ARGUS shape	ζ_i	$\zeta_i + \Delta\zeta_i$	$\zeta_i - \Delta\zeta_i$
yield for $i = K^{*\pm} \to K^{\pm}\pi^0$	57.6±10.4	55.3±10.5	59.8±10.9
yield for $i = K^{*0} \to K^+\pi^-$	135.71±13.27	133.50±13.3	137.8±13.21

Table 6.6: *The fitted signal yields for different ARGUS offset parameters* $\Delta\zeta$.

6.4 Results for the Branching Fraction

Having ultimately collected all ingredients needed for the determination of the branching fractions, the individual $\mathcal{B}(B \to K^*\gamma)$ measurements can now be computed and,

together with the total systematic errors, be combined to yield the overall results for the neutral and charged B decays.

6.4.1 Individual Results

The individual branching fraction measurements are calculated by:

$$\mathcal{B}(B \to K^*\gamma) = \frac{N_{sig}}{N_{B\overline{B}} \cdot \epsilon_{sig} \cdot \mathcal{B}(K^*)} \tag{6.9}$$

where the involved quantities that are listed in table 6.7 are:

- The signal yield N_{sig} observed in on-resonance data.
- The signal reconstruction efficiency ϵ_{sig} determined in section 5.1.
- The isospin factor $\mathcal{B}(K^*)$, i.e. the branching fraction for the particular mode, i.e. the relative branching fraction of the K^* meson. For example, in the $K^{*0} \to K_S\pi^0$ mode we have $\mathcal{B}(K^{*0} \to K^0\pi^0) = 1/3$ for the branching fraction of the K^*, and half of the K^0 mesons decay as K^0_S. Furthermore, the branching fraction for the K_S decay is $\mathcal{B}(K^0_S \to \pi^+\pi^-) = (68.6 \pm 0.28)\%$ [37], leading to an overall value of 11.4%.
- The number $N_{B\overline{B}}$ of $B\overline{B}$ pairs recorded by *BABAR*. $N_{B\overline{B}}$ is measured by a method applying hadronic event selection criteria, which makes the assumption that the increase in the ratio of hadronic events to muon pairs between on- and off-resonance data is due to $\Upsilon(4S)$ production [64]. For the 20.7 fb^{-1} in RUN 1, the number of $B\overline{B}$ pairs produced was $(22.74\pm0.36)\times10^6$, assuming a ratio of $B^0\overline{B}^0$ to B^+B^- decays of the $\Upsilon(4S)$ of $f_0/f_+ \approx 1$. The relative systematic error on $\mathcal{B}(B \to K^*\gamma)$ from $N_{B\overline{B}}$ is 1.6%.

Mode	N_{sig}	ϵ_{sig}	$\mathcal{B}_{K^*}$	branching fraction $[10^{-5}]$
$K^{*\pm} \to K^\pm\pi^0$	53.78±10.43	12.86±0.25	0.333	$5.52 \pm 1.07(stat) \pm 0.38(sys)$
$K^{*\pm} \to K_S\pi^\pm$	26.16 ± 6.57	17.2±0.3	0.222	$3.01 \pm 0.76(stat) \pm 0.21(sys)$
$K^{*0} \to K^+\pi^-$	134.71 ± 13.27	21.0±0.4	0.667	$4.24 \pm 0.41(stat) \pm 0.22(sys)$
$K^{*0} \to K_S\pi^0$	13.40±5.59	12.57±0.24	0.114	$4.10 \pm 1.71(stat) \pm 0.42(sys)$

Table 6.7: *The final signal yields N_{sig}, signal reconstruction efficiencies ϵ_{sig}, isospin factors $\mathcal{B}(K^*)$, and the individual results for the branching fractions of the four $B \to K^*\gamma$ modes, obtained using equation 6.9. The statistical uncertainties originate from the statistical errors in the signal yields. The systematic errors are the total uncertainties from table 6.8.*

6.4.2 Summary of Systematics

Along with the description of the reconstruction, the cuts, and the signal fit of the analysis, the corresponding systematic uncertainties have been treated in parallel throughout this work. Table 6.8 delivers the summary of all systematics on the measurement of the branching fractions and the overall systematic errors for the four $B \to K^*\gamma$ modes, obtained by combining the individual errors in quadrature.

Section	Uncertainty	Mode					
		$K^+\pi^0$ Error [%]	$K_S\pi^+$ Error [%]	Error of $K_S\pi^+$ and $K^+\pi^0$ correlated?	$K^+\pi^-$ Error [%]	$K_S\pi^0$ Error [%]	Error of $K^+\pi^-$ and $K_S\pi^0$ correlated?
6.3.1	M_{ES} Line Shape	1.9	1.7	no	-	7.4	no
6.3.3	Background Shape	3.8	-	no	1.0	-	no
6.1.2	Cross-Feed Modelling	1.2	1.0	no	1.0	1.5	no
5.1.2	Kaon Identification	1.0	-	no	0.7	-	no
5.1.1	$K^\pm/\pi^\pm$ Track Efficiency	1.3	1.2	no	2.4	-	no
5.1.3	K_S Efficiency	-	4.5	no	-	4.5	no
5.1.4	Photon Efficiency	1.3	1.3	yes	1.3	1.3	yes
4.7.2	Photon Distance Cut	2.0	2.0	yes	2.0	2.0	yes
5.1.4	π^0 Efficiency	2.5	-	no	-	2.5	no
4.7.2	π^0/η veto	1.0	1.0	yes	1.0	1.0	yes
6.2.1	Energy Resolution	2.5	2.5	yes	2.5	2.5	yes
6.2.1	Energy Scale	1.0	1.0	yes	1.0	1.0	yes
5.1	MC Statistics	2.1	1.5	no	1.9	2.4	no
6.4.1	Number of $B\overline{B}$	1.6	1.6	yes	1.6	1.6	yes
	Total	7.0	6.7		5.3	10.3	

Table 6.8: *The summary of the relative systematic uncertainties in the measurement of the branching fraction $\mathcal{B}(B \to K^*\gamma)$ for the four covered modes.*

6.4.3 Combination of the Results

The appropriate format of presenting the branching fraction measurements is to give combined results for $\mathcal{B}(B^0 \to K^{*0}\gamma)$ and $\mathcal{B}(B^\pm \to K^{*\pm}\gamma)$ since the individual values for the charged and neutral $B \to K^*\gamma$ decay agree within 1σ. The errors of the individual measurements are partially correlated, which is taken into account by using the complete covariance matrix that consists of three components: the diagonal matrix of the statistical errors, the diagonal matrix of the uncorrelated systematic errors, and the non-diagonal matrix of the correlated systematic errors. The combination technique is elucidated in detail in appendix E.5.

The result for the branching fraction of the charged B decay is:

$$\mathcal{B}(B^\pm \to K^{*\pm}\gamma) = (3.83 \pm 0.62 \pm 0.22) \cdot 10^{-5}$$

The value for the branching fraction of the neutral B decay is:

$$\mathcal{B}(B^0 \to K^{*0}\gamma) = (4.23 \pm 0.40 \pm 0.22) \cdot 10^{-5}$$

The calculation of the decay-rate asymmetry $\Delta_{0\pm}$ in the neutral and charged case, $\Gamma(B^0 \to K^{*0}\gamma) = \mathcal{B}(B^0 \to K^{*0}\gamma)/\tau_{B^0}$ and $\Gamma(B^\pm \to K^{*\pm}\gamma) = \mathcal{B}(B^\pm \to K^{*\pm}\gamma)/\tau_{B^\pm}$, is performed according to equation 2.36 and yields:

$$\Delta_{0\pm}(B \to K^*\gamma) = 0.082 \pm 0.094 \pm 0.028$$

Here, the PDG values of $\tau_{B^\pm} = (1.548 \pm 0.032) \cdot 10^{-12} s$ and $\tau_{B^\pm} = (1.653 \pm 0.028) \cdot 10^{-12} s$ have been used [37]. The determination of the statistical and systematic uncertainty on $\Delta_{0\pm}$ using the covariance matrices of the statistical and systematic errors of the four $\mathcal{B}(B \to K^*\gamma)$ modes is explained in appendix E.5.

Comparison to Existing Measurements

There are two further measurements of $\mathcal{B}(B \to K^*\gamma)$ besides the results presented here; the first has been realized by CLEO [11] and the second is by the BELLE collaboration [94] (see table 6.9). The branching fraction from this study is entirely consistent with both experiments but contains smaller uncertainties in both $B \to K^*\gamma$ modes. The values of the world average for $\mathcal{B}(B^\pm \to K^{*\pm}\gamma)$ and $\mathcal{B}(B^0 \to K^{*0}\gamma)$, calculated as the weighted mean of the results from the three experiments, are also given in table 6.9. Using these world-average branching fractions to calculate the world-average decay-rate asymmetry leads to a value of $\Delta_{0\pm}(B \to K^*\gamma) = 0.11 \pm 0.07$.

	$\mathcal{B}(B^\pm \to K^{*\pm}\gamma)$	$\mathcal{B}(B^0 \to K^{*0}\gamma)$
CLEO	$(3.76^{+0.89}_{-0.83} \pm 0.28) \cdot 10^{-5}$	$(4.55^{+0.72}_{-0.68} \pm 0.34) \cdot 10^{-5}$
BELLE	$(3.89 \pm 0.93 \pm 0.41) \cdot 10^{-5}$	$(4.96 \pm 0.67 \pm 0.45) \cdot 10^{-5}$
BABAR	$(3.83 \pm 0.62 \pm 0.22) \cdot 10^{-5}$	$(4.23 \pm 0.40 \pm 0.22) \cdot 10^{-5}$
World average	$(3.82 \pm 0.47) \cdot 10^{-5}$	$(4.44 \pm 0.35) \cdot 10^{-5}$

Table 6.9: *The $\mathcal{B}(B \to K^*\gamma)$ measurements of the CLEO, BELLE, and BABAR collaboration. The world average is given by the weighted mean of the three experiments, assuming no correlations.*

6.4.4 Interpretation of the $\mathcal{B}(B \to K^*\gamma)$ Measurements

The measured decay fractions of $B \to K^*\gamma$ are roughly 40-50% smaller than the central values of the most recent predictions by Bosch & Buchalla [7] and Beneke [8] presented in section 2.3. Unfortunately the uncertainties of the calculations, which are due to the lack of knowledge about the involved form factors and remaining scale dependences, are of the same order as the discrepancy between theory and experiment itself, and hence one order of magnitude larger than the experimental errors. This renders a definite conclusion about the validity of the SM impossible. Nevertheless, the measured magnitude and sign of the asymmetry between the neutral and charged decay rate meets the theoretical value stated by Kagan & Neubert [9] within a small fraction of the theoretical and experimental uncertainties.

Several hypotheses may explain the difference between the theoretically predicted and experimentally observed decay rates:

- The first possibility is a modification of the SM at short distances that would result in a smaller value of the most important Wilson coefficient $|C_7|$. However, this is almost ruled out by the agreement between theory and experiment in the inclusive decay rate $b \to s\gamma$. It also appears implausible that any new interactions would only modify the spectator quark scattering and not show up in the inclusive rate. The explanation must hence be sought in the understanding of the QCD effects, but most of the NLO enhancement is related to the non-factorizable form-factor-type correction which also appears in a nearly identical form in the inclusive decay, and therefore cannot be simply dismissed without putting the agreement for the inclusive decay into question.
- A second scenario is to invoke a large $1/m_b$ correction to the heavy-quark limit that would render the current predictions less reliable. Given the smallness of the non-factorizable hard scattering correction, it is not obvious how such a large dynamical enhancement of $1/m_b$ terms could be explained, particularly since large $1/m_b$ corrections known such as large weak annihilation contributions are absent for decays into vector mesons. One therefore has to consider seriously the possibility that the form factors at small q^2, which are still needed, are substantially different from what they are assumed to be in the QCD sum rule approach or in quark models.

Chapter 7

Extraction of the CP Asymmetry

The search for direct CP violation in penguin decays of B mesons like $B \to K^*\gamma$ is a very promising field to look for non-standard physics since, as pointed out in section 2.3.3, only in models beyond the Standard Model CP asymmetries A_{CP} larger than 1% are conceivable. After the definition of A_{CP}, the background is first examined for asymmetric effects before the asymmetry of the signal is extracted by a simultaneous extended maximum-likelihood fit. The chapter concludes with the investigation of systematic uncertainties and the presentation of the measured A_{CP}-values.

7.1 Definition of the CP Asymmetry

To search for direct CP violation, the asymmetry A_{CP} is defined at quark level by the rates Γ. The rates are directly proportional to the measured number of events since the B life-times are believed to be the same for the CP-conjugate states:

$$A_{CP} = \frac{\Gamma(b) - \Gamma(\overline{b})}{\Gamma(b) + \Gamma(\overline{b})} \tag{7.1}$$

Therefore, at meson level with $B^- = \overline{u}b$, $\overline{B}^0 = \overline{d}b$, $B^+ = u\overline{b}$, and $B^0 = d\overline{b}$ we get with the rates Γ of $B \to K^*\gamma$ decays and the CP conjugate decays:

$$\begin{aligned} A_{CP}^{\pm} &= \frac{1}{1-2\eta}\frac{\Gamma(B^- \to K^{*-}\gamma) - \Gamma(B^+ \to K^{*+}\gamma)}{\Gamma(B^- \to \overline{K}^{*-}\gamma) + \Gamma(B^+ \to K^{*+}\gamma)} \\ A_{CP}^{0} &= \frac{1}{1-2\eta}\frac{\Gamma(\overline{B}^0 \to \overline{K}^{*0}\gamma) - \Gamma(B^0 \to K^{*0}\gamma)}{\Gamma(\overline{B}^0 \to \overline{K}^{*0}\gamma) + \Gamma(B^0 \to K^{*0}\gamma)} \end{aligned} \tag{7.2}$$

Here η is the mis-tag rate, e.g. the fraction of $B^0 \to K^{*0}\gamma$ reconstructed as $\overline{B}^0 \to \overline{K}^{*0}\gamma$ and vice-versa. The asymmetry in both charged $B^\pm \to K^{*\pm}\gamma$ modes and the neutral mode with $K^{*0} \to K^+\pi^-$ is measured. The channel with $K^{*0} \to K_S\pi^0$ cannot be used since no distinction is possible between the decays of the CP eigenstates B^0 and $\overline{B}^0$. The mis-tag rate η is estimated from Monte Carlo to be $\eta < 0.003$ for all modes, resulting in a negligible correction smaller than 1.006 to the measured asymmetry. The unimportance of this effect is the merit of the low kaon- and pion-misidentification rate provided by the DIRC (see section 4.5.3).

7.2 Fit of Signal Asymmetry

Before extracting the signal asymmetry in on-resonance data, the background is investigated for asymmetric effects in the on-resonance sidebands and the off-resonance data (see figure 6.1), but also in the continuum and signal Monte Carlo in order to validate the *CP* symmetry of the reconstruction code. The background asymmetries are obtained from the yields by simply counting events and using equation 7.2. For all test samples they are consistent with zero. The A_{CP} values for off-resonance data are listed in table 7.1. Also, the background shapes ζ for the reconstructed conjugate B mesons and their *CP*-conjugate partners are fitted individually and turn out to agree within statistical errors.
Since there are no asymmetric effects in the background samples, the central value of the signal asymmetry is evaluated under the assumption that the background is C-symmetric with possible small effects only coming from detector asymmetries that are covered by the systematic error on A_{CP} from tracking and PID (see section 7.3).

7.2.1 The Simultaneous Extended Maximum Likelihood Fit

The *CP*-violating charge asymmetry, $A_{CP}(B \to K^*\gamma)$ is extracted via a simultaneous unbinned extended maximum-likelihood fit [95] that determines the total signal yield and its asymmetry between the conjugate-B decays. Here, "simultaneous" has two meanings:

- As in the *CP*-averaged fit of the branching fraction measurement, two additional real-data background samples, namely the on-resonance ΔE^* sideband and the off-resonance data, are fitted together with the on-resonance data to determine a common background ARGUS shape parameter ζ for all samples.
- The on-resonance sample is divided into two disjoint sub-samples corresponding to the flavour of the B candidates, whose asymmetry is fitted simultaneously.

The likelihood introduced in section 6.3.1 with the normalised PDF only measures the probability of getting the measured shapes and signal fractions from the distributions of the dependent variables in a sample of events, assuming that the total number of expected events is independent of the parameter values. But in this case of the A_{CP} fit we have two signal samples which are coupled by the fact that we directly fit their signal asymmetry and total signal yield. If we want to determine a parameter corresponding to the expected number of events η, a factor has to be added to the likelihood that describes the probability of observing the actual number of events N, given this parameter η. This probability is given by the Poisson distribution and the likelihood including this factor is referred to as the *extended likelihood* $\tilde{\mathcal{L}}$ which is maximised by the fit:

$$\tilde{\mathcal{L}} = \frac{e^{-\sum_j n_j}}{N!} \prod_{i=1}^{N} \sum_{j=1}^{m} n_j P_j(\alpha_j) \tag{7.3}$$

Here, n_j are the number of events for the j^{th} hypothesis (signal, background). P_j is the total probability for each of these hypotheses which is a function of the vector of

parameters α_j describing each hypothesis. The product runs over the total number of input data points N, and the extended likelihood function contains the relevant Poisson term. The n_j and α_j are the parameters that can be determined by the fit (for the non-extended likelihood fit this applied only for α_j) though some may be fixed absolutely or relative to another parameter.
As in section 6.3.1, the *categories* c are introduced to fit several independent samples at the same time and determine a common set of parameters. c corresponds to the type of events being used in the fit. The overall likelihood has the form of equation 6.5, it is factorised into four samples (instead of three) corresponding to the signal band with separate B and $\overline{B}$ components ($\tilde{\mathcal{L}}^B_{sig}, c = 1$ and $\tilde{\mathcal{L}}^{\overline{B}}_{sig}, c = 2$), the ΔE^* sideband ($\tilde{\mathcal{L}}_{side}, c = 3$), and the off-resonance data ($\tilde{\mathcal{L}}_{off}, c = 4$), each of them of the form in equation 7.3. The two samples of B and $\overline{B}$ candidates in on-resonance data are coupled by the common parameters $N^{tot}_{sig} = N^B_{sig} + N^{\overline{B}}_{sig}$ and $A_{CP}(N^B_{sig}, N^{\overline{B}}_{sig})$. The product of the four individual likelihoods has to be maximised:

$$\tilde{\mathcal{L}}(\vec{p}) = \tilde{\mathcal{L}}^B_{sig}(\vec{p}) \cdot \tilde{\mathcal{L}}^{\overline{B}}_{sig}(\vec{p}) \cdot \tilde{\mathcal{L}}_{side}(\vec{p}) \cdot \tilde{\mathcal{L}}_{off}(\vec{p}) \tag{7.4}$$

For $\tilde{\mathcal{L}}_{sig}$ there are two event hypotheses, leading to $m = 2$. The signal band is represented by a Gaussian or a Novosibirsk distribution and the background, for which an ARGUS function is assumed. For $\tilde{\mathcal{L}}_{side}$ and $\tilde{\mathcal{L}}_{off}$, only the ARGUS threshold shape is used and consequently $m = 1$. In principle, for the latter two data samples themselves there is no need for an extended likelihood as the *normalisation* of these PDFs has no impact on the fit results in the other samples, just the *shape* plays a role. But for technical software reasons of the simultaneous fit together with other samples that need an extended likelihood, also these samples are treated this way. The extended term becomes an overall constant and has no effect on the result.
The free parameters in the fit are:

- The total signal yield N^{tot}_{sig} in on-resonance data for the sum of both samples, B and $\overline{B}$, and the signal asymmetry $A_{CP} = \frac{N^{\overline{B}}_{sig} - N^B_{sig}}{N^{\overline{B}}_{sig} + N^B_{sig}}$.
- A common ARGUS background shape ζ across all four data samples.
- The background yield in the B and $\overline{B}$ samples which is constrained to be identical. This unisonous normalisation means that the background asymmetry is set to zero, based on the *a priori* knowledge that the continuum background is charge-symmetric. Detector-related effects in tracking and particle identification are taken as a separate systematic error in section 7.3.
- The number of background events in the ΔE^* sideband and off-resonance data. Yet, no information about this background normalisation in the ΔE^* sideband and the off-resonance data is used to determine the background yield in the on-resonance signal band; only the ARGUS shape parameter ζ is common.
- The signal PDF parameters, i.e. the peak, width, and tail, which are fixed or floating, depending on the mode. The values of the fixed parameters are those used in the *CP*-averaged fit (see table 6.4). The signal PDF parameters are common, i.e. $\overline{M}_{ES}$, $\sigma_{M_{ES}}$, and $\tau_{M_{ES}}$ are constrained to be the same for the B and $\overline{B}$ samples.

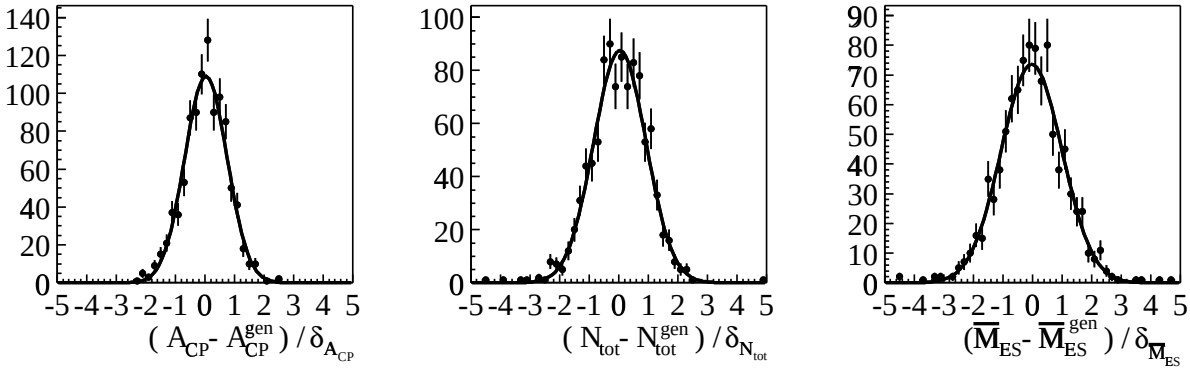

Figure 7.1: *The pull distributions of the* CP *asymmetry A_{CP}, the total signal yield N_{sig}^{tot}, and the signal peak $\overline{M}_{ES}$ in the simultaneous extended likelihood fit. In this example of the toy MC studies, the generated value of A_{CP} is zero.*

The performance of the fit procedure is tested by a toy Monte Carlo study as in the measurement of the branching fraction. One thousand statistically independent data samples are generated and fitted using the same PDF for five different values of A_{CP} between zero and 20%. The pull distributions have been checked for consistency for all fitted variables and are shown for the examples of A_{CP}, N_{sig}^{tot}, and $\overline{M}_{ES}$ in figure 7.1.

A_{CP}-Fit Results

The simultaneous fit of the M_{ES} spectra for the on-resonance *CP*-conjugate B samples are shown in figure 7.2 for the example of the mode $B^{\pm} \to K^{*\pm}\gamma$, $K^{*\pm} \to K^{\pm}\pi^0$,

Quantity	Mode		
	$K^{*\pm} \to K^{\pm}\pi^0$	$K^{*\pm} \to K_S\pi^{\pm}$	$K^{*0} \to K^{+}\pi^{-}$
N_{sig}^{tot}	55.9±10.1	28.1±6.6	135.6±13.3
A_{CP}	0.044±0.155	-0.190±0.210	-0.049±0.094
$\overline{M}_{ES}$ [MeV]	5279.7±0.7	5280.2±0.8	5280.0 ±0.2
$\sigma_{M_{ES}}$ [MeV]	4.09±0.64	3.08 (fixed)	3.06±.23
$\tau_{M_{ES}}$	-0.15 (fixed)	-	-
N_{bkg}^{tot}	110.1±13.6	62.9±8.9	157.4±14.1
A_{CP}^{bkg}	0 (fixed)	0 (fixed)	0 (fixed)
ζ	-59.9±8.5	-53.6±6.2	-53.8±6.2
A_{CP}^{off}	-0.022±0.105	-0.080±0.080	-0.011±0.104

Table 7.1: *The total signal yield N_{sig}^{tot}, signal asymmetry A_{CP}, signal peak $\overline{M}_{ES}$, width $\sigma_{M_{ES}}$ and tail $\tau_{M_{ES}}$, background yield N_{bkg}^{tot}, background asymmetry A_{CP}^{bkg} (fixed to zero), and the ARGUS background shape parameter ζ. Furthermore the asymmetry of the number of events in off-resonance data A_{CP}^{off}.*

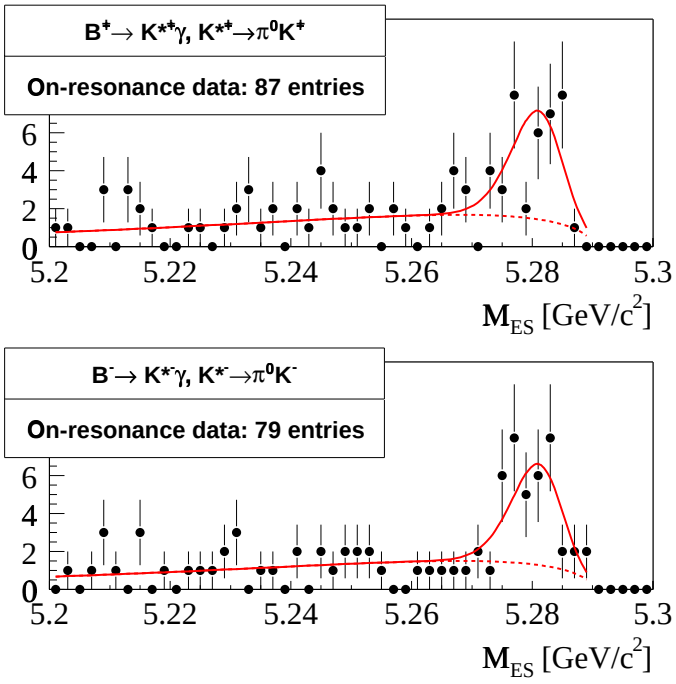

Figure 7.2: *The unbinned maximum log likelihood fit of the ARGUS+Novosibirsk function to the M_{ES} distribution of the positive (TOP) and negative (BOTTOM) on-resonance B sample in the $B^{\pm} \to K^{*\pm}\gamma$, $K^{*\pm} \to K^{\pm}\pi^0$ mode. The fit to the signal asymmetry A_{CP} is done simultaneously and also includes the on-resonance ΔE^* sideband and off-resonance data to constrain the background shape.*

using the fitting method as presented above. Table 7.1 compiles the results for the fitted signal asymmetries A_{CP} for all three modes obtained from the combined fit, as well as the other fit parameters like the M_{ES} shape variables, the ARGUS shape ζ, and the total signal yields, which all turn out to be in agreement with the results from the *CP*-averaged branching fraction measurement (table 6.4). The error matrices of the A_{CP} fits are unveiled in appendix E.4.

7.3 Systematic Uncertainties on A_{CP}

By definition of the asymmetry, most of the systematic effects cancel except for those that are different for positive and negatively charged particles and can hence fake an asymmetry.

After studying possible influence of the assumptions on the signal shape, the systematic effects of the tracking and PID will be assessed; concerning the detector there are many known effects, all of them small, which can cause charge biases. They divide into two broad categories, geometric and matter-interaction effects. Both affect tracking and PID. If the asymmetry arising from these differences alone is A_{sys}, then for small $A_{sys} \ll 100\%$ we can write:

$$A_{obs} = A_{cp} + A_{sys}, \qquad A_{sys} = A_{trk} + A_{pid}, \qquad A_i = \frac{\epsilon_i^+ - \epsilon_i^-}{\epsilon_i^+ + \epsilon_i^-}, \quad i = trk, pid. \tag{7.5}$$

Consequently, equation 7.2 could be non-zero even in the absence of *CP* violation.

Systematics from Assumptions on Signal Shape

As in the case of the $\mathcal{B}(B \to K^*\gamma)$ measurements, certain fit parameters are fixed in the A_{CP} fits by using information from simulated data; the tail parameter $\tau_{M_{ES}}$ of the Novosibirsk signal function is fixed to the Monte Carlo expectation for the $K^{*\pm} \to K^\pm\pi^0$ mode. For the Gaussian width $\sigma_{M_{ES}}$ in the $K^{*\pm} \to K_S\pi^\pm$ mode, the Monte Carlo value is scaled by the spread obtained from the $K^{*0} \to K^+\pi^-$ mode (see section 6.3.1). To conservatively estimate any systematic uncertainty on the A_{CP} measurement that could be due to the fact that we rely on the simulation for certain fit parameters, the fits are redone for $K^{*\pm} \to K^\pm\pi^0$ letting $\tau_{M_{ES}}$ float within the physically meaningful region below zero. In the case of $K^{*\pm} \to K_S\pi^\pm$, the width $\sigma_{M_{ES}}$ is varied within the statistical error on the $K^{*0} \to K^+\pi^-$ data width. The difference in the asymmetry is assigned to the conservative systematic error due to the M_{ES}-shape uncertainty, which comes out as 0.018 for the $K^{*\pm} \to K^\pm\pi^0$ mode and 0.004 for $K^{*\pm} \to K_S\pi^\pm$.

Particle-ID Systematics for A_{CP} Measurement

A potential source of fake *CP*-asymmetries is the PID. Considering the interactions of kaons with material in the detector, the total cross-section for $K^\pm p^+$ scattering is different for positive and negative kaons. A slight charge asymmetry of the kaon-selection efficiency is present below momenta of 1.5 GeV/c [71] and should hence not have considerable impact on our kaons. Nevertheless, possible asymmetries in the kaon PID selection can affect our two modes containing $K^\pm$ mesons and are thus examined, referring to the same slow-pion tagged D^* sample as in the systematic studies for the branching fractions. The asymmetries $A_{pid}^{kaon}(p)$ as a function of momentum are derived from the momentum-dependent PID efficiencies ϵ_i^+ and ϵ_i^- of the positive and negative kaons, respectively. The weighted average and its errors, resulting from the propagated errors on the efficiencies, are:

$$\overline{A_{pid}}(p) = \frac{\sum\limits_{tracks} A_{pid}(p)}{\sum\limits_{tracks}}, \qquad \overline{\delta A_{pid}}(p) = \frac{\sum\limits_{tracks} \delta A_{pid}(p)}{\sum\limits_{tracks}} \tag{7.6}$$

Averaging the results for block 1 and 2 of RUN 1, representing the two different DCH voltage settings of 1900 V and 1960 V, the expected A_{pid} values are compatible with zero. We assign δA_{pid} to the systematic uncertainty due to possible asymmetries in the particle ID criterion, expelling 0.009 for $K^{*\pm} \to K^\pm\pi^0$, and 0.007 for $K^{*0} \to K^+\pi^-$.

Tracking Systematics for A_{CP} Measurement

Discrepancies in the performance of the track reconstruction between positive tracks and negative tracks would directly affect the reconstruction efficiency of $B \to K^*\gamma$ and $\overline{B} \to \overline{K}^*\gamma$ candidates, depending on the analysis, and consequently impact the asymmetry A_{CP}. Such discrepancies must be expected because the detector is composed entirely of electrons, protons, and neutrons and is therefore completely C-asymmetric. The interaction cross-section for mesons with material is charge dependent. Production

Sample	Monte Carlo A_{trk}^{const}	Real data A_{trk}^{const}
Block 1 (1900 V)	$(-0.12 \pm 0.18)\%$	$(-0.35 \pm 0.12)\%$
Block 2 (1960 V)	$(-0.02 \pm 0.12)\%$	$(-0.29 \pm 0.10)\%$

Table 7.2: *The comparison of the overall asymmetry A_{trk}^{const} due to the track reconstruction in real and MC data. The values are based on a study on 3+1 τ events.*

of certain resonances is possible with mesons of one sign, e.g. π^+, while impossible with the other, i.e. π^-.
Other detector-related effects involve geometry; the magnetic field created by the super-conducting solenoid bends positive and negatively charged tracks into opposite directions. Rotational misalignments between the silicon vertex tracker and the drift-chamber will influence the matching of SVT and DCH tracks. The curvature of one sign will artificially be enhanced, yet the curvature of the other sign will be diluted, causing charge-dependent mis-measurement of momentum. Another artifact is produced by the asymmetry of the DCH cells since a different entrance angle of different-sign tracks has an impact on the drift of charge and thus on the hit efficiency in the track reconstruction.

Systematics from Overall Tracking Efficiency

As in the C-averaged case, the tracking efficiencies for differently charged tracks have been studied using 3+1 τ events [81] and an overall asymmetry A_{trk}^{const}, averaged across the entire phase space, has been extracted from the reconstruction efficiencies for positive and negative tracks. The A_{trk}^{const} magnitudes in block 1 and 2 of the RUN 1 data are listed in table 7.2. They are very small, yet statistically significant, and may suggest the presence of effects in real data that are not simulated in Monte Carlo.
In direct CP-violation searches involving final states with unequal numbers of positive and negative tracks like $B^+ \to K^{*+}\gamma$ and its charge conjugate mode, the numbers in table 7.2 translate directly into an asymmetry in the reconstruction efficiency. Based on this study we attribute a systematic uncertainty of 0.5% to the A_{CP} measurement in the charged B-decay modes, which encompasses the apparent but tiny tracking asymmetry as well as its statistical uncertainties. In modes involving an equal number of positive and negative tracks as in $B^0 \to K^{*0}\gamma$, overall tracking asymmetries of this kind have no affect on A_{CP}; the difference in track reconstruction enters the decay in question and its conjugate identically and the effect cancels.

Systematics from Momentum-Dependent Tracking Efficiency

On top of an overall tracking asymmetry there also is a momentum-dependent effect, arising from the different phase-space of the kaons and pions in $B \to K^*\gamma$ (see figure 4.3); the kaon-momentum spectrum is harder than for the pions. Therefore, if the asymmetry of the tracking efficiency varies with track momentum, one expects deviations from the averaged A_{trk}^{const} also for the $K^{*0} \to K^+\pi^-$ mode (where A_{trk}^{const} is zero). The asymmetry at each momentum is quantified by a study on inclusive $K_S \to \pi^+\pi^-$

Section	Systematic Uncertainty	Mode		
		$K^+\pi^-$	$K_S\pi^+$	$K^+\pi^0$
7.3	M_{ES} Line Shape	-	0.004	0.018
7.3	Particle identification	0.007	-	0.009
7.3	Overall Tracking efficiency	-	0.005	0.005
7.3	Momentum dependent Tracking efficiency	0.010	0.010	0.004
	Overall systematic uncertainty	0.012	0.012	0.021

Table 7.3: *The summary of the systematic uncertainties for the measurement of the direct CP-asymmetry A_{CP}.*

decays, providing a clean sample of pion tracks of both signs [14]. Comparing the momentum distributions of the π^+ and π^-, which should be identical in the symmetric decay, allows to quantify any asymmetry of the tracking efficiency at a particular momentum from the distortions of the spectrum of one sign with respect to the other. *Overall* tracking asymmetries cannot be measured with this method since a sample of reconstructed $K_S \to \pi^+\pi^-$ decays contains the same number of reconstructed positive and negative tracks by definition.
Weighting the momentum-dependent A_{trk}-values with the momentum spectra of the respective tracks in the $B \to K^*\gamma$ samples like in equation 7.6 leads to the expected $\overline{A_{trk}}(p)$, motivating the systematic uncertainty of 0.01 for $K^{*0} \to K^+\pi^-$ and $K^{*\pm} \to K_S\pi^\pm$ and 0.004 for $K^{*\pm} \to K^\pm\pi^0$.

7.4 Combined Result for A_{CP}

To finalise the search for direct *CP*-violation, the A_{CP} measurements are completed by adding the overall systematic errors compiled in table 7.3, resulting in the values listed in table 7.4. These data from the individual modes are combined using the same formalism as in section 6.4.3, including the covariance matrices of the statistical and systematic errors. The full covariance matrix is given in appendix E.5. We find the conclusive overall value of

$$A_{cp}(B \to K^*\gamma) = -0.044 \pm 0.076 \pm 0.012,$$

setting with 90% confidence: $-0.17 < A_{cp} < 0.08$.

7.4.1 Interpretation of the A_{CP} Measurement

The measured *CP*-asymmetry is entirely compatible with the small SM-prediction of 0.5% presented in section 2.3.3. It has to be noted that the reason could well be the relatively small number of available signal events. Within these limited statistics, there is no hint for New Physics and some of the most ventured theories predicting large *CP*-asymmetries at a level of 20% can be ruled out already. Yet, various NP scenarios are still within the realms of possibility since there remains enough space for NP models predicting A_{CP} values in the order of 5% as illustrated in section 2.3.3.

Mode	A_{cp}
$A_{cp}(B^{\pm} \to K^{*\pm}\gamma,\ K^{*\pm} \to K^{\pm}\pi^0)$	$0.044 \pm 0.155 \pm 0.021$
$A_{cp}(B^{\pm} \to K^{*\pm}\gamma,\ K^{*\pm} \to K_S\pi^{\pm})$	$-0.190 \pm 0.210 \pm 0.012$
$A_{cp}(B^0 \to K^{*0}\gamma,\ K^{*0} \to K^{+}\pi^{-})$	$-0.049 \pm 0.094 \pm 0.012$
$A_{cp}(B \to K^{*}\gamma)$	$-0.044 \pm 0.076 \pm 0.012$

Table 7.4: *The results for A_{CP} in the individual $B \to K^*\gamma$ modes and the averaged measurement.*

Nevertheless, the establishment of the A_{CP} analysis for the $B \to K^*\gamma$ decay mode bodes well that with the higher integrated luminosity and number of events which will be available to the *BABAR* experiment within the next years, either more and more NP models will be restricted, or flaws within the SM will be uncovered.

Chapter 8

Summary

The Standard Model (SM) of particle physics describes our current knowledge of the fundamental interactions between the elementary particles. One of the major remaining unsolved issues of the SM is the electroweak mixing sector, represented by the CKM matrix, and the origin of the associated *CP*-violation. Rare decays of B mesons can be exploited to over-constrain the Unitary Triangle in order to verify the validity of the SM. The radiative electroweak "penguin" decay $B \to K^*\gamma$, involving the loop transition $b \to s\gamma$, provides the possibility to test the current calculation techniques within the SM and to search for New Physics beyond.

This study of $B \to K^*\gamma$ has been performed within the *BABAR* experiment, located at the e^+e^--storage ring PEP-II at the Stanford Linear Accelerator Center (SLAC), California. The analysis is based upon the data sample recorded by *BABAR* in 1999 and 2000. It consists of an integrated luminosity of 20.7 fb^{-1} at the $\Upsilon(4S)$ resonance ("on-resonance"), corresponding to 22.7×10^6 $B\overline{B}$ meson pairs, and 2.6 fb^{-1} at 40 Mev below this energy ("off-resonance").

The branching fractions have been measured in the two charged modes, $B^\pm \to K^{*\pm}\gamma$, $K^{*+} \to K^+\pi^0$, $K_S\pi^+$, and the two neutral modes $B^0 \to K^{*0}\gamma$, $K^{*0} \to K^+\pi^-$, $K_S\pi^0$, with $K_S \to \pi^+\pi^-$. The neutral candidates are detected by the electromagnetic calorimeter. The reconstruction of tracks is realised by the silicon vertex tracker and the drift chamber, whereas the particle identification relies mainly on the Cherenkov detector, DIRC. Selection criteria are optimised using Monte Carlo simulated data to suppress the abundant background arising dominantly from continuum *udsc* events. The signal efficiency is determined by signal Monte Carlo and corrected for data-MC differences. An unbinned maximum-likelihood fit is performed simultaneously to the reconstructed B-mass distributions of the on- and off-resonance data samples in order to dispose of the maximal available information on the background shape in the extraction of the signal yields. Extensive studies of systematic uncertainties have been carried out for each step of the analysis.

The weighted average of the respective two charged and neutral B decay-modes yields the branching fractions $\mathcal{B}(B^0 \to K^{*0}\gamma) = (4.23 \pm 0.40(\text{stat.}) \pm 0.22(\text{sys.})) \times 10^{-5}$ and $\mathcal{B}(B^\pm \to K^{*\pm}\gamma) = (3.83 \pm 0.62(\text{stat.}) \pm 0.22(\text{sys.})) \times 10^{-5}$, consistent with recent measurements by the CLEO and Belle collaborations [11, 94], yet containing smaller errors. The experimental results have roughly half the size of the central values in current theoretical predictions [7, 8, 9]. Nevertheless they are still consistent within 1 σ_{theo} due

to large theoretical uncertainties σ_{theo}, originating dominantly from the form factors involved in the calculation of QCD-corrections.
A search for direct *CP*-violation has been carried out for the three self-tagging modes with $K^{*+} \to K^+\pi^0$, $K_S\pi^+$ and $K^{*0} \to K^+\pi^-$. For this purpose, the reconstructed B and $\overline{B}$ samples have been separated and their *CP*-violating charge asymmetry A_{CP} has been fitted simultaneously in an extended unbinned maximum-likelihood procedure. Combining the individual modes leads to a *CP*-asymmetry of $A_{CP}(B \to K^*\gamma) = -0.044 \pm 0.076(\text{stat.}) \pm 0.012(\text{sys.})$, constraining the *CP*-violating charge asymmetry to $-0.17 < A_{CP}(B \to K^*\gamma) < 0.08$ at 90% confidence level and being completely compatible with the theoretical SM-prediction of $A_{CP} \approx 0.5\%$ [10].
The results presented here have been accepted as a *BABAR* publication by Physical Review Letters [12]. Moreover, the establishment of the $B \to K^*\gamma$ analysis was the starting point and provided the procedures for a whole program of further analyses of radiative-penguin decays in *BABAR*, which are currently on the way and will lead to more precise results as the integrated luminosity increases.

Furthermore, a comparative study of the π^0-reconstruction efficiency and the π^0-mass peak and width in RUN I data and Monte Carlo simulation has been carried out. The π^0 mesons are gained from $\tau\tau$ 1-on-1 decays containing one or two π^0 mesons. For π^0 energies up to $E_{\pi^0} = 3.5$ GeV, a correction factor of $(-5.0 \pm 2.5)\%$ has been determined for the Monte-Carlo π^0-efficiency . The π^0-mass peak and width have been found to increase from 134.3 MeV/c^2 to 136.2 MeV/c^2 and from 6.5 MeV/c^2 to 8.0 MeV/c^2, respectively, between 1 GeV$< E_{\pi^0} <$4 GeV. Whereas above $E_{\pi^0} = 2$ GeV, data and Monte Carlo agree for the mass peak and width, below $E_{\pi^0} = 2$ GeV the discrepancy is up to 0.5 MeV/c^2 for the π^0-mass peak and 0.5 MeV/c^2 for its width.

Appendix A

Supplement to Theory

A.1 The Pauli Matrices

The Dirac matrices are three linear independent hermitian 2×2 matrices with trace zero:

$$\sigma_1 = \begin{pmatrix} 0 & 1 \\ 1 & 0 \end{pmatrix}, \qquad \sigma_2 = \begin{pmatrix} 0 & -i \\ i & 0 \end{pmatrix}, \qquad \sigma_3 = \begin{pmatrix} 1 & 0 \\ 0 & -1 \end{pmatrix} \tag{A.1}$$

A.2 The Coupling Constants

The electromagnetic interaction is generated by the electromagnetic potential $A^\alpha = (A^0, \vec{A})$. Its propagator is the photon and it is represented by the coupling constant α, which is correlated to the electron charge e.
The weak interaction is generated by the weak fields W^α and B. Its propagators are the $W^\pm$ and Z^0 and it is represented by the Fermi constant G_F, which is correlated to the weak coupling g and the W mass.
The propagators of the strong interaction are the gluons, represented by the strong coupling g_S:

$$\alpha = \frac{e^2}{4\pi}, \qquad \frac{G_F}{\sqrt{2}} = \frac{g^2}{8M_W^2}, \qquad \alpha_S = \frac{g_S^2}{4\pi} \tag{A.2}$$

The fundamental correlation between the electroweak coupling constants and the elementary charge is:

$$e = g' \cos\theta_W = g \sin\theta_W \tag{A.3}$$

The coupling constant g' is connected to g by the weak mixing angle, also called *Weinberg angle* θ_W:

$$\cos\theta_W = \frac{g}{\sqrt{g^2 + g'^2}} \tag{A.4}$$

A.3 Operator Product Expansion

A.3.1 The Effective Vertices

The rules for effective vertices involving an on-shell photon and gluon, and consequently being relevant for $B \to X_s\gamma$, are given in the *t'Hoooft-Feynman (HF)* gauge for the $W^{\pm}$ propagator as follows:

$$\begin{array}{lcl} \overline{s}\gamma' b & = & i\overline{\lambda}_i \frac{G_F}{\sqrt{2}} \frac{e}{8\pi^2} D_0'(x_i)\overline{s}[i\sigma_{\mu\lambda}q^{\lambda}[m_b(1+\gamma_5)]]b \\ \overline{s}G'^a b & = & i\overline{\lambda}_i \frac{G_F}{\sqrt{2}} \frac{e}{8\pi^2} E_0'(x_i)\overline{s}_{\alpha}[i\sigma_{\mu\lambda}q^{\lambda}[m_b(1+\gamma_5)]]T^a_{\alpha\beta}b_{\beta}, \end{array} \tag{A.5}$$

with the CKM factors $\lambda_i = V_{is}^* V_{id}$ and $\overline{\lambda}_i = V_{is}^* V_{ib}$. Here, m_s is set to be zero. Furthermore, the effective vertices depend on the masses of internal quarks or leptons, represented by:

$$x_i = m_i^2/M_W^2, \qquad i = u, c, t \tag{A.6}$$

The basic functions in equation A.5 are explicitly given in dependence on m_t by:

$$\begin{array}{lcll} D_0'(x_t) = & -\frac{(8x_t^3+5x_t^2-7x_t)}{12(1-x_t)^3} + \frac{x_t^2(2-3x_t)}{2(1-x_t)^4}\ln x_t & = 0.244 x_t^{0.30} \\ E_0'(x_t) = & -\frac{x_t(x_t^2-5x_t-2)}{4(1-x_t)^3} + \frac{3}{2}\frac{x_t^2}{(1-x_t)^4}\ln x_t & = 0.145 x_t^{0.19} \end{array} \tag{A.7}$$

A.3.2 The Wilson Coefficients

The Wilson coefficients in the NDR scheme, obtained by matching at scale $\mu_W = M_W$, are given by:

$$\begin{array}{lcl} C_1(M_W) & = & \frac{11}{2}\frac{\alpha_s(M_W)}{4\pi} \\ C_2(M_W) & = & 1 - \frac{11}{6}\frac{\alpha_s(M_W)}{4\pi} \\ C_3(M_W) & = & -\frac{\alpha_s(M_W)}{24\pi}\tilde{E}_0(x_t) \\ C_4(M_W) & = & \frac{\alpha_s(M_W)}{8\pi}\tilde{E}_0(x_t) \\ C_5(M_W) & = & -\frac{\alpha_s(M_W)}{24\pi}\tilde{E}_0(x_t) \\ C_6(M_W) & = & \frac{\alpha_s(M_W)}{8\pi}\tilde{E}_0(x_t), \end{array} \tag{A.8}$$

where

$$\tilde{E}_0(x_t) = -\frac{2}{3}\ln x_t + \frac{x_t(18-11x_t-x_t^2)}{12(1-x_t)^3} + \frac{x_t^2(15-16x_t+4x_t^2)}{6(1-x_t)^4}\ln x_t - \frac{2}{3} \tag{A.9}$$

The relevant Wilson coefficients at scale μ_b are extracted by applying the evolution $C_i(\mu_b) = \sum_j U_{ij}(\mu_b, \mu_W)C_j(\mu_W)$ with $U_{ij}(\mu, \mu_W)$ being an integral over a function of the anomalous dimension $\hat{\gamma}$:

$$\hat{\gamma}(\alpha_s) = \hat{\gamma}^{(0)}\frac{\alpha_s}{4\pi} + \hat{\gamma}^{(1)}\left(\frac{\alpha_s}{4\pi}\right)^2 \tag{A.10}$$

The explicit numerical values of $C_i(\mu_b)$ are given in [29].

A.4 Renormalisation Theory

A.4.1 The Naive Dimensional Regularisation

The Naive Dimensional Regularisation is defined by a set of computational rules. The D-dimensional metric tensor g satisfies:

$$g_{\mu\nu} = g_{\nu\mu}, \qquad g_{\mu\rho}g^{\rho}_{\nu} = g_{\mu\nu}, \qquad g^{\mu}_{\mu} = D \tag{A.11}$$

The Dirac matrices obey:

$$\{\gamma_\mu, \gamma_\nu\} = 2g_{\nu\mu}, \qquad \{\gamma_\mu, \gamma_5\} = 0 \tag{A.12}$$

A.4.2 The Renormalisation Group Equations

The renormalisation group equations are derived using the fact that bare quantities are μ-independent:

$$\begin{array}{lll} \frac{dg(\mu)}{d\ln\mu} = -\epsilon g + \beta(g) & \text{with} & \beta(g) = -g\frac{1}{Z_g}\frac{dZ_g}{d\ln\mu} \\ \frac{dm(\mu)}{d\ln\mu} = -\gamma(g(\mu))m(\mu) & \text{with} & \gamma(g) = \frac{1}{Z_m}\frac{dZ_m}{d\ln\mu} \end{array} \tag{A.13}$$

Appendix B

Used Data

The following real and Monte Carlo data have been used for the $B \to K^*\gamma$ analysis:

B.1 Real Data

The RUN 1data are separated in two blocks for the two Drift-chamber voltage settings of 1900V (Block1) and 1960V (Block2). The list of official chunks is shown in table B.1.

Data set	Run	luminosity $[pb^{-1}]$
1999, Block 1, Chunk 0	On-Resonance	410.061
2000, Block 1, Chunk 0	On-Resonance	607.112
2000, Block 1, Chunk 1	On-Resonance	546.819
2000, Block 1, Chunk 2	On-Resonance	1561.124
2000, Block 1, Chunk 3	On-Resonance	268.155
2000, Block 1, Chunk 4	On-Resonance	706.922
2000, Block 1, Chunk 5	On-Resonance	2051.387
2000, Block 1, Chunk 6	On-Resonance	4406.229
2000, Block 2, Chunk 0	On-Resonance	289.339
2000, Block 2, Chunk 1	On-Resonance	1522.728
2000, Block 2, Chunk 2	On-Resonance	844.890
2000, Block 2, Chunk 3	On-Resonance	4133.854
2000, Block 2, Chunk 4	On-Resonance	2088.693
	On-Resonance Total	19437.313
2000, Block 1, Chunk 1	Off-Resonance	138.621
2000, Block 1, Chunk 2	Off-Resonance	175.476
2000, Block 1, Chunk 4	Off-Resonance	108.959
2000, Block 1, Chunk 5	Off-Resonance	311.411
2000, Block 1, Chunk 6	Off-Resonance	448.048
2000, Block 2, Chunk 1	Off-Resonance	370.119
2000, Block 2, Chunk 2	Off-Resonance	913.472
	Off-Resonance Total	2466.106

Table B.1: *The real data used for the $B \to K^*\gamma$ analysis.*

B.2 Monte Carlo Data

The Monte Carlo data used are the $B \to K^*\gamma$ signal modes, higher resonance $K^*\gamma$ modes and $X_{su}\gamma/X_{sd}\gamma$ modes (Ali-Greub model [89] used for generator), continuum background, and generic $B\overline{B}$ and τ decays, which are listed in table B.2.

Mode	Amount
$B^\pm \to K^{*\pm}\gamma, K^{*\pm} \to K^\pm\pi^0$	19,000
$B^0 \to K^{*0}\gamma, K^{*0} \to K^0_S\pi^0$	19,000
$B^0 \to K^{*0}\gamma, (K^{*0} \to K^+\pi^-)$	18,000
$B^+ \to K^{*+}\gamma, (K^{*+} \to K^0_S\pi^+)$	29,000
$B^+ \to X_{su}\gamma$	16000
$B^0 \to X_{sd}\gamma$	22000
$B \to K^{*+}(1273)\gamma$	16000
$B \to K^{*+}(1402)\gamma$	16000
$B \to K^{*+}(1410)\gamma$	14000
$B \to K^{*+}(1430)\gamma$	22000
$B \to K^{*+}(1680)\gamma$	17000
$B \to K^{*0}(1273)\gamma$	14000
$B \to K^{*0}(1402)\gamma$	14000
$B \to K^{*0}(1410)\gamma$	14000
$B \to K^{*0}(1430)\gamma$	22000
$B \to K^{*0}(1680)\gamma$	16000
$e^+e^- \to c\overline{c}$	15,439,900
$e^+e^- \to u\overline{u}, d\overline{d}, s\overline{s}$	24,824,000
$B^0\overline{B}^0$ generic decays	4,183,361
B^+B^- generic decays	4,857,402
$e^+e^- \to \tau^+\tau^-$	5,224,000

Table B.2: *The Monte Carlo data used for the $B \to K^*\gamma$ analysis.*

Appendix C

K^*-Mass Shape

C.1 The Relativistic Breit-Wigner Function

The relativistic P-wave Breit-Wigner shape with Blatt-Weisskopf barrier functions used for the fit of the K^*-mass distribution in on-resonance data is given by:

$$f_{relBW}(M) \propto \frac{M \cdot \Gamma_{rel}}{(M^2 - \overline{M}^2)^2 + (\overline{M} \cdot \Gamma_{rel})^2} \tag{C.1}$$

$$\Gamma_{rel} = \Gamma \left(\frac{p}{\overline{p}}\right)^{2l+1} \left(\frac{\overline{M}}{M}\right) \left(\frac{\overline{b}_{Blatt-Weiss}}{b_{Blatt-Weiss}}\right) \tag{C.2}$$

$$b_{Blatt-Weiss}(p, r, l = 1) = 1 + (pr)^2 \tag{C.3}$$

where:

- M is the reconstructed mass
- $\overline{M}$ is the peak of the resonance
- $\overline{p}$ is the outgoing momentum of the daughter at the resonance peak
- p is the outgoing momentum of the daughter in the resonance rest frame
- Γ is the resonance width
- l is the orbital angular momentum (1 in this case)
- r is the barrier radius (3 GeV^{-1})
- $b_{Blatt-Weiss}$ is the Blatt-Weisskopf barrier function evaluated at p, r, l
- $\overline{b}_{Blatt-Weiss}$ is the Blatt-Weisskopf barrier function evaluated at $\overline{p}$

Appendix D

π^0 Study

D.1 The Zernike Moments

The expansion of lateral shower shapes in the EMC is provided in terms of Zernike moments:

$$A_{nm} = \sum_{r_i \leq R_0}^{n} \frac{E_i}{E} \cdot f_{nm}\left(\frac{r_i}{R_0}\right) \cdot e^{-im\Phi_i}, \qquad R_0 = 15\,\mathrm{cm}, \tag{D.1}$$

with

$$f_{nm}\left(\rho_i \equiv \frac{r_i}{R_0}\right) = \sum_{s=0}^{(n-m)/2} \frac{(-1)^s (n-s)! \rho_i^{n-2s}}{s![(n+m)/2-s]![(n-m)/2-s]!} \tag{D.2}$$

Here n, $m \geq 0$ are integers, $n - m$ is even, and $m \leq n$. The azimuthal variation in shower shape enters only for moments with $m \geq 2$. A cut on the Zernike moment A_{42} exploits the fact that hadronic showers in the EMC tend to be more irregular than electromagnetic showers.

D.2 π^0 Mass Fits

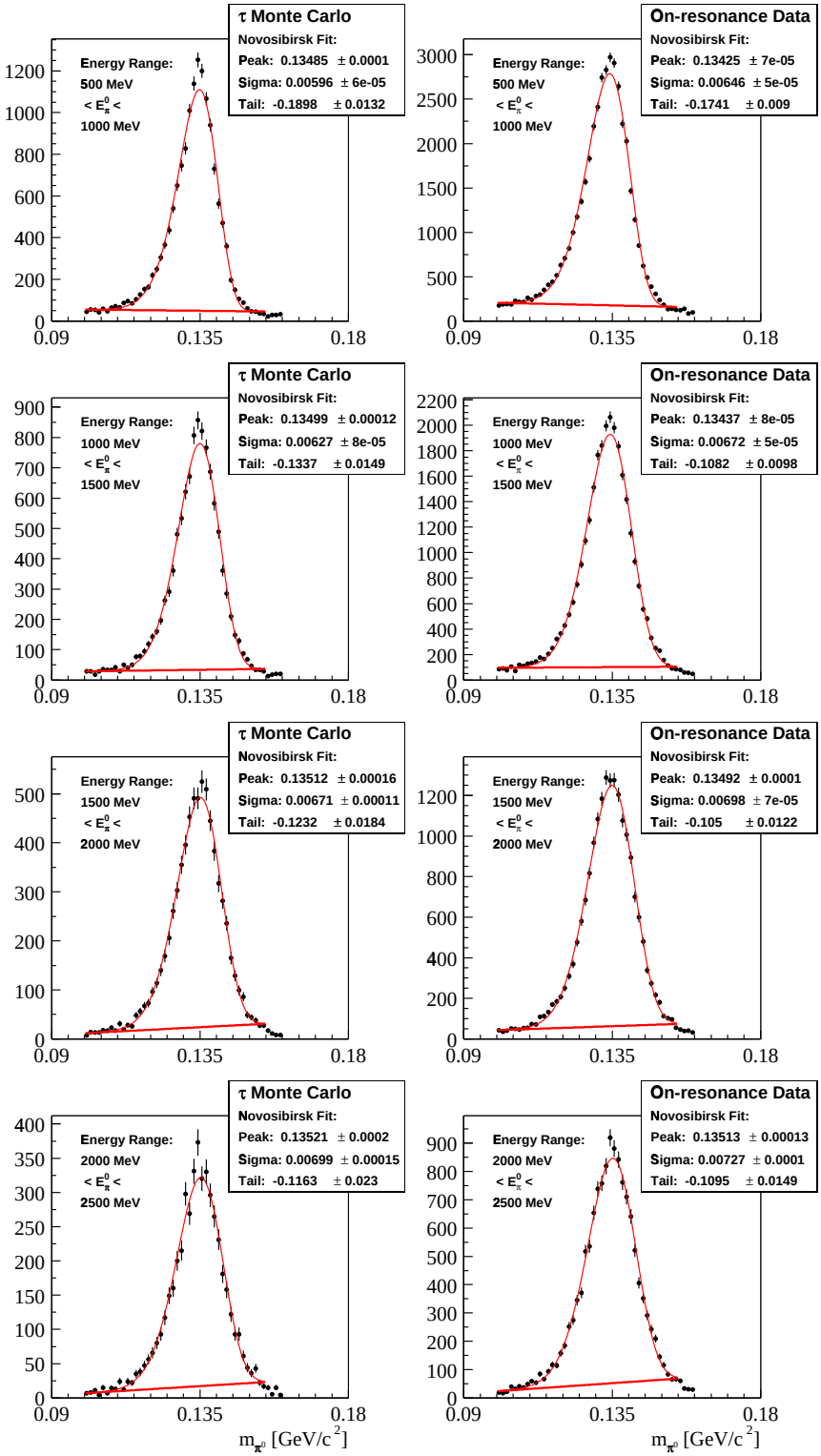

Figure D.1: *Novosibirsk fits to the π^0 mass distributions for different π^0-energy ranges. The π^0 mesons are obtained by a selection of $\tau\tau$ "1-on-1" decays (see section 5.2).*

Appendix E

Background Composition Studies

In this section, the studies of the expected background-composition from Monte Carlo in M_{ES} and ΔE^* are presented via the example of the mode $K^{*\pm} \to \pi^0 K^\pm$.

E.1 M_{ES}-Background Composition for $K^{*\pm} \to \pi^0 K^\pm$

The M_{ES} distribution consists of contributions from continuum background, cross- and down-feed (see 6.1.2), and the signal mode. The yield for all contributing modes is determined by running the $K^{*+} \to K^+\pi^0$ analysis over the continuum Monte Carlo (see 6.1.1), $K^*\gamma$, higher $K^*\gamma$, and the $X_{su}\gamma$ and $X_{sd}\gamma$ samples listed in table E.1. A Crystal-Ball function (equation 4.13) is fitted to the M_{ES} distribution in each mode and the obtained shape parameters are given in table E.1. Examples for such fits are shown in figure E.1 for cross- and down-feed.
To model the overall M_{ES} distribution, a toy Monte Carlo is generated for each mode using the shapes and expected yields in table E.1. Figure 6.5 shows the contributions in M_{ES} and the resulting predicted overall distribution.

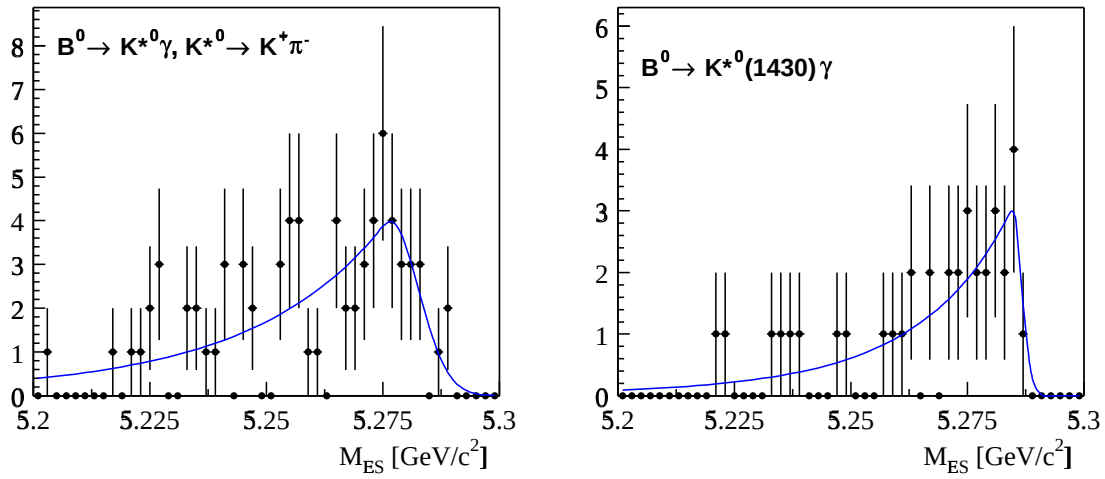

Figure E.1: *Crystal-Ball fits to the M_{ES} distributions of the cross-feed example $K^{*0} \to K^+\pi^-$ (LEFT) and the down-feed example $B \to K^{*0}(1430)\gamma$ (RIGHT).*

Mode (Monte Carlo)	events	decay fraction $[10^{-5}]$	M_{ES} peak [GeV]	M_{ES} width [GeV]	M_{ES} cut	events for [5.2, 5.3 GeV]	events for [5.27, 5.29 GeV]	exp. events in data for [5.2, 5.3 GeV]	exp. events in data for [5.27, 5.29] GeV]
$B^+ \to K^{*+}\gamma$ $(K^{*+} \to K^+\pi^0)$	19000	≈1.25	Novosibirsk fit instead of Crystal-Ball fit			2652	2587	39.7	38.7 ± 0.76
$B^+ \to K^{*+}\gamma$ $(K^{*+} \to K^0_S\pi^+)$	20000	≈1.1	-	-	-	0	0	-	-
$B^0 \to K^{*0}\gamma$ $(K^{*0} \to K^+\pi^-)$	18000	≈3.3	5.277 ± 0.004	0.006 ± 0.002	0.21 ± 0.10	73	29	3.0	1.2 ± 0.22
$B^0 \to K^{*0}\gamma$ $(K^{*0} \to K^0_S + \pi^0)$	19000	≈0.52	5.279 ± 0.004	0.006 ± 0.003	2.00 ± 0.004	3	3	0.0	0.0
Cross-feed								3.0	1.2 ± 0.22
$B^+ \to X_{su}\gamma$	16000	≈11	5.280 ± 0.002	0.003 ± 0.001	0.16 ± 0.09	4	2	0.63	0.32 ± 0.23
$B^0 \to X_{sd}\gamma$	22000	≈11	5.285 ± 0.002	0.003 ± 0.001	0.11 ± 0.06	15	9	1.71	1.02 ± 0.34
$B \to K^{*+}(1273)\gamma$	16000	≈0.5	5.274 ± 0.001	0.002 ± 0.0007	0.7 ± 0.4	6	5	0.04	0.04 ± 0.02
$B \to K^{*+}(1402)\gamma$	16000	≈0.5	5.283 ± 0.002	0.002 ± 0.0003	0.14 ± 0.06	17	12	0.12	0.09 ± 0.03
$B \to K^{*+}(1410)\gamma$	14000	≈0.5	5.286 ± 0.002	0.002 ± 0.0009	0.5 ± 0.3	5	5	0.04	0.04 ± 0.02
$B \to K^{*+}(1430)\gamma$	22000	≈1.7	5.278 ± 0.003	0.006 ± 0.002	0.6 ± 0.4	16	13	0.28	0.23 ± 0.06
$B \to K^{*+}(1680)\gamma$	17000	≈0.5	5.279 ± 0.002	0.002 ± 0.001	0.13 ± 0.08	5	3	0.03	0.02 ± 0.01
$B \to K^{*0}(1273)\gamma$	14000	≈0.5	5.278 ± 0.001	0.0044 ± 0.001	0.9 ± 0.4	31	27	0.25	0.22 ± 0.04
$B \to K^{*0}(1402)\gamma$	14000	≈0.5	5.2835 ± 0.001	0.002 ± 0.002	0.22 ± 0.06	24	20	0.19	0.16 ± 0.04
$B \to K^{*0}(1410)\gamma$	14000	≈0.5	5.284 ± 0.002	0.003 ± 0.001	0.3 ± 0.2	22	13	0.18	0.11 ± 0.03
$B \to K^{*0}(1430)\gamma$	22000	≈1.7	5.285 ± 0.001	0.002 ± 0.001	0.1 ± 0.02	36	21	0.63	0.37 ± 0.08
$B \to K^{*0}(1680)\gamma$	16000	≈0.5	5.277 ± 0.002	0.002 ± 0.001	0.07 ± 0.05	7	2	0.05	0.01 ± 0.01
Down-feed		29.4						4.16	2.63 ± 0.43
Continuum MC			ARGUS fit instead of Crystal-Ball fit			56	19	97.6	33.1 ± 7.6
Total MC								144.5	75.6 ± 7.7
On-Peak data								166	81 ± 9

Table E.1: *Expected number of events from cross- and down-feed in M_{ES} for $K^{*+} \to K^+\pi^0$. The displayed shape parameters shown are the peak, width and cut parameter of the Crystal-Ball function, its power parameter is fixed to 10.*

E.2 Composition of ΔE Background for $K^{*\pm} \to \pi^0 K^\pm$

Like in section E.1, the composition of the background in ΔE is obtained by investigating the contributions from continuum, and cross- and down-feed. To determine the ΔE shape in each mode, a Crystal-Ball function is fitted the ΔE distributions for 5.27 GeV/c^2 $< M_{ES} <$ 5.29 GeV/c^2. The expected yields for the $K^*\gamma$, higher $K^*\gamma$, and the $X_{su}\gamma$ and $X_{sd}\gamma$ samples are listed in table E.2.

Toy MC Study of ΔE composition

To determine the expected ΔE distribution in data, a toy Monte Carlo is generated using the shapes and expected yields in table E.2 for each mode. Figure 6.5 shows the contributions in ΔE and the overall distribution.

Mode (Monte Carlo)	ΔE peak [MeV]	ΔE width [MeV]	ΔE cut	events for [-0.3 GeV, 0.3 GeV]	expected events in data for [-0.3 GeV, 0.3 GeV]
$B^+ \to K^{*+}\gamma$ ($K^{*+} \to K^+\pi^0$)	2.2 ± 6.0	56.5 ± 3.4	0.716 ± 0.313	2682	40.15
$B^+ \to K^{*+}\gamma$ ($K^{*+} \to K^0_S\pi^+$)	-	-	-	-	-
$B^0 \to K^{*0}\gamma$ ($K^{*0} \to K^+\pi^-$)	-39.0 ± 26.9	178.3 ± 26.6	1.400 ± 0.571	39	1.63
$B^0 \to K^{*0}\gamma$ ($K^{*0} \to K^0_S + \pi^0$)	-209.4 ± 34.6	100.3 ± 27.0	1.076 ± 0.895	6	0.04
$B^+ \to X_{su}\gamma$	-265 ± 103	224.7 ± 82.9	1.05 ± 4.00	7	1.1
$B^0 \to X_{sd}\gamma$	-141.4 ± 39.2	68.9 ± 26.0	0.32 ± 0.23	11	1.25
$B \to K^{*+}(1273)\gamma$	-198.9 ± 35.9	155.2 ± 29.1	1.94 ± 3.80	9	0.07
$B \to K^{*+}(1402)\gamma$	-237.5 ± 14.4	72.1 ± 11.3	1.21 ± 0.54	22	0.16
$B \to K^{*+}(1410)\gamma$	-260.5 ± 18.5	76.7 ± 14.5	1.24 ± 0.78	16	0.13
$B \to K^{*+}(1430)\gamma$	-144.5 ± 37.2	160.4 ± 30.7	2.07 ± 5.17	15	0.26
$B \to K^{*+}(1680)\gamma$	-263.2 ± 27.4	93.6 ± 20.5	2.42 ± 1.71	7	0.05
$B \to K^{*0}(1273)\gamma$	-215.2 ± 10.5	80.1 ± 7.5	3.41 ± 7.56	35	0.29
$B \to K^{*0}(1402)\gamma$	-196.5 ± 5.7	43.6 ± 6.8	0.43 ± 0.07	28	0.23
$B \to K^{*0}(1410)\gamma$	-254.6 ± 11.7	85.0 ± 8.6	2.77 ± 6.86	39	0.32
$B \to K^{*0}(1430)\gamma$	-218.6 ± 16.8	120.4 ± 12.9	2.34 ± 4.34	31	0.54
$B \to K^{*0}(1680)\gamma$	-292.6 ± 27.1	102.4 ± 21.3	3.27 ± 0.50	5	0.04
Continuum MC				19	33.1
Total MC					79.4
On-Peak data					90

Table E.2: *Expected event numbers and fitted shapes from cross- and down-feed in ΔE for $K^{*+} \to K^+\pi^0$.*

E.3 Covariance Matrices of $\mathcal{B}(B \to K^*\gamma)$ Fits

The tables E.3-E.6 compile the error matrices of the $\mathcal{B}(B \to K^*\gamma)$ fits for the four analysed modes described in section 6.3.1.

	Peak	Width σ	Shape ζ	Fraction
Signal peak	5.53528e-07	-9.42577e-08	-0.000322247	-5.97915e-06
Signal width σ	-9.42577e-08	4.64598e-07	0.00135025	1.43177e-05
ARGUS shape ζ	-0.000322247	0.00135025	75.1618	0.187223
Signal fraction	- 5.97915e-06	1.43177e-05	0.187223	0.00321158

Table E.3: *The covariance matrix of the* $\mathcal{B}(B^\pm \to K^{*\pm}\gamma, K^{*\pm} \to K^\pm\pi^0)$ *fit.*

	Peak	Shape ζ	Fraction
Signal peak	5.957e-07	3.048e-05	-2.227e-06
ARGUS shape ζ	3.048e-05	1.559e+02	2.424e-01
Signal fraction	-2.227e-06	2.424e-01	4.168e-03

Table E.4: *The covariance matrix of the* $\mathcal{B}(B^\pm \to K^{*\pm}\gamma, K^{*\pm} \to K_S\pi^\pm)$ *fit.*

	Peak	Width σ	Shape ζ	Fraction
Signal peak	9.654e-08	-2.691e-09	-1.086e-05	-4.818e-07
Signal width σ	-2.691e-09	5.411e-08	1.797e-04	1.607e-06
ARGUS shape ζ	-1.086e-05	1.797e-04	3.885e+01	5.374e-02
Signal fraction	-4.818e-07	1.607e-06	5.374e-02	1.320e-03

Table E.5: *The covariance matrix of the* $\mathcal{B}(B^0 \to K^{*0}\gamma, K^{*0} \to K^+\pi^-)$ *fit.*

	Peak	Shape ζ	Fraction
Signal peak	2.2538e-06	-0.00303572	-3.42578e-05
ARGUS shape ζ	-0.00303572	476.977	1.13822
Signal fraction	-3.42578e-05	1.13822	.0130053

Table E.6: *The covariance matrix of the* $\mathcal{B}(B^0 \to K^{*0}\gamma, K^{*0} \to K_S\pi^0)$ *fit.*

E.4 Covariance Matrices of $A_{CP}(B \to K^*\gamma)$ Fits

In the tables E.7-E.9, the error matrices of the A_{CP} fits in the three considered $B \to K^*\gamma$ modes are listed (see section 7.2.1).

	Total signal yield	Signal asymmetry A_{CP}	signal peak	signal width σ	background yield	background ARGUS shape ζ
Signal yield	106.823	0.0451249	-0.000505629	-0.0013324	-21.3364	18.8089
A_{CP}	0.0451249	0.0241098	-1.96955e-08	-4.85006e-06	-0.0414475	0.0252486
Signal peak	-0.000505629	-1.96955e-08	5.2624e-07	-5.12574e-08	0.00052428	-0.000364479
Signal width	-0.0013324	-4.85006e-06	-5.12574e-08	4.09794e-07	0.00139505	-0.00102448
Bkg yield	-21.3364	-0.0414475	0.00052428	0.00139505	186.136	-18.5002
Bkg shape ζ	18.8089	0.0252486	-0.000364479	-0.00102448	-18.5002	72.9044

Table E.7: *The covariance matrix of the A_{CP} fit for $B^\pm \to K^{*\pm}\gamma$,$K^{*\pm} \to K^\pm\pi^0$.*

	Total signal yield	Signal asymmetry A_{CP}	signal peak	background yield	background ARGUS shape ζ
Signal yield	48.9224	-0.127409	-2.576e-04	-14.595	21.5646
A_{CP}	-0.12741	4.110e-02	4.024e-06	0.1992	-0.24784
Signal peak	-2.576e-04	4.024e-06	5.750e-07	1.922e-04	5.499e-05
Bkg yield	-14.595	0.1992	1.925e-04	79.868	-14.996
Bkg shape ζ	21.570	-0.2478	5.499e-05	-14.996	163.895

Table E.8: *The covariance matrix of the A_{CP} fit for $B^\pm \to K^{*\pm}\gamma$,$K^{*\pm} \to K_S\pi^\pm$.*

	Total signal yield	Signal asymmetry A_{CP}	signal peak	signal width σ	background yield	background ARGUS shape ζ
Signal yield	1.760e+02	1.963e-03	-1.385e-04	4.674e-04	-4.034e+01	1.568e+01
A_{CP}	1.963e-03	8.765e-03	4.340e-07	-2.174e-07	-1.969e-03	1.503e-03
Signal peak	-1.385e-04	4.340e-07	9.660e-08	-2.657e-09	1.383e-04	-9.734e-06
Signal width	4.674e-04	-2.174e-07	-2.657e-09	5.406e-08	-4.670e-04	1.779e-04
Bkg yield	-4.034e+01	-1.969e-03	1.383e-04	-4.670e-04	1.978e+02	-1.569e+01
Bkg shape ζ	1.568e+01	1.503e-03	-9.734e-06	1.779e-04	-1.569e+01	3.873e+01

Table E.9: *The covariance matrix of the A_{CP} fit for $B^0 \to K^{*0}\gamma$,$K^{*0} \to K^+\pi^-$.*

E.5 Combination of Results

This section is devoted to the description of the combination procedure for the measurements of the $B \to K^*\gamma$ branching fractions and *CP* asymmetries, and the evaluation of the rate-asymmetry error.

General Formalism for combining errors

Let us consider a couple of measurements $\mathcal{B}_1, ..., \mathcal{B}_n$ which have to be combined to $\mathcal{B}_{comb}(\mathcal{B}_1, ..., \mathcal{B}_n)$. The error $\sigma_{\mathcal{B}_{comb}}$ on the combined measurement is given by:

$$\sigma^2_{\mathcal{B}_{comb}} = \vec{D}^T_{\mathcal{B}} \mathbf{V} \vec{D}_{\mathcal{B}}, \tag{E.1}$$

where the covariance matrix $\mathbf{V}$ and the vector $\vec{D}_{\mathcal{B}}$ are:

$$V_{ij} = cov(\mathcal{B}_i, \mathcal{B}_j) = \langle \mathcal{B}_i \mathcal{B}_j \rangle - \langle \mathcal{B}_i \rangle \langle \mathcal{B}_j \rangle, \qquad \vec{D}_{\mathcal{B}} = \left(\frac{\partial \mathcal{B}_{comb}}{\partial \mathcal{B}_1}, ..., \frac{\partial \mathcal{B}_{comb}}{\partial \mathcal{B}_n} \right) \tag{E.2}$$

Each measurement $\mathcal{B}_i$ has three types of errors, a statistical error σ, a systematic κ that is unique to the particular measurement, and a systematic S that can be common to several measurements. If individual errors are independent, the covariance between the different components vanishes, i.e. each set of uncorrelated errors gives a diagonal matrix. On the other hand, each correlated error is incorporated by the addition of a matrix with nonzero elements for the completely correlated variables. The covariance matrix is then

$$\mathbf{V} = \mathbf{E} + \mathbf{K} + \mathbf{S} = \begin{pmatrix} \sigma_1^2 + \kappa_1^2 & & 0 \\ & \ddots & \\ 0 & & \sigma_n^2 + \kappa_n^2 \end{pmatrix} + \begin{pmatrix} S_{11}^2 & \cdots & S_{n1}^2 \\ \vdots & \ddots & \vdots \\ S_{1n}^2 & \cdots & S_{nn}^2 \end{pmatrix} \tag{E.3}$$

The weighted mean is derived by finding the best estimate for the quantity $\mathcal{B}_{comb}$, i.e. the χ^2 is minimised:

$$d\chi^2 / d\mathcal{B}_{comb} = 0, \qquad \chi^2 = \vec{\mathcal{B}}^{\,T} \mathbf{V}^{-1} \vec{\mathcal{B}}, \qquad \vec{\mathcal{B}} = (\mathcal{B}_1 - \mathcal{B}_{comb}, ..., \mathcal{B}_n - \mathcal{B}_{comb}) \tag{E.4}$$

The covariance Matrix for combined $\mathcal{B}(B \to K^*\gamma)$ measurements

The four measurements with $K^* \to K^+\pi^-$, $K_S\pi^0$, $K_S\pi^+$, $K^+\pi^0$ have correlated errors arising from the fact that systematics are associated with the individual particles in the reconstruction. There is also a common systematic uncertainty in the number of used B mesons. The covariance matrix is given by:

$$
\begin{aligned}
V \;=\; & \begin{pmatrix} \sigma^2_{K^\pm\pi^-} + \kappa^2_{K^\pm\pi^-} & 0 & 0 & 0 \\ 0 & \sigma^2_{K_S\pi^0} + \kappa^2_{K_S\pi^0} & 0 & 0 \\ 0 & 0 & \sigma^2_{K_S\pi^\pm} + \kappa^2_{K_S\pi^\pm} & 0 \\ 0 & 0 & 0 & \sigma^2_{K^\pm\pi^0} + \kappa^2_{K^\pm\pi^0} \end{pmatrix} \\
+ & \begin{pmatrix} 0 & 0 & 0 & 0 \\ 0 & S^2_{\pi^0} & 0 & S^2_{\pi^0} \\ 0 & 0 & 0 & 0 \\ 0 & S^2_{\pi^0} & 0 & S^2_{\pi^0} \end{pmatrix} + \begin{pmatrix} 0 & 0 & 0 & 0 \\ 0 & S^2_{K_S} & S^2_{K_S} & 0 \\ 0 & S^2_{K_S} & S^2_{K_S} & 0 \\ 0 & 0 & 0 & 0 \end{pmatrix} + \begin{pmatrix} S^2_{K^\pm} & 0 & 0 & S^2_{K^\pm} \\ 0 & 0 & 0 & 0 \\ 0 & 0 & 0 & 0 \\ S^2_{K^\pm} & 0 & 0 & S^2_{K^\pm} \end{pmatrix} \\
+ & \begin{pmatrix} S^2_\gamma & S^2_\gamma & S^2_\gamma & S^2_\gamma \\ S^2_\gamma & S^2_\gamma & S^2_\gamma & S^2_\gamma \\ S^2_\gamma & S^2_\gamma & S^2_\gamma & S^2_\gamma \\ S^2_\gamma & S^2_\gamma & S^2_\gamma & S^2_\gamma \end{pmatrix} + \begin{pmatrix} S^2_{N_{B\overline{B}}} & S^2_{N_{B\overline{B}}} & S^2_{N_{B\overline{B}}} & S^2_{N_{B\overline{B}}} \\ S^2_{N_{B\overline{B}}} & S^2_{N_{B\overline{B}}} & S^2_{N_{B\overline{B}}} & S^2_{N_{B\overline{B}}} \\ S^2_{N_{B\overline{B}}} & S^2_{N_{B\overline{B}}} & S^2_{N_{B\overline{B}}} & S^2_{N_{B\overline{B}}} \\ S^2_{N_{B\overline{B}}} & S^2_{N_{B\overline{B}}} & S^2_{N_{B\overline{B}}} & S^2_{N_{B\overline{B}}} \end{pmatrix}
\end{aligned}
$$

The covariance matrix is constructed by

$$S_{ij} = \epsilon_i \cdot \mathcal{B}_i \cdot \epsilon_j \cdot \mathcal{B}_j, \tag{E.5}$$

where the i, j indices represent the mode number, ϵ_i is the respective systematic error, and $\mathcal{B}_i$ is the measured branching fraction for the mode. The measured branching fractions and contributions to the systematic error are given in table 6.7 and 6.8, respectively. The full, quantitative covariance matrix $\mathbf{V}$ is the sum of the statistical and systematic covariance matrix, $\mathbf{E}$ and $\mathbf{V'}$, respectively:

$$
\mathbf{E} = \begin{pmatrix} 0.168 & 0 & 0 & 0 \\ 0 & 2.924 & 0 & 0 \\ 0 & 0 & 0.578 & 0 \\ 0 & 0 & 0 & 1.145 \end{pmatrix}, \quad \mathbf{V'} = \mathbf{K} + \mathbf{S} = \begin{pmatrix} 0.052 & 0.029 & 0.021 & 0.041 \\ 0.029 & 0.178 & 0.045 & 0.052 \\ 0.021 & 0.045 & 0.040 & 0.027 \\ 0.041 & 0.052 & 0.027 & 0.150 \end{pmatrix}
$$

$$
\Rightarrow \mathbf{V} = \mathbf{E} + \mathbf{V'} = \begin{pmatrix} 0.220 & 0.029 & 0.021 & 0.041 \\ 0.029 & 3.102 & 0.045 & 0.052 \\ 0.021 & 0.045 & 0.618 & 0.027 \\ 0.041 & 0.052 & 0.027 & 1.295 \end{pmatrix} \tag{E.6}
$$

Combination of the Branching Fractions $\mathcal{B}(B \to K^*\gamma)$

In our case, the neutral modes and the charged modes are combined separately, being equivalent to two separate 2×2 $\mathbf{V}$-matrices, which both take the form:

$$\mathbf{V} = \begin{pmatrix} \sigma_1^2 + \kappa_1^2 & 0 \\ 0 & \sigma_2^2 + \kappa_2^2 \end{pmatrix} + \begin{pmatrix} S^2 & S^2 \\ S^2 & S^2 \end{pmatrix} \tag{E.7}$$

Solving equation E.4 for the combined measurement $\mathcal{B}$ yields:

$$\mathcal{B}_{comb} = \frac{\sum_i w_i \mathcal{B}_i}{\sum_i w_i}, \qquad \frac{d\mathcal{B}_{comb}}{d\mathcal{B}_j} = \frac{w_j \mathcal{B}_j}{\sum_i w_i}, \qquad w_i = \frac{1}{\sigma_i^2 + \kappa_i^2} \tag{E.8}$$

The common systematic errors for the neutral and charged modes are extracted in table 6.8 and the used weights in the averaging are listed in table E.10. The overall statistical and systematic errors of the combined branching fractions are determined by propagating the individual errors according to equation E.1, using the purely-statistical error matrix $\mathbf{E}$ and the purely systematical error matrix $\mathbf{V'}$, respectively.

Mode	σ_i	κ_i	$\omega_i = \frac{1}{\sigma_i^2+\kappa_i^2}$	Mode	σ_i	κ_i	$\omega_i = \frac{1}{\sigma_i^2+\kappa_i^2}$
$i=1 \equiv K^+\pi^-$	0.41	0.14	5.33	$i=3 \equiv K_S\pi^+$	0.76	0.16	1.66
$i=2 \equiv K_S\pi^0$	1.71	0.39	0.33	$i=4 \equiv K^+\pi^0$	1.07	0.31	0.81

Table E.10: *Weights used for the neutral and charged branching-fraction combination.*

Error Propagation for the Rate Asymmetry $\Delta_{0\pm}(B \to K^*\gamma)$

The asymmetry $\Delta_{0\pm}$ of the neutral and charged $B \to K^*\gamma$ decay rate is given by:

$$\Delta_{0\pm} = \frac{\Gamma_0 - \Gamma_\pm}{\Gamma_0 + \Gamma_\pm}, \qquad \Gamma_m = \mathcal{B}_m/\tau_{B^m}, \qquad \text{with} \qquad m = \begin{cases} 0 \equiv B^0 \to K^{*0}\gamma \\ \pm \equiv B^\pm \to K^{*\pm}\gamma \end{cases},$$

$$\text{and} \qquad \mathcal{B}_0 = \frac{\omega_1\mathcal{B}_1 + \omega_2\mathcal{B}_2}{\omega_1 + \omega_2}, \qquad \mathcal{B}_\pm = \frac{\omega_3\mathcal{B}_3 + \omega_4\mathcal{B}_4}{\omega_3 + \omega_4} \tag{E.9}$$

The statistical and systematic error, $\sigma^{stat}_{\Delta_{0\pm}}$ and $\sigma^{sys}_{\Delta_{0\pm}}$, respectively, are determined by propagating the individual errors and using the covariance matrices from equation E.6 and the vector of derivatives $\vec{D}_{\Delta_{0\pm}}$:

$$\sigma^{stat\ 2}_{\Delta_{0\pm}} = \vec{D}^T_{\Delta_{0\pm}}\mathbf{E}\vec{D}_{\Delta_{0\pm}}, \qquad \vec{D}_{\Delta_{0\pm}} = \left(\frac{\partial\Delta_{0\pm}}{\partial\mathcal{B}_1}, .., \frac{\partial\Delta_{0\pm}}{\partial\mathcal{B}_4}\right) \tag{E.10}$$

$$\sigma^{sys\ 2}_{\Delta_{0\pm}} = \vec{D}^T_{\Delta_{0\pm}}\mathbf{V}'\vec{D}_{\Delta_{0\pm}} + \left(\frac{\partial\Delta_{0\pm}}{\partial\tau_{B^0}}\right)^2 d\tau_0^2 + \left(\frac{\partial\Delta_{0\pm}}{\partial\tau_{B^\pm}}\right)^2 d\tau_\pm^2 \tag{E.11}$$

Here, the values and errors on τ_{B^0} and $\tau_{B^\pm}$ are provided by the PDG [37].

Combination of A_{CP}

The combination procedure of the three A_{CP} measurements in the modes $K^{*0} \to K^+\pi^-$, $K^{*\pm} \to K_S\pi^\pm$, and $K^{*\pm} \to K^\pm\pi^0$ is equivalent to the treatment of the branching fractions. The full, quantitative covariance matrix is given by:

$$\mathbf{V} = \begin{pmatrix} 0.009 & 0.0001 & 0.0002 \\ 0.0001 & 0.0442 & 0.0001 \\ 0.0002 & 0.0001 & 0.0229 \end{pmatrix}$$

Bibliography

[1] A. D. Sakharov, *Violation of CP invariance; C asymmetry, and baryon asymmetry of the universe*, JETP **5** (1967) 32

[2] M. Kobayashi and T. Maskawa, *CP Violation in the Renormalizable Theory of Weak Interaction*, Prog. Theor. Phys. **49** (1973) 652

[3] J. H. Christenson, J. W. Cronin, V. L. Fitch and R. Turlay, *Evidence for the 2π Decay of the K_2^0 Meson*, Phys. Rev. Lett. **13** (1964) 138

[4] K. R. Schubert, *Search for CP Violation in B Meson Decays*, Nucl. Physics. B **89** (2000) 117-128

[5] *BABAR* Collaboration: B. Aubert *et al.*, *Measurement of CP-Violating Asymmetries in B^0 Decays to CP Eigenstates*, Phys. Rev. Lett. **86** (2001) 2515-2522, hep-ph/0102030 (23Feb2001)

[6] Super-Kamiokande Collaboration: S. Fukuda *et al.*, *Solar ^8B and* hep *Neutrino Measurements from 1258 Days of Super-Kamiokande Data*, Phys. Rev. Lett. **86** (2001) 5651-5655, hep-ph/0103032 (20Mar2001)

[7] S. W. Bosch and G. Buchalla, *The Radiative Decays $B \to V\gamma$ at Next-to-Leading Order in QCD*, hep-ph/0106081 (07Jun2001)

[8] M. Beneke *et al.*, *Systematic approach to exclusive $B \to Vl^+l^-, V\gamma$ decays*, hep-ph/0106067 (10Jul2001)

[9] A. L. Kagan and M. Neubert, *Isospin Breaking in $B \to K^*\gamma$ Decays*, hep-ph/0110078 (5Oct2001)

[10] A. L. Kagan and M. Neubert, *Direct CP Violation in $B \to X_s\gamma$ Decays as a Signature of New Physics*, Phys. Rev. D **58** (1998) 094012, hep-ph/9803368 (15May1998)

[11] CLEO Collaboration: T. E. Coan *et al.*, *Study of exclusive radiative B Meson Decays*, Phys. Rev. Lett. **84** (2000) 5283-5287, hep-ex/9912057 (11May2000)

[12] *BABAR* Collaboration: B. Aubert *et al.*, *Measurement of $B \to K^*\gamma$ Branching Fractions and Charge Asymmetries*, hep-ex/0110065 (26Oct2001)

[13] T. Colberg, *BABAR* Analysis Document 133: *Measurement of the decay fractions of* $B^{\pm} \to K^{*\pm}\gamma$, $(K^{*\pm} \to \pi^0 K^{\pm})$ *and* $B^0 \to K^{*0}\gamma$, $(K^{*0} \to \pi^0 K^0_s)$

[14] C. Jessop *et al.*, *BABAR* Analysis Document 33: *Measurement of* $\mathcal{B}(B \to K^*\gamma$ *and Search for Direct* CP *Violation*

[15] T. Colberg, *BABAR* Analysis Document 196: *Study of* π^0 *Efficiencies using* $\tau\tau$ *1-on-1 Decays*

[16] E. Lohrmann, *Hochenergiephysik*, Teubner Taschenbücher Verlag, Stuttgart 1992.

[17] P. Schmüser, *Feynman-Graphen und Eichtheorien für Experimentalphysiker*, Springer Verlag, Berlin 1995.

[18] M. Neubert, *B Decays and CP Violation*, Int. J. Mod. Phys. A **11** (1996) 4173, hep-ex/9604412 (26Apr1996)

[19] P. W. Higgs, *Spontaneous Symmetry Breakdown without Massless Bosons*, Phys. Rev. Lett. **145** (1966) 1156

[20] A. Ali, *B Decays - Introduction and Overview*, in *B Decays* by S. Stone, World Scientific Publishing (1994) 1-80

[21] *BABAR* Collaboration: P. F. Harrison and H. R. Quinn, *The BABAR physics book: Physics at an asymmetric B-Factory*, Sec. 1.4 (1998)

[22] N. Cabibbo, *Unitarity Symmetry and Leptonic Decays*, Phys. Rev. Lett. **10** (1963) 531

[23] N. Cabibbo, *Unitarity Symmetry and Nonleptonic Decays*, Phys. Rev. Lett. **12** (1964) 62

[24] L. Wolfenstein, *Parametrization of the Kobayashi-Maskawa matrix*, Phys. Rev. Lett. **51** (1983) 1945

[25] S. L. Glashow, J. Iliopoulos and L. Maiani, *Weak Interactions with Lepton-Hadron Symmetry*, Phys. Rev. D **2** (1970) 1285-1292

[26] G. Buchalla, A. J. Buras and M. E. Lautenbacher, *Weak Decays beyond Leading Logarithms*, Rev. Mod. Phys. **68** (1996) 1125, hep-ph/9512380 (15Dec1995)

[27] K. Lingel *et al.*, *Penguin Decays of B Mesons*, hep-ex/9804015 (27Apr1998)

[28] K. Chetyrkin, M. Misiak and M. Münz, Phys. Lett. B **400** (1997) 206, B **425** (1998) 414 (E)

[29] A.J. Buras, *Weak Hamiltonian, CP Violation and Rare Decays*, hep-ex/9806471 (24Jun1998)

[30] P. Ball and V. M. Braun, *Exclusive Semileptonic and Rare B-Meson Decays in QCD*, Phys. Rev. D **58** (1998) 094016, hep-ph/9805422 (10Jul1998)

[31] Z. Ligeti and M. B. Wise, $B \to K^* \gamma$ *from* $D \to K^* \bar{l} \nu$, Phys. Rev. D **60** (1998) 117506, hep-ph/9905277 (10May1999)

[32] M. Beneke *et al.*, *QCD factorization for* $B \to \pi\pi$ *decays*, Phys. Rev. Lett. **83** (1999) 1914, hep-ph/9905312 (11May1999)

[33] J. Charles *et al.*, *Heavy-to-Light Form Factors in the Final Hadron Large Energy Limit of QCD*, Phys. Rev. D **60** (1999) 014001, hep-ph/9812358 (25Jan1999)

[34] M. Beneke *et al.*, *QCD factorization for exclusive non-leptonic B-meson decays*, Nucl. Phys. B**591** (2000) 313, hep-ph/0006124 (13Jun2000)

[35] H. H. Asatryan, H. M. Asatrian and D. Wyler, *NLL Corrections for B-Meson Radiative Exclusive Decays*, Phys. Lett. B **470** (1999) 223, hep-ph/9905412 (20May1999)

[36] M. Beneke and T. Feldmann, *Symmetry-breaking corrections to heavy-to-light B meson form factors at large recoil*, Nucl. Phys. B **592** (2001) 3 hep-ph/0008255 (6Nov2000)

[37] The Particle Data Group, *Review of Particle Physics*, The European Physical Journal C **15** (2001) Number 1-4

[38] M. Misiak, *Theory of radiative B decays*, hep-ph/0002007 (1Feb2000)

[39] M. Neubert, *Light Rays of New Physics: CP Violation in* $B \to X_s \gamma$ *decays.* Phys. Rev. Proc. Suppl. **74** (1999) 260-267, hep-ex/9809343 (11Sep1998)

[40] M. Beneke, G. Buchalla, M. Neubert and C. T. Sachrajda, *QCD Factorization for* $B \to \pi\pi$ *Decays: Strong Phases and CP Violation in the Heavy Quark Limit.*, Phys. Rev. Lett **83** (1999) 1914-1917, hep-ph/9905312 (11May1999)

[41] M. Bander, D. Silverman and A. Soni, CP *Noninvariance in the Decays of Heavy Charged Quark Systems*, Phys. Rev. Lett **43** (1979) 242-245

[42] A. L. Kagan, Phys. Rev. D **51** (1995) 6196

[43] M. Ciuchini, E. Gabrielli and G. F. Giudice, Phys. Lett. B **388** (1996) 353

[44] F. M. Borzumati and C. Greub, *2HDMs predictions for* $B \to X_s \gamma$ *in NLO QCD*, Preprint ZU-TH 31/97, hep-ph/9802391 (23Feb1998)

[45] J. Seeman *et al.*, *The PEP-II Storage Rings*, To appear in Nucl. Instrum. Meth., slac-pub-8786 (2001)

[46] *BABAR* Collaboration: P. F. Harrison and H. R. Quinn, *The BABAR physics book: Physics at an asymmetric B-Factory*, Sec. 3.1 (1998)

[47] *BABAR* Collaboration: B. Aubert *et al.*, *The BABAR Detector*, Chapter 1, To appear in Nucl. Instrum. Meth., hep-ex/0105044 (16May2001)

[48] *BABAR* Collaboration: P. F. Harrison and H. R. Quinn, *The BABAR physics book: Physics at an asymmetric B-Factory*, Sec. 3.3 (1998)

[49] *BABAR* Drift Chamber Collaboration: G. Sciolla *et al.*, *The BABAR drift chamber*, Nucl. Instrum. Meth. A **419** (1998) 310

[50] A. Boyarski, D. Briggs and P. Burchat, *Studies of helium based drift chamber gases for high luminosity low-energy machines*, Nucl. Instrum. Meth. A **323** (1992) 267

[51] W. W. Allison and P. R. Wright, *The Physics of Charged Particle Identification: dE/dx, Cerenkov and transition Radiation*, OXFORD-NP-35-83

[52] *BABAR* Collaboration: P. F. Harrison and H. R. Quinn, *The BABAR physics book: Physics at an asymmetric B-Factory*, Sec. 3.5 (1998)

[53] *BABAR* Collaboration:*BABAR Technical Design Report*, Chapter 6 (1995)

[54] *BABAR* Collaboration:*BABAR Technical Design Report*, Chapter 7 (1995)

[55] G. M. Haller and D. R. Freytag, *BABAR Note 285: Analog Floating Point BiCMOS Sampling Chip and Architecture of the BABAR CsI Calorimeter Front End Electronics System at the SLAC B Factory*

[56] J. Button-Shafer *et al.*, *BABAR Note 322: Use of radioactive photon sources with the BABAR electromagnetic calorimeter*

[57] Y. I. Skovpen, *BABAR Note 356: Calibration of Calorimeter with Bhabha Events*

[58] S. Menke, *BABAR Note 528: Calibration of the BABAR Electromagnetic Calorimeter with π^0s* (2000)

[59] A. Bukin and H. Marsiske, *BABAR Note 433: Absolute Photon Energy Calibration in the BABAR Calorimeter Using π^0s* (1999)

[60] Y. I. Skovpen, *BABAR Note 357: Calibration of Photon Energy with Radiative Bhabha Events*

[61] S. Gehrig, *BABAR Note 380: Design and Simulated Performance of the Level 1 Trigger System* (1997)

[62] S. Panacek, *ROOT: An Object-Oriented Data Analysis Framework* (2001)

[63] C. Touramanis *et al.*, *BABAR* Analysis Document 229: *Luminosity measurement for the RUN 1data*

[64] C. Hearty *et al.*, *BABAR* Analysis Document 134: *Measurement of the Number of $\Upsilon 4S$ Mesons produced in RUN1 (B-Counting)*

[65] *BABAR* Collaboration: P. F. Harrison and H. R. Quinn, *The BABAR physics book: Physics at an asymmetric B-Factory*, Sec. 3.6 (1998)

[66] *BABAR* Collaboration: B. Aubert *et al.*, *The BABAR Detector*, Chapter 9, To appear in Nucl. Instrum. Meth., hep-ex/0105044 (16May2001)

[67] G. Lynch *et al.*, *BABAR* Note 488: *BABAR Drift Chamber Tracking Conventions*

[68] P. Billoir and S. Qian, *Fast vertex fitting with a local parametrization of tracks*, Nucl. Instr. and Meth. A **311** (1992) 139

[69] *BABAR* Collaboration: B. Aubert *et al.*, *The BABAR Detector*, Chapter 5, To appear in Nucl. Instrum. Meth., hep-ex/0105044 (16May2001)

[70] *BABAR* Collaboration: B. Aubert *et al.*, *The BABAR Detector*, Chapter 7, To appear in Nucl. Instrum. Meth., hep-ex/0105044 (16May2001)

[71] G. Mancinelli and S. Spanier, *BABAR* Analysis Document 116: *Kaon Selection at the BABAR Experiment*

[72] U. Egede *et al.*, *BABAR* Analysis Document 13: *Beamspot determination and use in BABAR*

[73] E. Maly, *Rekonstruktion neutraler π-Mesonen mit dem BABAR-Kalorimeter*, Diploma Thesis, Inst. für Kern- u. Teilchenphysik, Technische Universität Dresden, 1999

[74] C. Jessop *et al.*, *BABAR* Analysis Document 201: *High-Energy Photons at BABAR*

[75] R. Seitz, *BABAR* Note 294: *Describing Energy Deposit in CsI Crystals*

[76] M. Bona *et al.*, *BABAR* Analysis Document 19: *Studies on $K^0_S \to \pi^+\pi^-$ reconstruction*

[77] ARGUS Collaboration: A. Drescher *et al.*, Nucl. Instrum. Meth. A **237** (1985) 464

[78] *BABAR* Collaboration: B. Aubert *et al.*, *The BABAR Detector*, Chapter 3, To appear in Nucl. Instrum. Meth., hep-ex/0105044 (16May2001)

[79] T. Skwarnicki, *A Study of the Radiative Cascade Transition Between the Upsilon-Prime and Upsilon Resonances*, DESY F31-86-02, 1986

[80] C. Varnes *et al.*, *BABAR* Analysis Document 157: *Measurement of the GoodTracksLoose efficiency using SVT tracks*

[81] E. Varnes, *BABAR* Analysis Document 87: *Measurement of the Tracking Efficiency Using* $3 + 1\tau$ *Events*

[82] The CLEO Collaboration, Phys. Rev. Lett. **70** (1993) 1207

[83] U. Langenegger *et al.*, *BABAR* Analysis Document 90: *Cut-Based Electron Identification*

[84] C. Hearty *et al.*, *BABAR* Analysis Document 139: *Measurement of Inclusive Production of Charmonium States in B Meson Decays*

[85] *GEANT Detector Description and Simulation Tool*, CERN Program Library Long Writeup W **5013**

[86] C. Touramanis *et al.*, *BABAR* Analysis Document 20: *Studies on* π^0 *reconstruction: Status report: Neutral Identification and Reconstruction AWG*

[87] J. Olsen *et al.*, *BABAR* Analysis Document 90: *Measurement of Branching Fractions for Charmless* $B^+ \to h\prime^+ h^0$ *Decays*

[88] ARGUS Collaboration: H. Albrecht *et al.*, Z. Phys. C **48** (1990) 543

[89] A. Ali and C. Greub, Phys. Lett. B **361** (1995) 146

[90] CLEO Collaboration, $B \to s\gamma$ *Branching Fraction and CP Asymmetry*. hep-ex/9908022 (CLEO CONF 10Aug1999)

[91] *MINUIT Minimization Package*, CERN Program Library Long Writeup D **506**

[92] R. Faccini *et al.*, *BABAR* Analysis Document 12: *Measurements of Branching Ratios of Charged and Neutral B Mesons into Charmonium + K Final States*

[93] R. Faccini *et al.*, *BABAR* Analysis Document 39: *Measurement of* B^0 *and* B^+ *meson masses from* $B \to J/\Psi$ *decays*

[94] Belle Collaboration: J. Ushiroda, 4^{th} International Conference of B Physics and CP Violation, *Radiative B Meson Decay*, Ise-Shima, Japan, February 2001

[95] D. Kirkby *et al.*, *BABAR* Analysis Document 18: *A User's Guide to the RooFitTools Package for Unbinned Maximum Likelihood Fitting*

Aknowledgements

The completion of this thesis is the outcome of the support and help of various people who I attempt to acknowledge here. I would like to thank...

... Prof. Dr. Klaus R. Schubert for giving me the opportunity of working and studying within an international collaboration, including a ten-month stay at the *BABAR* experiment in Stanford/California and the participation in the conference "Frontiers in Physics 2001" in Nashville/Tennessee. Professor Schubert gave me a lot of guidance and help when I could use it at the beginning of the thesis, and a lot of freedom once I had acquainted myself with the world of particle-physics analysis.

... Prof. Dr. Bernhard Spaan for his persistent productive criticism, and many answers to physics questions.

... Prof. Dr. Gerald Eigen for accepting to act as the third referee of this dissertation.

... The *Bundesministerium für Bildung und Forschung (BMBF)* for the financial support provided for this work.

... Hiro Tanaka for the good co-operation from the professional point of view, but especially for numerous great barbequeues, discussions, and many other activities beyond physics.

... all other members of the Radiative Penguin Analysis Working Group, especially Colin Jessop, Teela Pulliam, and Francesca Di Lodovico, for the common effort.

... the members of the $B \to K^*\gamma$ Review Comittee, namely Paul Dauncey, Jean-Pierre Lees, and Mark Convery, for the sensible and productive collaboration.

... Christos Touramanis for the motivation and assistance during the π^0-efficiency study, but also for the chats in front of building 280 during his cigarette breaks.

... Stefan Bosch for his patience and endurance in explaining the theoretical aspects of radiative penguin decays to an experimental physicist like me.

... Rolf Dubitzky for being more than just an office mate, and for answering a lot of questions, but also for posing many critical ones. Without him, the numerous (late) hours in the office might have been pretty sad sometimes.

... all further members of the IKTP group for their helpfulness whenever I encountered a problem, mentioning Rainer Schwierz who provides our computing environment with his indefatigable work, Martin Dickopp, Jens Brose, Ralph Müller-Pfefferkorn, Enrico Maly (the latter three also for proof-reading parts of this report), Leif Wilden and Thorsten Brandt.

... my family and friends. For a seaman cruising around, the significance of his home harbour goes way beyond the little time he actually manages to spend there.

... Alexandra.

Versicherung

Hiermit versichere ich, dass ich die vorliegende Arbeit ohne unzulässige Hilfe Dritter und ohne Benutzung anderer als der angegebenen Hilfsmittel angefertigt habe; die aus fremden Quellen direkt oder indirekt übernommenen Gedanken sind als solche kenntlich gemacht. Die Arbeit wurde bisher weder im Inland noch im Ausland in gleicher oder ähnlicher Form einer anderen Prüfungsbehörde vorgelegt.

Diese Dissertation wurde am Institut für Kern- und Teilchenphysik der Technischen Universität Dresden unter der wissenschaftlichen Betreuung von Prof. Dr. Klaus R. Schubert angefertigt.

Dresden, 21. Februar 2002

Tilmann Colberg

HSSS AdminTools (c) 2001, last visited: Tue Jun 04 10:04:46 GMT+02:00 2002